Experimental and computational studies of metals doped α/β-PbO nanoparticles and lead oxide thin films for photocatalytic application

By

Fikadu Takele Geldasa

A PhD Dissertation Submitted to the department of Applied Physics

School of Applied Natural Science

Presented in Partial Fulfillment of the Requirements for the Degree of Doctor of Philosophy in Applied Physics (Material Physics)

Office of the Graduate Studies

Adama Science and Technology University

June 2023

Adama, Ethiopia

Experimental and computational studies of metals doped α/β-PbO nanoparticles and lead oxide thin films for photocatalytic application

Ph.D. Candidate:
Fikadu Takele Geldasa

Major-supervisor:
Dr. Fekadu Gashaw Hone[1] (Associate Prof. of Physics)
Co-supervisors:
Dr. Megersa Wodajo Shura[2] (Associate Prof. of Physics)
Dr. Mesfin Abayneh Kebede[3] (Prof. of Physics)
[1]Addis Ababa University, Department of Physics, P.O. Box: 1176, Addis Ababa, Ethiopia.
[2]Adama Science and Technology University, Department of Applied Physics, P. O. Box 1888, Adama, Ethiopia
[3]Institute for Nanotechnology and Water Sustainability, College of Science, Engineering and Technology, University of South Africa, Florida Science Campus, Johannesburg, 1710, South Africa.

A Dissertation Submitted to the department of Applied Physics,
School of Applied Natural Science

Presented in Partial Fulfillment of the Requirement for the Degree of Doctor of Philosophy in Applied Physics (Specialization in Materials Physics)

Office of Graduate Studies
Adama Science and Technology University

June 2023
Adama, Ethiopia

DECLARATION

I hereby declare that this Dissertation entitled "**Experimental and computational studies of metals doped α/β-PbO nanoparticles and lead oxide thin films for photocatalytic application**" is my original work conducted at the Applied Physics Department, Adama Science and Technology University under the supervision of Dr. Fekadu Gashaw Hone, Dr. Megersa Wodajo Shura and Dr. Mesfin Abayneh Kebede. That is, it has not been submitted for the award of any academic degree, diploma or certificate in any other university. All sources of materials used for this thesis have been duly acknowledged through appropriate citations.

Fikadu Takele		05/07/2023
Name of student	Signature	Date

Post Graduate Office Dean

RECOMMENDATION

We, the supervisors of this dissertation, hereby certify that we have read and revised the dissertation entitled "**Experimental and computational studies of metals doped α/β-PbO nanoparticles and lead oxide thin films for photocatalytic application**" prepared under our guidance by **Fikadu Takele Geldasa** submitted in partial fulfillment of the requirements for the degree of Doctor of Philosophy in **Applied Physics (Material Physics)**. Therefore, we recommend the submission of the dissertation to the department for further review and defense.

Dr. Fekadu Gashaw		05/07/23
Major Supervisor	Signature	Date
Prof. Mesfin Haregot		05/07/23
Co-supervisor	Signature	Date
Dr. Megersa Wodajo		05/07/23
Co-supervisor	Signature	Date

APPROVAL SHEET

We hereby certify that the recommendations and suggestions made by the board of examiners are appropriately incorporated into the final version of the dissertation entitled "**Experimental and computational studies of metals doped α/β-PbO nanoparticles and lead oxide thin films for photocatalytic application**" by **Fikadu Takele Geldasa**.

Dr. Fekadu Tolessa		07/07/23
Major Supervisor	Signature	Date
Prof. Yestin Abayneh		07/07/23
Co-supervisor	Signature	Date
Dr. Megersa Wodajo		05/07/23
Co-supervisor	Signature	Date

We, the undersigned, members of the Board of Examiners of the dissertation open defense by **Fikadu Takele Geldasa** have read and evaluated the dissertation entitled "**Experimental and computational studies of metals doped α/β-PbO nanoparticles and lead oxide thin films for photocatalytic application**" and examined the candidate during open defense. This is, therefore, to certify that the dissertation is accepted for partial fulfillment of the requirement of the degree of Doctor of Philosophy in Applied Physics (**Material Physics**).

Dr. Feradu Tolessa		07/07/23
Chairperson	Signature	Date
Dr. Alemu Kebede		05/07/23
Internal Examiner 1	Signature	Date
Dr. Solomon T.		05/07/23
Internal Examiner 2	Signature	Date
Dr. Paulos Taddesse		05/07/23
External Examiner 1	Signature	Date
Dr. Belayneh Mesfin		05/07/23
External Examiner 2	Signature	Date

Finally, approval and acceptance of the dissertation is contingent upon submission of its final copy to the Office of Postgraduate Studies (OPGS) through the candidate's Department Graduate Council (DGC) and School Graduate Committee (SGC).

ፍቃዱ ቶለሳ ማሬሚ (ዶ/ር) Fekadu Tolessa Maremi (phD)		07/07/23
Department Head	Signature	Date
ከሮ ጀማል አደም (ዶ/ር) Kero Jemal Adem (PhD)		07/07/23
School Dean	Signature	Date
ለገሠ ለመቻ አብሡ (ዶ/ር) Legesse Lemecha Obsu (Ph.D)		14/07/23
የድህረ ምረቃ ጽ/ቤት ዲን Office Dean Postgraduate Studies, Dean	Signature	Date

ACKNOWLEDGEMENT

First and foremost, I would like to thank and praise God, the Almighty, who has granted me countless blessings and shield around me. Almighty God, I have experienced your guidance all time. In all my ways, I acknowledge you, and you will facilitate all my future careers. I will keep on praising to you for the rest of all my life.

Apart from my efforts, the accomplishment of this dissertation depends hugely on the guidelines and encouragement of my supervisors. Words cannot express my gratitude to my major supervisor Dr. Fekadu Gashaw Hone for his invaluable patience and feedback. His generosity, tremendous support and advice are difficult to express in words. This dissertation would not have materialized without his guidance and encouragement. I also could not have undertaken this journey without my co-supervisors, Dr. Megersa Wodajo Shura and Dr. Mesfin Kebede Abayneh, who generously spent their precious time in giving me guidance, encouragement, suggestion, and constructive comments for this dissertation.

I am also grateful to Applied Physics staff members for their moral support. Specifically, I thank Prof. Abebe Belay for his encouragement during my experimental work. I also thank Dr. Fekadu Tolosa, head of the Applied Physics department, for his patience and endless support in writing me supportive letters to different departments during my laboratory work. Special thanks go to Dr. Mesfin Asfaw for his encouragement and support in completing my Ph.D. courses. Thanks should also go to the laboratory assistant Mr. Guta Amanu Department of Applied Chemistry, for his equipment support. I would like to express my deepest appreciation to the Department of Material Science and Engineering for their material support and for allowing me to carry out the Experiments of this dissertation. I would also like to thank Addis Ababa University, Department of Physics, for their support in sample characterization. Additionally, this endeavor would not have been possible without the generous support from the Adama Science and Technology University and Oda Bultum University in financing my research.

Lastly, I would like to thank my family, especially, my mother Alemitu Chali, my father Takele Geldasa and all my brothers and sisters. I would give special thanks for their understanding and continuous support during my study. It would be difficult to find adequate words to express my gratitude for their belief in me that kept my spirits and motivation high, but I can say thank you again, and may God bless you.

TABLE OF CONTENTS

LIST OF TABLES

LIST OF FIGURES

LIST OF ACRONYMS AND ABBREVIATIONS

AA	Ascorbic acid
ALD	Atomic layer deposition
AMCSD	American Mineralogist Crystal Structure Database
AOP	Advanced oxidation process
BFGS	Broyden-Fletcher-Goldfarb-Shanno
BM	Burstein–Moss
BZ	Brillouin zones
CASTEP	Cambridge Serial Total Energy Package
CB	Conduction band
CBD	Chemical bath deposition
CBM	Conduction band minimum
CBZ	Carbamazepine
CVD	Chemical vapor deposition
DFT	Density functional theory
DRS	Diffuse reflectance spectroscopy
EDTA-2Na	disodium ethylenediaminetetraacetate
EDX	Energy dispersive X-ray analysis
EELS	Energy loss electron spectrum
FWHM	Full width at half maximum
GGA	Generalized Gradient Approximations
IPA	Isopropyl alcohol
IUPAC	International Union of Pure and Applied Chemistry
JDOS	Joint density of states
LDA	Local Density Approximations
MAO	Monoamine oxidase
MB	Methylene blue
MBE	Molecular beam epitaxy
MONPs	Metal oxide nanoparticles
NHE	Normal hydrogen electrode
JCPDS	Committee on Powder Diffraction Standard

PAW	Projector augmented wave
PDOS	Partial density of states
PL	Photoluminescence spectrometer
PVD	Pulse vapor deposition
ROS	Reactive oxygen species
SEM	Scanning electron microscopy
SIESTA	Spanish Initiative for Electronic Simulations with Thousands of Atoms
TC	Tetracycline
TDOS	Total density of states
USPP	Ultrasoft pseudopotential
VASP	Vienna Ab initio Simulation Package
VB	Valence band
VBM	Valence band maximum
XRD	X-ray diffractometer

ABSTRACT

Photocatalysts are promising materials to suppress the environmental pollution and energy crisis encountered in the world. In this research, undoped and different metals (Sn, Co, Cu, Ni, and Li) doped α-PbO and β-PbO phases nanoparticles were successfully synthesized by a facile chemical precipitations method and utilized for the degradation of Methylene blue dye under visible light irradiation. The synthesized nanoparticles were further studied by using different characterization techniques. The XRD results confirmed that the prepared nanoparticles were pure α-PbO and β-PbO phases that are free of the mixture of the two and other PbO phases. The obtained optical band gaps from UV-Vis DRS analysis were 2.03 eV, 2.68 eV, 1.61 eV, 1.78 eV, 1.67 eV, and 2.00 eV for pristine α-PbO, Sn, Co, Cu, Ni, and Li doped α-PbO respectively. For pristine β-PbO, Co, Cu, Ni, Li, and Sn doped β-PbO, the obtained band gap was 2.68 eV, 1.88 eV, 2.01 eV, 2.65 eV, 2.64 eV, and 2.70 eV respectively. The results from the PL emission reveals that, the lowest PL intensity of the doped samples indicated the low recombination of the electron-hole pairs that improved the photocatalytic performance of pristine α-PbO and β-PbO nanoparticles. The SEM and EDX were used to analyze the surface morphology and composition of the synthesized nanoparticles, respectively. The photocatalytic activities of the prepared nanoparticles were assessed through the degradation of the Methylene Blue (MB) dye under visible light irradiation. The UV-Visible spectrophotometer analysis showed that the MB dye concentration decreased as the irradiation time varied from 0 to 100 min for α-PbO and from 0 to 80 min for β-PbO. The results show that within 100 minutes, the Sn-doped α-PbO nanoparticles possessed the maximum degradation efficiency compared to other metal-doped α-PbO nanoparticles, with 100% MB dye degradation compared to 94.76 % by pristine α-PbO. This is attributed to the broader light harvesting in the visible region to facilitate in photocatalytic degradation of MB dye. All doped β-PbO nanoparticles exhibit enhanced photocatalytic activity compared to pristine β-PbO towards the degradation of MB dye under visible light irradiation. In particular, Cu and Co-doped β-PbO exhibit 99.45% and 99.39% degradation rates of MB dye after 80 min of irradiation, respectively, whereas pristine β-PbO exhibit only 75.13%. After doping, the band gap narrowing, formation of impurity states, enhanced specific surface area, higher carrier concentration, reduced carriers recombination, surface roughness, the action of dopant ions, and microstructural changes in the catalyst aspects are enhanced the photocatalytic activity of pristine β-PbO. Additionally, PbO thin films with nanorods, nanosheets, and cauliflower-shaped were produced using a one-step chemical synthesis approach by just varying the cation concentrations to identify PbO phases. Density functional theory (DFT) is also used to characterize the material's properties for photocatalysis applications. The obtained indirect bandgap, the impurity level induces the bandgap narrowing, enhanced optical properties, and the decrease of effective masses of photogenerated carriers in the DFT study of different metal doped α-PbO and β-PbO shows the trends of improvement of photocatalytic performance. The indirect bandgap property is indicated by the calculation of electronic band structure, with spin-up bandgap values of 2.28 eV, 0.68 eV, 1.01 eV, 1.57 eV, 1.79 eV, and 1.76 eV for pristine, Co, Ni, Cu, Li, and Sn doped β-PbO, respectively by using PBE exchange functional. The bandgap values of 1.75 eV, 1.14 eV, 1.36 eV, 1.30 eV, 1.57 eV, and 1.53 eV were also obtained for pristine, Co, Ni, Cu, Li, and Sn-doped α-PbO, respectively using the same method. The DFT result provides in-depth functional characteristics for guiding laboratory working experiments and the applications of the materials in various fields such as photocatalysis, energy storage, and solar cells.

Keywords: *α-PbO, β-PbO, Chemical precipitation, Photocatalysis, CBD, DFT, Thin film, Dyes*

1. INTRODUCTION

1.1. Background of the study

Nowadays, environmental pollution and the energy crisis are the two main concerns of our world. With urban growth and rapid industrialization, our globe is in an era of prosperity and wealth. The increasing of world population and continuous development of urban, industrial, and agricultural processes cause the increase of trend pollutants in air and water sources. Human activity due to population growth like households and the development of industrial and agricultural byproducts are mostly organic pollutants. If these organic contaminants are biodegradable, they can be treated by biological processes. However, pollutants from industries such as textiles, pharmaceuticals, and agriculture often contain low biodegradability. Other activities such as chemicals, microbes, metal plating, pulp, refineries, and food processing are waste-generating businesses that discharge many wastes contaminating terrestrial land, our atmosphere, and water sources (Qumar et al., 2022).

Textiles industries byproducts pollute the environment, particularly the water resources, due to the discharges of various types of dyes to the water sources and the random use of dyes. Thus, the textile industry's polluted water source contains a variety of organic dyes and chemicals that make the chemical composition of these effluents a major environmental problem (Touati et al., 2016). On the other hand, antibiotics are used to treat animal and human diseases. The consumption of these antibiotics leads its compositions to be released into the environment after incomplete metabolism. The entering of these compounds into the environment through wastewater from the pharmaceutical industry, human and animal waste deposits, and hospitals cause environmental pollution and it is impossible to remove by using traditional treatments (Olama et al., 2018). Agricultural waste products also cause environmental pollution, including water sources. For the development of modern agriculture, pesticides are used. Pesticides and agro-waste water are risks to human health and aquatic ecosystem (Kushniarou et al., 2019).

Moreover, the synthetic dyes which are widely used in the textile industries and agriculture are physically and chemically stable compounds that enormously affect the environment. Some of these organic pollutants are persistent and identified at a significant level in surface and groundwater, soil, and wastewater effluents (Z. Wang et al., 2019). Different conventional

techniques such as biological treatment, anaerobic, electrochemical, aerobic, oxidation, adsorption, flotation, reduction, precipitation, flocculation, etc., have been used in wastewater treatment (Adeel et al., 2021). However, these techniques cannot fully degrade the organic pollutants. On the other hand, we can classify the developed methods to eliminate or reduce organic pollutants into four types (Al-Tohamy et al., 2022; Q. Li et al., 2021; Slama et al., 2021): (i) physicochemical which includes membrane bioreactor, adsorption, sedimentation, coagulation, filtration, and flocculation; (ii) chemical treatment which includes chemical reduction, electrochemistry, advanced oxidation process (AOP), ozone oxidation, enzymes, and photocatalytic degradation; (iii) bioremediation which includes biological oxidation, and activated sludge; (iv) the combined process. Physicochemical treatment has advantages such as low cost, high treatment efficiency, and easy operation, but its degradation ability is low. Bioremediation can remove organic pollutants from large areas at a very low cost, but it is with low efficiency. Chemical treatment has an incredible efficiency to mineralize organic pollutants, but it can cause secondary pollution.

Over the previous decade, researchers around the world made great efforts to develop a more powerful, newer, and promising technique called advanced oxidation process (AOP) (Uddin et al., 2020). The AOP is the most attractive method to remove organic pollutants in wastewater (Mehrjouei et al., 2015). This method is an alternative to traditional techniques such as adsorption and coagulation because the AOP process mineralizes the organic pollutants rather than moving from place to place. Thus, photocatalysis is a promising AOP and is a green method to decompose organic pollutants non-selectively and quickly from wastewater by using semiconductor metal oxides as photocatalyst materials (Ndabankulu et al., 2019). This meant that, for overcoming environmental pollution, the degradation of harmful and toxic contaminant organic compounds using semiconducting photocatalysts is of great significance (Zhou et al., 2021). Photocatalysis is a more proficient technique that involves the breakdown or decomposition of different organic pollutants, various dyes, and harmful viruses and fungi using UV or visible light solar spectrum (Muthukumaran et al., 2020). Photocatalysis is discovered in 1972 during the oil crisis in 1973 and the energy crisis in 1979 for the production of hydrogen production by water splitting (Boyjoo et al., 2017). It has progressed rapidly since the photoelectrochemical water-splitting reaction with semiconductors was discovered by Fujishima and Honda in 1972 (Fujishima & Honda, 1972). Nowadays,

photocatalysis oxidation processes through semiconductor metal oxide nanoparticles is globally accepted and is the most advanced techniques (Sood et al., 2015).

After the discovery of photocatalysis technology, the researchers' mind is attracted to an understanding of the fundamental mechanisms of photocatalysis and improving the photocatalytic properties of the discovered photocatalysts. The photocatalysis technique depends on the reaction between powerful oxidizing and reducing agents (holes and electrons) generated through the illumination of UV or visible solar spectrum on the surface of photocatalyst materials and harmful organic pollutants (D. Zhu & Zhou, 2019). The photo-induced electrons and holes react with oxygen (O_2), water (H_2O), and hydroxyl groups to generate reactive oxygen species (ROS) such as hydroxyl radicals (•OH) and superoxide radical anions (O_2•−) with strong oxidation abilities. These ROS are the foremost accountable species for the degradation of persistent organic pollutants in wastewater. These phenomena can be utilized to solve the main problems of our world today in the energy crisis by the process of water splitting to generate hydrogen gas which is used as fuel and environmental pollution through the degradation of organic pollutants in wastewater (Mehtab et al., 2022). Thus, the application of photocatalysis is not limited to the degradation of organic pollutants; it is also applied in a bacterial disinfectant and for the removal of antibiotics from the water. It has great potential in the evolution of hydrogen (H_2) by water splitting as green energy fuel, in the production of hydrocarbon fuel by reducing carbon dioxide (CO_2), and the potential of changing NO and NO_2 into nitrate which is used as fertilizer to stimulate the growth of plants (Luo et al., 2019; Zahid & Han, 2021).

According to the researcher's investigation, the nanosized particles show an essential photocatalysis process, due to their unique chemical and physical properties, high surface-to-volume ratio, fast dissolution, strong sorption, and high reactivity with respect to their bulk of the same compositions (Ayodhya & Veerabhadram, 2018; Sapna Yadav et al., 2022). Among these nanosized materials, metal oxide nanoparticles (MONPs) are used as prominent photocatalysts. MONPs have a wide range of applications including environmental remediation, energy storage, electrochemistry, sensors, lubrication, coatings, and other various areas of nanotechnology (Qumar et al., 2022). Various semiconducting metal oxide photocatalyst materials have been developed to date. Semiconducting metal oxides such as TiO_2, ZnO, SnO_2, Cu_2O, Fe_2O_3, $SrTiO_3$, zinc germanium oxide, bismuth oxides, copper

oxides, and WO_3 have got much attention due to their ability in the degradation of various organic pollutants (Djurišić et al., 2014; Zhou et al., 2021). Their effective advantages are attributed to their large surface area, small size, enhanced optical and chemical properties, and electrical conductivity properties (Sukumar et al., 2020). However, there are some shortcomings of metal oxide semiconductor photocatalysts such as a small range of the solar spectrum absorption abilities, wide bandgap, and fast recombination rates of photogenerated electrons and holes which reduce their photocatalytic activities (Danish et al., 2021; Mehtab et al., 2022). A photocatalyst material with wide bandgap value requires more energy to be absorbed for charge carrier separation. In addition, the photogenerated electrons and holes could recombine without forming oxidation and reduction which reduces the photocatalytic activities of these photocatalysts. The fast recombination rate results in a lower number of photogenerated ROS that are available on surface reaction sites to carry out the photodegradation process. Hence, the overall photocatalytic activity is significantly reduced. Many researchers have been working on the modification of photocatalysts or engineering new photocatalysts to address these concerns. The introduction of a hetero-atom doping agent into the bulk metal oxides semiconductor modifies the photocatalytic activities of metal oxide semiconductors. Through doping with different metals the photocatalytic activity of MONPs can be enhanced under visible light spectrum (Siriwong et al., 2012). Thus, it provides a large dipole moment to change the electron transfer kinetic, and more electrons can be transferred from the valence band to the conduction band of the photocatalyst, hence narrowing the bandgap value (Danish et al., 2021; Siriwong et al., 2012). The low bandgap value indicates better absorption ability in visible light or natural sunlight. Good photocatalyst materials will now be able to reduce the recombination of photogenerated electron-hole pairs and able to absorb the visible light range of the visible solar spectrum. Additionally, materials used as photocatalysts should be abundant on earth, and cost-effective.

A lead oxide nanoparticle is among the MONPs and abundant material on earth. Lead oxide compounds are widely used in field effective transistors, photoresistors, imaging labeling, lasers, hybrid organic solar cells, diodes, and optical detector applications (Nafees et al., 2017). It has several oxide forms such as PbO, PbO_2, Pb_3O_4, and Pb_2O_3 (Noukelag et al., 2019). PbO and Pb-based oxide materials have attracted the researchers' focus due to their exceptional properties, such as mechanical, optical, and electrical (Nafees et al., 2017). PbO is

a photoactive semiconducting material and an important industrial material that has been used widely as gas sensors, pigments and paints, storage devices, UV blockers, and modifiers in oxide glasses (Arulmozhi & Mythili, 2013; Senvaitiene et al., 2007; Urhan et al., 2019). The red α-PbO and yellow β-PbO are the two polymorphic of PbO. The red α-PbO has a tetragonal structure which is known as litharge and is stable at low temperatures whereas yellow β-PbO has an orthorhombic structure which is known as massicot and is stable at high temperatures (Noukelag et al., 2019). At high temperatures, the α-PbO phase can be changed to the β-PbO phase. Their different band gap of 1.92 eV for α-PbO and 2.7 eV for β-PbO make them attractive for various applications.

The photocatalytic activity of PbO nanoparticles has been investigated for the degradation of organic pollutants (Borhade et al., 2013, 2012; Weidong Li et al., 2017). However, for photocatalysis applications of PbO, there are only very few reports, but the coupled PbO with other semiconductors has been widely reported. Thus, the combination of PbO with different metal oxide semiconductors has advantages such as shifting the ultraviolet activity of materials to visible light active by controlling bandgap and modifying the structure and morphology of the newly formed composite photocatalyst. For photocatalytic degradations, synthesis and discovery of materials which are low cost and abundant are required. Moreover, nanotechnology includes both research and engineering of new materials at the nanoscale level. Therefore, different synthetic techniques such as solvothermal (Pasha & Chidambaram, 2014), sol-gel (Ali et al., 2021), electrochemical (Urhan et al., 2019), co-precipitation (Güngör et al., 2017), oxidation of lead sheets (Yousefi et al., 2015), green methods (Khalil et al., 2017; Noukelag et al., 2019), hydrothermal (Yonggang Wang et al., 2013), microwave assisted method (Bapitha & Alagar, 2017), thermolysis (Aliakbari et al., 2014), ball milling (Tayebee et al., 2017), sonochemical (P. Gao et al., 2013; Jaafar et al., 2017), solid state thermal decomposition (Mehdi & Mehdi, 2017), laser ablation (Fu et al., 2020), thermal decomposition (S. Li et al., 2005; Salavati-Niasari et al., 2009), etc., have been used for the synthesis of lead oxide nanoparticles. Lead oxide can also be formed by the reduction of lead dioxide. Among the method of synthesizing the two polymorphs of PbO nanoparticles, chemical precipitation has the advantages such as cheap salt precursors, mass production, simple, industrial scale-up, and rapid processing.

Generally, PbO nanoparticles can be synthesized by physical, biological, and chemical

methods. The physical method is energy consuming, difficult in obtaining homogeneous particle size, and not cost-effective, whereas the chemical method such as sol-gel, Microemulsion, hydrothermal/solvothermal, and precipitations has high acceptance in control over the synthesis products (Bangi et al., 2013). Due to the simple phase changes of PbO, synthesizing high-purity PbO phases without the mixture of each is not easy. Thus, the two phases may exist together, but with different degrees of existence. In this research, the two phases of PbO nanoparticles have been synthesized independently and doped with different metals through the chemical precipitation method. However, the prepared PbO thin film in this research is the mixture of α-PbO and β-PbO phases with the major existence of the β-PbO phase. PbO can be synthesized in different nanostructures such as nanoparticles, thin films, and bulk forms. Besides α-PbO and β-PbO nanoparticles, PbO thin film can be prepared by different methods using the same precursor. Thin films deposited by physical methods have the advantages of controllable electronic properties and compositions. However, the low cost and scalability of chemical solution-based thin film deposition make them attractive alternatives (Napari et al., 2021). Among all chemical solution methods, chemical bath deposition (CBD) is a simple, extremely cheap, and reliable method for preparing PbO thin film requiring only aqueous solutions relatively at minimal infrastructure and low temperatures to obtain three different morphologies of PbO thin film. For the formation of thin films by CBD, different parameters such as bath temperature, pH, stirring rate, and concentration of the solution have great effects on the deposition of thin films. Herein, the present work focused on the effects of cation concentrations. PbO thin films with 0.1 M, 0.15 M, 0.2 M, and 0.25 M cation molar concentrations have been prepared successfully.

After successfully synthesizing different metals doped nanoparticles and various molar concentrations of thin films the structural, optical properties, and morphological properties were analyzed. For different metals doped α-PbO and β-PbO nanoparticles their photocatalytic activities towards the degradation of methylene blue dye have been investigated. However, for PbO thin film its photocatalytic activity evaluation is not included. In addition to the experimental study, the structural, electrical, optical properties, and photocatalytic activities of metals doped α-PbO and β-PbO nanoparticles have also been studied by the computational density functional theory (DFT) method. DFT is a theoretical method intensively advantageous to corroborate the obtained experimental results for

materials that can be appropriate for photocatalysis applications. In this research, the photocatalytic activity of the two polymorphs of PbO and different metals doped PbO have also been investigated using the DFT study method.

This research document is arranged into five sections. In the introduction (section 1), the background of photocatalysis, semiconductor photocatalyst, metal oxide nanoparticles, and the two polymorphs of PbO has been highlighted. The statements of the problem, general and specific objectives, scope of the study, and significance of this study have also been included in the introduction section. In the literature review (section 2), different synthesis approaches, computational DFT concepts, challenges in photocatalysis, various types of dyes discharged from textile industries, health risks of dyes, and different photocatalyst materials have been discussed in detail. In section 3, the methodologies used in this research both the experimental and DFT methods have been described. In section 4, the results obtained from both the experimental and DFT methods have been investigated in detail. The photocatalytic activity of different metal-doped α-PbO and β-PbO nanoparticles towards the degradation of methylene blue dye is also discussed in detail. In section 5, the summary, conclusion, and recommendation of this research are summarized.

1.2. Statement of the problem

Textile industries use MB dyes in large amounts and the discharged wastewater of the textile industries containing MB dye causes a serious problem in contaminating natural water sources. High oxidizing power, easy availability, and photosensitivity has made TiO_2 and ZnO as popular choices for the application of photocatalysis to degrade the textile industries discharged effluents containing MB dyes released into the water. However, they are relatively active only under ultraviolet light to establish photodegradation due to their wide optical bandgap which limits their applicability in the small area since the production of ultraviolet is expensive. The major drawbacks of photocatalysts are the high recombination rate of photogenerated electron-hole pairs, the ultraviolet light activity limitations, and low surface coverage. Visible light comprises 45% of the solar spectrum and it is abundant and ubiquitous naturally, whereas ultraviolet comprises less than 5% of the solar spectrum and is expensive. To overcome the above drawbacks, the discovery of a photocatalyst of suitable bandgap with visible light or modification of the existing photocatalyst is becoming very attractive for photocatalysis technology. Among the modifications of photocatalysts doping hetero-atom is

the most popular choice taken by many researchers. In this research, the narrow bandgap α-PbO and β-PbO nanoparticles doped with different metals which are appropriate for visible light activation, overcomes the ultraviolet response limitations of TiO_2 and ZnO photocatalysts. To enhance the photocatalytic activity of both α-PbO and β-PbO nanoparticles for the degradations of methylene blue dye, different metals such as Sn, Co, Cu, Ni, and Li have been incorporated into the two polymorphs. These dopants introduce new energy levels and defects near the valence band maximum or near the conduction band minimum which traps the photogenerated electrons and retarded the recombination rates of electron-hole pairs. Thus, the generated impurity level due to metals doping into the crystal lattice largely improved the carrier separation. In addition to these, the incorporated dopant increases the electron-hole production generated under visible light due to its enhanced light absorption. There is an experimental finding gap on the influence of metal dopants that we used in this research on the photocatalytic activity of both α-PbO and β-PbO nanoparticles elaborated by the theoretical analysis using density functional theory (DFT). By DFT calculation we can predict the photocatalytic activity of materials through the obtained electrical and optical properties. For PbO thin film deposition by varying its cation molar concentration by a chemical bath deposition method, there is a research gap.

1.3. Objectives

1.3.1. General objective

The general objective of this research is to synthesize various metals doped α-PbO and β-PbO nanoparticles and investigate their photocatalytic activities for the degradation of methylene blue dye under visible light using experimental and theoretical DFT methods and also to prepare lead oxide thin films.

1.3.2. Specific objectives

The specific objectives of this research are:

- to design and optimize low cost and environmental friendly facile chemical synthesis approach to prepare high purity α-PbO and β-PbO nanoparticles,
- to synthesize different metals (Sn, Co, Cu, Ni and Li) doped α-PbO and β-PbO nanoparticles by chemical precipitation method,
- to study the influence of different metal dopants on the structural, morphological, and

optical properties of the prepared nanoparticles by advanced characterization techniques,

- ❖ to evaluate the photocatalytic activity of different metals doped α-PbO and β-PbO nanoparticles for the degradation of methylene blue dye under visible light,
- ❖ to synthesize PbO thin film with various cation concentration by chemical bath deposition,
- ❖ to design a high-throughput computational method using density functional theory (DFT) to study the effects of doping on the structural, electrical, and optical properties of α-PbO and β-PbO nanoparticles.

1.4. Scope of the study

This research is focused on the synthesis of high purities of α-PbO and β-PbO nanoparticles and different metals doped α-PbO and β-PbO nanoparticles through the chemical precipitation method for the photocatalytic degradation of methylene blue dye. The two polymorphs of PbO nanoparticles are selected due to their simple production in a mass and low cost. Different metals such as Sn, Co, Cu, Ni, and Li are selected as dopants due to their exceptional properties in enhancing the photocatalytic activity of metal oxide nanoparticles. The selected dopants are Li from group I alkali metals; Co, Ni, and Cu from transition metals; and Sn from the post-transition metals. Alkali metals are monovalent elements and when doped into α-PbO and β-PbO, they have the capability of reducing charge recombination because Pb is a divalent ion, and during photodegradation, the charge is transferred for charge compensation, hence photocatalytic activity will be enhanced. When transition metals are incorporated into metal oxides, it improves the light absorption and conductivity of host materials by introducing impurity states and their aliovalent property is also attractive to observe their effects. Sn is among the post-transition metals and it has a well-matched ionic radius with Pb and it can occupy the sites of Pb atom. Thus in this work, the effects of each group of metals on α-PbO and β-PbO were investigated which help us to identify which group of metals has great effects on the enhancement of the photocatalytic activity of α-PbO and β-PbO. Hence, this research focuses on the photocatalysis of different metals doped α-PbO and β-PbO because there is no detailed investigation reported on their photocatalytic activities. Among the method of synthesizing, chemical precipitation has the advantages such as cheap salt precursors, mass production, simple, industrial scale-up, and rapid processing. Therefore, we have used this method for the synthesis of metals doped α-PbO and β-PbO nanoparticles.

There are different methods under the DFT for the investigation of the structural, electrical and optical properties of the materials. Quantum ESPRESSO is a simple widely used and freely available implemented method. Thus, Quantum ESPRESSO is used in this work to investigate the structural, electrical, and optical properties of different metals doped α-PbO and β-PbO. Methylene blue dye is selected as an organic pollutant model as it is extensively used in textile industries and due to the fact that a large amount of MB dye is discharged in the wastewater. In addition to the synthesis of high purity α-PbO and β-PbO nanoparticles, this research also focused on the preparation of PbO thin films by using a facile, simple, and low-cost chemical bath deposition method.

1.5. Significance of the study

This research enabled the synthesis of high-purity tetragonal α-PbO and orthorhombic β-PbO nanoparticles. This research study also solves and gives the way to overcome the high recombination rate of photogenerated electron-hole pairs, and the ultraviolet light activity limitations in photocatalysis technology. The doping strategies resulted in high mobility of electron/hole, enhanced visible light absorption, and formation of new energy states within the bandgap of α-PbO and β-PbO which has enhanced the photocatalytic activities of the pristine α-PbO and β-PbO nanoparticles. The prepared nanoparticles exhibited well visible light absorption and degradation of methylene blue dyes with high degradation efficiency. Methylene blue dye is one of the most popular dyes found on a large scale in the textile industries wastewater. Our country Ethiopia is among the developing countries establishing many industries for prosperity and wealth. According to the data from different studies, developing countries are widely discharging the textile industries' wastewater to the environment without effective and efficient management. Therefore, this research study has put the direction in which removing or degrading the dyes that exist in textile industry wastewater for environmental remediation. Finally, this research will be a valuable and relevant reference material for researchers, students and research institutes working in the same and/or related fields.

2. LITERATURE REVIEW

2.1. Metal oxide nanoparticles

Metal oxide nanoparticles (MONPs) are semiconducting materials that have tremendous applications in different areas of science and technology. Thus, nanosized metal oxides have more imperative physicochemical properties than their bulk of the same composition and have received large attention due to their electronic, catalytic, and magnetic properties (Mirzajani et al., 2018). These materials have unique properties such as cold welding, superparamagnetic behavior, higher ductility at elevated temperatures than coarse-grained ceramics, unique catalytic properties, sensitivity, and selective activity that make them indispensable tools in modern nanotechnology (Chavali & Nikolova, 2019; S. Wang et al., 2009). Additionally, they exhibit fast diffusivity, and unique adsorption properties, which makes them different from their bulk materials of the same compositions (Aliakbari et al., 2014). Low density, high surface-to-volume ratio, and quantum properties of nanoparticles are the enchanted properties of nanoparticles (Akbay et al., 2019; Güngör et al., 2017). More importantly, MONPs have potential applications that attract researchers from the fields of medicine, materials chemistry, materials science, physics, agriculture, electronics, information technology, energy, biomedical, catalysis, sensor, and environment (Tayebee et al., 2017; Yazdani Darki et al., 2021). Specifically, MONPs have been attracted for their development of new and effective strategies in environmental remediation and energy production. Among these MONPs, CuO, ZnO, Al_2O_3, Fe_2O_3, ZrO_2, MgO, AgO, SnO_2, TiO_2, CeO_2, PbO etc. are the most attractive one (Chavali & Nikolova, 2019).

As nanotechnology includes searching for and manufacturing non-existed materials at the nanoscale level, several synthetic techniques and strategies were successfully used in the development of nanotechnology. In general, there are two types of approaches to the synthesis and fabrication of nanomaterials (Baig et al., 2021; Yuliang Wang & Xia, 2004). They are (i) bottom-up approach: this approach includes miniaturization of materials components up to atomic level with further self-assembly process (physical forces operating at the nanoscale are used to combine basic units into larger stable structures) leading to the formation of nanostructures. This approach organizes atomic or molecular components to form clusters and then to grow into different morphologies. Quantum dots or nanoparticles formed from colloidal dispersion are examples of a bottom-up approach; (ii) the top-down approach starts from bulk structures, to reduce to nanostructure materials (Galstyan et al., 2018).

Nanotechnology techniques can be classified as wet, dry, and computational engineering as shown in Figure 1. Wet nanotechnology handles the process which takes place in a wet environment mostly using living organisms and different components present in the tissue, organs, and cells in living systems. Dry engineering deals with the engineering of different technological applications and it includes (i) electronics, optoelectronic, and photonics; (ii) information processing, storage, and transmission; (iii) food packing and storage; (iv) pigments, protective glasses, textiles; and (v) sensors and energy devices. Computational engineering deals with the development and use of computer-based quantum and molecular design, modeling, and simulation of properties of systems relevant to nanotechnology (Chavali & Nikolova, 2019).

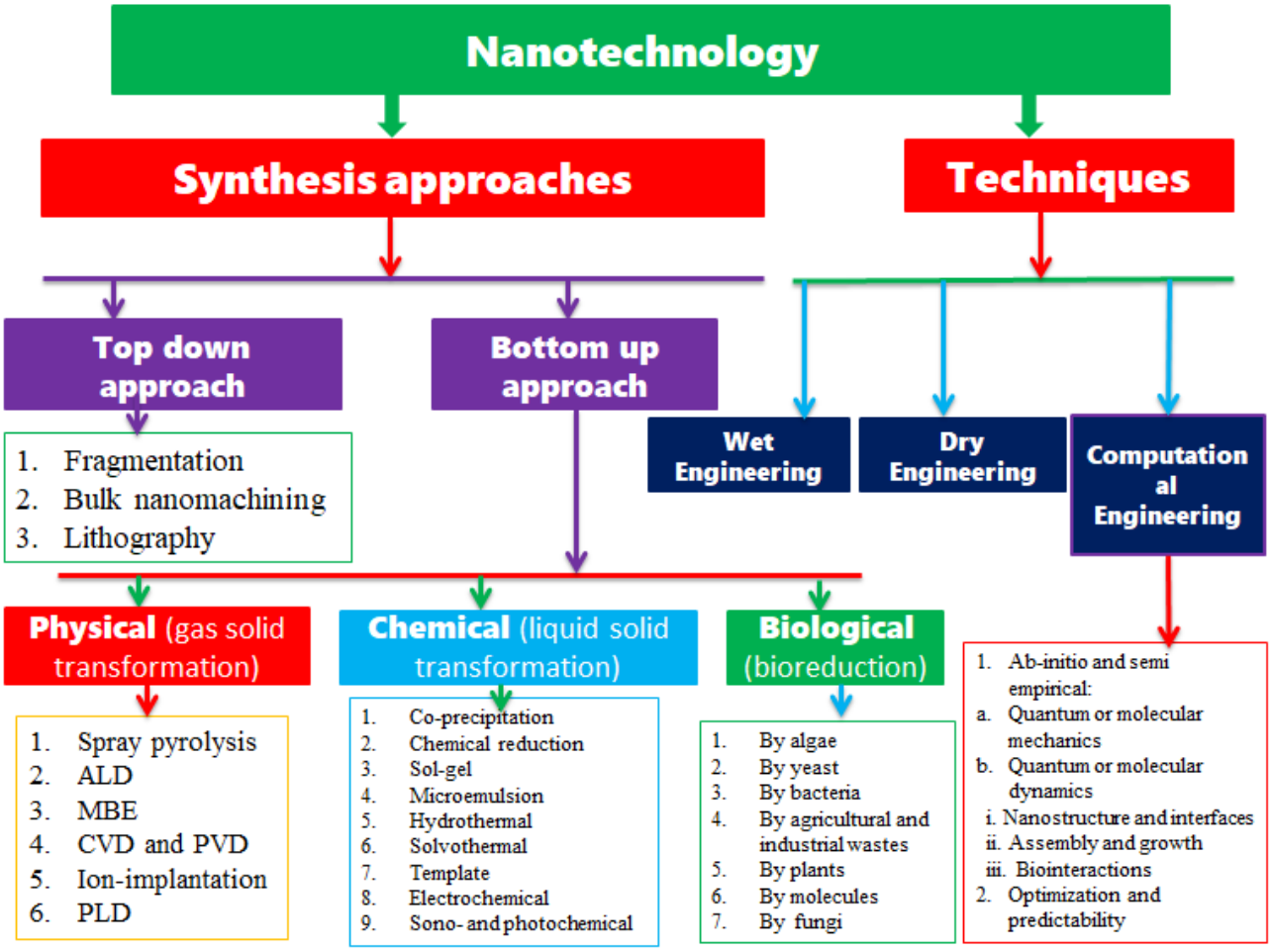

Figure 1: The major synthesis approaches of MONPs and techniques used in nanotechnology.

2.2. Synthesis of metal oxide nanoparticles

Strategies of synthesis of MONPs can be classified into top-down and bottom-up approaches

as shown in Figure 1. The top-down approach is reducing the large particle size either macro or microparticles to nanosized, whereas the bottom-up approach begins atomic growth up to nanosized particles (Medhi et al., 2020). As presented in Figure 1, the top-down approach includes fragmentation, bulk nanomachining, and lithography, whereas the bottom-up approach can be classified into physical, chemical, and biological methods. The physical methods are the process of gas transformation to solids. The physical methods under the bottom-up approaches for the synthesis of nanoparticles include spray pyrolysis, atomic layer deposition (ALD), molecular beam epitaxy (MBE), chemical vapor deposition (CVD), physical and pulse vapor deposition (PVD), ion implantation, etc., and the biological method is a green synthesis method of nanoparticles by extracting from algae, yeast, bacteria, agricultural and industrial wastes, plants, molecules, fungi, etc. The chemical methods for nanoparticle synthesis include co-precipitations, chemical reduction, sol-gel, Microemulsion, hydro and solvothermal, template, electrochemical, sono-and photochemical, etc. In this research, we only reviewed some of the chemical synthetic methods which are widely used for the synthesis of metal oxide nanoparticles.

2.2.1. Sol-Gel Process

The sol-gel process is a simple, eco-friendly, and inexpensive method that enables to control of the high purity and homogeneity of the final metal oxide nanoparticles product and also to control the size and growth of particles, and supports the addition of large concentrations of doping agents (Chakhtouna et al., 2021). The sol-gel process is used to prepare a high-quality metal oxide nanoparticle and metal oxide nanocomposite which is done by the hydrolysis process of metal alkoxides dissolved in alcohol or water. From this, the corresponding hydroxide has resulted. Thereafter, by the condensation of the formed hydroxide, a metal hydroxide polymer is formed in a densely packed gel form. To obtain the metal oxide powder of targeted particle size, the formed gel is heated and dried. Generally, the sol-gel process steps are (i) hydrolysis, (ii) polycondensation, (iii) aging, (iv) drying, and (v) thermal decomposition (Bokov et al., 2021; Parashar et al., 2020). The finally heated and dried have the possibility to give us metal oxide in a form of bulk materials, nanoparticles, or oxygen vacant based on the heat treatment process done (Danish et al., 2021). A variety of metal oxide nanoparticles like ZnO (Mahdavi & Talesh, 2017), TiO_2 (Arularasu, 2019), MgO (S. Liu et al., 2021), ZrO_2 (Heshmatpour & Aghakhanpour, 2011), CuO (Siddiqui et al., 2018),

and Nb_2O_5/SiO_2 (Lima et al., 2020) were synthesized by sol-gel process. For example, Patel et al. (Patel et al., 2022) have reported the synthesized CuO and ZnO by sol-gel process using copper (II) nitrate and zinc nitrate as starting materials respectively.

2.2.2. Co-precipitation

In the synthesis of metal oxide nanoparticles by using the co-precipitation process, the reaction takes place at ambient temperature. In this method, a solution of metal salt and a precipitating media produces a precipitated oxo-hydroxide in a solvent. KOH, NaOH, and ammonia solutions are commonly used as precipitating mediums. Thus, the alkaline nature and pH of the solution highly influence the properties and morphologies of metal oxide nanoparticles. In order to come up with the desired morphology and properties of metal oxide nanoparticles the amount, rate, and mode of alkali solution added to the reaction mixture must be added take care off. By adding surfactants it is possible to narrow the size of the produced nanoparticles as surfactants are very useful and crucial in the tailoring of surface characteristics of metal oxide nanoparticles. This method is the highly used synthesis method for metal oxide nanoparticles due to its simplicity, low cost, scale-up, and low-temperature reaction rates. It is also possible to control particle size and crystal structure by varying mediums pH and at times large amounts of nanoparticles can be prepared by using the co-precipitation method (M. et al., 2019). Various metal oxide nanoparticles such as MnO_2 (Jamil et al., 2018), ZnO (Kotresh et al., 2021), MgO (P. Yadav et al., 2022), $BiVO_4$ (Helal et al., 2020), Ni-doped SnO_2 (Kandasamy et al., 2018), N and Fe doped TiO_2 (D. Liang et al., 2019), CuO (Uma et al., 2021), Cu doped ZnO (Lemecho et al., 2022), $PbWO_4$ (Pourmasoud et al., 2017) etc. were synthesized by using co-precipitation method. Kotresh et al. (Kotresh et al., 2021) have synthesized ZnO nanoparticles via co-precipitation process at 50 ^oC and 70 ^oC reaction temperatures by using sodium hydroxide as precipitating media and zinc nitrate hexahydrate as Zn^{2+} precursor. Buraso et al. (Buraso et al., 2018) also used the same synthesizing approach for the preparation of TiO_2 by using titanium (IV) isopropoxide as a precursor. Rangel et al. (Rangel et al., 2020) have used the co-precipitation method to synthesize CuO nanoparticles by using copper chloride and copper sulfate as a precursor.

2.2.3. Hydrothermal Synthesis

Hydrothermal synthesis is a solution reaction-based method and the process is called

hydrothermal because water is used as solvent whereas in solvothermal synthesis organic solvents are used. In this method, wide range of temperature and pressure (above ambient temperature and pressure) is used for the formation of nanoparticles. By controlling the reaction pressure the morphology of the prepared nanoparticles can be controlled either decreasing or increasing pressure conditions. In this method, the aqueous mixture is heated in a sealed stainless steel autoclave above the water boiling point and increasing pressure in the reaction above atmospheric pressure. This method has significant advantages over other synthesis approaches. It can generate nanoparticles that cannot be prepared at low temperatures or room temperature and it can also produce nanoparticles if the materials have a high vapor pressure (Gan et al., 2020). During the reaction in an autoclave, the particles can be agglomerated. To prevent the agglomeration of the particles it is necessary to use a suitable stabilizer or capping agent. Several metal oxide nanoparticles such as SnO_2 (Godlaveeti et al., 2022), TiO_2 (Shahat et al., 2021), Fe_2O_3 (Abhilash et al., 2019), NiO (Khashaei et al., 2022), $BiVO_4$ (Wei et al., 2013), etc. were prepared by using hydrothermal synthesis process. Bade et al. (Bade et al., 2021) have prepared copper oxide nanoparticles by using copper sulfate pentahydrate as a precursor and NaOH as stabilizing agent via hydrothermal synthesis. Suthakaran et al. (Suthakaran et al., 2019) reported high-quality SnO_2 nanoparticles synthesized by hydrothermal synthesis and they studied the photocatalytic activity of these nanoparticles by degrading methyl violet dye.

2.2.4. Microemulsion

Stankic et al. (Stankic et al., 2016) reviewed the Microemulsion method consisting of oil and water immiscible phases. These immiscible phases are separated by surfactant molecules creating an oil/surfactant and water surfactant binary system. The surfactant molecules have properties of a hydrophobic tail which is dissolved in the oil phase and a hydrophilic head which is grouped to the water phase. To synthesize the homogenized phase the proper amounts of metallic precursor, surfactant, water, and oil are mixed while stirring at room temperature. For the precipitation of nanoparticles, oxidizing agent, reducing agent and precipitating agent are added while stirring vigorously and thereafter, followed by centrifugation subsequently washing and drying or annealing takes place. The shape and size of metal oxide nanoparticles synthesized by this method can be easily manipulated. Different metal oxide nanoparticles like Fe_2O_3 (Wongwailikhit & Horwongsakul, 2011), CeO_2 (Shlapa

et al., 2019), NiO (Du et al., 2012), ZnO (Yildirim & Durucan, 2010), TiO_2 (Zori, 2011), CuO (A. Kumar et al., 2013), etc. were synthesized by using Microemulsion method.

2.2.5. Sonochemical Synthesis

The sonochemical method uses ultrasound to facilitate the chemical reaction in which the ultrasound induces a chemical effect on the reaction process. In sonochemical synthesis, a starting material is dissolved in a solvent to get a solution. Thereafter, the resulting solution is irradiated with ultrasonic waves with a frequency above 20 kHz. The ultrasonic irradiation causes acoustic cavitation that leads to the formation, growth, and implosive collapse of bubbles in a liquid (Stankic et al., 2016). The implosive collapse of millions of bubbles in the liquid generates extremely high energy (temperature 5000 K and pressure 20 MPa) and is subsequently released thereby heating the solution. In general, for metal oxide preparation we follow three steps: (i) formation of metal hydroxide precursor's precipitate, (ii) ultrasonic irradiation, (iii) transformation to metal oxide nanoparticles through heat treatment. The rate at which the solution is cooled affects the crystal shape and morphology of the resulting metal oxide nanoparticles. This method is advantageous as it is rapid, non-hazardous and it produces metal oxide nanoparticles of high surface area, uniform size, and high purity products. In addition to this, sonochemical is a low-cost process and also produces small particle sizes (Dheyab et al., 2021). Various metal oxide nanoparticles such as TiO_2 (Guo et al., 2011), Cu-doped CeO_2 (Mousavi-Kamazani & Azizi, 2019), La-doped CeO_2 (Kishor Kumar & Kalathi, 2018), ZnO (Noman et al., 2020), Zn_2SnO_4-V_2O_5 nanocomposite (Ramasamy Raja et al., 2018), MoO_3 (Manivel et al., 2015), Ag̊-$PbMoO_4$ (Gyawali et al., 2013), Co and Mn co-doped W_3O_8 (Arunadevi et al., 2019), Cu_2O (Muthukumaran et al., 2020), etc. were produced by using this method. H-Roshan et al. (Hassanjani-Roshan et al., 2011) have prepared iron oxide nanoparticles by using the sonochemical method and they argued that morphology and size of the final product were influenced by the parameters such as power of ultrasonication, temperature, and sonication time. Noman et al. (Noman et al., 2020) reported the successfully prepared ZnO nanoparticle by the sonochemical process for photocatalytic applications.

2.3. Dyes

Dyes are used for the coloration of several materials such as textile fibers, cosmetics, paper, food, tannery, leather, pharmaceutical products, etc., (Slama et al., 2021). Generally, dyes can

be classified as natural and synthetic. Natural dyes are the naturally existing dyes originating from plants part including leaves, berries, wood, fungi, lichens, and bark, while synthetic dyes are man-made dyes synthesized from chemicals, petroleum derivatives, and earth minerals (Hitam & Jalil, 2020). Various synthetic dyes and their applications are presented in Figure 2. These dyes are mostly used in food and beverages, printing, textile industries, and pharmaceuticals. The textile industry is the main contributor to the dyes released into the environment. The annually worldwide fabricated dyes are about 7×10^7 tons and over 10,000 different types of dyes are used by textile industries (Al-Tohamy et al., 2022). Azo dye, for instance, aniline yellow dye is used in textile industries in the production of nylon and silk. Acid dye like acid blue is used in the production of cosmetics, wool, and leather. Reactive dye, reactive red 198, is applied in the production of nylon, silk, and wool. Sulfur dye, thiazine, is used in the fabrication of paper, silk, and cotton. Mordant dye, mordant red 11, is used in the production of anodized aluminum, and wool. Direct dye, direct yellow 11, is applied in the fabrication of paper, cotton, and leather. Disperse dye, disperse red 60, is used in the production of plastic, polyamide, and nylon. A basic dye, methylene blue, is used in the ink, and medicine fabrication.

These dyes are used as coloration in textile industries and discharging textile industry wastewater into water bodies is not important as the color prevents re-oxygenation in receiving water by cutting off the penetration of sunlight. These organic dyes have a complex structure and can produce aromatic amines as they are released into the environment. These carcinogens and hazardous dyes resist the sunlight entering into the water bodies resulting in influencing the natural aquatic processes such as biodegradable and photosynthesis (Koe et al., 2020). When they are released into the environment, they cause environmental pollution and are highly toxic to aquatic life, microorganisms, and human beings as they are mutagenic and carcinogenic (Uddin et al., 2020). Dyes found in wastewater discharge or dust produced in the textile industry pose a serious health concern to the human being as presented in Figure 3. These dyes affect our body systems such as the immune, respiratory, and reproductive and also affect vital organs including the heart, liver, kidney, and brain (Slama et al., 2021). They cause diseases either directly via inhalation such as nausea, respiratory problems, allergy, asthma, dermatitis, and eye or skin irritation, or indirectly via the food chain including tuberculosis, gene mutations, cancer, heart disease, and hemorrhage.

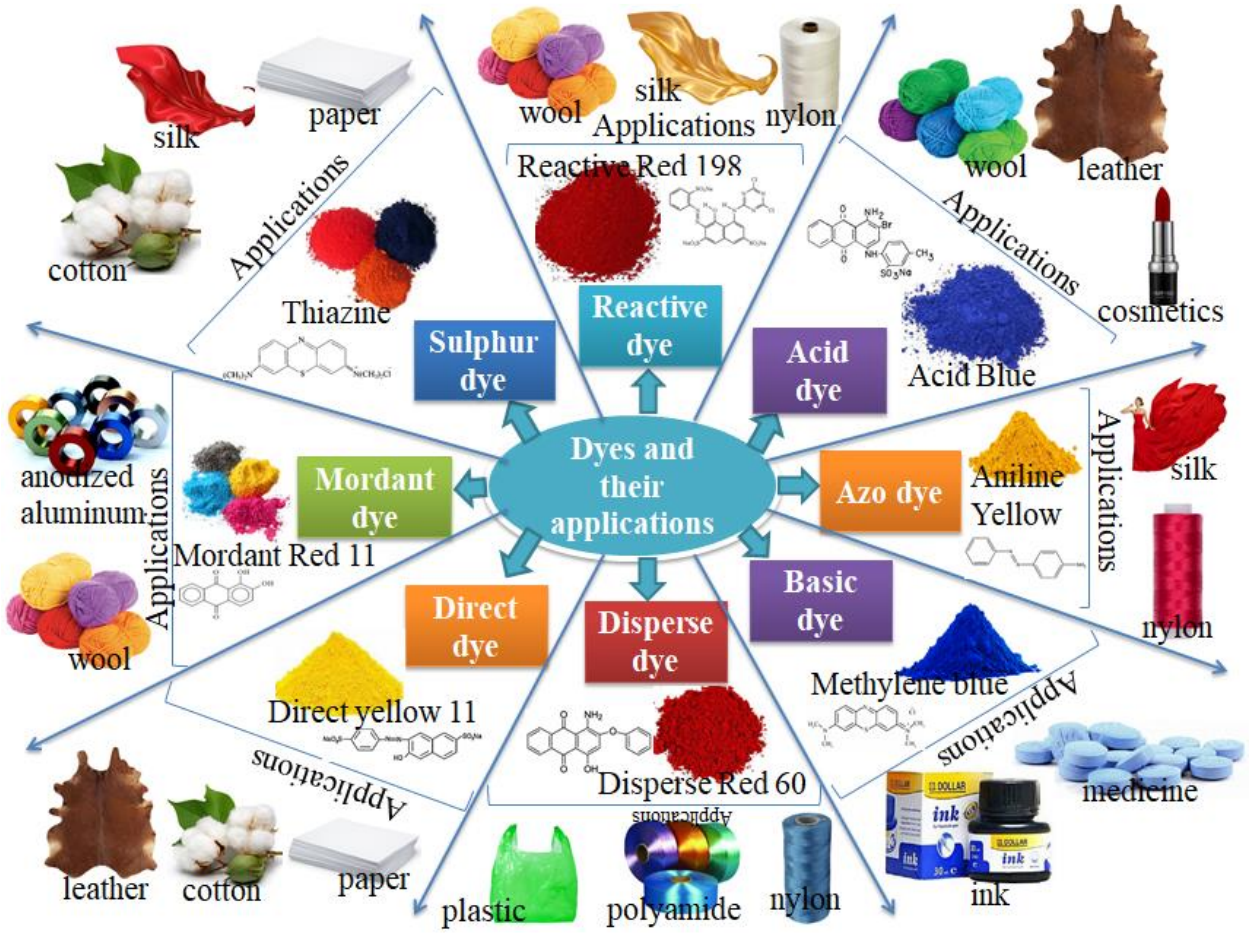

Figure 2: Different types of dyes and their application in industries (colors online) (Al-Tohamy et al., 2022).

2.3.1. Toxicity of Methylene Blue

The fabrication of synthetic dyes is on the way to increasing due to their highly demanded in the textile and clothing industries. In addition to the aforementioned dyes, dyes such as crystal violet, aniline blue, basic fuchsin, congo red, toluidine blue, and methylene blue are also a few examples of synthetic dyes. These synthetic dyes are remains in the environment when directly or indirectly released to the environment because most of them are non-biodegradable and are not completely removed during conventional water treatment. Thus, they persist in the environment because of their high stability to light, temperature, water, and other substance such as detergent and soap (Oladoye et al., 2022). Effluents from textiles and factories using dyes release highly colored dyes which can damage the aquatic environment (Krishna Moorthy et al., 2021).

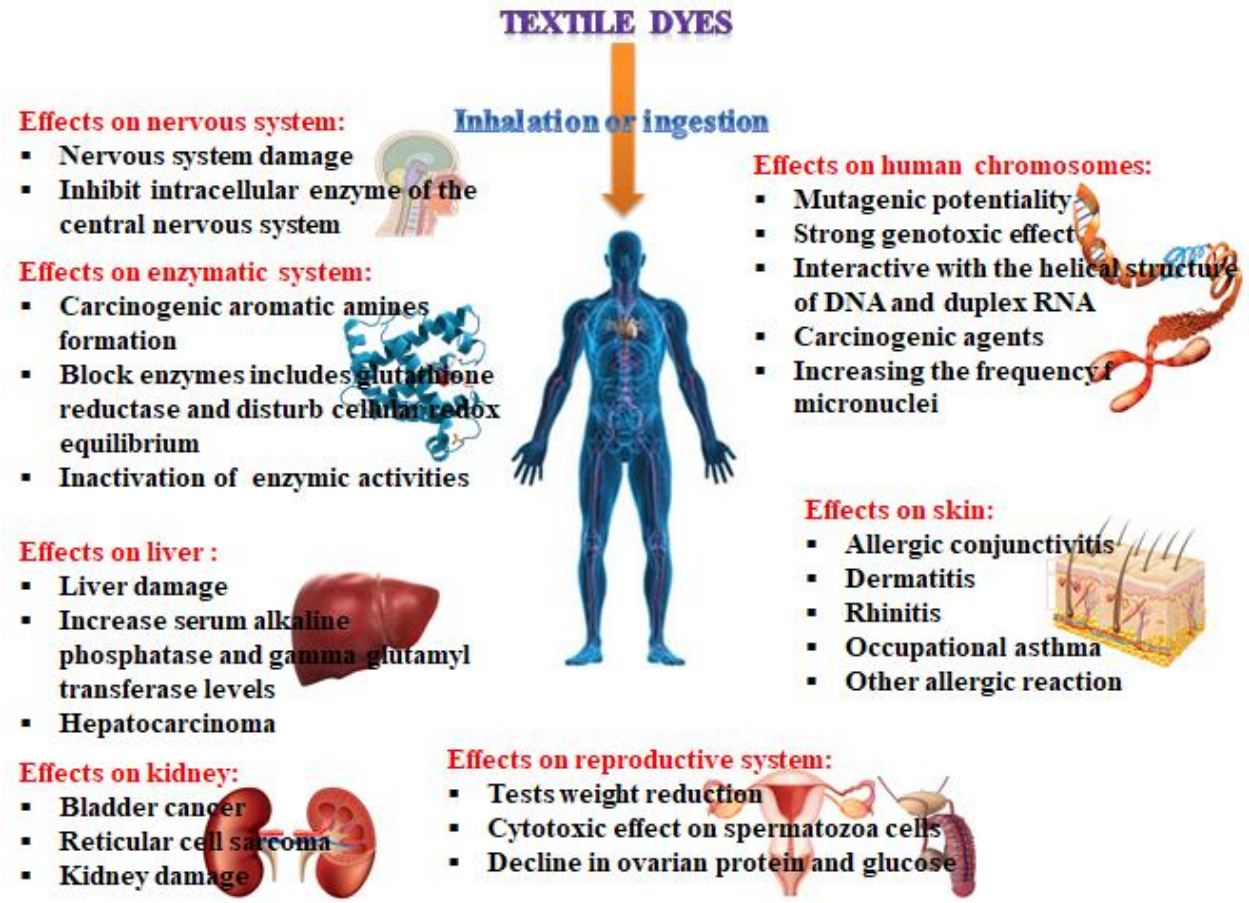

Figure 3: Negative effects of textile dyes on human health on different parts of the body (colors online) (Al-Tohamy et al., 2022).

MB dye is applied in a huge amount as a colorant for silk, paper, cotton, and in wool. In addition to these, cosmetics, food, and pharmaceutical industries consume large amounts of MB dye in their fabrications (Dardouri & Sghaier, 2017). MB is a cationic dye and a heterocyclic aromatic compound with a planar structure (Oladoye et al., 2022; Ong et al., 2005). It has $C_{16}H_{18}N_3SCl$ chemical formula with a molecular weight of 319.85 g/mol. MB is highly soluble in water and forms a stable solution at room temperature. MB is a class of phenothiazine with an International Union of Pure and Applied Chemistry (IUPAC) name [3,7-bis(dimethylamino) phenothiazine chloride tetra methylthionine chloride] with color index (CI) 52015 (Khan et al., 2022; Saeed et al., 2016). MB is non-biodegradable and carcinogenic having to characteristic stability of aromatic ring molecular structure as presented in Figure 4. When released partially or without treating the MB dye contaminated wastewater from any of the industries that uses MB dye could cause a lot of human health

risks. For example, it will cause vomiting, increased heart rate, Heinz body formation, shock, quadriplegia, cyanosis, jaundice, and tissue necrosis in human beings (Khodaie et al., 2013). Among the health risks associated with the discharge of untreated MB-loaded wastewater also includes respiratory disorder, genitourinary complications, gastrointestinal complications, cardiovascular issues, central nervous system, and dermatological effects (Ramsay et al., 2007). The discharge of MB dye wastewater into the environment also causes risks such as reduction of pigment, growth inhibition, and protein content of microalgae *Spirulina platensi* and *Chlorella vulgaris* in plants (Krishna Moorthy et al., 2021). Moreover, the discharge of untreated MB dye-loaded water to either groundwater or surface water recently causes a shortage of clean water in society. Commonly, developing countries released large amounts of MB dye-loaded wastewater into the physical environment without efficient and effective managements (Fito et al., 2020).

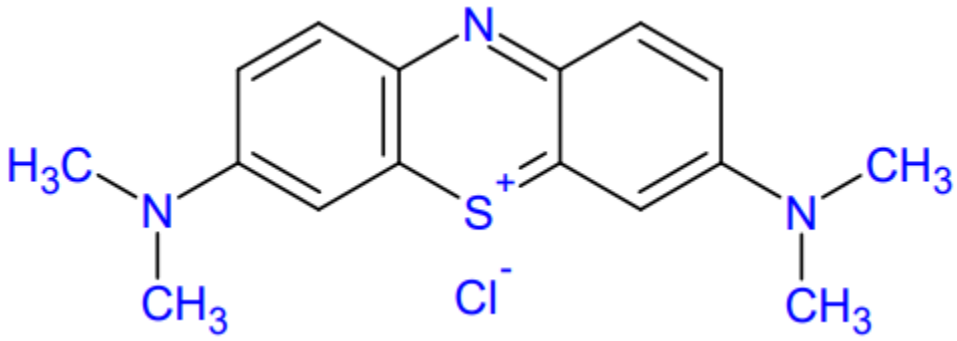

Figure 4: Molecular structure of Methylene Blue.

Additionally, it is known that MB is commonly an inert dye, but it has acted as a potent reversible monoamine oxidase (MAO) inhibitor (MAOI) which makes it to find applications in medicine by ameliorating a clinical condition known as hypotension and improving hyper-dynamic and hypoxia circulation in cirrhosis of the liver and severe hepatopulmonary syndrome (Gillman, 2006; McDonnell et al., 2012; Oladoye et al., 2022). However, if infused intravenously at a dosage higher than the recommended concentration, MAOI may precipitate serious serotonin toxicity (Gillman, 2006; Prashant & Jyothi, 2010). Serotonin toxicity, also called serotonin syndrome, is a deadly disorder that is linked to elevated serotonergic activity in the spinal cord and brain (McDonnell et al., 2012). Also, skin contacting MB by using improperly or untreated MB-loaded water causes redness and itching, and skin necrosis; which causes the death of cells in tissues and organs (Shakoor & Nasar, 2017). Generally, the

discharge of MB-loaded wastewater from any utilization causes devastating effects on the environment. Therefore, it shall be removed or degraded before being exposed to the environment. However, it cannot easily be removed by a traditional treatment because of its non-biodegradability and persistence. The photocatalytic mechanism is the most effective way to degrade these dyes.

2.4. Photocatalytic Applications of Metal Oxides

Various metal oxides are used as photocatalyst in photocatalysis technology. Photocatalysis is potentially applied in the fields including (i) photodegradation of organic pollutants, (ii) for hydrogen evolution by water splitting, (iii) photoreduction of CO_2 into renewable fuels such as CH_4 and CH_3OH (He & Zhang, 2019). Metal oxide nanoparticles have been used in different areas including the removal of heavy metals, poisonous gas sensing, energy conversation and storage, biomedical, photocatalytic removal of organic pollutants, etc. in this review paper, we only overview the applications of different metal oxide nanoparticles in photocatalysis technology and we start our discussion with the mechanisms of photocatalysis.

2.4.1. General Mechanism of Photocatalysis

Photocatalysis is a chemical reaction that triggers or accelerates the specific reduction and oxidation (redox) reactions with the irradiated semiconductors (He & Zhang, 2019). The major reactions involved in photodegradation are listed in Equations (1) to (5). The mechanism of photocatalytic degradation takes place with three general processes: (i) charge separation (hole and electron separation) under light irradiation, when the irradiated light match or exceeds the bandgap of photocatalyst; (ii) distribution of charge carriers to the photocatalyst surface (MONPs); (iii) oxidation and reduction takes place on the surface of the photocatalyst (Luo et al., 2019). The process starts from the light absorption of the photocatalyst by a certain wavelength when the light fall on the surface of the photocatalyst which results in the excitation of electrons (e^-) from the valence band (VB) to the conduction band (CB) leaving holes (h^+) in the valence band as shown in Equation (1) (Ajmal et al., 2014; Qumar et al., 2022). When the photocatalyst materials came in contact with organic pollutants the holes created in the valence band split water molecules or react with OH^- by resulting in hydroxyl free radical •OH as shown in Equation (2) (Ajmal et al., 2014) while electrons (e^-) excited to the conduction band are react with O_2 to create super oxygen radical $O_2^{\bullet -}$ species

as shown in Equation (3) (Velempini et al., 2021). Both •OH and O_2•− are highly reactive species and they react with organic pollutants adsorbed/absorbed on the surface of the photocatalyst materials by degrading these pollutants or reducing them into H_2O and CO_2 as shown in Equation (5). The general photodegradation mechanism of photocatalysis is presented in Figure 5.

$$\text{MONPs} + h\upsilon \rightarrow (\text{MONPs})(h^+)_{VB} + (\text{MONPs})(e^-)_{CB} \quad (1)$$

$$(\text{MONPs})(h^+)_{VB} + H_2O \rightarrow H^+ + \bullet OH \quad (2)$$

$$(\text{MONPs})(e^-)_{CB} + O_2 \rightarrow O_2\bullet^- \quad (3)$$

$$(\text{MONPs})(e^-)_{CB} + O_2\bullet^- + 2H^+ \rightarrow \bullet OH + OH^- \quad (4)$$

$$\text{pollutants} + \bullet OH \rightarrow \text{degradation byproducts } (CO_2 + H_2O) \quad (5)$$

Oxidation and reduction (Qumar et al., 2022):

$$\text{organic pollutants} + \text{photocatalyst } (\text{MONPs}(h^+)_{VB}) \rightarrow \text{oxidation products} \quad (6)$$

$$\text{organic pollutants} + \text{photocatalyst } (\text{MONPs}(e^-)_{CB}) \rightarrow \text{reduction products} \quad (7)$$

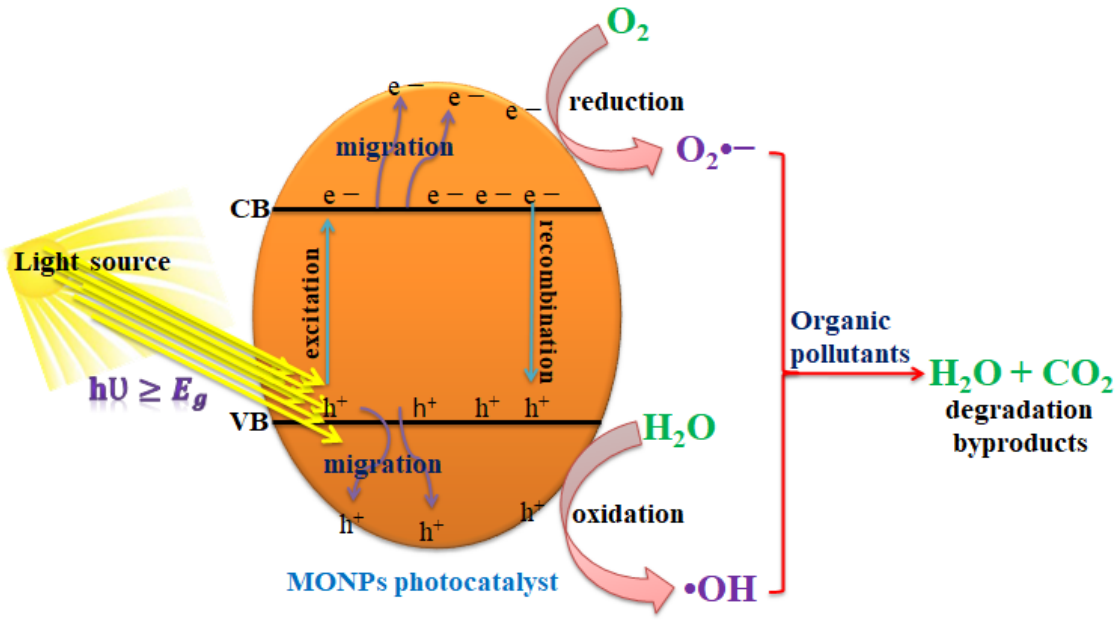

Figure 5: Schematic diagram of photocatalysis reaction mechanisms.

The photocatalytic reaction takes place at ambient temperature and pressure without the production of additional sludge and a significant reduction of catalyst. The excited electrons

are produced with strong reducibility while holes in the valence band with strong oxidability together result in the formation of the oxidation-reduction or shortly redox generated on the surface of the photocatalyst. The redox reaction takes place on the photocatalyst surface as the photogenerated electrons and holes are scattered on the surface of the photocatalyst. Oxidation reaction takes place by the cathode holes in the valence band reacting with the moisture on the surface of the photocatalyst to create the hydroxyl radicals. If oxygen is delivered from outside to the photocatalytic reactor it acts as an electron acceptor and delays the rate of charge recombination.

In metal oxide semiconductors, when the conduction band electrons possess a chemical potential of +0.5 to -1.5 V versus normal hydrogen electrode (NHE), then they act as reductants; while the valence band holes possess a strong oxidative potential of +1.0 to +3.5 V versus NHE (He & Zhang, 2019; Tong et al., 2012). Thus, for a semiconductor to be photochemical active as a photocatalyst for the generation of •OH radicals the redox potential of the photoinduced valance band hole must be sufficiently positive; whereas the redox potential of the photoinduced conduction band electrons must be sufficiently negative for the reduction of the adsorbed O_2 to superoxide (J. Zhu & Zäch, 2009).

There are constraints to the photocatalytic mechanism. Only the photons with energy equal or larger than the bandgap of the photocatalyst are used in the target reaction. Thus, optimization and tuning of the bandgap is required to achieve high efficiency of the photocatalyst. Another main challenge in the processes of photodegradation is the rapid recombination of charges (electron-hole pair's recombination) in photocatalysts without forming free radicals. In order to solve these challenges many interesting options such as manipulation of experimental conditions, producing low bandgap photocatalyst and modification of the discovered photocatalyst are among the taken strategy to overcome these challenges.

2.4.2. Performance evaluation of a photocatalyst

Photocatalyst performance can be measured by degradations of concetrations in liquid. The degradation efficiency of photocatalyst can be calculated by Equation (8) (Nazim et al., 2021):

$$\text{degradtion efficiency} = \frac{C_0 - C}{C_0} \times 100\% \quad (8)$$

where C_0 is the concentration (absorbance) of dye before light irradiation and C is the

concentration after a certain light illumination time (Sangpour et al., 2010). Beer-Lambert law given by $A = \varepsilon cd$ is used to calculate the concentration of the organic compound in the liquid, where A is the absorbance, ε is the molar extinction coefficient, c is the absorber concentration of the absorbing species, and d is the optical path length (Xiao et al., 2008).

The kinetic model, the Langmuir-Hinshelwood model, is used to evaluate the performance of the photocatalytic reaction occurring in the solid-liquid interface (Asenjo et al., 2013; K. V. Kumar et al., 2008). The concentration of the organic pollutant, the reaction parameters, the temperature, and the light irradiate intensity can be covered within the frame of the Langmuir-Hinshelwood model. For the first-order reaction, the Langmuir-Hinshelwood model is given as

$$\frac{dC}{dt} = kC \tag{9}$$

where, t is the time, and k is the first-order rate constant given by the slope of the graph of $ln\left(\frac{C}{C_0}\right)$ versus time *t*. From the first-order plot the rate constant can be calculated according to the equation (Nazim et al., 2021):

$$\ln\left(\frac{C}{C_0}\right) = -kt \tag{10}$$

2.4.3. Challenges in photocatalysis

The photocatalytic activity of the photocatalyst highly depends on its optical, crystallinity, structure, surface chemistry, and electronics. However, substantial challenges such as the high cost of semiconductors, lower solar energy utilization rate, and rapid recombination of photogenerated electron-hole pairs limit its potential applications in small-scale environmental areas (Anwer et al., 2019). The stability, photocorrosion, and availability are also challenges (Mohammed et al., 2021). The main challenge for the photocatalytic performance is associated with its metal oxide semiconductors including mismatch of solar spectrum and bandgap of metal oxides, materials instability, and inefficient separation and transport of charges. The incident photon absorption efficiency of the photocatalyst is determined by its bandgap. Thus, most of the discovered photocatalysts such as TiO_2 and ZnO have wide bandgap which led them to be active only under the ultraviolet region of the solar spectrum. The solar spectrum consists the UV 5%, visible 45%, and infrared (IR) 50% which means that

UV is expensive and limits the wide applications in a different areas. Therefore, bandgap tailoring is the fundamental challenge in photocatalysts to be solved. Recombination of photogenerated electron-hole pairs is another key issue influencing the photocatalytic activity of metal oxides. The recombination can be occurred either in bulk or on the catalyst surface by dissipating energy as non-radiative (heat) or radiative (light) reducing the photocatalytic activity. The low surface chemistry also influences the photocatalytic activity of semiconductor metal oxides. In the photocatalytic reaction, surface energy plays a great role in transferring electrons between reactants. The strategies to suppress these challenges are described in a detail in the next sections.

2.4.4. Doping in metal oxide nanoparticles

Doping is adding or substituting foreign elements either metals or non-metals into parent elements which can induce changes in the electronic and crystal structure of parent oxide (Y. Liu et al., 2019). Doping into host semiconductors is one of the most effective methods to manipulate the electronic structures and separating charges efficiently (Luo et al., 2019). The main advantage of doping is to tune the bandgap of parent oxides either by increasing or decreasing the bandgap of metal oxides. Non-metal dopants are fluorine, nitrogen, chlorine, carbon, iodine, phosphorus, selenium, sulfur, and tellurium which are commonly used as dopants in metal oxides. These dopants can substitute in the site of oxygen or can exist as an interstitial dopants (Medhi et al., 2020). The contribution of orbital states of these dopants creates mixed or localized states at the edges of the valence band and/or conduction band edges which cause to narrowing of the band gap of metal oxides and subsequently enhance the visible light activity of metal oxides (X. Lin et al., 2013). The foreign dopant can also create an additional dopant impurity level at the middle of the bandgap which initiates new excitations and increase the concentrations of photogenerated electrons and holes (Ji et al., 2019). The added or substituted impurity can also lead to the formation of defects which can trigger new optical characteristics. Moreover, in photocatalysis applications, they can create an additional trapping state which suppresses the rapid charge recombination and increases the lifetime of charge carriers (Leijtens et al., 2016). Metal dopants such as alkaline earth metals, transition metals, rare earth metals, and post-transition metals can also be used in the bandgap engineering of metal oxides (Medhi et al., 2020; Peng et al., 2009; Pradeev raj et al., 2018). Metal ion dopants have the advantage of inducing defects and changing diffusion behaviors

which can improve electron mobilities and charge transport, enhancing electrical properties (Medhi et al., 2020; D. Zhu & Zhou, 2019). Metal doping can also activate the surface of the photocatalyst to boost the reaction. Generally, metal doping has the advantages such as improving the mobility rate of electron-hole pairs, formation of new energy states either inside or beyond the bandgap of host semiconductor metal oxides, and enhancing the visible light adsorption by red-shifting of the adsorption edge (D. Zhu & Zhou, 2019).

2.5. Metal Oxides in Photocatalytic Degradation

A huge number of semiconductor metal oxide nanoparticles have been discovered for the degradation of pollutants in wastewater and air for a green and suitable environment. Among these metal oxides, TiO_2 is the foremost discovered photocatalyst which attracted many researchers around the world to engineer new photocatalyst materials. Thus, after the discovery of TiO_2 in 1972 many other metal oxides are discovered for photocatalysis applications. Photocatalysts are generally divided into two main categories: (i) homogeneous catalysts and (ii) heterogeneous catalysts. When a catalyst is present in the same phase as that of the reagents it is defined as homogeneous, which means that the catalysts are present as solutes in a homogeneous catalytic reaction system. In contrast, a catalyst is said to be heterogeneous if it is present in a different phase in the reaction mixture (Mishra & Chun, 2015). In heterogeneous photocatalysis, the photocatalyst act as an active surface for the reaction or mineralizing of organic pollutants by generating free radicals which are capable of complete mineralization of organic pollutants through complex mechanisms (Z. Wang et al., 2019). In this section, we have overviewed the commonly used metal oxide nanoparticles in photocatalysis technology.

2.5.1. TiO_2 Photocatalyst

Titanium dioxide **(**TiO_2) is the leading photocatalytic material since its discovery in 1972 due to its low cost, resist of corrosion, strong oxidizing power, and photochemical and chemical stability. TiO_2 is an n-type semiconductor metal oxide and it has the capability of oxidizing organic pollutants into nonhazardous products completely (Narkbuakaew & Sujaridworakun, 2019; Sakaguchi Miyamoto et al., 2018). Despite its high performance in the photocatalytic degradation of polluted air and wastewater pollutants, its photocatalytic activities are limited due to the rapid recombination of the photogenerated electron and hole pairs, poor sensitivity

to visible solar radiation because of its wide band gap, and TiO_2 particles aggregated when produced in nanoparticle form which blocks the active sites to adsorb/absorb pollutants that hinders its activity in photocatalysis technology (Danish et al., 2021). Many researchers are interested to suppress these challenges by taking different options to improve the photocatalytic activity of TiO_2 nanoparticles. In order to enhance its poor sensitivity to the visible light region it is important to reduce the bandgap and it is necessary to decrease the rate of charge recombination to improve its lifetime for photocatalysis applications.

Researchers have proposed a strategic approach to address the challenges that encountered TiO_2 photocatalyst. The well-studied and sufficient approach is metal-ion doping which introduces additional energy levels and reduces the bandgap. Metal-ion doping also introduces a charge-trapping site which decreases the rapid recombination of photogenerated electron and hole pairs. Different metal-ion doped TiO_2 is extensively studied with the advantage of increasing its absorption spectrum in visible light because the visible light region of the solar spectrum is freely available everywhere. Miyamoto et al. (Sakaguchi Miyamoto et al., 2018) synthesized lutetium (III) ion-doped TiO_2 by sol-gel method to modify the photocatalytic performance of TiO_2 for photocatalytic degradation of adenosine 5*'*-triphosphate (ATP) under UV irradiation. Their result showed that the lutetium (III) ion doped TiO_2 nanoparticles indicated higher photoreactivity than undoped TiO_2. Garza-Arévalo et al. (Garza-Arévalo et al., 2016) synthesized Fe-doped TiO_2 by sol-gel method and evaluated the removal of Arsenic (III) from groundwater under visible light. The incorporation of Fe into TiO_2 extends the absorption of TiO_2 to visible light region, and induces oxygen vacancies which initiate the photocatalytic oxidation of Arsenic (III), and retarded the fast recombination of photogenerated electrons and holes. Ndabankulu et al. (Ndabankulu et al., 2019) reported different lanthanides (Ce, Dy, Lu, and Sm) doped TiO_2 by sol-gel process and evaluated the photocatalytic activity and efficacy of four different lanthanides doped TiO_2 for the degradation of caffeine under visible light irradiation. Sood et al. (Sood et al., 2015) reported iron (III)-doped TiO_2 nanoparticle photocatalyst synthesized by hydrothermal method and examined its photocatalytic activity under the illumination of visible light spectrum using para-nitrophenol as a model pollutant. The maximum degradation efficiency they obtained was 92 % in 5h with 0.05 mol% of Fe^{3+} which was attributed to the high crystalline structure, small size, maximum charge separation, retarded electron-hole recombination, and better

visible light response of the prepared Fe^{3+} doped nanoparticle. Xie et al. (Xie et al., 2018) reported Se^{4+} doped TiO_2 nanoparticles synthesized by the sol-gel method for the degradation of Rhodamine B under visible light irradiation. The Se^{4+} introduces extra electronic states in the bandgap of TiO_2 and narrowed the bandgap of TiO_2. The smallest bandgap they obtained was 2.17 eV and due to the extended absorption range, the photocatalytic activity of TiO_2 was improved. However, as the percentage concentration of Se^{4+} increased to 25 % the bandgap started to increase, hence the photocatalytic activity also decreased.

Depositing noble metals such as Ag, Pd, Au, and Pt on the surface of TiO_2 retards the fast recombination of photogenerated electron-hole pairs. Narkbuakaew and Sujaridworakun reported the Ag metal deposited on the surface of anatase TiO_2 prepared by chemical reduction followed by the calcination method for the degradation of rhodamine B and the deposition of silver nanoparticles significantly inhibited the fast recombination of photogenerated electron-hole pairs (Narkbuakaew & Sujaridworakun, 2019). Metal doping is another strategy for reducing charge recombination and enhancing the visible light response of TiO_2 photocatalyst. Karuppasamy et al. (Karuppasamy et al., 2021) synthesized different transition metals (Zn, Zr, Cu) doped TiO_2 by sol-gel method and utilized them for the decoloration of methylene blue dye under visible light irradiation. Among the doped TiO_2, the Zn-doped photocatalyst showed greater photocatalytic activity than pristine TiO_2 or other doped photocatalysts. Thus, the enhanced photocatalytic activity of Zn-doped TiO_2 is attributed to the decrease in optical bandgap compared to pristine and other dopants. Khlyustova et al. (Khlyustova et al., 2020) synthesized Al, Cu, Mo, and W doped TiO_2 by sol-gel method and tested the photocatalytic activity of the doped and pristine TiO_2 by using rhodamine B as pollutant model under the illumination of visible light. The doped photocatalysts own enhanced photocatalytic performance compared to the pristine TiO_2. Thus, the doped photocatalysts own a higher kinetic rate constant than pristine TiO_2, which resulted in enhanced photocatalytic performance due to the formation of a new energy level near the conduction band. However, metal doping possesses disadvantages such as photocorrosion and high cost specifically, when using noble metals as a dopant. In order to solve these problems non-metal doping such as iodine, sulfur, nitrogen, etc. were used as dopants to enhance the photocatalytic performance of TiO_2. Saroja et al. (Saroj et al., 2020) reported the iodine-doped TiO_2 synthesized through the solution combustion method and investigated the effects of

iodine dopant concentration on the photocatalytic activity of TiO_2 for the photodegradation of Direct Blue 199. They observed that the visible light response of iodine-doped TiO_2 enhanced as dopant concentration increased.

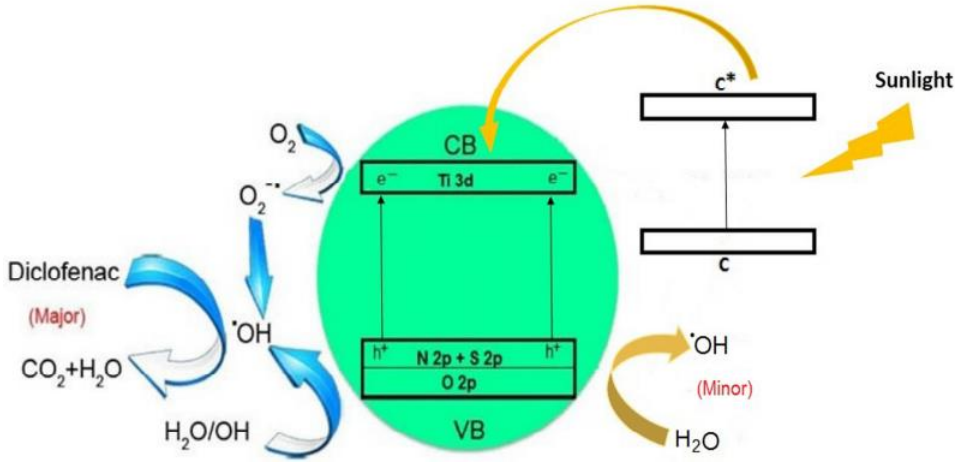

Figure 6: Schematically representation of the improvement in the photoactivity of C-S-N-tri doped TiO_2 photocatalyst (Ramandi et al., 2017).

Non-metal co-and triple-doped TiO_2 for the enhancement of its photocatalytic activity was also reported by different groups. For instance, Ramandia et al. (Ramandi et al., 2017) reported C–N–S–tri doped TiO_2 anatase phase synthesized by sonochemical method. They studied the photocatalytic activity of the prepared photocatalysts using Diclofenac as a model pollutant under sunlight irradiation. The photocatalytic degradation mechanism of the C–N–S triple-doped TiO_2 is shown in Figure 6. Each non-metal dopant has its own advantages in enhancing the photocatalytic activity of TiO_2 by generating new impurity levels such as N 2p, S 2p, and C 1s. Thus, the doped C acts as a photosensitizer which injects electrons into the conduction band (CB) under sunlight irradiation, while the N and S doped modifies the electronic band structure of TiO_2 by mixing the O 2p of TiO_2 with N 2p and S 2p orbitals which was resulted in narrowing the bandgap of TiO_2. According to this report electrons in the CB and the trapped electrons trap the adsorbed O_2 molecules to generate the superoxide (O_2•−). The main oxidative and reactive species were electrons and •OH radicals, holes were the minor oxidative species, and O_2•− has considerable effects on the degradation of Diclofenac. The •OH radicals can be obtained in two ways as shown in Equations (11) to (13). In Equation (11) the molecular O_2 react with electrons (e^-) in the CB and resulted in O_2•−. Then O_2•− reacts with water molecules to produce •OH radical species as shown in Equation

(12). On the other hand, as shown in Equation (13) the h^+ can react with H_2O on the surface of photocatalyst to produce •OH radical species.

$$O_2 + e^- \rightarrow O_2\bullet - \quad (11)$$

$$O_2\bullet - + 2H_2O \rightarrow 2\bullet OH + 2OH^- + O_2 \quad (12)$$

$$h^+ + H_2O + \bullet OH \quad (13)$$

Immobilization of TiO_2 on carriers such as activated carbon, metallic oxides, etc. is also an effective technique to retard the fast charge recombination and extend the visible light region response of TiO_2 photocatalyst. Saqib et al. (Saqib et al., 2019) reported zeolite immobilized TiO_2 nanoparticles synthesized using the conventional liquid impregnation method for the efficient degradation of methylene blue dye. The presence of zeolite improves the photocatalytic degradation of methylene blue by four folds compared to pure TiO_2. Coupling TiO_2 with other semiconductors to develop heterojunctions is also another method for enhancing the photocatalytic activity of TiO_2. Coupling TiO_2 with other semiconductors expands the visible light spectrum to the near-infrared response of TiO_2 as well as promotes charge separations (Danish et al., 2021). Song et al. (L. N. Song et al., 2018) synthesized a novel TiO_2/Bi_2MoO_6 heterostructures via a solvothermal process for partial oxidation of aromatic alkanes under visible light illumination. They observed that compared to single components TiO_2 and Bi_2MoO_6 the heterostructures TiO_2/Bi_2MoO_6 showed better photocatalytic performance and also the charge separation was improved.

Heterojunction modes of metal oxide photocatalysts with similar bandstructure when coupled enhance the transfers, separation, and stability of photogenerated electrons and holes. For instance, Abdel-Wahab et al. (Abdel-Wahab et al., 2017) reported the coupled heterojunctions TiO_2/Fe_2O_3 with the bandgap of TiO_2 was ~3.2 eV and Fe_2O_3 bandgap ~2.2 eV. When TiO_2/Fe_2O_3 heterojunction was irradiated the electron-hole pairs were generated. Thereafter, the photogenerated electrons transfer from the CB of Fe_2O_3 to the CB of TiO_2, with lower potential, whereas the photogenerated holes transfer from the VB of TiO_2 to VB of Fe_2O_3, with higher potential. The photogenerated electrons eventually reacted with oxygen molecules to produce $O_2\bullet-$ active species, while the photogenerated holes reacted with water molecules to produce •OH radicals. The prepared TiO_2/Fe_2O_3 heterojunction was applied for the

degradation of paracetamol.

2.5.2. ZnO Photocatalyst

Recently, many researchers are highly interested in zinc oxide (ZnO) nanoparticles due to its simple synthesis, low cost, and unique physical and chemical properties which made it compete with TiO_2 in photocatalytic degradation of organic pollutants. It has excellent photocatalytic activity under UV irradiation but is less stable compared to TiO_2 (Djurišić et al., 2014). ZnO is an n-type semiconductor having a wide bandgap of 3.37 eV (Ghoderao et al., 2018). Compared to TiO_2, ZnO is responding to broader ranges of the light spectrum including the visible light spectrum.

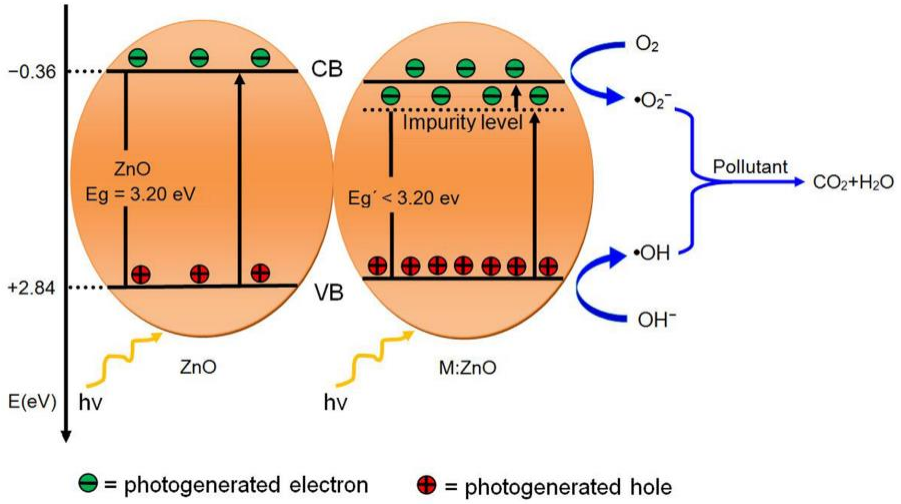

Figure 7: Photocatalytic schematic diagram of ZnO with impurity level was introduced (Ji et al., 2019).

The photocatalytic activity of ZnO is widely studied and the synthesis method affects the specific surface area of ZnO nanoparticles which subsequently affects the photocatalytic activity of ZnO nanoparticles. Uribe-Lopez et al. (Uribe-López et al., 2021) reported the effect of the synthesis method on the photocatalytic activity of ZnO nanoparticles synthesized by precipitation and sol-gel method. They obtained hexagonal rod-like geometries with 50 nm diameters for the ZnO nanoparticle synthesized via the sol-gel method, while quasi-spherical with 100 nm diameters for ZnO nanoparticles via the precipitation method. They estimated the photocatalytic activity of the synthesized ZnO via both methods by degradation of phenol and achieved 100 % degradation after 120 min for nanoparticles via precipitation method, whereas 80 % of degradation for nanoparticles via sol-gel after 120 min. Pure ZnO nanoparticles only responses the UV light spectrum which only covers approximately 4 % of the solar spectrum,

thus it is important to enhance the visible light response because visible light covers approximately 43 % of the solar spectrum which is much larger than UV spectrum (Ba-Abbad et al., 2013). In addition to this, because of the wide bandgap of ZnO, the photogenerated electrons and holes easily recombine which limits its photocatalytic performance.

To improve the visible light irradiation response and slow down the fast charge recombination of photogenerated electrons-holes pairs of ZnO nanoparticles, different approaches have been developed. Doping with metal-ions and metals is the famous approach in which it reduces electrons-holes recombination and expands the visible light spectrum responses. Ji et al. (Ji et al., 2019) reported the Fe^{3+} doped, Sn^{4+} doped, and Fe^{3+} and Sn^{4+} co-doped ZnO nanoparticles prepared by a simple low-temperature solution method and evaluated its photocatalytic activity by the degradation of methylene blue dye. The low to high photocatalytic activity sequence was ZnO, $Fe_{0.01}ZnO$, $Fe_{0.01}Sn_{0.01}ZnO$, and $Sn_{0.05}ZnO$. Pristine ZnO nanoparticle only achieved 45.88 % of methylene blue dye degradation, whereas $Sn_{0.05}ZnO$ achieved the highest degradation of 99.61% of all four materials. When Fe^{3+} and Sn^{4+} were incorporated into ZnO an impurity level below near to conduction band was formed which allows the electrons in the valence band to transition with less energy as shown in Figure 7. Consequently, the concentrations of photogenerated electrons and holes increased and also improved the photocatalytic performance of ZnO nanoparticles. Alam et al. (Alam et al., 2018) synthesized different rare earth metals (La, Nd, Sm, and Dy)-doped ZnO nanoparticles by sol-gel process and investigated the photocatalytic degradation of methylene blue and rhodamine B by improved photocatalyst due to the doped rare earth metals. Qia et al. (Qi et al., 2020) reported transition metal ions (Mn, Fe, Co, Ni, or Cu) doped ZnO nanoparticles synthesized via a solvothermal method. They studied the photodegradation of methylene blue dye under the simulation of visible light. The photocatalytic activity of the doped ZnO was increased compared to bare ZnO. Among all doped photocatalysts, Cu-doped ZnO showed greater photocatalytic activity than bare ZnO and other doped photocatalysts. Thus, the Cu-doped ZnO has the highest rate constant than other photocatalysts.

Non-metal doped ZnO photocatalyst with improved photocatalytic activity under visible light irradiation is also reported. Mirzaeifard et al. (Mirzaeifard et al., 2020) reported sulfur-doped ZnO synthesized by hydrothermal method and utilized it for the degradation of rhodamine B under visible light irradiation. They have optimized the dosage of the catalyst for the best

degradation of rhodamine B. Among those, the photocatalyst with 0.10 g containing 0.5 wt % of S showed a 100 % rate degradation of rhodamine B (5 ppm) at pH = 5 in 90 min. Immobilizing the ZnO nanoparticles on the polymer supports is another method to improve the photocatalytic activity of ZnO. Mochane et al. (Mochane et al., 2022) reviewed the ZnO nanoparticles immobilized in various matrices such as polymers and ceramics. They have discriminated that the ZnO nanoparticles immobilized on polymer because of high durability, chemical inertness, and low cost.

ZnO coupled with other semiconductor metal oxide nanoparticles such as SnO_2, TiO_2, WO_3, etc. is also another approach to improve the photocatalytic activity of ZnO under the irradiation of visible light. Mugunthan et al. (Mugunthan et al., 2019) reported the visible light irradiation photocatalytic degradation of the pharmaceutical compound diclofenac in wastewater using a ZnO-WO_3 composite semiconductor photocatalyst synthesized through a hydrothermal method. The prepared composite photocatalyst extended the optical response to the visible light spectrum and it showed better stability in retaining the degradation efficiency of 80%. Lin et al. (J. Lin et al., 2018) also synthesized ZnO–SnO_2 (ZS) nanocomposites with different compositions by a simple coprecipitation method. The aqueous solution of methylene blue dye color becomes colorless with increasing the irradiation time. Among the composition of the synthesized nanocomposite, the 25 % of SnO_2 showed the optimum rate constant. When ZnO–SnO_2 composites were irradiated, the photogenerated electrons flow from low potential to high potential while holes flow in opposite directions. As a result, electrons accumulated in the conduction band of SnO_2, and the holes accumulated in the valence band of ZnO. Thus, the sufficiently separated photogenerated electrons and holes provided the enhanced photocatalytic performance of the ZnO–SnO_2 composite.

2.5.3. WO_3 Photocatalyst

The first experiment on the photocatalysis of tungsten oxide (WO_3) was reported in 1976 (Butler et al., 1976). Tungsten oxide is an inexpensive metal oxide semiconductor having high and promising photocatalytic performance. It has advantages such as good response to the visible solar spectrum due to its narrow optical bandgap (2.5−2.8 eV), tunable stoichiometric structure, earth abundance, high oxidizing of holes, and stability (Danish et al., 2021). Despite its high photocatalytic performance, the photocatalytic efficiency of WO_3 is limited due to the rapid recombination of photogenerated electrons and holes and less reduction of O_2 molecules

because of the relatively low conduction band level lies above the reduction potential of $O_2/O_2^{\bullet-}$. These challenges have inspired researchers to find promising techniques to suppress by tuning the structure and optical bandgap of WO_3. These techniques include manipulation of particles morphology, deposition of noble metal on WO_3, doping of elements, carbon-based composite and forming heterojunctions by coupling with other semiconductors.

The particle morphology control reduces the fast photogenerated electrons and holes recombination and improves charge separation and enhances the overall photocatalytic activity. Rong and Wang synthesized novel hierarchical hollow nest-like WO_3 micro/nanostructures (HNWMs) by hydrothermal method without a template and surfactant (Rong & Wang, 2021). Effects of different parameters such as time of reaction, pH, and annealing conditions have been investigated according to this report. The morphological structure of the synthesized WO_3 retained an improved photocatalytic activity towards an aqueous solution of tetracycline (TC) under visible light and possesses good stability and reusability.

Metal doping can narrow the bandgap and retarded the fast charge recombination of the WO_3 photocatalyst. Ramkumar and Rajarajan synthesized nanocrystalline Ni-doped WO_3 thin film deposited by chemical bath deposition method and evaluated its photocatalytic activity by the photodegradation of methyl orange, methylene blue and phenol (Ramkumar & Rajarajan, 2017). The photocatalytic activity of Ni-doped WO_3 was remarkably improved. Noble metal deposition and coupling with other semiconductors also enhances the photocatalytic performance of WO_3 under visible light irradiation. Wang et al. (Changhua Wang et al., 2014) reported the multiple heterojunctions containing WO_3 nanorods and Pt and TiO_2 nanoparticles for the degradation of gaseous acetaldehyde, rhodamine B dye, and phenol under the illumination of visible light. The multiheterojunction (WO_3–Pt)/TiO_2 photocatalysts higher performance was attributed to the synergistic effect of efficient electrons and holes transferred at the WO_3/Pt interface and WO_3/TiO_2 interface respectively.

Graphene, reduced graphene oxide, and other carbon-based composites also enhance the photocatalytic performance of WO_3 (Esencan Türkaslan et al., 2022; Jeevitha et al., 2018). Jeevitha et al. (Jeevitha et al., 2018) prepared WO_3-GO nanocomposite via the ultrasonic method and investigated the photocatalytic activity, antibacterial and anticancer of the

prepared nanocomposite. The irregular spherical shape and small pores of WO_3 greatly improved the photocatalytic activity. This report compared the obtained photocatalytic degradation of methylene blue dye under the illumination of visible light. Pure WO_3 in 270 min couldn't completely degrade the methylene blue dye. However, the WO_3-GO nanocomposite achieved a 97.03% rate of degradation of methylene blue dye in 180 min.

2.5.4. Cu_2O Photocatalyst

Copper oxide nanoparticle is the most candidates of promising photocatalytic materials for the degradation of organic pollutants. It possesses high optical absorption properties and optimal optical bandgap. Copper oxide nanoparticles can be produced at a low cost due to its precursor materials being highly abundant in the earth's crust (Muthukumaran et al., 2020). It has two semiconducting phases: cupric oxide (CuO) and cuprous oxide (Cu_2O) which possesses approximately 1.6 eV and 2.4 eV optical bandgap respectively. Cu_2O is a p-type metal oxide semiconductor with a 2.4 eV bandgap (Kangralkar et al., 2019). Since its bandgap is suitable for the application of photocatalysis under visible light illumination, it is the preferable candidate for photocatalytic activity. Muthukumaran et al. (Muthukumaran et al., 2020) synthesized cuprous oxide (Cu_2O) nanoparticles photocatalyst via the sonochemical method for the degradation of Malachite green under the illumination of visible light. The prepared nanoparticle achieved 91.89 % degradation efficiency after 45 min of visible light illumination. There are various green syntheses reported on the cuprous oxide (Cu_2O) nanoparticles for photocatalytic degradation of organic pollutants. Kerour et al. (Kerour et al., 2018) synthesized Cu_2O nanoparticles by a green method using Aloe Vera leaves plants extracted for the degradation of methylene blue dye and were able to completely degrade methylene blue after 10 min of visible light illumination. Yadav et al. (Sushma Yadav et al., 2021) used sugarcane bagasse to synthesize Cu_2O nanoparticles eco-friendly for the degradation of methyl red, congo red, methylene blue, and methyl orange organic dyes.

Despite the achievement and simple green synthesized Cu_2O nanoparticles, the rate of recombination of photogenerated electrons and holes, stability and photocorrosion are challenging it for photocatalysis applications (Mohammed et al., 2021). For instance, during the photocatalysis process when Cu_2O is irradiated it can be converted into CuO through photooxidation which shows the deactivation of the photocatalytic process (Masudy-Panah et al., 2019). In order to suppress these challenges and improve the photocatalytic activity of

Cu_2O different ideas have been generated by researchers. The preparation of Cu_2O nanoparticles with good control on morphology significantly influences its chemical and physical properties in using as photocatalyst materials (H. Gao et al., 2013). Prado-Chay et al. (Prado-Chay et al., 2020) synthesized hierarchical Cu_2O microspheres by simple chemical method at room temperature with enhanced photocatalytic activity for the degradation of methyl orange under visible light irradiation.

Coupling with other metal oxides to create heterojunctions is another method to enhance the photocatalytic performance of Cu_2O. Wang et al. (Yanfen Wang et al., 2018) reported ZnO/Cu_2O heterojunctions designed by self-templating method for degradation of rhodamine B and achieved 96 % degradation efficiency within 40 min under visible light irradiation. Making composite with Carbon-based materials is also another strategy to boost the photocatalytic activity of Cu_2O. K. Polat produced a 2D thin film catalyst Cu_2O/2D graphene on copper foil having photocatalytic activity under the visible light spectrum (Polat, 2020). Karthikeyan et al. (Karthikeyan et al., 2020) reported hierarchical Cu_2O nanospheres and Cu_2O/rGO nanocomposites for the degradation of 4-chlorophenol and production of H_2 under the illumination of visible light which is attributable to enhance visible absorption. Z-scheme modification is also the most effective technique to improve the photocatalytic activity of Cu_2O. Chen et al. (K. Chen et al., 2020) synthesized a Z-scheme Cu_2O-(rGO-TiO_2) photocatalyst for the degradation of 2,2*'*,4,4*'*-tretrabromodiphenyl ether. The reported Z-scheme photocatalytic performance by this group was greater than either single or composite of Cu_2O and TiO_2 under the same reaction condition.

2.5.5. CuO Photocatalyst

Because of its desirable properties, such as easy preparation, low cost, and nontoxicity, CuO nanoparticles acquired great interest in the research field such as photocatalysis, solar cells, supercapacitors, biodiesel, water pollutant removal, and electrocatalysis (Sukumar et al., 2020). CuO nanoparticle is an outstanding and efficient photocatalytic material for the degradation of organic pollutants. However, just like Cu_2O, CuO has also limitation that comes from rapid photogenerated recombination and photocorrosion. Hence, researchers have employed various techniques to address these concerns. Among these CuO composite with carbon-based materials found great attention. Banu et al. (Banu et al., 2022) synthesized GO/CuO nanocomposite by hydrothermal method for photocatalytic degradation of Azure-B

dye with an efficiency of 95%. The enhanced photocatalytic activity of the prepared nanocomposite was attributed to the small size and high surface area of GO/CuO. Coupling it with Cu_2O and graphene oxide also enhances its photocatalytic performance. Zhang et al. (Z. Zhang et al., 2020) reported CuO-Cu_2O/GO nanocomposite for the degradation of tetracycline and methyl orange and achieved 90% and 95% degradation efficiency after 120 min under visible light irradiation.

Coupling with other metal oxide semiconductors also enhances the photocatalytic performance of CuO nanoparticles. Sakib et al. (Sakib et al., 2019) synthesized CuO/ZnO nanocomposite through the mechanochemical combustion method for the degradation of methylene blue under visible light irradiation. They achieved methylene blue degradation was 81% and 98% using ZnO and CuO/ZnO respectively. Forming a p-n junction heterostructure has the advantages of widening the light harvesting and retarding the fast recombination of photogenerated electrons and holes. Malwala and Gopinath synthesized the 3D hierarchical nanostructured n-type ZnO and Fe_3O_4 deposited on p-type CuO via thermal oxidation followed by microwave-assisted deposition for the formation of p-n heterojunctions (Malwal & Gopinath, 2016). The prepared p-n heterojunctions enhanced the photocatalytic activity for the degradation of Congo red dye under solar light irradiation. The enhanced photocatalytic performance was attributed to the effective and sufficient charge separation formation of the p-n junction heterostructures at the interface of p-type (CuO) and n-type (ZnO/Fe_3O_4) semiconductors.

Metal doping is another effective strategy to improve the photocatalytic performance of CuO. George et al. (George et al., 2022) synthesized nanoflower-like 3D transition metal doped CuO nanostructure by sonication method for the degradation of methylene blue dye under visible light illumination. The 3D transition metal incorporated into CuO played a great role in tuning the structure, morphology, and optical properties. Maraj et al. (Maraj et al., 2021) reported Mo-doped CuO nanoparticles synthesized by the sol-gel process and utilized for the degradation of methylene blue under visible light irradiation. Islam et al. (Islam et al., 2021) synthesized Ce-doped CuO nanoparticles through the sol-gel auto-combustion method and utilized it for the degradation of methylene blue under the illumination of visible light. Ce-doped CuO nanoparticles exhibited better photocatalytic activity than undoped CuO nanoparticles.

2.5.6. SnO_2 Photocatalyst

Tin dioxide (SnO_2) is an n-type semiconductor and has a wide range of applications in areas such as catalysts, gas sensors, transistors, batteries, and transparent electrodes (Kim et al., 2016). SnO_2 in its nanoparticles has a high surface-to-volume ratio that enhances the active sites and is expected to exhibit good photocatalytic activity. Pure SnO_2 is rarely studied because of the simultaneous formations of Sn^{2+}, and Sn^0 during the photocatalysis process. Thus, it can be presented as SnO_2, SnO, or Sn in the catalyst. Moreover, in photocatalysis applications, it is found as a composite form with other semiconductors to suppress instability, and the composite of SnO_2 with other semiconductors has been widely reported. SnO_2 is also an ultraviolet-active metal oxide semiconductor due to its wide bandgap of 3.6 eV similar to TiO_2 (Yuanyuan Li et al., 2018). To date, numerous efforts such as building heterojunctions, morphology control, metal or non-metal doping, carbon-based materials composite, etc., have been developed to suppress these challenges. G. Devi and R. Shyamala synthesized SnO_2 and α-Fe_2O_3 by sol-gel method and combined them by mixing and grinding to form a SnO_2–α-Fe_2O_3 composite (Devi & Shyamala, 2018). They studied the photocatalytic activity of the prepared composite using phenol as a pollutant model. Due to the redshifts of bandgap, the prepared composite showed higher extent absorption in the visible light region.

Combining SnO_2 with other metal oxide and carbon-based materials also enhances its visible light activity. Yao et al. (S. Yao et al., 2019) reported SnO_2/TiO_2/RGO nanocomposite synthesized by hydrothermal method with enhanced photocatalytic activity under visible light illumination for the degradation of rhodamine B. The superior photocatalytic activity of the synthesized nanocomposite is attributed to the great efficiency of light absorption and outstanding charge separation and transfers. Wang et al. (Chunlan Wang et al., 2022) synthesized micron-sized spherical SnO_2 and flower In_2O_3 by hydrothermal method and prepared the In_2O_3/SnO_2 composite by two-step method. According to this report, the bandgap of the prepared materials in decreasing order is SnO_2, In_2O_3, and In_2O_3/SnO_2 respectively. For the photocatalytic degradation study of the prepared photocatalyst, they used Rhodamine B as a model organic pollutant and the In_2O_3/SnO_2 composite showed the highest degradation rate of 97% after 240 min irradiation which was twice that of pure SnO_2 or In_2O_3. The photocatalytic mechanism of the prepared composite is shown in Figure 8. In this report, the superoxide (O_2•−) and holes play a great role in the degradation of rhodamine B, while •OH

has played an auxiliary role. The energy band positions of the two compounds matched well as shown in Figure 8 in which the photogenerated electrons and holes separated effectively. An electron (e^-) was generated in the conduction band and a hole (h^+) was generated in the valence band.

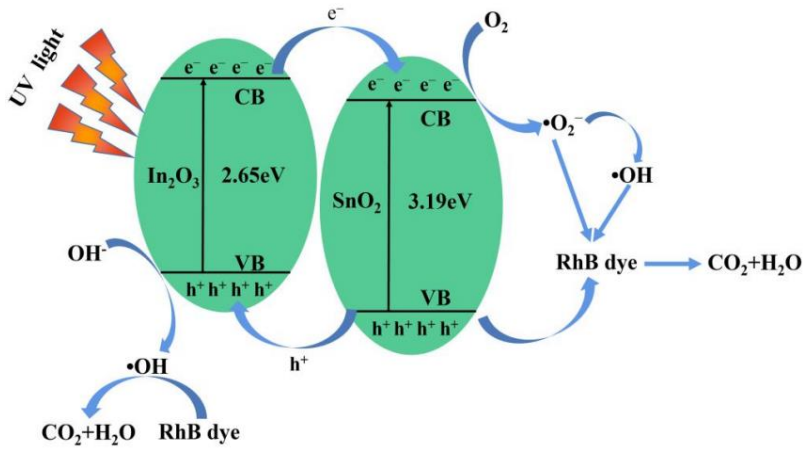

Figure 8: Schematic illustration of the separation and migration mechanism of photogenerated electron–hole pairs of In_2O_3/SnO_2 composite (Chunlan Wang et al., 2022).

When the two compounds were irradiated electrons and holes were generated as shown in Equations (14) and (15). The photogenerated holes of SnO_2 transferred to the valence band of In_2O_3 (Equation (16)) and photogenerated electrons of In_2O_3 transferred to the conduction band of SnO_2 (Equation (17)). Thereafter, e^- reacts with O_2 to form superoxide ($O_2\bullet-$) (Equation (18)) and the photodegradation process of rhodamine B is shown in Equations (19-21) (Chunlan Wang et al., 2022).

$$SnO_2 + h\upsilon \rightarrow SnO_2(h^+)_{VB} + SnO_2(e^-)_{CB} \quad (14)$$

$$In_2O_3 + h\upsilon \rightarrow In_2O_3(h^+)_{VB} + In_2O_3(e^-)_{CB} \quad (15)$$

$$SnO_2(h^+)_{VB} \rightarrow In_2O_3(h^+)_{VB} \quad (16)$$

$$In_2O_3(e^-)_{CB} \rightarrow SnO_2(e^-)_{CB} \quad (17)$$

$$SnO_2(e^-)_{CB} + O_2 \rightarrow O_2 \bullet - \quad (18)$$

$$\text{Rhodamine B} + O_2 \bullet - \longrightarrow H_2O + CO_2 \quad (19)$$

$$\text{Rhodamine B} + h^+ \longrightarrow H_2O + CO_2 \quad (20)$$

$$\text{Rhodamine B} + \bullet OH \rightarrow H_2O + CO_2 \quad (21)$$

Combining SnO_2 with noble metals also enhances its photocatalytic activity and its visible light response. Ansari et al. (Ansari et al., 2014) synthesized Ag–SnO_2 nanocomposites in

water at room temperature using electrochemically active biofilm and utilized it for the degradation of methylene blue, methyl orange, 2-chlorophenol, and 4-nitrophenol under visible light irradiation. The prepared nanocomposite showed enhanced photocatalytic activity compared to pure SnO_2. Doping with metals is also an effective method to slow down the photogenerated electron-holes recombination and expand the visible light activity of SnO_2. Ran et al. (Ran et al., 2015) have reported hollow-structured Ti-doped SnO_2 prepared using silica microspheres as templates for the decomposition of methylene blue under UV and visible-light irradiation. Compared with pristine SnO_2 hollow spherical, Ti-doped SnO_2 showed enhanced photocatalytic activity of 92% rate of degradation under UV light irradiation and 54% under visible light irradiation decomposition of methylene blue within 135 min of degradation time. Baig et al. (Ali Baig et al., 2021) have synthesized a Zn-doped SnO_2 photocatalyst by hydrothermal method for the degradation of methylene blue under visible light illumination. The effects of Zn-doping is clearly understood that prolonging the photo-absorption to the visible region and decreasing electron-holes recombination.

2.4.7. Fe_2O_3 Photocatalyst

Iron oxide can be present in different phases such as maghemite (υ-Fe_2O_3), magnetite (Fe_3O_4), hematite (α-Fe_2O_3), and wustite (FeO). Among these phases, Fe_2O_3 and Fe_3O_4 are the most common phases of iron oxide in nature. Because of the easy manipulation of morphology, structures, and dimension orientation to provide stability, Fe_2O_3 is applied in various industrial applications (Velempini et al., 2021). Fe_2O_3 has four polymorphic phases: namely, ε-Fe_2O_3, γ-Fe_2O_3, β-Fe_2O_3, and α-Fe_2O_3 (hematite) (Koe et al., 2020). Among these crystallographic phases, α-Fe_2O_3 (hematite) is the most stable and widely used in different applications such as sorbents, catalysts, biomedical devices, and solar cells (Machala et al., 2011). The nanosized α-Fe_2O_3 has better magnetic behavior (ferromagnetic) than ferum (Fe) (Hoque et al., 2018; Yuan Wang et al., 2021). This magnetic behavior helps to separate the photocatalyst materials from the solution after the process of photocatalytic treatment.

Moreover, α-Fe_2O_3 has been used as photocatalyst material due to its energy bandgap being appropriate for the photocatalysis process. However, pure Fe_2O_3 is limited in its application in photocatalysis because of disadvantages such as lower minority charge carriers mobility, sluggish surface kinetics, the short diffusion length of photogenerated carriers, and high recombination rate of photogenerated electron-holes pairs (N. Li et al., 2021). Different

strategies have been developed to address these problems. The suitably positioned bandgap of α-Fe_2O_3 makes it to form a composite with other metal oxides to reduce the recombination of photogenerated electron-hole pairs. Senthil et al. (Senthil et al., 2018) reported α-Fe_2O_3/WO_3 composite photocatalyst designed by a simple physical mixing process and utilized for the photodegradation of methylene blue under visible light irradiation. The prepared composite exhibited excellent photocatalytic activity, which was attributed to the strong absorption of α-Fe_2O_3/WO_3 composite and slow down recombination of electron-hole pairs. The polymer coating is also another method to enhance the photocatalytic activity of α-Fe_2O_3. Zhang et al. (T. Zhang et al., 2020) have synthesized nitrogen-rich cross-linked copolymer, poly(1,4,8,11-cyclotetradecane [2,2-bipyridine]-5,5-dicarboxamine) (PNH). This polymer covered Fe_2O_3 by moderate hydrothermal treatment to form Fe_2O_3@PNH which had shown excellent photocatalytic activity for the degradation of tetracycline with catalytic performance of ~90 % under visible light illumination which was three times greater than Fe_2O_3.

Doping is another effective strategy to address the aforementioned problems that generate electron trap centers. Li et al. (N. Li et al., 2021) synthesized different metal-doped Fe_2O_3 nanoparticles by using fabric filter dust as starting materials for the degradation of methyl orange. The different metal doped showed an 82.99% degradation rate under the illumination of visible light, whereas the undoped Fe_2O_3 achieved only 38.94%. Non-metal doping can also improve the photocatalytic activity of Fe_2O_3 nanoparticles. Alvarez et al. (Mendiola-Alvarez et al., 2019) have synthesized phosphorus-doped Fe_2O_3-TiO_2 by sol-gel method and utilized it for the degradation of sulfamethazine under visible light irradiation. The doped composite has shown improved photocatalytic performance compared to either the Fe_2O_3-TiO_2 composite or TiO_2 which was attributed to the reduced bandgap, small crystallite size, increased existence of hydroxyl on the catalyst surface, and high surface area. Graphene is a type of carbonaceous material having excellent transparency, lightweight, high electrical conductivity, unique structure, high adsorption capacity, and high specific surface area properties which enhances the photocatalytic performance of α-Fe_2O_3 when it made hybrid. S. Frindy and M. Sillanpää synthesized α-Fe_2O_3 hybridized with graphene by hydrothermal method for the degradation of rhodamine B under visible light irradiation and it showed high catalyst activity of ~98% (Frindy & Sillanpää, 2020). They demonstrated that the incorporation of graphene into α-Fe_2O_3 nanoparticles resulted in high photocatalytic activity

compared to pure α-Fe_2O_3 or α-Fe_2O_3 loaded on other carbonaceous materials.

2.5.8. Bi_2O_3 Photocatalyst

Bismuth oxide (Bi_2O_3) is found in various crystals forms such as triclinic (ω), orthorhombic (ε), face-centered cubic (δ), body-centered cubic (γ), monoclinic (α), tetragonal (β), and hexagonal assembly (Zahid & Han, 2021). Bi_2O_3 has an excellent photocatalytic activity for wastewater treatment, CO_2 reduction, nitrogen fixation, and water splitting under the irradiation of visible light solar spectrum. However, Bi_2O_3 is now confronted with a larger recombination rate of the electron-hole pairs, which significantly reduces its photocatalytic activity for the degradation of organic pollutants (T. Li et al., 2020). To boost the overall photocatalytic efficiency of Bi_2O_3 many strategies including composition with other materials, morphology, shape, microstructure, surface structure, interface-engineering, oxygen vacancy, and doping with metal and non-metal have been developed. For instance, when it is coupled with other semiconductors its photocatalytic activity becomes more favored. Hsieh et al. (Hsieh et al., 2013) have synthesized Bi_2O_3/CeO_2 composite via the hydrothermal method and compared the photocatalytic performance of pristine Bi_2O_3, CeO_2, and Bi_2O_3/CeO_2 composite in which the composite showed excellent catalytic performance under visible light illumination for the degradation of Orange II dye.

Doping is also an effective and efficient strategy to reduce the large recombination rate of electron-hole pairs. Li et al. (T. Li et al., 2020) reported the La-doped Bi_2O_3 prepared via the sol-gel method in which the La^{3+} doping creates oxygen vacancies on the surface of Bi_2O_3 and also as an efficient scavenger to capture the photoinduced electrons. The prepared material was used for the degradation of methyl orange (MO) and phenol and showed an enhanced photocatalytic activity which was attributed to the strong synergistic effects of La^{3+}-doping and oxygen vacancies (OVs) as shown in Figure 9. According to this report, the photocatalytic mechanism for the degradation of methyl orange and phenol are as follows:

$$\mathrm{La-Bi_2O_3} + h\upsilon \rightarrow \mathrm{h^+} + (\mathrm{e^-})_{CB} \tag{22}$$

$$\mathrm{La-Bi_2O_3} + h\upsilon \rightarrow \mathrm{h^+} + (\mathrm{e^-})_{OVs} \tag{23}$$

$$\mathrm{La^{3+}}(5d^0 6s^0) + (\mathrm{e^-})_{OVs} \rightarrow \mathrm{La^{2+}}(5d^0 6s^1) + \mathrm{h^+} \tag{24}$$

$$\mathrm{La^{2+}}(5d^0 6s^1) + O_2 \rightarrow \mathrm{La^{3+}}(5d^0 6s^0) + O_2^{\cdot -} \tag{25}$$

$$\mathrm{MO/Phenol} + O_2^{\cdot -}/h^+ \rightarrow CO_2 + H_2O + \cdots \quad (26)$$

Singha and Sharma also reported the Ni-doped Bi_2O_3 synthesized by the chemical precipitation method (Singh & Sharma, 2018). They used the doped photocatalyst for the degradation of methylene blue under the illumination of visible light and Ni dopant was served as a trapping energy site for the photogenerated charge carriers which resulted in greatly enhanced photocatalytic activity of Bi_2O_3 photocatalyst.

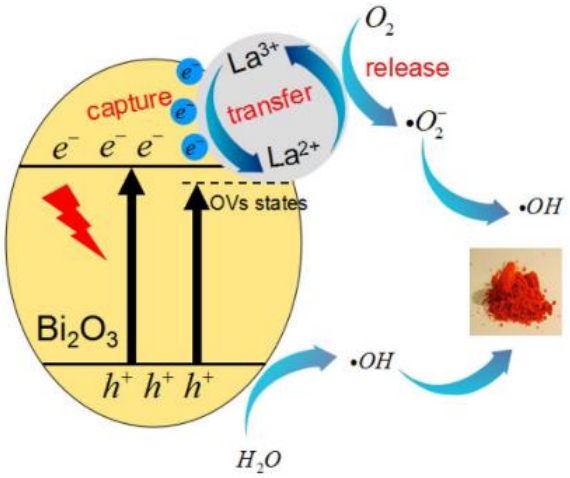

Figure 9: A proposed schematic photodegradation mechanisms for MO over 2% La–Bi_2O_3 sample under visible light irradiation (T. Li et al., 2020).

2.6. Lead monoxide (PbO)

Among many important lead compounds, lead oxide has attracted attention due to its good reactivity, cost-effectiveness, experimental simplicity, and recyclability (Geldasa et al., 2022) (Tayebee et al., 2017). Lead oxide exists in Pb^{4+} (PbO_2) and Pb^{2+} (PbO) oxidation states. PbO_2 is mainly used as electrode materials in lead-acid battery which is used in motor vehicles as internal combustion engines (Poll & Payne, 2014). On the other hand, PbO_2 and PbO possess good chemical stability, optical transparency, and micro-hardness which make them suitable for optoelectronic industry applications (J. Li et al., 2021; Mebed et al., 2022; Najafi et al., 2019). Lead oxide can also be found in the form including Pb_3O_4, PbO_2, Pb_2O_3 (α, β, and amorphous), and PbO (α, β) (Karami et al., 2008). Recently, both α and β-PbO nanoparticles has attracted many researchers' attention due to their phase changes by simple methods. The α-PbO nanoparticle is red, has a tetragonal structure, and is also known as litharge. The β-PbO nanoparticle is yellow, has an orthorhombic structure, and is also known as a massicot

(Geldasa et al., 2022). Litharge (α-PbO) is stable at low temperatures (below 488 °C (910 °F) whereas massicot (β-PbO) stable at high temperatures (above 488 °C). The two forms of PbO are insoluble in water but dissolves in acids to form salts containing Pb^{2+} ions and to form plumbites in alkalis, which have PbO_2^{2-} ion. Litharge which can be produced by air oxidation of lead is importantly used as starting materials to produce lead compounds and considerable quantities of PbO is consumed in manufacturing the plates of lead acid storage batteries. High quality glassware contains 30 percent of litharge, which is used in increasing the refractive index of the glass and makes it resonant, brilliant, and strong. Litharge also employed in varnishes as drier and also in making sodium plumbites, which is used in for removing malodorous thiols from gasoline. In perovskite thin films, PbO is used as interfacial layer engineering for superior UV stability (X. Liang et al., 2016). Lead monoxide synthesized in 2D form of nanostructures possesses excellent optical response. Song et al. (Y. Song et al., 2019) verified PbO nanosheets as excellent optical absorber.

Due to the simple phase changes of PbO, synthesizing high-purity PbO phases is not easy. Thus, the two phases may exist together, but with different degrees of existence. Noukelag et al. (Noukelag et al., 2019) synthesized PbO nanoparticles through the green method using the leave extract of rosemary as a chelating agent resulting in the production of the mixing of the two PbO phases. Nafees et al. (Nafees et al., 2017) have prepared tetragonal PbO by thermally decomposing lead oxalate, with very little existence of the β-PbO phase. Nevertheless, there are also reports on the synthesis of high pure α and β-PbO nanoparticles without the mixture of the two phases. Perry and Wilkinson have prepared the high-purity of the two polymorphs of PbO, i.e. high pure α-PbO and high pure β-PbO separately (Perry & Wilkinson, 2007). According to their report, there had been extremely taken actions such as choice of reaction labware, purity of starting reagents and following very precise procedures during the production of a high pure PbO. For the synthesis of high purity α-PbO and β-PbO, they considered the effect of labware. Thus, they used Teflon labware for the high-purity synthesis of α-PbO, whereas quartz glassware for the high-purity of β-PbO nanoparticles. Arulmozhi and Mythili have synthesized tetragonal α-PbO nanoparticles by using a chemical method (Arulmozhi & Mythili, 2013).

Mythili and Arulmozhi have also used a simple chemical precipitation method to synthesize α-PbO and confirmed the purity of α-PbO from XRD analysis and have studied the dielectric

and electric properties as a function of frequency and temperature of applied electric field (Mythili & Arulmozhi, 2015). Liu et al. (W. Liu et al., 2017) have produced pure α-PbO fine powder by desulfination of $PbSO_4$ using $(NH_4)_2CO_3$ to produce $PbCO_3$ and subsequently calcined $PbCO_3$ at 450 ^oC. Liu et al. (N. Liu et al., 2020) have produced a high purity α-PbO. They used the leaching process for $PbSO_4$ from the spent lead acid battery by dissolving in conjugated $(NH_4)_2SO_4$-NH_3, $PbCO_3$ was obtained by carbonizing and ultimately the high purity α-PbO was obtained via thermal decomposition of $PbCO_3$. Shin and Min synthesized tetragonal α-PbO nanoparticles from lead (II) nanoflower coordination polymer prepared via the sonochemical method (Hyun-jun Shin, 2013). Li et al. (S. Li et al., 2005) have obtained pure α-PbO via microwave irradiation technique after calcining at 400 ^oC. They also increased calcining temperature to 500 ^oC but they obtained the mixture of the two phases of PbO.

Synthesis of pure β-PbO phase without the existence of α-PbO is very challenging because of its low stability at low temperatures. Zhan et al. (Zhan et al., 2017) have prepared a mixture of both PbO phase nanostructure in nanorod and nanosheet from waste Pb-Sn solders of electric and electronic equipment by directly oxidizing and evaporating with β-PbO containing the major phases. They observed the formation of α-PbO at the beginning, but it disappeared during the condensation process and transformed into the β-PbO phase. Wang et al. (Yonggang Wang et al., 2013) have used the hydrothermal growth method to obtain both phases in bulk forms by adding transition metal as additives Ni^{2+} for obtaining the α-PbO and Cr^{3+} for β-PbO. They conducted an unexpected phase transition from β-PbO to α-PbO under anisotropic pressure. Güngör et al. (Güngör et al., 2017) have synthesized both phases of PbO nanoparticles. To synthesize the β-PbO phase they decreased the molar ratio of NaOH/lead acetate trihydrate to equal or below 10, then the green and shiny sample was observed and were substantially in the form of the β-PbO phase. Recently, Darki et al. (Yazdani Darki et al., 2021) synthesized the mixture of the two phases of PbO nanostructures by using ultrasonic waves and they investigated the effects of polyvinylpyrrolidone surfactant and different alkalis on the size and morphologies.

Other groups have also reported the preparation of high-purity β-PbO phase. Pasha and Chidambaram have prepared pure β-PbO by dissolving lead acetate in propanol at room temperature (Pasha & Chidambaram, 2014). After keeping the solution pH to 9 they increased the temperature to 75 ^oC and stirred for 10 hours to obtain pure β-PbO and confirmed the

orthorhombic structure of the prepared β-PbO by using XRD structural analysis. Chen et al. (K. C. Chen et al., 2011) have reported the pure β-PbO nanoparticle prepared at the air/water interface through hydrolysis of Pb^{2+} ions. Orthorhombic β-PbO can also be synthesized with different morphologies. Lambat et al. (Lambat et al., 2019) have synthesized mesoporous orthorhombic PbO nanoparticles by mixing methanolic lead nitrate with sodium hydroxide and sodium dodecyl and used it as a heterogeneous catalyst for the synthesis of arylbezodioxy xanthenedion scaffolds. They suggested that PbO nanoparticles are inexpensive, non-corrosive, and easily accessible. Orthorhombic β-PbO can be applied as electrodes for lead acid batteries. Ali et al. (Ali et al., 2021) have prepared orthorhombic PbO nanoparticles by sol-gel method and recommended that the prepared PbO nanoparticles can be used as electrodes of lead-acid batteries. The β-PbO phase can also be synthesized by thermal decomposition. Behzad et al. (Behzad et al., 2015) have reported the orthorhombic PbO nanoparticle obtained from lead (II) coordination polymer that thermally decomposed directly at 600 ^{o}C. Li et al. (S. Li et al., 2005) have obtained a pure β-PbO phase after calcining at 600 ^{o}C for 2 h which was prepared via microwave irradiation technique. In order to show the effect of heating they also calcined at 500 ^{o}C but it results in a mixture of the two phases.

2.6.1. Metals doped PbO

In the literature, it has been reported that the undoped/dopant surface could act as regulation sites for the separation of photoinduced electrons-holes pairs and improves the photocatalytic performance (Luo et al., 2019). Despite the successful synthesis of high purity of both α-PbO and β-PbO, there are few reports on the different metal-doped PbO nanoparticles. Srichai et al. (Srichai et al., 2021) have used a chemical precipitation method for the antimony (Sb^{3+}) doped PbO nanoparticles. They argued that the tetragonal α-PbO phase was obtained before and after Sb^{3+} was doped. The energy bandgap of the Sb^{3+} doped α-PbO nanoparticles was decreased in comparison with the undoped PbO nanoparticles. Azarang et al. (Azarang et al., 2018) have prepared Zn-doped PbO nanoparticles and deposited it on fluorine-doped tin oxide as a photoanode to measure the photocurrent response of SnSe nanoparticles. From the XRD result, they observed that the undoped PbO nanoparticle has a mixture of both β-PbO and α-PbO phases. However, the Zn-doped PbO nanoparticles showed only the β-PbO phase as they confirmed by Raman spectra results.

2.6.2. PbO thin film

Due to its high volatility relatively at low temperatures, the preparation of PbO thin films is often complicated (Suryawanshi et al., 2018). Various physical and chemical methods have been developed for the synthesis of PbO thin films. Pulsed laser-assisted deposition (Eisa, 2020), spray pyrolysis (Suryawanshi et al., 2018), electrodeposition (Yu et al., 2009), electroplating (Poll & Payne, 2014), Chemical vapor deposition (Naeem et al., 2017), atomic layer deposition (Harjuoja et al., 2006), and thermal evaporation (Droessler et al., 2012) has been developed for PbO thin film preparations. The two phases of the PbO (α-PbO and β-PbO) can exist together during synthesis since the deposition of a single PbO phase with a certain crystal form is difficult due to the existence of PbO in many phases (Suganya et al., 2014).

While all the above-mentioned techniques are used in PbO thin film synthesis, they are not cost-effective and not simple. The chemical solution chemical bath deposition (CBD) method is simple, low-cost, and rapid. Not only these, thin films deposited by CBD is adherent and uniform. The CBD technique has been applied for the synthesis of different metal sulfide and metal oxide thin films (Hodes, 2007). For example, Ashok et al. (Ashok et al., 2020) synthesized CdS thin films as buffer layers for solar cells by CBD. Hone and Dejene have grown polycrystalline lead sulphide thin films on a glass substrate by CBD (Hone & Dejene, 2018). CBD has also been applied for the deposition of metal oxide thin films. Shaikh et al. (Shaikh et al., 2016) used the CBD method to prepare a ZnO thin film based UV photoconductive detector. Nwanya et al. (Nwanya et al., 2013) deposited AgO thin film by CBD under different deposition times. M. Martínez-Gil et al. (Martínez-Gil et al., 2017) have prepared NiO thin film via CBD using nickel sulfate and triethanolamine. Gunjakara et al. (Gunjakar et al., 2016) synthesized Ag_3PO_4 thin films by CBD method with enhanced visible light photocatalytic activity. It is clear that the film deposition takes place at super-saturation, when the ionic product exceeds the solubility product, thus when the precipitations of the positive and negative ions occur. That is $Pb(OH)_2$ is formed when the ionic product of Pb^{2+} and OH^- exceeds the solubility product of $Pb(OH)_2$ in PbO deposition. Solubility product is the point at which the maximum number of ions that solution can handle is formed, while ionic product is when excess ions are formed in the solution. When the ionic product is equal to the solubility product it is called saturation solution whereas it is called super-saturation when the ionic product exceeds the solubility product.

Hence, at a super-saturation solution, precipitation occurs and cations and anions combine on the immersed substrate and in the solution to form nuclei.

2.6.3. Pb-based oxide Photocatalysts

All the metal oxide photocatalysts we overviewed in the aforementioned sections inspired us to study the photocatalytic activity of lead oxides. Actually, there is no detailed investigation reported so far on the photocatalytic activity of α-PbO and β-PbO. Therefore, the metal oxides overviewed in the previous sections help us to investigate the photocatalytic activity of α-PbO and β-PbO because both α-PbO and β-PbO are also a type of metal oxide semiconductor. Depending on that information we will evaluate and investigate the photocatalytic activity of metals doped α-PbO and β-PbO in this research. The earth's abundance of α-PbO and β-PbO and easy recyclability also exited us to evaluate its photocatalytic activity because low-cost material is one of the criteria to select materials for photocatalytic applications.

Lead oxide in its nanostructure is more interesting than its bulk form. Recently, Elsafi et al. (Elsafi et al., 2021) analyzed the effect of particle size on radiation shield which resulted in the same amount of radiation absorption for bulk and nanoparticles PbO the needed mass lower for the nanoparticles making the nanoparticles more desirable if the mass is the concern. PbO can be found in different nanostructure forms including nanopowders (Kashani-Motlagh & Mahmoudabad, 2011), nanorods (Hanifehpour et al., 2012; B. Jia & Gao, 2006; Zhan et al., 2017), quantum dot (Leelavathi et al., 2013), nanotubes and nanosheets (Fu et al., 2020; P. Kumar et al., 2018), nanowires (Hai et al., 2013) nanoplates, nanodendrite and nanostars (K. C. Chen et al., 2011). PbO nanoparticles have a wide range of applications including energy storage devices, luminescence materials, gas sensors, modifiers in glass, lead crystals, pigments, nanoelectronic devices, lead glazes, UV blockers, pigments, and in decorative potteries (Aliakbari et al., 2014; Arulmozhi & Mythili, 2013; Behzad et al., 2015; Noukelag et al., 2019; Yazdani Darki et al., 2021). It also used as shielding materials for gamma radiation protection (Al-Attiyah et al., 2019).

Lead oxide nanoparticles can also be used as photocatalytic degradations (Borhade et al., 2013, 2012; Weidong Li et al., 2017). However, for photocatalysis applications, PbO is not widely reported alone but coupled PbO with other semiconductors have been widely reported. The PbO composite with different metal oxide semiconductors have advantages such as

shifting the ultraviolet activity of materials to visible light active by controlling bandgap and modifying the structure and morphology of the newly formed composite photocatalyst. For instance, Bhachu et al. (Bhachu et al., 2014) deposited PbO nanoclusters onto titanium dioxide (anatase) polycrystalline films on a glass substrate by chemical vapor deposition method to form PbO/TiO_2 composite. The PbO-modified TiO_2 introduced new electronic states above the valence band maximum of TiO_2 which resulted in the enhancement of the photocatalytic activity of TiO_2 in the visible light region. Leelavathi et al. (Leelavathi et al., 2013) have designed PbO quantum dot dispersed on anatase TiO_2 to form heterostructures by combining non-hydrolytic sol–gel and combustion methods for the separation of photogenerated charge carriers. They observed that the bare PbO showed very poor photocatalytic activity. They obtained 77% and 50% of the photodegradation percentage of orange G for TiO_2/PbO and TiO_2 respectively within 2 hrs. The nanocomposites of PbO quantum dot on TiO_2 showed enhanced photocatalytic activity which was assigned to a synergistic effect of higher number of active sites, higher surface area, and engineered bandgap in the heterostructure.

PbO has also been used in other different metal oxide nanoparticles to modify their photocatalytic activity. Mebed et al. (Mebed et al., 2022) prepared PbO–Al_2O_3 nanocomposite by microwave irradiation method and utilized it for the removal of methylene blue from wastewater under UV-visible or visible light irradiations. Al_2O_3 possesses a very wide bandgap of approximately 9 eV. However, compositing it with PbO made it to response visible light irradiation and improves the overall physicochemical properties. Wang et al. (Z. Wang et al., 2018) reported Sb_2O_3/PbO coupled semiconductor photocatalyst synthesized by hydrothermal method for the degradation of carbamazepine (CBZ). They selected PbO for coupling with Sb_2O_3 due to its high stiffness, high thermal stability, and high tensile strength. Wang et al. (Z. Wang et al., 2019) have synthesized PbO/TiO_2 and Sb_2O_3/TiO_2 photocatalysts for the degradation of UV filter Benzophenone-3 under UV-C irradiation and PbO/TiO_2 completely degraded the UV filter Benzophenone-3 within 120 min. They studied the effect of pH by varying from 3 to 11. The degradation rate increased as pH value increased from 3 to 9 for the photocatalyst with PbO ratio with TiO_2 (1:2). However, the degradation rate slightly decreased as pH increased to 11 compared to 9. Figure 10 represents the schematic of photocatalytic mechanism of PbO/TiO_2 nanocomposite. Reactive holes (h^+) generated on the

surface of PbO and reactive electrons (e^-) generated on the surface of TiO_2 under the UV-C irradiation. The photogenerated electrons reduced the dissolved O_2 to superoxide radicals ($O_2\bullet-$). Then $O_2\bullet-$ radicals undergo the oxidation process with the photogenerated h^+ to produce $^1O_2$ as shown in Equations (27-29).

$$PbO/TiO_2 + h\upsilon \rightarrow TiO_2(e^-) + PbO(h^+) \quad (27)$$

$$(TiO_2)e^- + O_2 \rightarrow O_2\bullet- \quad (28)$$

$$(PbO)h^+ + O_2\bullet- \rightarrow {}^1O_2 \quad (29)$$

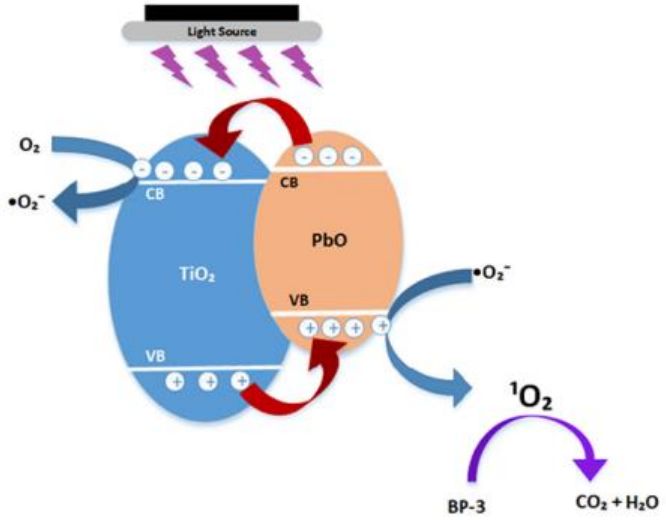

Figure 10: Mechanism of photocatalytic degradation of BP-3 by using PbO/TiO_2 (Z. Wang et al., 2019).

Pb-containing metal oxides photocatalyst has also been reported by different groups. For instance, Pourmasoud et al. (Pourmasoud et al., 2017) have reported $PbWO_4$ synthesized by co-precipitation method for the degradation of methyl orange from wastewater under UV irradiation and achieved a 97% rate of degradation. Gyawali et al. (Gyawali et al., 2013) reported an Ag-$PbMoO_4$ photocatalyst synthesized by the sonochemical method for the degradation of Indigo Carmine dye under simulated solar light irradiation.

Perovskites containing Pb in their compositions have a potential application in solar energy conversions, but recently they are studied to use as photocatalysts. In photocatalysis, perovskites are used as means of energy production and water purification (Temerov et al., 2022). The combination of PbO with perovskite photocatalysts has also been reported by different scholars. Liu et al. (F. Y. Liu et al., 2018) synthesized $PbBiO_2I$/PbO nanocomposite by using the hydrothermal method and used it as a photocatalyst for the degradation of crystal

violet (CV) dye. According to this report, the formation of a composite between $PbBiO_2I$ and PbO suppresses the rapid recombination of photogenerated electrons and holes pairs and improves the photocatalytic activity of the individual $PbBiO_2I$ and PbO by 3 and 20 times respectively. The charge carrier transfers and photocatalytic mechanism of the prepared $PbBiO_2I$/PbO are shown in Figure 11. As one can be observed from the depicted Figure 11 the valence band maximum (VBM) and conduction band minimum (CBM) of $PbBiO_2I$ was higher than that of PbO. Therefore, the photogenerated electrons able to occur on the surface of $PbBiO_2I$ could be transferred to the PbO conduction band whereas holes existing on the surface of PbO can transfer to $PbBiO_2I$. Thus, the charge transfer between the two semiconductors effectively hinders electron-hole recombination, hence improving photocatalytic efficiency. When electrons and holes reached CB and VB of $PbBiO_2I$/PbO the active oxygen species which degrades CV is formed Equation 30 and 31. As observed in Figure 11 in the photosensitized and photocatalytic process, photogenerated and photosensitized electrons react with O_2 on the surface of the photocatalyst and produced superoxide (O_2•−). $^1O_2$ is also generated upon the reaction between O_2 and photocatalyst. The combination of perovskites, PbO, and other semiconductors to form heterojunctions has also been reported. Wang et al. (Y. C. Wang et al., 2018) synthesized $PbBiO_2Br$/PbO/g-C_3N_4 heterojunctions by hydrothermal without using a template and they demonstrated that the enhancement of the photocatalytic activity of this photocatalyst corresponded to the heterojunctions formed between $PbBiO_2Br$, PbO, and g-C_3N_4. Thus, PbO contributes to the enhancement of the photocatalytic activities of this heterojunction.

$$(\text{organic pollutant})\text{CV} + / \, {}^1O_2/h^+ \rightarrow \text{degraded compounds} \quad (30)$$

$$(\text{organic pollutant})\text{CV}^+ + O_2\bullet - / \, {}^1O_2/h^+ \rightarrow \text{degraded compounds} \quad (31)$$

Pb-containing composition of compounds has also been used for the removal of microbiological contaminants from drinking water. Li et al. (Yang Li et al., 2019) synthesized Pb-$BiFeO_3$/rGO photocatalyst via the hydrothermal method and evaluated the photocatalytic disinfection efficiencies toward gram-negative *Escherichia coli (E. coli)* and gram-positive *Staphylococcus aureus (S. aureus)* under the illumination of visible light. According to their report, the complete inactivation of *E. coli* and *S. aureus* was achieved within 30 min and 90 min respectively. In this report, the intercalated Pb coordinate with Bi^{3+} was to provide actives

sites for the reaction, hence improving the photocatalytic activity of $BiFeO_3$.

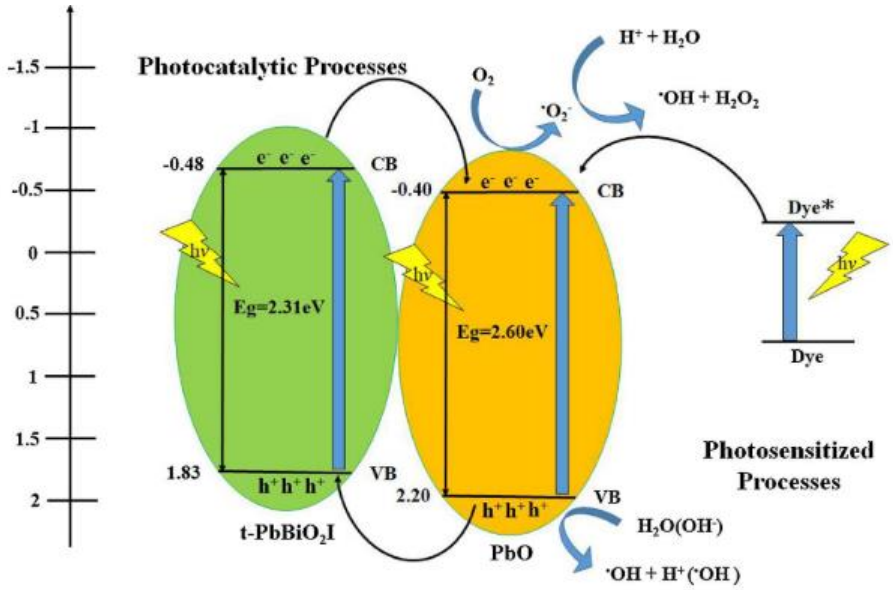

Figure 11 Schematic illustration of the band gap structures of t-$PbBiO_2I$/PbO (F. Y. Liu et al., 2018).

2.6.4. Toxicology aspects

Lead (Pb) is known to be one of the post-transition metals in group 14 (IVA) of the periodic table. Properties of lead, such as ease of welding, ductility, high density, low melting point, and ability to absorb gamma and x-ray radiation make it applicable in different areas. Despite the attractive applications of lead and its compounds in various technologies, the toxicity of Pb is hindering its sustainability for broad applications. Lead is among the 275 most toxic substances and it can enter the body through smoking, food, industrial means, water, and skin, leading to heavy metal poisoning. Lead and its compounds are toxic and are retained by the body, accumulating for a long period. The toxicity of lead compounds increases as their solubility increases. The tetraethyl lead ($Pb(C_2H_5)_4$), which is used as an antiknock additive in gasoline pollutes air and water, and it is water soluble salt produced by dissolving litharge (PbO) in concentrated acetic acid. Important elements in hydroxyapatite in bones such as Zn^{2+}, Cu^{2+}, and Fe can be replaced by lead ions when lead ions are absorbed by the human body, which causes damage to bones (Kamel et al., 2019). Water could also be polluted with lead ions through the corrosion of pipes and causing health concerns. Lead has detrimental effects on human health in different organ systems (Basak et al., 2017). Some studies have indicated that blood lead concentrations below 100 mgL^{-1} in children are associated with intellectual impairment and compromised cognition and more children may be adversely affected

by lead from the environment than previously estimated (Bazzi et al., 2008).

Materials containing lead such as lead halide perovskites have got much attention due to their high efficiency in solar cells. However, there are many concerns due to the presence of lead which hinders the practical applications of these perovskites (Ibrahim & Chung, 2022). When exposed to the environment, the main degradation product of perovskite solar cells is PbI_2, which then transforms into $Pb(OH)_2$ and HI. The acidification of the medium by HI is more harmful than the uptake of $Pb(OH)_2$, which is much smaller than typical organometallic lead compounds such as the infamous tetrabutyl lead (Schileo & Grancini, 2021).

Lead oxide nanoparticles are widely used in various industrial process (Tulinska et al., 2022). From high temperatures processes such as lead smelters, battery plants, steel and iron production, waste burning, and nonferrous foundries PbO can be released into the environment. Lead can be found as elemental lead, lead ore, inorganic and organic lead compounds. Among these classifications, the organic lead compound is the most dangerous which can be easily absorbed through the skin and is much more toxic than inorganic lead compounds (Shimoni-Livny et al., 1998). To measure and evaluate the toxicity of lead oxide different researchers have done evident measurements. For instance, Ng et al. (Ng et al., 2019) used adult medaka fish as a model animal to examine the availability and toxicity of both nanoscale and bulk PbO_2 particles. They observed that in dechlorinated tap water the two particles were stable chemically with low solubility in water. However, as they confirmed from the X-ray absorption near-edge structure analysis and quantification of lead speciation both nanoscale and bulk PbO_2 could be reductively dissolved into Pb(II)aq in gills and intestine of the modeled fish. Thus, this in vivo evidence implies that from PbO_2 particles in the digestive system through drinking water, there is the possibility of increased risk of Pb dissolution, which increases the bioavailability of Pb uptake and toxicity in humans. Although the possibility of removing PbO NPs from target organs such as kidney, lung, blood, liver, bone, and spleen has been examined and reported so far (Dumková et al., 2020). In 2016 about 11144000 tones (an increase of 38% from 2008) of lead was produced globally and 42% was extracted from lead ore, while the rest percent were from recycling. Lead has high recyclability and about 80% of Pb recycling has been reached in the US. Thus, it can be kept from releasing to the environment due to its high recyclability (Schileo & Grancini, 2021). About 23600 ppm Pb is suggested as a safe level in soil and would contribute less than 5 mg dL^{-1} to the total blood lead of children below 12 years (Sharda et al., 2021).

Despite their toxicity lead compounds are importantly used in different modern technologies due to their plenty properties such as malleability, softness, ductility, and corrosion resistivity (Wani et al., 2015). Different inorganic lead compounds such as PbS (Abargues et al., 2019), PbSe (Congjun Wang et al., 2007), PbO_2 (Murata et al., 2014) and PbO (F. Y. Liu et al., 2018) have been studied so far for the removal of organic contaminants in wastewater. There are some strategic techniques of identifying and removing lead ions from drinking water (Bayuo et al., 2022). For instance, Kamel et al. (Kamel et al., 2019) reported the detection and removal of Pb ions from drinking water by using Acid Red 94. Pb can be accumulated in all organs and causes inflammation which leads to a delay in wound recovery. To suppress this Sharda et al. (Sharda et al., 2021) reported the capturing system of Pb ions from the circulatory system to achieve effective healing of Pb poisoned system by using paramagnetic nickel–insulin quantum clusters. Basak et al. (Basak et al., 2017) successfully removed Pb ions from wastewater by discovering a hydrogelator.

2.7. Computational method

2.7.1. Overview of DFT

Density functional theory (DFT) is a modern calculation widely used in the fields like condensed matter physics, quantum chemistry, and materials science and it is a practical electronic-structure calculation computational method (Islam et al., 2021). Additionally, DFT is an exact elegant reformulation of the quantum many-body problem, which has led to new ways of thinking in the field (Toulouse, 2019). DFT is primarily a theory of electronic structure calculations at ground states couched in terms of electron density (Kohn et al., 1996). In order to be familiar with DFT it is good if we describe a little bit theory background of DFT. DFT framework provides a computationally easy and controllable way to solve and approximate many-body problems for electrons both in excited state and ground state (Andrade et al., 2021). The background of DFT starts from the influential Schrödinger equation given by Equation (32). Quantum mechanics search around finding the solution to the Schrödinger equation. Schrödinger equations has limitations such as its complexity and for system having many electrons it is high computational cost (Makkar & Ghosh, 2021).

$$\widehat{H}\psi = E\psi \tag{32}$$

where, $\widehat{H}$ is the Hamiltonian operator and ψ is wavefunction or a set of solutions of the

Hamiltonian.

In atoms there are different interactions in which the Hamiltonian $\widehat{H}\psi$ is described. If we have nuclei M with mass M_n at positions ($\mathbf{R}_1 \ldots \mathbf{R}_n$) and another nuclei at positions ($\mathbf{R}_1 \ldots \mathbf{R}_m$) and N electrons with mass m_e at positions ($\mathbf{r}_1 \ldots \mathbf{r}_i$) and another electrons at positions ($\mathbf{r}_1 \ldots \mathbf{r}_j$) the Hamiltonian consisting both kinetic and potential energy can be determined (Capelle, 2006). The kinetic energy of electrons ($\widehat{T}_{\mathbf{r}}$) and nuclei ($\widehat{T}_{\mathbf{R}}$) is given by Equation (33) and (34) respectively,

$$\widehat{T}_{\mathbf{r}} = -\sum_{i=1}^{N} \frac{\hbar^2}{2m_e} \nabla_i^2 \tag{33}$$

$$\widehat{T}_{\mathbf{R}} = -\sum_{n=1}^{N} \frac{\hbar^2}{2M_n} \nabla_n^2 \tag{34}$$

Electron-electron interaction (repulsion potential energy ($\widehat{V}_{\mathbf{r}}$)) is given by

$$\widehat{V}_{\mathbf{r}} = \frac{1}{4\pi\varepsilon_0} \frac{1}{2} \sum_{i \neq j}^{N} \frac{e^2}{|\mathbf{r}_i - \mathbf{r}_j|} \tag{35}$$

Nucleus-nucleus repulsion potential energy ($\widehat{V}_{\mathbf{R}}$) is given as

$$\widehat{V}_{\mathbf{R}} = \frac{1}{4\pi\varepsilon_0} \frac{1}{2} \sum_{n \neq m}^{N} \frac{Z_n Z_m e^2}{|\mathbf{R}_n - \mathbf{R}_m|} \tag{36}$$

Electron-nucleus attraction potential energy ($\widehat{V}_{\mathbf{r},\mathbf{R}}$) is given by

$$\widehat{V}_{\mathbf{r},\mathbf{R}} = -\frac{1}{4\pi\varepsilon_0} \frac{1}{2} \sum_{i,n}^{N} \frac{Z_n e^2}{|\mathbf{r}_i - \mathbf{R}_n|} \tag{37}$$

The Born-Oppenheimer approximation is developed to solve the complex Schrödinger equation. Nuclei are much heavier and slower than electrons, thus, from the perspective of the electrons, nuclei positions are static and from the perspective of nuclei, electrons positions update instantaneously (Flick et al., 2017). These informations allows to approximate nuclei as fixed with respect to electrons. Therefore, the kinetic energy of nuclei is zero and the nucleus-nucleus repulsion potential energy term is constant. Then, only the electrons terms are left and the Born-Oppenheimer Hamiltonian, $\widehat{H}_{\mathrm{BO}}$ (Takahashi, 2016) is equal to the

Hamiltonian of the electron, $\widehat{H}_{\mathrm{e}}$:

$$\widehat{H}_{BO} = \widehat{H}_e = -\sum_{i=1}^{N} \frac{\hbar^2}{2m_e} \nabla_i^2 - \frac{1}{4\pi\varepsilon_0} \frac{1}{2} \sum_{i \neq j}^{N} \frac{e^2}{|\mathbf{r}_i - \mathbf{r}_j|} - \frac{1}{4\pi\varepsilon_0} \frac{1}{2} \sum_{i,n}^{N} \frac{Z_n e^2}{|\mathbf{r}_i - \mathbf{R}_n|} \tag{38}$$

In short it can be written as

$$\widehat{H}_{BO} = \widehat{H}_e = \widehat{T}_{\mathbf{r}} + \widehat{V}_{\mathbf{r}} + \widehat{V}_{\mathbf{r},\mathbf{R}} \tag{39}$$

Then Schrödinger equation is reduced to:

$$\widehat{H}_e \psi_e(\mathbf{r}_1, \dots, \mathbf{r}_N) = E_e \psi_e(\mathbf{r}_1, \dots, \mathbf{r}_N) \tag{40}$$

ψ_e is a wave function of electron position $\mathbf{r}_i$ only. A complete description of each electron includes its three spatial variables and its spin. However, for simplicity the electron spin (spin up and spin down) has been neglected.

The electron wavefunction that gives the minimum or lowest E_e is termed as the ground state. Due to electron-electron interaction in Equation (38) and (39) is many-body problem, it is not trivial to find ψ_e, where all electrons must be simultaneously considered. Thus, the wavefunction cannot be measured directly. However, the probability of that the N electrons at some particular set of coordinates can be measured in principle. The probability is given by

$$|\psi(\mathbf{r}_1, \dots, \mathbf{r}_N)|^2 = \psi^*(\mathbf{r}_1, \dots, \mathbf{r}_N)\psi(\mathbf{r}_1, \dots, \mathbf{r}_N) \tag{41}$$

where, the asterisk indicates a complex conjugate.

$\psi(\mathbf{r}_1, \dots, \mathbf{r}_N)$ can be approximated as a product of individual electron wavefunction:

$$\psi(\mathbf{r}_1, \dots, \mathbf{r}_N) \cong \psi_1(\mathbf{r})\psi_2(\mathbf{r}), \dots, \psi_N(\mathbf{r}) \tag{42}$$

The product of the individual electron wavefunction is known as Hartree product. Electrons cannot be distinguished by labeling as electron 1, electron 2, etc. A closely related quantity to the probability is the electron density is given by:

$$n(\mathbf{r}) = 2 \sum_{i=1}^{N} \psi^*{}_i(\mathbf{r})\psi_i(\mathbf{r}) \tag{43}$$

The number 2 indicates that each individual electron wavefunction occupied by two separated electrons with opposite spin. What we have to remember here is the electron density ($n(\vec{r})$) is

a function of only three coordinates. However, it contains lots of information that is actually observable from the full wavefunction, which is a function of 3N coordinates.

Generally, DFT depends on two fundamental theorems developed by Kohn and Hohenberg (King-Smith & Vanderbilt, 1993) (P. Hohenberg & W. Kohn, 1994):

Theorem I: The ground state energy E from Schrödinger's equation is a unique functional of the ground state of electron density ($n_0(\mathbf{r})$).

$$E = E[n_0(\mathbf{r})] \tag{44}$$

Theorem II: The electron density that minimizes the energy of the universal functional $E[n(\vec{r})]$ is the exact electron density ($n_0(\mathbf{r})$), corresponding to the full solution of the Schrödinger equation. Thus, the ground state is the global minimum value of this functional and the electron density $n(\mathbf{r})$ that minimizes the functional is the true electron density $n_0(\mathbf{r})$

A complete energy functional is composed of known and exchange-correlational terms:

$$E[\{\psi_i\}] = E_{known}[\{\psi_i\}] + E_{XC}[\{\psi_i\}] \tag{45}$$

The known energy functional consists:

$$\begin{aligned} E_{known}[\{\psi_i\}] = \frac{\hbar^2}{m_e}\sum_i \int \psi_i^* \nabla^2 \psi_i d^3\mathbf{r} + \int V(\mathbf{r})\, n(\mathbf{r}) d^3\mathbf{r} \\ + \frac{e^2}{2}\iint \frac{n(\mathbf{r})n(\mathbf{r}')}{|\mathbf{r}-\mathbf{r}'|} d^3\mathbf{r} d^3\mathbf{r}' + E_{ion} \end{aligned} \tag{46}$$

While the energy functional of exchange-correlation is to includes all the quantum mechanical effects those not included in the known energy functional.

Kohn and Sham showed finding the right electron density involves solving a set of equations (each involving only single electron) of the form (Capelle, 2006):

$$\left[-\frac{\hbar^2}{2m_e}\nabla^2 + V(\mathbf{r}) + V_H(\mathbf{r}) + V_{XC}(\mathbf{r})\right]\psi_i(\mathbf{r}) = \varepsilon_i \psi_i(\mathbf{r}) \tag{47}$$

where, $V(\vec{r})$ is the potential due to the interaction between an electron and a collection of atomic nuclei; $V_H(\mathbf{r})$ is the Hartree potential; and $V_{XC}(\mathbf{r})$ is the potential that defines the exchange and correlation contributions to the single electron equations.

$$V_H(\mathbf{r}) = \int \frac{n(\mathbf{r})}{|\mathbf{r} - \mathbf{r}'|} d^3\mathbf{r}' \tag{48}$$

The exchange-correlational potential is given as

$$V_{XC}(\mathbf{r}) = \frac{\delta E_{XC}(\mathbf{r})}{\delta n(\mathbf{r})} \tag{49}$$

Energy E is the summation of ε_i

$$E = \varepsilon_i + \cdots + \varepsilon_N \tag{50}$$

Kohn-Sham effective potential is given by

$$V_{KS}^{eff.}(\mathbf{r}) = V(\mathbf{r}) + V_H(\mathbf{r}) + V_{XC}(\mathbf{r}) \tag{51}$$

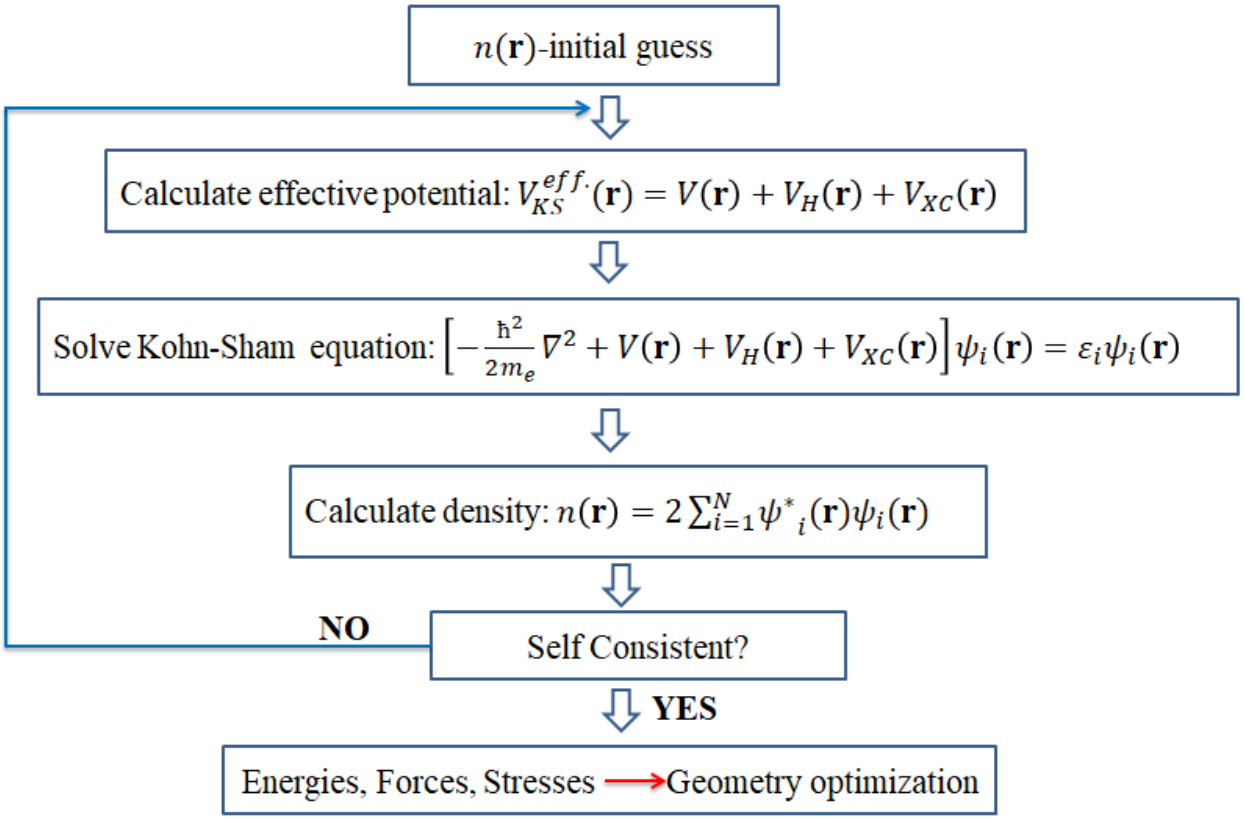

Figure 12: Flowchart of self-consistent Kohn-Sham calculation.

To solve Kohn-Sham equation the Hartree potential is required; to find the Hartree potential electron density is required; to find electron density known single electron wavefunction is required; and to know single electron wavefunction requires solving Kohn-Sham equation.

Generally, we follow an iterative way as mentioned in the following algorithm and also as presented in Figure 12:

i. Guess an initial trial electron density $n(\mathbf{r})$;
ii. Solve the Kohn-Sham equations defined using the trial electron density to find the single particle wavefunction, $\psi_i(\mathbf{r})$;
iii. Calculate electron density defined by the Kohn-Sham single particle wavefunction from step ii, $n_{KS}(\mathbf{r}) = 2\sum_i {\psi^*}_i(\mathbf{r})\psi_i(\mathbf{r})$;
iv. Compare the calculated electron density, $n_{KS}(\mathbf{r})$, with the trial electron density used to solve the Kohn-Sham equations, $n(\mathbf{r})$. If these densities are the same, this is the ground state electron density. Otherwise, update the trial electron density somehow and begin again at step ii.

To solve the Kohn-Sham equations requires specifying the exchange functional whose true form is in general not known and must be approximated. The most commonly used for the approximations of the exchange-correlational are the Local Density Approximations (LDA) and the Generalized Gradient Approximations (GGA).

$$V_{XC}(\mathbf{r}) = V_{XC}^{electron\ gas}[n(\mathbf{r})] \tag{52}$$

As there are many ways the information from the gradient of the electron density can be included in a GGA functional, there are numerous distinct functionals. The most commonly used GGA functionals for solids are the Perdew-Wang (PW91) (John P. Perdew et al., 1996) or Perdew-Burke-Ernzerhof (PBE) functionals (J. P. Perdew et al., 1998) (Ernzerhof & Scuseria, 1999). Other functional beyond LDA and GGA such as hybrid functional, DFT+U, are also presented but these are very expensive functionals. The norm-conserving pseudopotential is used to calculate the optical properties of materials. For optical property analysis, the momentum matrix element and Kramers-Kronig-relation to get imaginary and real parts of dielectric functions, respectively is used (W. Jia et al., 2019). The real and imaginary parts of dielectric function, ε_r and ε_i, respectively are given by:

$$\varepsilon_r(E) = 1 + \frac{2}{\pi} P_{\mathrm{r}} \int_0^{\infty} \frac{\omega \varepsilon_i(E)}{\omega'^2 - \omega^2} d\omega \tag{53}$$

$$\varepsilon_i(E) = \frac{C}{\omega^2} \sum_{cb,vb} \int_{BZ} \frac{2}{(2\pi^3)} \left|P_{cb,vb}(k)\right|^2 \times \delta(E_{cb}^k - E_{vb}^k - E) d^3k \quad (54)$$

where P_r is Cauchy principal value, C is constant, the subscript cb and vb represent conduction band and valence band, BZ is Brillioun zone, k is wave vector, $\left|P_{cb,vb}(k)\right|^2$ is momentum matrix element, ω is frequency, E_{cb}^k and E_{vb}^k intrinsic levels of conduction and valence band, respectively and E is energy of photoelectrons. The complex dielectric function is given by

$$\varepsilon(\omega) = \varepsilon_r(\omega) + i\varepsilon_i(\omega) \quad (55)$$

Other optical properties such as refractive index (n), extinction coefficient (k), absorption coefficient (α), reflectivity (R), electron energy loss spectrum (L), and optical conductivity (σ) are calculated from real part and imaginary part of dielectric function (Eddiouane et al., 2018; W. Jia et al., 2019; Kale et al., 2021; Ramaswamy et al., 2019).

$$n(E) = \left[\frac{\sqrt{\varepsilon_r^2(E) + \varepsilon_i^2(E)} + \varepsilon_r(E)}{2}\right]^{1/2} \quad (56)$$

$$k(\omega) = \left[\frac{\sqrt{\varepsilon_r^2(E) + \varepsilon_i^2(E)} - \varepsilon_r(E)}{2}\right]^{1/2} \quad (57)$$

$$\alpha(E) = \frac{4\pi k}{\lambda} \; or = \frac{2\omega k}{c} \quad (58)$$

$$R(E) = \frac{(n-1)^2 + k^2}{(n+1)^2 + k^2} \quad (59)$$

$$L(\omega) = \frac{\varepsilon_2(E)}{\varepsilon_r^2(E) + \varepsilon_i^2(E)} \quad (60)$$

$$\sigma(E) = \frac{\omega\varepsilon_r(\omega)}{4\pi} \; or = \frac{\alpha nc}{4\pi} \quad (61)$$

where, c is speed of light.

For materials calculations, Quantum ESPRESSO, Vienna Ab initio Simulation Package (VASP), Cambridge Serial Total Energy Package (CASTEP), DMol, and Spanish Initiative for Electronic Simulations with Thousands of Atoms (SIESTA) are the most commonly used

codes in DFT. In this research, Quantum ESPRESSO is used due to its freely available and effectiveness. The detailed review of DFT calculation for different semiconductor photocatalysts is reviewed by Opoku et al. (Opoku et al., 2017b).

DFT simulation is applied for the study of metal oxides and to understand the improvement of the properties of metal oxides by applying different strategies for different technological applications. In order to understand the enhancement of metal oxide properties by the DFT method, strategies such as doping with metal or non-metal, oxygen vacancy, and coupling with other semiconductors to form heterojunctions are among the intensively studied. For instance, Iwaszuk and Nolan studied the PbO and PbO_2 nanoclusters supported on TiO_2 anatase (001) and rutile (110) surface by the first principle DFT method for the modification of TiO_2 photocatalyst (Iwaszuk & Nolan, 2013). They investigated the effects of Pb oxidation states on the PbO_x modifications of TiO_2 photocatalysts which showed a dramatic impact on the nature of band edge modification of TiO_2 and on the separation mechanism of electron-hole. New states were introduced in the pure rutile and anatase when PbO and PbO_2 adsorbed on the surface of TiO_2. Thus, the adsorbed PbO and PbO_2 nanoclusters induced the visible light activation of the TiO_2 photocatalyst and predicted the reduction of fast charge recombination.

Islam et al. (Islam et al., 2021) used DFT calculation to investigate the effects of Ce doping into CuO photocatalyst. After replacing Ce in the place of Cu the crystal structure of CuO was distorted and the symmetry of the system was reduced. Due to the distortion of the structure and lack of symmetry, the centers of the negative and positive charges can get separated. Thus, the photocatalytic performance of the Ce-doped CuO was enhanced due to the reduced recombination of photogenerated electron-hole pairs. The Ce 4f orbital greatly affected the valence and conduction band by introducing defect states near the valence and conduction band. The introduced defect state trapped the photogenerated charges and reduced the fast recombination of photogenerated electrons and holes. They have also calculated the real part and imaginary part of the dielectric constant and concluded that the higher the real part of the dielectric is the lowers the recombination of photogenerated electrons and holes.

Kitchamsetti et al. (Kitchamsetti et al., 2021) also used first-principles DFT calculation to identify the formation of O_2 radicals on the surface of NiO (110) which was believed to

initiate the degradation of rhodamine B dye. Huang and Hart studied the capability of photocatalytic water splitting of various tungstate oxides by DFT calculations (Huang & Hart, 2020). Singha and Sharma have used DFT calculations to investigate the effects of Ni doping into α-Bi_2O_3 on its photocatalytic activities (Singh & Sharma, 2018). Pure α-Bi_2O_3 possesses a direct bandgap. However, after Ni was doped an indirect bandgap bandstructure was obtained. Thus, the Ni-doped α-Bi_2O_3 owns an increased charge separation and retarded electron-hole pair's recombination, which was attributed to the time elongation for the charge transit conduction band to the valence band.

Different semiconducting heterojunctions are also studied by using DFT to obtain a better understanding of its photocatalytic activities. The construction of heterojunction structures is among the most effective method for improving the efficiency of photocatalysts by accelerating the separation and transport of electron-hole. When heterojunction is formed a potential difference is created between the conduction band and valence band at the interface. When irradiated, electrons can be easily excited and immediately form electron-hole pairs. Hence, the photogenerated electrons are transferred to the conduction band of other semiconductors rather than recombining with holes in the valence band. Yao et al. (W. Yao et al., 2022) reported the DFT studied g-C_3N_4/BiOBr(001) heterojunction for a better understanding of its photocatalytic activity by analyzing the electronic and geometric structures. According to their study, they presented ultrathin g-C_3N_4/BiOBr(001) heterojunction formed by stacking g-C_3N_4 on the top of BiOBr with 3.55 Å of the interlayer distance. In the complete relaxation of the heterojunction, the interaction between the g-C_3N_4 monolayer and the surface of BiOBr resulted in g-C_3N_4 flakes with 2.95 Å interlayer distance, which is the van der Waals distance.

To investigate the reason for a high photocatalytic activity they have calculated the density of states. The optical bandgap of g-C_3N_4 and BiOBr was 2.7 eV and 2.8 eV respectively. However, the bandgap of g-C_3N_4/BiOBr(001) heterojunctions was reduced to 1.68 eV which indicated the high efficiency of charge transfer from the valence band to the conduction band g-C_3N_4/BiOBr. The valence band maxima (VBM) of BiOBr(001) was lower than g-C_3N_4, whereas the conduction band minima (CBM) g-C_3N_4 was higher than BiOBr(001), which indicates that the g-C_3N_4/BiOBr(001) heterojunction has typical type-II energy band alignment. This is reasonable for the greater photoresponse to visible light of g-

C_3N_4/BiOBr(001) heterojunction compared to g-C_3N_4 and BiOBr(001). The g-C_3N_4/BiOBr(001) heterojunction absorbs visible light and electrons excited from VB to CB leaving holes behind in the valence band. Some of the photogenerated electrons by the g-C_3N_4 layer were transferred to CB of BiOBr(001), while some of the photogenerated holes by BiOBr(001) were transferred to VB of g-C_3N_4. This process resulted in the effective separation of photogenerated electrons and holes at the different surfaces by the built-in electric field. Thus, the fast recombination of photogenerated electrons and holes is reduced and the photocatalytic performance will be improved efficiently. Oktavianti et al. (Oktavianti et al., 2021) have also used the DFT method to study the adsorption of methylene blue dye on Ni-doped ZnO clusters. They have investigated the adsorption interaction between methylene blue dye and pure ZnO or Ni-doped ZnO in terms of bond length, energy gap, adsorption energy, and Mulliken charge transfer to evaluate the adsorption of ZnO or Ni-doped ZnO towards methylene blue dye.

In the next section, the materials and methodologies used in this research are investigated in detail.

3. MATERIALS AND METHODS

3.1. Materials

Lead (II) acetate trihydrate ($Pb(CH_3COO)_2.3H_2O$) used as a precursor of Pb^{2+} for the synthesis of high purity α-PbO and β-PbO as well as for PbO thin film deposition was purchased from Loba Chemie. Stannous chloride dehydrates ($SnCl_2.2H_2O$), cobalt (II) nitrate hexahydrate ($Co(NO_3)_2.6H_2O$), cupric acetate monohydrate ($Cu(CH_3COO).H_2O$), and nickel acetate tetrahydrate ($Ni(CH_3COO)_2.4H_2O$) were purchased from Loba Chemie and lithium nitrate ($LiNO_3$) was from Alpha Chemika which were used as Sn, Co, Cu, Ni, and Li dopants precursors respectively. Hydrochloric acid (HCl) and Sodium hydroxide (NaOH) purchased from Loba Chemie were used as reducing agents and pH adjusters. Methylene blue dye ($C_{16}H_{18}ClN_3S$) purchased from Loba Chemie, was used as an organic pollutant model. Ascorbic acid obtained from Loba Chemie, isopropyl alcohol bought from CARELABMED India, and disodium ethylenediaminetetraacetic acids bought from Loba Chemie were used as scavengers for active species trapping experiments. Distilled water was used as solvent throughout all experiments. Ammonia solution purchased from Loba Chemie was used as a complexing agent and OH^- sources for thin film deposition. The chemicals we used in this research were utilized as bought without further purification. Microscope slide glass with 75 mm long × 25 mm wide size and 1.35 mm thickness purchased from Power Industrial Company (India) was used as substrate and ethanol was purchased from Fine Chemical, and acetone was obtained from Loba Chemie were used to clean the glass substrate.

3.2. Synthesis of nanoparticles

The chemical precipitation method was used for the preparing of high-purity pristine α-PbO and β-PbO, and metals doped α-PbO and β-PbO nanoparticles. For the preparation of pristine α-PbO and β-PbO, 0.5 M of $Pb(CH_3COO)_2.3H_2O$ was dissolved in 50 mL of distilled water. This solution was stirred continuously until clear solution is formed. Next, the pH controller and reducing agent was prepared by adding a 9.5 M of NaOH into 50 mL of distilled water in a separated beaker. Then, 20 mL of sodium hydroxide solution was added dropwisely to the lead (II) acetate trihydrate solution. The reaction temperature was fixed to 85 ^oC under continuously stirring. As the sodium hydroxide solution was added to the initially clear solution of $Pb(CH_3COO)_2.3H_2O$, the solution was changed to milky like color. As more sodium hydroxide

is added dropwisely, the solution becomes cloudy. Then upon a continuous stirring for two hours, the solution is changed to orange and ultimately changed to deep red color. The red precipitate was filtered using Whatman paper. The filtered precipitate was washed with distilled water and ethanol three times respectively to remove any organic compounds. The washed precipitate was dried in hot air oven at 100 ^{o}C for an hour. Finally, the oven dried sample was calcined at 250 ^{o}C in furnace for two hours to obtain high purity α-PbO nanoparticles, whereas the high purity β-PbO nanoparticles obtained by calcining at 700 ^{o}C for two hours. The entire synthesis process of α-PbO and β-PbO nanoparticles is shown in Figure 13.

Similar procedures were followed for the preparation of different metal doped α-PbO nanoparticles, but only the precursors of the dopants were added to the solution of lead (II) acetate trihydrate. For the dopants of Sn^{2+}, Co^{2+}, Cu^{2+}, Ni^{2+} and Li^{+}, the $SnCl_2.2H_2O$, $Co(NO_3)_2.6H_2O$, $Cu(CH_3COO).H_2O$, $Ni(CH_3COO)_2.4H_2O$, and $LiNO_3$ were used as dopant precursors, respectively. For the preparation of different metal doped α-PbO, each dopant precursors of 0.1 M were added into the lead (II) trihydrate solution. Lastly, the powders of each sample were collected and taken for further characterizations.

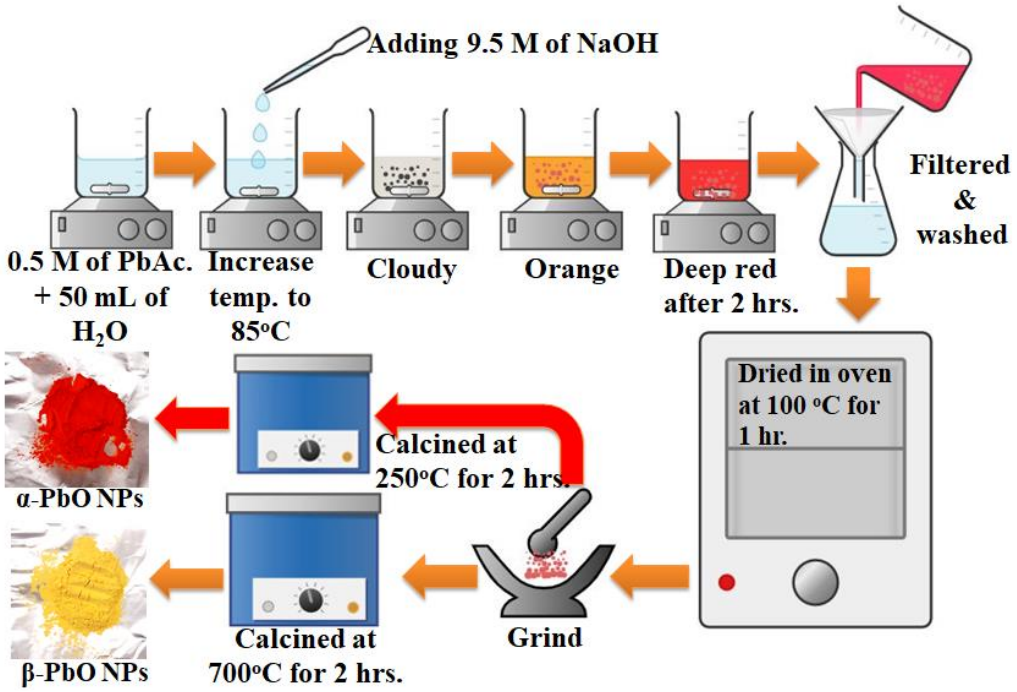

Figure 13: Synthesis process of α-PbO and β-PbO nanoparticles.

3.3. Photocatalytic Experiment

The photocatalytic experiments of pristine α-PbO and β-PbO, and different metals doped α-PbO and β-PbO nanoparticles were conducted using hydrogen lamps as sources of visible light for the degradation of methylene blue (MB) dye. A cylindrical Pyrex jacket was covering the lamp. The 1L Pyrex was used in the photoreactor as a container of suspension of methylene blue dye with a catalyst. For the preparation of an aqueous suspension, 0.065 g of catalysts for all doped and pristine α-PbO nanoparticles were added into 100 mL of methylene blue dye solution with an initial concentration of 10 ppm. A 0.5 M of NaOH dissolved in 100 mL of distilled water and the ratio of 10:100 HCl to distilled water were used as pH adjusting and the pH was adjusted to approximately 10. To establish adsorption–desorption equilibrium, the dark experiment was performed by stirring the aqueous suspension for 30 minutes. Then, the aqueous suspension was placed in the reactor and stirred simultaneously under visible light irradiation. Upon turning on the irradiation, the 8 mL of samples were withdrawn at 20 min time intervals. Then, the withdrawn samples of 8 mL were centrifuged for 30 min at rpm of 4000 to remove the nanoparticles. The centrifuged samples were then analyzed by using a Shimadzu UV–vis spectrophotometer at wavelength of 664 nm and the absorption spectra of the supernatant were collected.

The trapping experiment was carried out by using scavengers of holes, hydroxyl radicals, and superoxide radicals. Different scavengers such as ethylenediaminetetraacetate (EDTA), isopropyl alcohol (IPA), and ascorbic acid (AA) were added to detect reactive species like holes (h^+), hydroxyl radical (•OH), and superoxide anion radicals (O_2•−), respectively that involved in the degradation of MB dye. All the experimental conditions such as catalyst dosage, pH value, time of irradiations, and initial concentration of MB dye were similar for the photocatalyst tests of all the samples, except that, 3 mM of scavengers were added for the trapping experiments.

3.4. PbO thin film

3.4.1. Preparation of precursor solutions

The precursor solutions were prepared by dissolving 0.1 M, 0.15 M, 0.2 M, and 0.25 M of $(PbCOOH)_2.3H_2O$ in 100 mL distilled water, respectively. Then, the solutions were shaken until the reaction was completed and transparent precursor solutions were obtained.

3.4.2. Cleaning the substrate

The Microscope slide glass substrate was kept in HCl for 24 hours. Then it was washed with acetone and ethanol three times respectively. Next, it was cleaned with detergent and deionized water four times and rinsed in deionized water. Finally, it was dried in the air.

3.4.3. PbO thin film deposition

PbO thin films were deposited by the chemical bath deposition (CBD) method. First, 10 mL of the prepared precursor solutions were added to a 100 mL beaker by stirring for each concentration of lead acetate precursor's solution. Next, 20 mL of distilled water was added at room temperature under continuous stirring until the solution becomes colorless. Then, 25 mL of ammonia solution was added dropwisely to the above solution under continuous stirring until the solutions were changed to white color. The use of ammonia solution is to prevent spontaneous precipitations. Finally, 15 mL of distilled water was added to obtain 70 mL of the precursor solutions. Then, the cleaned substrate was suspended vertically in the bath of precursor solutions with the aid of synthetic foam. The precursor solutions were kept in the bath for 135 minutes at 75 ^{o}C while stirring. After 135 minutes heating, the substrate was removed from the bath and dried in the air. The thin film was deposited on the substrate as $Pb(OH)_2$. The as deposited $Pb(OH)_2$ thin film was annealed at 200 ^{o}C, 300 ^{o}C and 400 ^{o}C in a furnace for 1hr for each concentration to obtain PbO thin film. However, the PbO thin film that annealed at 400 ^{o}C observed to be well deposited and hence was selected for further characterization. The as-deposited thin films were almost white in color and their colors changed to yellow after annealing.

3.5. Characterizations

The structural analyses of the obtained samples were carried out by X-ray diffractometer (Shimadzu-7000) with the radiation CuKα wavelength 1.5406 Å. The UV-Vis DRS spectroscopy with UV-3600 Plus Series Model was used to study the spectral properties in the wavelength range 320 nm to 800 nm. The photoluminescence spectrometer (PL) with model HORIBA FluoroMax-4 Spectrofluorometer with excitation wavelength 352 nm was used to measure emission spectra. The scanning electron microscopy (SEM) model Jeol JSM-75000F Field Emission Scanning electron Microscope was used to analyze the surface morphology. The software Jeol PC-SEM was used for imaging. Thermo NSS software for the energy dispersive X-

ray analysis (EDX) was used to measure the elemental composition spectrum. The UV–visible spectrophotometer was also used to measure the absorbance of MB dye at different times of light irradiation.

3.6. Computational details

In this research, the theoretical calculations were carried out by Density functional theory (DFT) tools under the implemented Quantum Espresso package code (P. Giannozzi et al., 2017; Paolo Giannozzi et al., 2009). The generalized gradient approximation (GGA) with the Perdew-Burke-Ernzerhof (PBE) exchange functional was also employed. The calculation was also performed with Perdew-Zunger (PZ) functional within local density approximation (LDA) in order to compare the resulted electronic properties with GGA. The plane wave ultrasoft and norm-conserving pseudopotential were employed also. The pseudopotential have $5d^{10}$ $6s^2$ $6p^2$ and $2s^2$ $2p^4$ electron valence for Pb and O, respectively. The pseudopotentials of the dopants electrons valence are, Co, Ni, Cu, Li, and Co are $3d^8$ $4s^1$, $3d^9$ $4s^1$, $3d^{10}$ $4s^1$, $1s^2$ $2s^1$ and $4d^{10}$ $5s^2$ $5p^2$, respectively. A single atom of each dopant replaces the place of Pb atom.

The calculations for the undoped α-PbO was performed with different exchange correlation functional such as Perdew-Zunger (PZ) within local density approximation (LDA) and within the generalized gradient approximation (GGA), Perdew-Burke-Ernzerhof (PBE) and PBEsol have been used. The projector augmented wave (PAW) pseudopotential with Perdew-Burke-Ernzerhof (PBE) and PBEsol exchange-correlation functional was used in the GGA. An ultrasoft pseudopotential (USPP) type was used for PZ and PBE exchange functionals. Convergence for kinetic energy cut off and k-points have been done. For kinetic energy cut-off, 48 Ry that has been obtained from the convergence calculation and charge density cutoff 392 Ry were used throughout the study. For the representation of Brillioun zone integration the Monkhorst-pack-k-points scheme with 6×6×4 k-points that are obtained from the convergence calculations has been used. For partial density of states (PDOS) investigation, 22×22×12 k-point was used. For band structure calculations, the high symmetry k-points were used for the convenient purpose. For geometry optimizations and to find the ground state energy, the Broyden-Fletcher-Goldfarb-Shanno (BFGS) minimization method was used. For bulk structural relaxation, 48 Ry plane wave cutoffs and 6×6×4 k-point grid was used. The energy convergence criterion 1.0×10^{-8} eV for self-consistent relaxation was also used. The transition metals doped spin polarized calculation was performed to include the influence of spin polarization of these dopants.

For the computational description of β-PbO, similar method as of α-PbO was used, except that, the variations of values of some parameters used for calculations. Since the GGA with ultrasoft pseudopotential showed good approximation of electronic band structure calculation, PBE exchange potential through the calculations was selected for different metals doped β-PbO. Convergences for kinetic energy cut-off and k-points have been done. For kinetic energy cut-off, 625.86 eV (46 Ry), that has been obtained from the convergence calculation and charge density cutoff 413 Ry was used throughout the study. For the representation of Brillioun zone integration, the Monkhorst-pack-k-points scheme with 6×6×6 k-points obtained from the convergence calculations has been used. For PDOS investigation 22×22×22 k-point was used. For band structure calculations similar procedures to α-PbO the high symmetry k-points were followed for the convenient purpose. The crystal geometry was fully optimized by using variable cell relaxation calculation. The BFGS minimization method was also used to find the ground state energy. For bulk structural relaxation, 46 Ry plane wave cutoffs and 6×6×6 k-point grid was used. Similar procedure for α-PbO was followed to describe the energy convergence criterion 1.0×10^{-8} eV for self-consistent relaxation. In all calculations the spin polarized calculations was performed for different metals doped β-PbO.

For crystal structure visualization, modeling and designing, XCrySDen (Kokalj, 1999) and VESTA (Momma & Izumi, 2011) software were used. Norm-conserving pseudopotentials were employed in the calculations of optical properties. Furthermore, for optical property analysis, the momentum matrix element and Kramers-Kronig-relation to get imaginary and real parts of dielectric functions, respectively have been used (W. Jia et al., 2019). The frequency dependence in one-, two-, and three directions of the dielectric function in this study are explained as a function of energy.

4. RESULTS AND DISCUSSIONS

4.1. Experimental Results of metals doped α-PbO nanoparticles

4.1.1. XRD analysis

The tetragonal crystal structure of bulk α-PbO is shown in Figure 14. The bond between Pb^{2+} and O^{2-} forms squared pyramidal. The XRD patterns of pristine and different metal doped α-PbO are presented in Figure 15a. The XRD patterns of the synthesized materials show the polycrystallinity nature. The diffraction peaks are indexed as (001), (101), (110), (002), (200), (112), (211), (103), and (220) matching with JCPDS card number PDF#85-1287 (Bangi et al., 2017). No unknown peaks emerged for the pristine α-PbO that confirms the synthesized material is a high purity α-PbO phase. However, in Cu and Co doped α-PbO the peaks of β-PbO are revealed as shown in Figure 15a, that shows the phase transition properties. The emerged peaks of β-PbO may be attributed to the catalyst properties of transition metals dopant to form β-PbO phase. Except for the Co-doped, all peaks are strong and sharp, which shows the crystalline nature of pristine and metal-doped α-PbO nanoparticles. For pristine α-PbO, the highest intensities of characterized peaks are (101), (110), (112), (211), and (002), whereas the rest indexed to the tetragonal structure of α-PbO are the lower intensities. The (101) indexed plane is the predominance peak, which shows the orientation of the phase along the (101) direction. The predominance plane for Li, Sn, Ni, and Co-doped is the same as the pristine α-PbO except for the shifts of the peaks in some cases as shown in the extended XRD pattern presented in Figure 15b. For the Cu-doped α-PbO, the intensity of the (101) peak decreases, whereas the (002) peak intensity dominates.

Compared to the pristine α-PbO, the intensity of the (101) peak of the doped materials increases. The intensity of the (110) plane peaks for the Sn, Cu, Ni, and Co-doped α-PbO decrease when compared to that of pristine α-PbO, whereas, the intensity of the (110) plane peak for Li-doped α-PbO is approximately equal to the intensity of that of pristine α-PbO. The peaks (101), (110), (002), and (112) of different metals doped α-PbO show a phase shift when compared to that of pristine α-PbO. For Cu, Ni, and Li-doped α-PbO, the peaks shift towards the higher angle, whereas for Sn and Co-doped α-PbO, they shift towards the lower angle position. These shifts of the peaks are related to the extension and compression of lattice parameters. The higher or lower angle shifts of diffractions may also be attributed to the non-similar ionic radii between the

pristine and dopant ions. This can cause an increase or decrease in the crystallite size of the samples. The higher angle shift shows the lattice strain, while the lower angle shift shows the lattice relaxation. The shift in the 2θ position confirms the incorporation of metal dopants into the α-PbO nanoparticles. For Cu and Co-doped α-PbO, the additionally emerged peaks are revealed at 30.34^{o} and 30.28^{o}, respectively. The emergence of additional peaks may be due to the appearance of phase transition or may be due to lead compounds formed by the dopants. For Co-doped α-PbO, the patterns for the (101) plane is broadening, and this results in the degradation of the crystalline quality of Co-doped α-PbO.

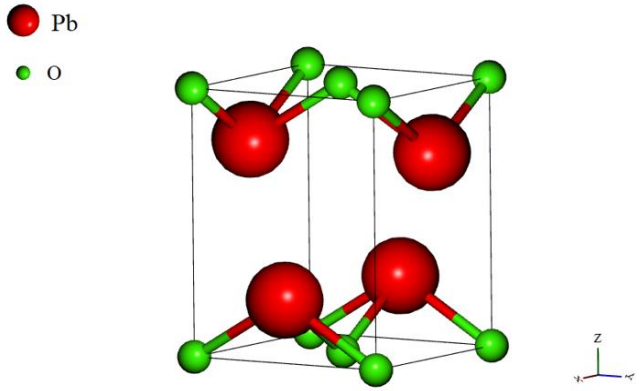

Figure 14: Crystal structure of bulk tetragonal α-PbO.

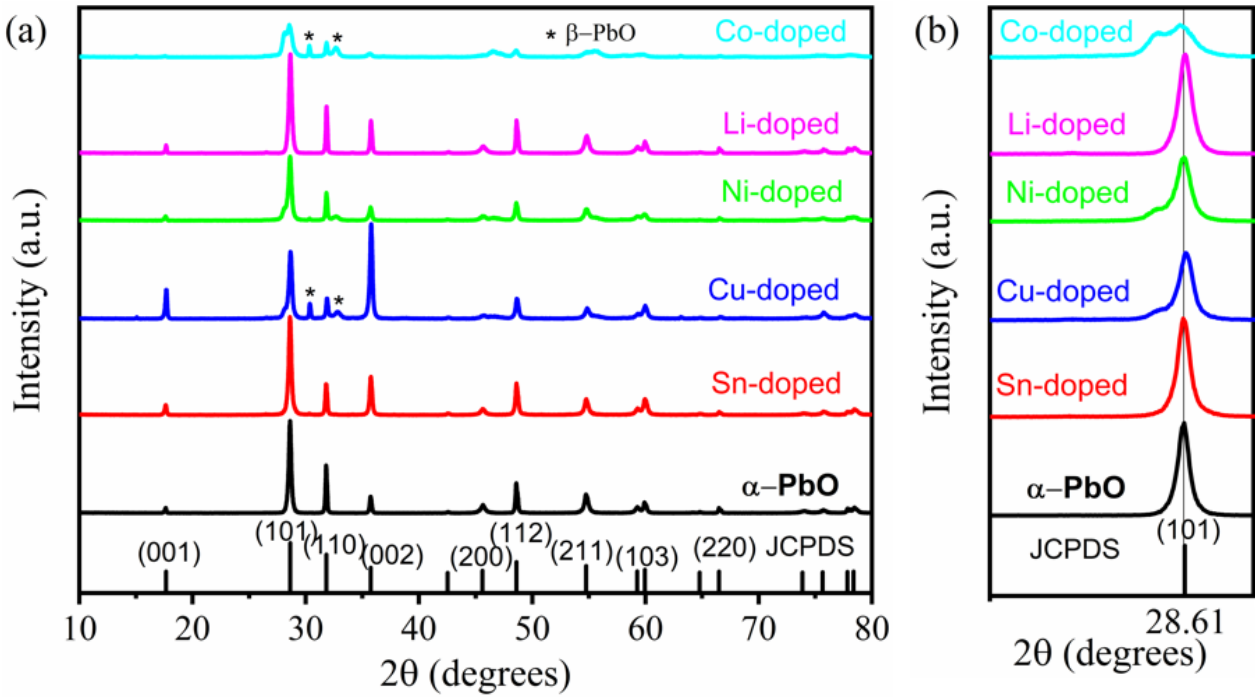

Figure 15: (a) XRD patterns of pristine and different metal doped α-PbO nanoparticles and (b) enlarged XRD patterns of the diffraction line of (101) crystal plane.

From XRD data we can easily calculate the d-spacing and lattice parameters. The lattice parameters and d-spacing of PbO nanoparticles can be estimated by using the Bragg's expression:

$$\lambda = 2d_{hkl}\, sin\, \theta_{hkl} \tag{62}$$

where, λ is wavelength of Cu Kα line which is 1.5406 Å, d is interplanar spacing, hkl are Miller indices and θ is the Bragg's diffraction angle. From this expression the d-spacing can be given as

$$d_{hkl} = \frac{\lambda}{2\, sin\, \theta_{hkl}} \tag{63}$$

The lattice parameters and d-spacing can be related as

$$d_{hkl} = \sqrt{\frac{a^2}{h^2} + \frac{b^2}{k^2} + \frac{c^2}{l^2}} \tag{64}$$

where *a*, *b*, and *c* are the lattice parameters. Since our crystal structure is tetragonal we can find lattice parameters from the d-spacing relations $a = b \neq c$:

$$\frac{1}{d_{hkl}^2} = \frac{h^2 + k^2}{a^2} + \frac{l^2}{c^2} \tag{65}$$

For (hkl) = (110) peaks position, the lattice parameters $a = b$ is calculated using Equation (66), where h = 1, k = 1, and l = 0.

$$a = \sqrt{2} d_{hkl} \tag{66}$$

For (hkl) = (101) peaks position, lattice parameter c is calculated using Equation (67),

$$c = \frac{a d_{hkl}}{\sqrt{a^2 - d_{hkl}^2}} \tag{67}$$

The calculated d-spacing and lattice parameters is given in Table 1. For pristine α-PbO the obtained lattice parameter $a = b$ is 3.9727 Å and lattice parameter c is 5.0217 Å. Lattice parameters $a = b$ is 3.9729 Å for Sn doped α-PbO which is slightly extended. However, it shrinks for the rest dopants. The extension and shrinks of lattice parameters are responsible for shift of diffraction peaks with respect to each dopant. The crystallite size of pristine and metal doped α-PbO can be calculated by using Scherrer's equation given by (Jahnavi et al., 2019):

$$D_{hkl} = \frac{K\lambda}{\beta_{hkl}\, cos\, \theta_{hkl}} \tag{68}$$

where, D_{hkl} is crystallite size, K is the shape factor which can be 0.62–2.08 and is usually taken as about 0.89, and β_{hkl} is the full width at half maximum (FWHM) in radians. The calculated

crystallite size for the (101) and (110) peaks is presented in Table 1. Thus, the crystallite for the predominant peak for the pristine α-PbO is 32.86 nm and 48.01 nm for (101) and (110) peaks, respectively. For the pristine α-PbO, these two planes have the highest intensity and dominate over the other peaks. Therefore, we can take its average size of 40.44 nm of crystallite size. In the case of doped, the average crystallite sizes are decreased compared to the pristine α-PbO, as given in Table 1. This may reveal the incorporations of the dopant metals into the α-PbO. The reduced crystallite size results in the deterioration of the quality of the crystal and increases in the grain boundary. For the Co-doped, it can be observed that there is a huge decrease in crystallite size and the lattice disorder induced in α-PbO. Thus, the size mismatch in the host materials and the dopants distorts the crystallinity of the materials. This is due to the induced strain and distortion of lattices created by the size mismatch of Pb and dopants ions.

Table 1: The calculated d-spacing, lattice parameters, crystallite size, strain and dislocation density.

Dopants	hkl	d-spacing (Å)		Lattice constants (Å)				Average D (nm)	ε [line^{-2}(nm)$^{-4}$) (× 10^{-4}]	δ [lines/(nm)^2) (× 10^{-4}]
		standard	calculated	standard		calculated				
				a	*c*	*a*	*c*			
α-PbO	110	2.8091	2.8091	3.9727		3.9727		40.44	8.66	6.80
	101	3.1156	3.1156		5.0217		5.0217			
Sn:α-PbO	110	2.8093	2.8093	3.9727		3.9729		34.58	9.94	8.82
	101	3.1151	3.1151		5.0217		5.0190			
Co:α-PbO	110	2.8049	2.8049	3.9727		3.9667		11.23	32.02	94.94
	101	3.1363	3.1363		5.0217		5.1224			
Cu:α-PbO	110	2.8029	2.8029	3.9727		3.9639		32.38	10.71	10.33
	101	3.1108	3.1108		5.0217		5.0193			
Ni:α-PbO	110	2.8071	2.8071	3.9727		3.9699		31.69	11.09	11.18
	101	3.1157	3.1157		5.0217		5.0278			
Li: α-PbO	110	2.8067	2.8067	3.9727		3.9693		33.77	10.38	9.78
	101	3.1123	3.1123		5.0217		5.0146			

The strain is calculated by using Stokes-Wilson equations:

$$\varepsilon_{hkl} = \frac{\beta_{hkl} \cos \theta_{hkl}}{4} \tag{69}$$

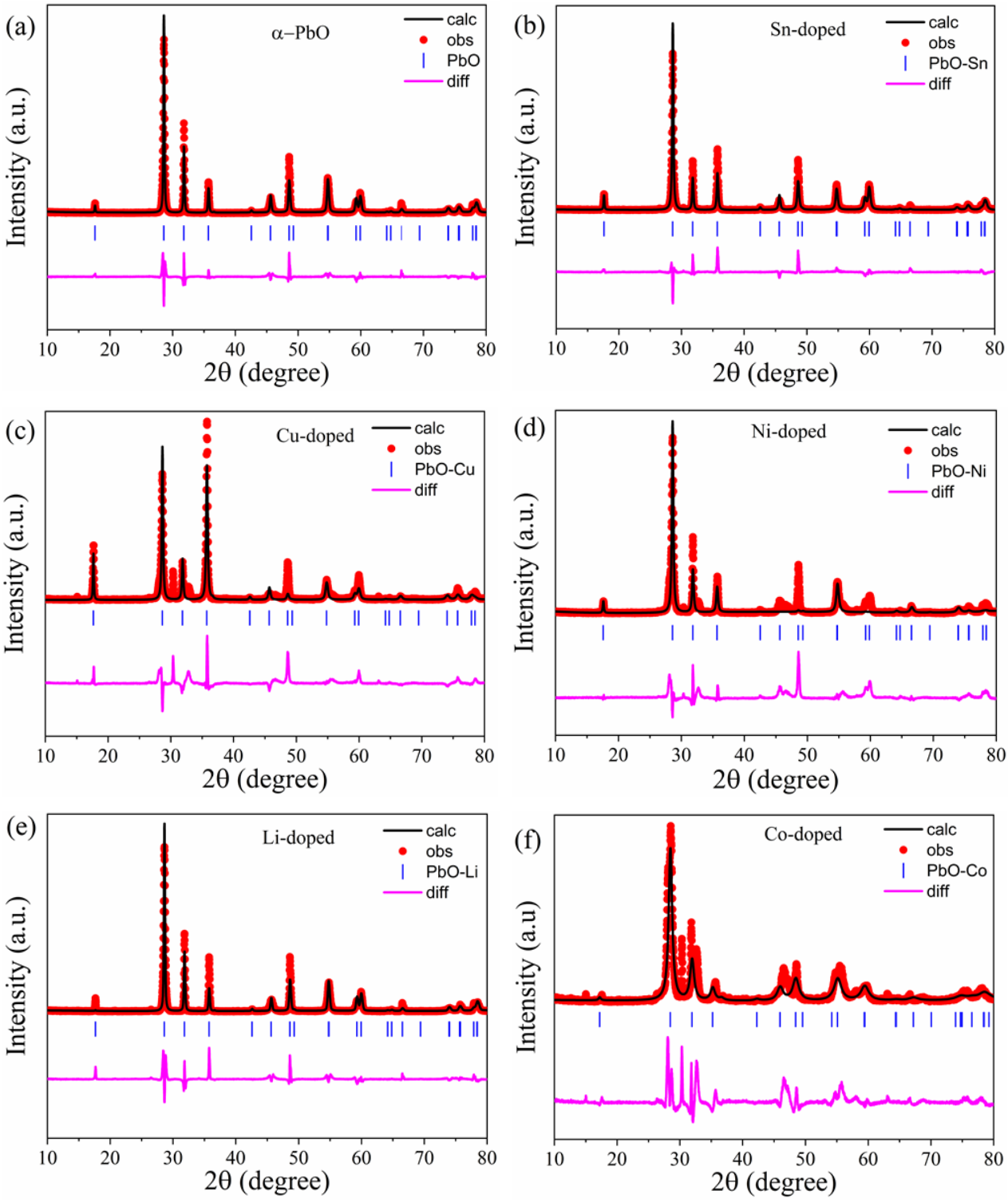

Figure 16: Rietveld refinement pattern of powder XRD data for (a) pristine α-PbO, (b) Sn-doped α-PbO, (c) Cu-doped α-PbO, (d) Ni-doped α-PbO, (e) Li-doped α-PbO, and (f) Co-doped α-PbO with the experimental data (red dots), calculated pattern (black line), difference curve (pink line), and Bragg diffraction positions (blue ticks for *P4/nmm* space group).

The calculated values of induced strain for pristine and doped α-PbO are presented in Table 1. It is clear that the calculated values of the induced strain increase for metals doped compared to the pristine α-PbO. As explained earlier, the increases in the induced strain confirm the crystalline quality deteriorations of the doped α-PbO. Specifically, for the Co-doped α-PbO, an induced strain increases more when compared with other doped materials; inversely, the crystallite size of Co-doped α-PbO decreases more, which shows a gigantic deterioration of crystalline quality. The substantial difference in the radii of Co^{2+} with the host Pb^{2+} and O^{2-} which is 0.135 nm, 0.119 nm, and 0.065 nm respectively is the main reason for the substantial induced strain in Co-doped α-PbO (Bhapkar et al., 2023). Thus, the Co-doped is added as an impurity into the materials in interstitial form rather than occupying the site of the host atom. As a result, the increase in induced strain in Co-doped α-PbO caused the XRD peak broadening as one can observe from Figure 15a. Thus, the crystal structure of the prepared material is distorted, and the crystal imperfection in Co-doped α-PbO caused the distribution of lattice strain.

The amounts of defects can strongly explain the optical and morphological properties. The amounts of defects can be known by calculating the dislocation density (δ) given by

$$\delta = D^{-2} \tag{70}$$

It can be observed from Table 1 that the calculated dislocation density is increasing for the doped α-PbO compared to the pristine α-PbO. Thus, the increase of dislocation density for the doped α-PbO shows the disorder and the crystalline quality degradation of α-PbO. The size mismatch of the dopant and Pb induces lattice distortion. The calculated dislocation density for Li and Sn doped is small but slightly larger than pristine α-PbO. For Co-doped α-PbO, the maximum dislocation density has been obtained, which results in the degradation of crystalline quality compared to other dopants.

Furthermore, Figure 16 shows the Rietveld refinement of XRD data of pristine and different metal-doped α-PbO by using GSAS-II software. The dot and the black-solid lines are the experimentally observed data and the calculated Rietveld refinement fit, respectively. The pink-solid line shows the difference between the observed and calculated at each step. The results obtained from the Rietveld refinements are given in Appendix Tables A20 and A21. In the Appendix of Tables A20 and A21, the obtained lattice parameters, hkl, 2-theta position, d-space,

and FWHM are mentioned. These informations confirmed that the prepared material is highly pure α-PbO without the mixture of any other phases for pristine α-PbO.

4.1.2. UV-Vis DRS

The UV-Vis diffuse reflectance spectra (UV-Vis DRS) of pristine and different metal doped α-PbO are presented in Figure 17a. The undoped α-PbO has low reflectance in ultraviolet and near-above-ultraviolet regions. Starting from 425 nm it starts to increase until 575 nm slightly. Moreover, it linearly increased from 575 nm to 625 nm, and in the visible region starting from 625 nm, it slowly increased. The Li-doped α-PbO has the same property as the pristine α-PbO except for its reflectance is greater in the ultraviolet until 625 nm. The Cu, Li, and Sn doped reflectance properties are low in ultraviolet and near above ultraviolet but their reflectance increases for the rest region of the visible regions. For the Sn-doped, it is linearly increasing after the ultraviolet region until 625 nm. For the Ni and Co-doped, the reflectance is low in ultraviolet and slowly decreases in the visible region. The low reflectance region is due to charge transfers from the valence band to the conduction band. In general, when we compared the reflectance of all samples, Co-doped own lower reflectance while Cu-doped, Ni-doped, Sn-doped, pristine α-PbO, and Li-doped α-PbO in increasing order. The optical band gap is approximated by using the Kubelka-Munk relation (Makuła et al., 2018; Palanivel et al., 2019):

$$F(R) = \frac{k}{s} = \frac{(1-R)^2}{2R} \tag{71}$$

where, $F(R)$ is Kubelka-Munk function, k is absorption coefficient, s is scattering coefficient, and R is the reflectance. The optical bandgap of pristine and doped α-PbO with different metals is presented in Figure 17b. Thus, the obtained optical band gap of pristine, Sn, Co, Cu, Ni, and Li doped α-PbO is 2.03 eV, 2.68 eV, 1.61 eV, 1.78 eV, 1.67 eV, and 2.00 eV respectively. Thus, the bandgap of pristine α-PbO and different metal doped are found in the visible light region which makes them more efficient and visible light responses for photocatalytic applications. Sn-doped has a higher bandgap than pristine α-PbO which might be because of the doping the wide bandgap SnO_2 can be formed and make a composite with α-PbO formed. However, in other dopants, the value of the bandgap is lower than the pristine α-PbO. Thus, it enhances the electrical and optical properties of the system.

Furthermore, the band gap variation may be due to the different ionic radii of dopants. The ionic radius of Co^{2+}, Ni^{2+}, Cu^{2+}, Li^{+}, and Sn^{2+} is 0.065 nm, 0.069 nm, 0.073 nm, 0.076 nm, and 0.118 nm, respectively. Among these dopants, Co^{2+} has the least ionic radius and Co-doped α-PbO has the least bandgap whereas, Sn^{2+} has the largest ionic radius as well as Sn-doped α-PbO has the largest bandgap. Various research results revealed the widening and narrowing of other oxide semiconductors due to doping. Saha et al. (Saha et al., 2015) reported the increase of bandgap with the increase of dopant concentration in Ga-doped ZnO. According to this report, particle size was not contributed in enhancing of the bandgap. However, the blue shift of the bandgap was attributed to the concentrations of Ga which formed free charge carriers in the host ZnO. Thus, the excess charge carriers occupied the lowest states in the conduction band and enhanced the effective bandgap. This phenomenon is known as the Burstein–Moss (BM) effect (Gahlawat et al., 2019). Due to the BM effect the raising of the Fermi level in the conduction band is responsible for the widening of the bandgap. The same condition has also been reported by De et al. (De et al., 2020) in Zn doping into Ag_2O. Karuppasamy et al. (Karuppasamy et al., 2021) also obtained the increased bandgap of TiO_2 when doping different transition metals for photocatalysis applications. In Zn-doped TiO_2 they obtained the decreased bandgap, whereas in Cu and Zr doping they obtained the increased bandgap.

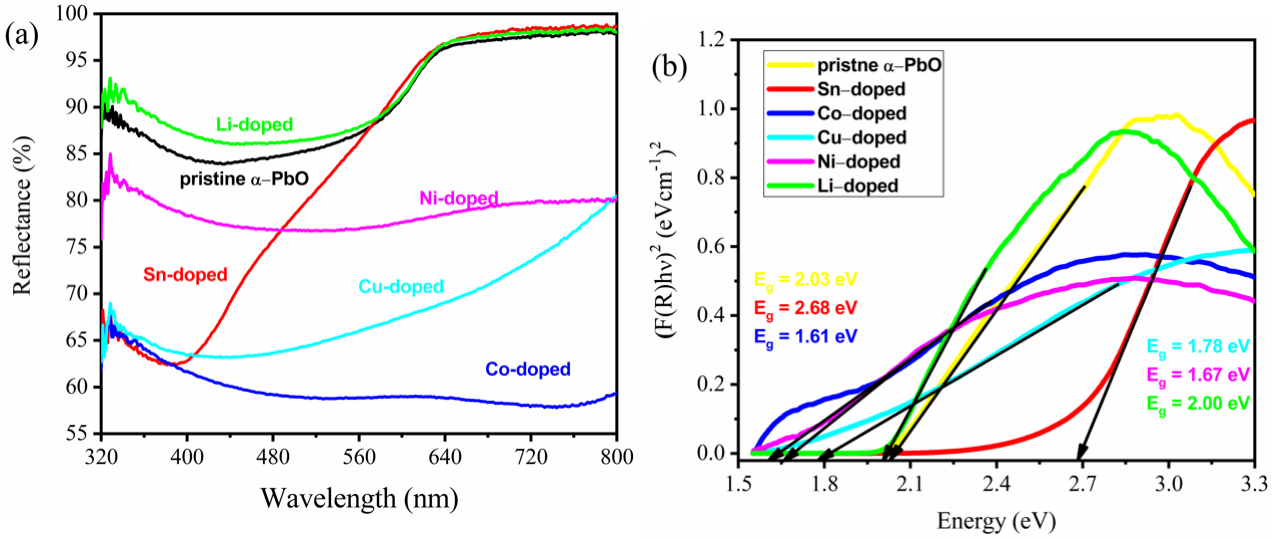

Figure 17: (a) UV-Vis diffusion reflectance spectra of pristine and different metal doped α-PbO and (b) optical energy band gap of pristine and different metal doped α-PbO nanoparticles.

4.1.3. PL emissions analysis

Photoluminescence (PL) spectroscopy is used to characterize the optical properties of metal oxide semiconductors. The powder of the synthesized nanoparticles is taken for PL characterizations. The PL emission spectra of pristine and different metal doped α-PbO nanoparticles under an excitation wavelength of 352 nm are presented in Figure 18. The pristine α-PbO shows strong green emission of 523 nm. The strong green emission spectra of Sn and Cu-doped slightly shifted to 524 nm, whereas for all the rest dopants 523 nm without showing shifts. The visible region green band emission can be attributed to various structural defects like O vacancies and interstitial defects. The interstitial atomic defect and oxygen vacancies create trap states which causes various emission peaks in the visible region. Here, the α-PbO NPs are synthesized by using water as a solvent which might result in a high density of oxygen vacancies. The oxygen vacancy can be found in three ways. Thus, it can be a double vacancy, singly ionized vacancy, and neutral. For the undoped α-PbO nanoparticles, the green emission band is related to the electronic transition from the conduction band to the singly ionized O vacancies (Mythili & Arulmozhi, 2014). The intense green band emission of pristine α-PbO at 523 nm may also be attributed to the Pb^{2+} vacancy (Gandhi & Wu, 2017). The weak bands observed for Sn-doped are 506 nm, 536 nm, 547 nm, and 623 nm broadband. The smaller the FHWM better the optical quality, which indicates the higher crystalline quality of the synthesized materials.

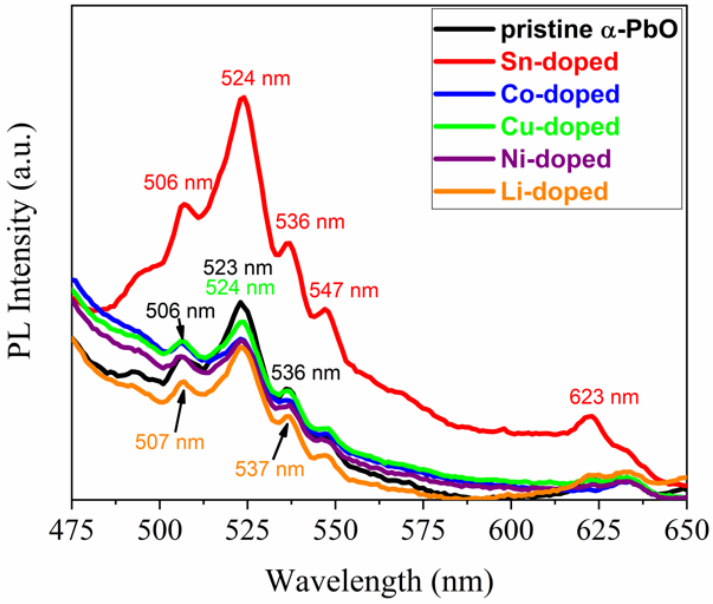

Figure 18: PL emission of pristine and different metal doped α-PbO nanoparticle.

The weak orange band observed at 623 nm can be attributed to an interstitial atomic defect. The weak band emission found at 506 nm and 507 nm are blue emissions that are attributed to oxygen vacancy and also attributed to recombination electrons in the conduction band and the doubly ionized oxygen vacancy. For pristine α-PbO and other doped α-PbO, the weak bands are 505 nm, 537 nm, and 547 nm, which are slightly shifted with very small numbers. Thus, it shows blue shifts. The observed small shift is due to the presence of defects from the dopants' impurity ion. Green emissions bands observed in 523 nm to 547 nm regions are attributed to Pb^{2+} interstitial, oxygen vacancies, and dopant impurity ions which attribute to the creation of defect energy levels. The formation of dopants impurity levels contributes to the retardation of fast recombination of photogenerated electrons and holes in the photocatalytic applications of the prepared samples. On the other hand, the higher intensity peaks of Sn-doped compared to the pristine α-PbO and other doped materials show the low interactions of the Sn-O bond. The increase in peak intensity due to doping is attributed to the increment in free charge carrier concentrations. The Li-doped possesses lower intensity compared to other doped materials, which may be attributed to the strong interaction of the Li-O bond (Rahmati et al., 2014). The PL emission intensity decrease might also be attributed to the transfer of electrons from the valence band to the donor level introduced by dopants. The lower the PL intensity, the less the recombination rate of charge carriers which has advantages in photocatalytic and solar cell applications (Shanmugam et al., 2016). The electron from the dopants shallow donor level enhances the PL emission intensity in the visible region by transiting to the oxygen vacancies deep acceptor (Rahmati et al., 2014). The defect formation decreases the rate of recombination of carriers. Thus, the O vacancy traps the excited electron, and dopants ions trap the hole (Shanmugam et al., 2016). There is no excitonic recombination due to the nonexistence of near-band edge transition, which causes ultraviolet emission. Nevertheless, Arulmozhi and Mythili have reported the ultraviolet emission of lead oxide nanoparticles by using oleic acid as a capping agent (Arulmozhi & Mythili, 2013).

4.1.4. SEM analysis

Surface morphology, particle size, and size distribution of the synthesized particles are characterized by SEM. The SEM micrograph image of pristine α-PbO and different metal doped α-PbO is presented in Figure 19. Particles are not uniformly distributed in all synthesized nanoparticles and for particle size distribution estimation ImageJ software was used. As shown in

Figure 19a, the pristine α-PbO has a flake-like and irregular shape joining each other to form large particles. From the Gaussian distribution, the average size of particles was calculated. The flake-like and irregularly shaped average particle size of pristine α-PbO obtained was 1.32 μm. Sn-doped α-PbO size distribution and surface morphologies are almost the same as the pristine α-PbO as presented in Figure 19b. However, the average particle size is decreased to 0.67 μm. The surface morphology and particle size distribution of Co-doped α-PbO is depicted in Figure 19c. In this sample the particle size is 0.16 μm with flake-like morphologies. The Cu-doped sample has flaked-like and irregular shape morphology with an average particle size of 0.11 μm. As depicted in Figure 19d the particle distribution of Cu-doped α-PbO was not uniform. The SEM micrograph of Ni-doped α-PbO shows the near-spheroid and flake-like shape morphology with highly agglomerated small particles as presented Figure 19e. The average particle size of the Ni-doped sample was 0.05 μm which is smaller than all the synthesized particles. The Li-doped sample has the distribution of tetragonal, rhombic dodecahedral, triangle, and flake-like shape morphology with an average particle size of 0.65 μm, as shown in Figure 19f.

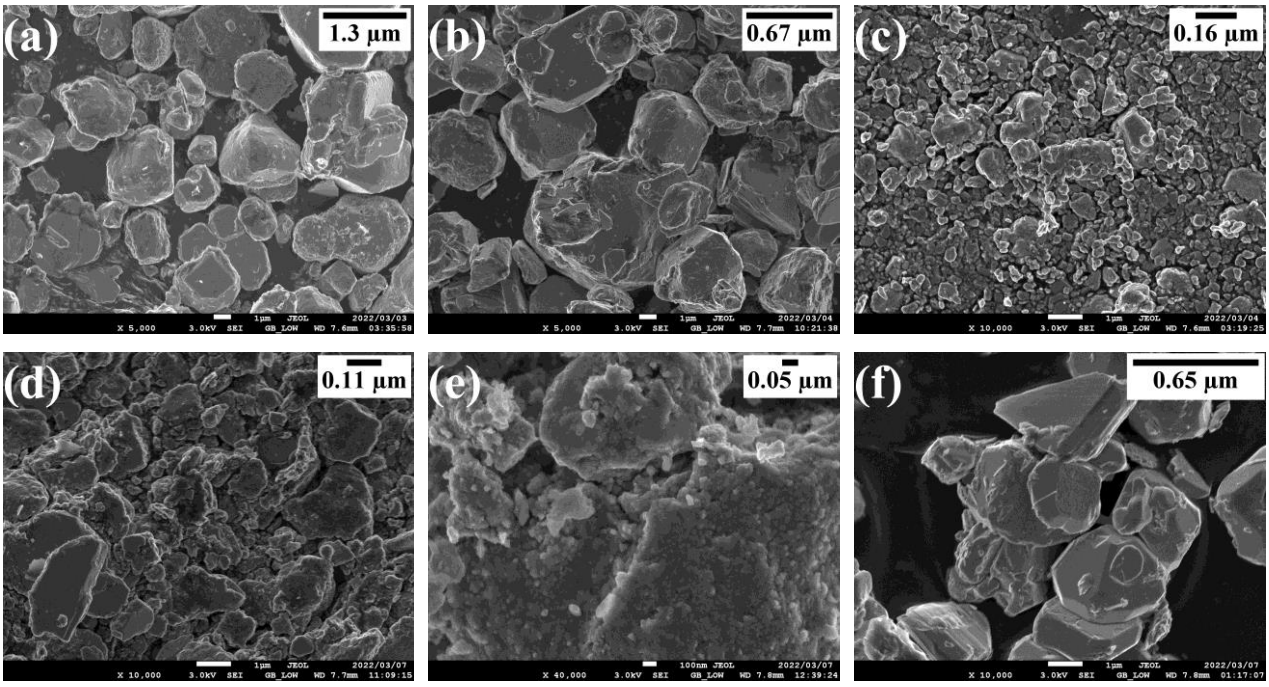

Figure 19: SEM micrograph image of (a) pristine, (b) Sn-doped, (c) Co-doped, (d) Cu-doped, (e) Ni-doped and Li-doped α-PbO.

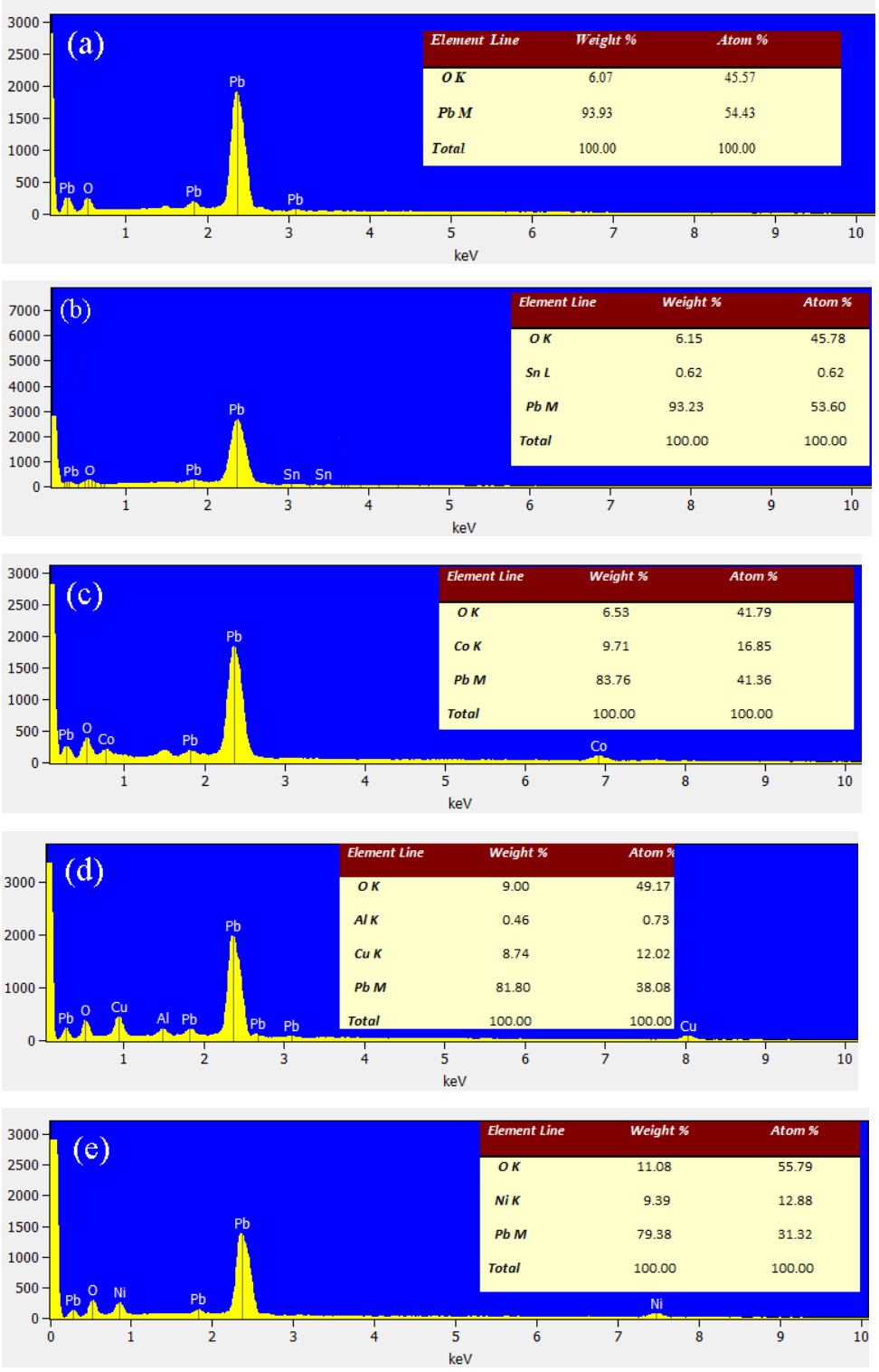

Figure 20: EDX spectrum of (a) pristine, (b) Sn doped, (c) Co doped, (d) Cu doped and (e) Ni doped α-PbO nanoparticles.

4.1.5. EDX analysis

The energy dispersive X-ray spectroscopy (EDX) spectra of the synthesized pristine α-PbO nanoparticles and different metal doped are presented in Figure 20(a-e). These spectra confirmed the existence of the required elements in the synthesized pristine α-PbO and different metal-doped nanoparticles. The inert Tables of Figure 20 (a-e) presents the weight and atom percentage of elements in the composition. In all compositions except the existence of a small Al percentage in the case of Cu-doped, only the required elemental compositions are revealed. The Al impurity in Cu-doped may be from the aluminum sheets during the measurements. For Li doped due to its small atomic number, the EDX spectra were not revealed because EDX cannot measure the elements with atomic numbers less than 6. However, as mentioned in the XRD and UV-Vis analysis the incorporation of this element in the α-PbO nanoparticles can be confirmed. In the pristine Figure 20a, the atom percentage of a lead atom is greater than the oxygen atom percentage. The existence of the dopant elements in the spectra also confirms the incorporation of these elements in the prepared α-PbO nanoparticles.

4.1.6. Photocatalytic degradation of MB dye

The photocatalytic activity of pristine α-PbO, Sn, Co, Cu, Ni, and Li doped α-PbO for the degradation of methylene blue (MB) dye was investigated under visible light irradiation. All photocatalytic experiments were carried out under the same situations. Controlling the pH of the solution is used to control the adsorbents of organic pollutants onto the photocatalyst's surface and the number of hydroxyl radicals created during the illumination time (Mugunthan et al., 2019). In this work, the effect of pH was evaluated at acidic and alkaline, which was taken at pH = 4 in acidic conditions and pH = 10 in alkaline conditions. As presented in Figure 21, the photodegradation efficiency of pristine α-PbO in acidic conditions was 50.77% after 100 min, whereas 94.76% of photodegradation efficiency was achieved in the base condition. Therefore, pH = 10 was selected throughout this work.

Figure 22(a-f) shows the absorption spectra of MB dye at a time interval between 0 to 100 min for pristine α-PbO and different metal doped α-PbO photocatalysts. The absorption revealed around 300 nm correspond to benzene ring absorption and the peaks at 664 nm are absorption corresponds to the heteropoly aromatic linkage of MB dye (Kim et al., 2016). It is observed that as the irradiation time increases the absorbance at maximum wavelength 664 nm of MB dye is

decreased. Thus, the maximum absorption peaks of MB dye at 664 nm were diminished gradually and disappeared as irradiation time increased in the presence of photocatalysts. Meanwhile, the MB dye with photocatalysts suspension colors changed gradually, indicating that the structure of MB dye was decomposed (Figure 23). This indicates that the MB dye is degrading successfully on the surface of photocatalysts as the time of irradiation was increasing. Compared to pristine α-PbO the photocatalytic activity was enhanced for all doped photocatalysts except the Co-doped α-PbO. The enhanced photocatalytic activity of the doped samples was attributed to reduced or increased bandgap by inserting an impurity state between the conduction band (CB) and valence band (VB), small size, retarded electron-hole recombination, high surface area and enhanced electron-hole generation and separation than pristine α-PbO. Among all doped materials, the Sn-doped showed the best MB dye degradation within short time intervals. The reasons for the highest photocatalytic activity of Sn-doped α-PbO are: (i) the efficient visible light region spectrum absorbance of Sn-doped α-PbO, which facilitated and provide efficient light energy for the utilization of photocatalytic activity for the degradation of MB; (ii) due to the metallic property of Sn, the α-PbO conduction band electron might be easily transferred to Sn metallic ion. It is well known that Sn exists in tetravalent and divalent forms. To prevent electron-hole recombination, it can be doped with Sn^{4+} ions, which have exceptional electron-hunting abilities, which can then be reduced to Sn^{2+} ions. In contrast, Sn^{2+} ions can release electrons that can be absorbed by oxygen molecules on the surface of the photocatalyst and change to Sn^{4+} ions.

The photocatalytic degradation efficiency can be calculated according to Beer-Lambert law given by Equation (8) (Nazim et al., 2021) in the literature review section. The photodegradation efficiency of pristine α-PbO and different metal-doped α-PbO is presented in Figure 24a. The consecutive degradation of MB dye at time intervals for all photocatalysts is also given in Table 2. The pristine α-PbO achieved 94.76% of degradation efficiency within 100 min. This result shows that pristine α-PbO is a promising photocatalyst for the degradation of MB dye. Each catalyst achieved the degradation efficiency of 94.76%, 100%, 83.46%, 98.50%, 95.27%, and 97.49% for pristine α-PbO, Sn-doped, Co-doped, Cu-doped, Ni-doped, and Li-doped α-PbO respectively as shown in Table 2.

The Sn-doped α-PbO achieved a 100% of degradation rate within 100 min and achieved 98.98% within 60 min which showed the fastest photodegradation rate of MB dye compared to pristine

and other metal-doped α-PbO. The color change of MB dye during the presence of Sn-doped α-PbO photocatalyst under visible light irradiation is shown in Figure 23.

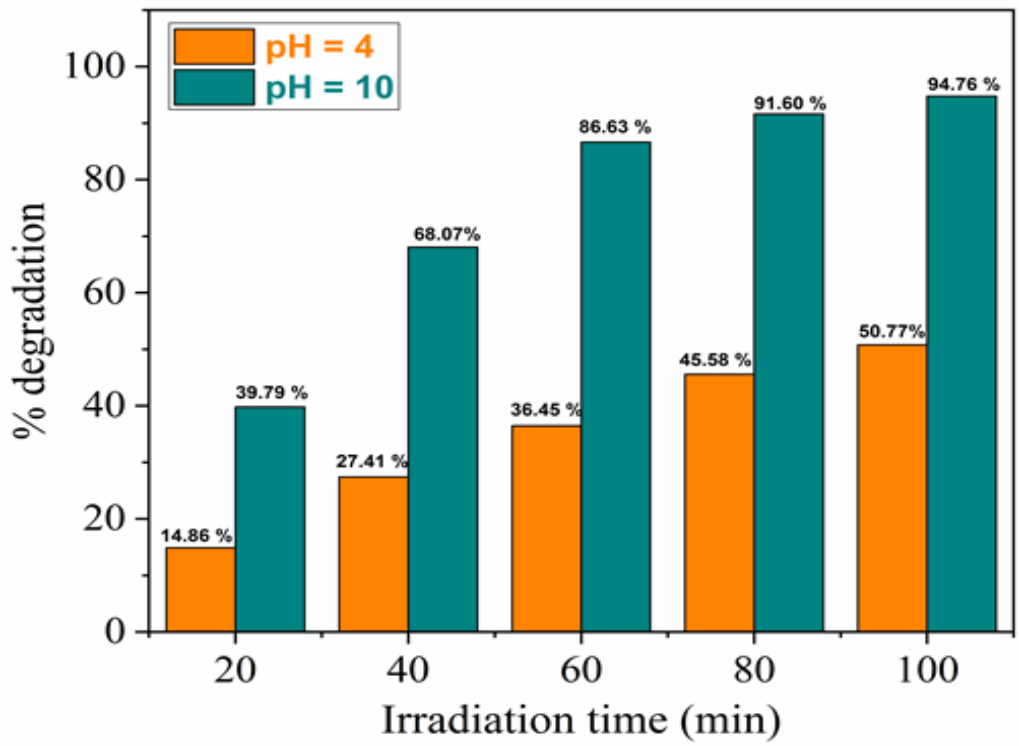

Figure 21: Photodegradation of MB dye by using pristine α-PbO photocatalyst at pH = 4 and pH = 10.

Table 2: Photodegradation efficiency of pristine α-PbO and different metal doped α-PbO.

	Degradation (%) of MB dye by different photocatalysts					
Time (min)	Pristine α-PbO	Sn-doped α-PbO	Co-doped α-PbO	Cu-doped α-PbO	Ni-doped α-PbO	Li-doped α-PbO
0	0	0	0	0	0	0
20	39.79	43.92	25.45	39.74	25.22	31.57
40	68.07	88.19	52.10	67.95	52.83	54.31
60	86.63	98.98	70.59	86.49	72.39	71.80
80	91.60	99.61	80.70	93.91	87.07	85.23
100	94.76	100	83.46	98.50	95.27	97.49

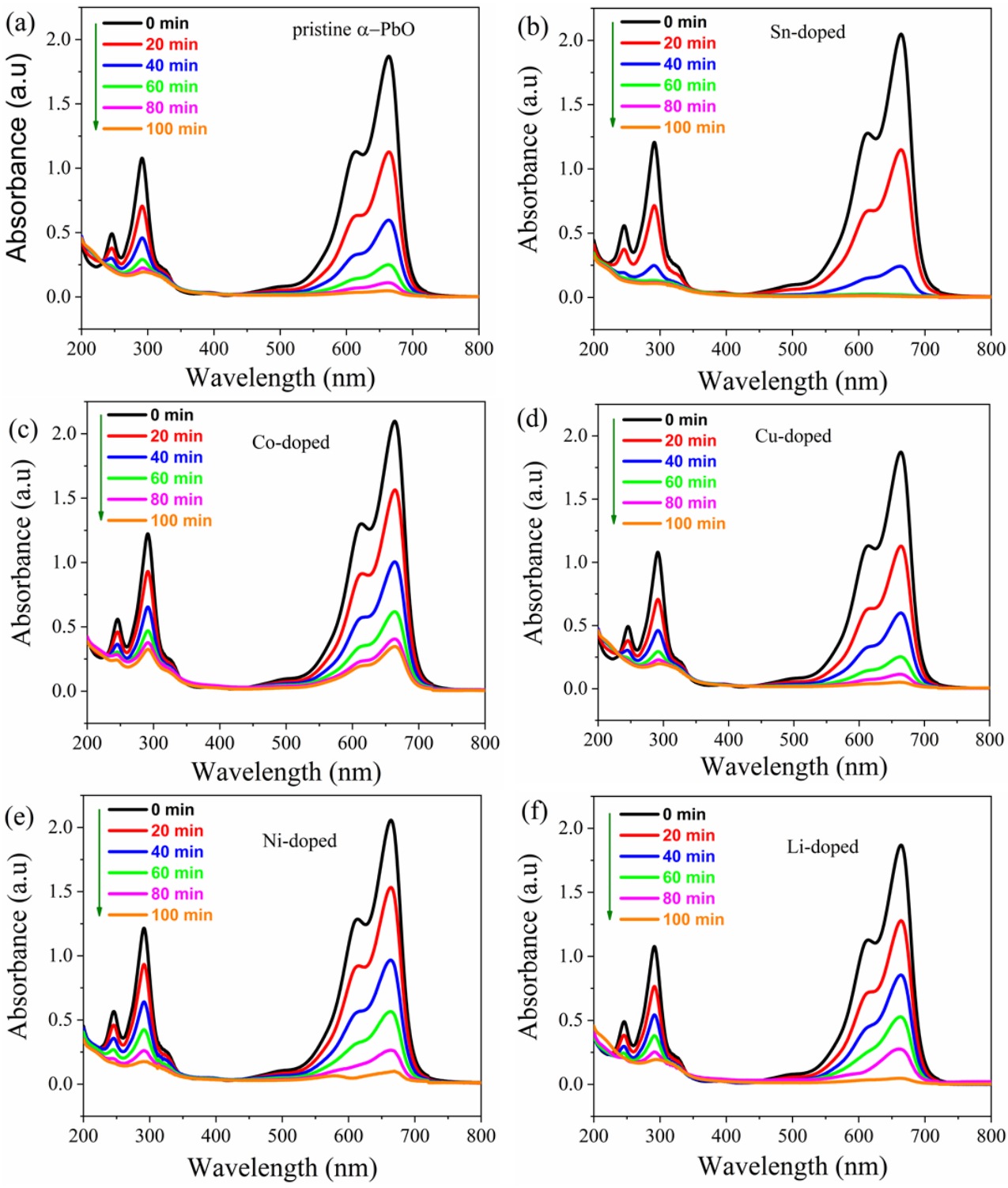

Figure 22: UV-Vis absorption spectra of methylene blue dye at different time duration in the presence of (a) pristine α-PbO; (b) Sn-doped; (c) Co-doped; (d) Cu-doped; (e) Ni-doped and (f) Li-doped α-PbO.

As shown in the PL emission (Figure 18) all the prepared catalysts owed approximately low PL intensity which might be the reason for the enhanced photocatalytic activity for the degradation of MB dye under the visible light irradiation. On the other hand, when we compare their PL intensity the Sn-doped photocatalyst possessed higher intensity than pristine α-PbO and other doped photocatalysts. Thus, Sn-doped α-PbO possessed higher free charge carrier concentrations which enhanced its photocatalytic activity compared to pristine α-PbO and other doped photocatalysts.

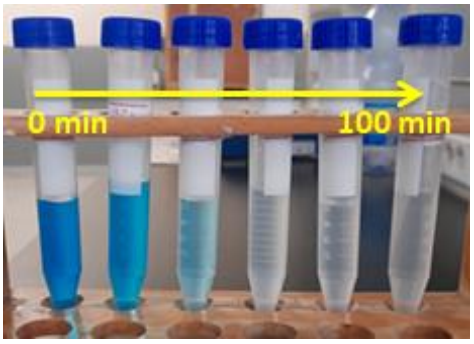

Figure 23: MB decoloration in the presence of Sn-doped α-PbO.

The enhanced photocatalytic activity of the prepared materials can also be related to their morphology. Sn-doped α-PbO has formed a rough surface structure at the interface of a single particle which can increase the absorbance of MB dyes to the surface of the photocatalyst and enhance the photocatalytic activity. Thus, materials with high surface roughness and surface area can absorb organic pollutants on their surfaces and improve photocatalytic performances (Sriwong et al., 2019). As one can observe from the SEM micrographic morphology, the more agglomerated particles owed enhanced photocatalytic activity. Small constituent of the particles aggregated and formed large particles in pristine α-PbO and Sn, Cu, Ni, and Li doped α-PbO. However, in Co-doped α-PbO, the small constituents were not well agglomerated which might be reason for its low photocatalytic activity compared to other catalysts. The low crystallinity of Co-doped α-PbO might also be attributed to its low photocatalytic activity. The smallest particle size is also reasonable for the enhanced photocatalytic activity of Ni-doped α-PbO. The surface area of the catalyst also plays a great role in the degradation of dyes. Thus, a catalyst with a large surface area has a high capability of organic pollutants adsorbing on its surface. Therefore, the enhanced photocatalytic activity of the doped α-PbO nanoparticles may also be attributed to the enhanced surface area of the prepared nanoparticles. As it is reported in the literature when Sn is

doped into oxide semiconductors, the surface area of the doped nanoparticles increase and as a result, its photocatalytic activity is enhanced (Siva et al., 2020).

The enhanced photocatalytic activity of Cu-doped and Li-doped α-PbO could also be explained by reduction of Cu and Li on the surface of α-PbO. Thus, when Cu and Li are doped on the surface of α-PbO as Cu^{+} and Li^{+} ions, they accept an electron for charge compensation and reduced to Cu atom and Li atom which plays a great role in charge separation and could act as reduction sites. Therefore, the recombination of photogenerated electron-hole pairs is reduced and enhanced the photocatalytic activity. The irradiation time has a great effect on the degradation of MB dye. In this work, despite the different properties of each dopant, the UV-Vis spectrum was measured for all photocatalysts for the same irradiation time between 0 and 100 min. If the irradiation times increase, the Co-doped α-PbO can also achieve 100% degradation rates, but it may take a too long time.

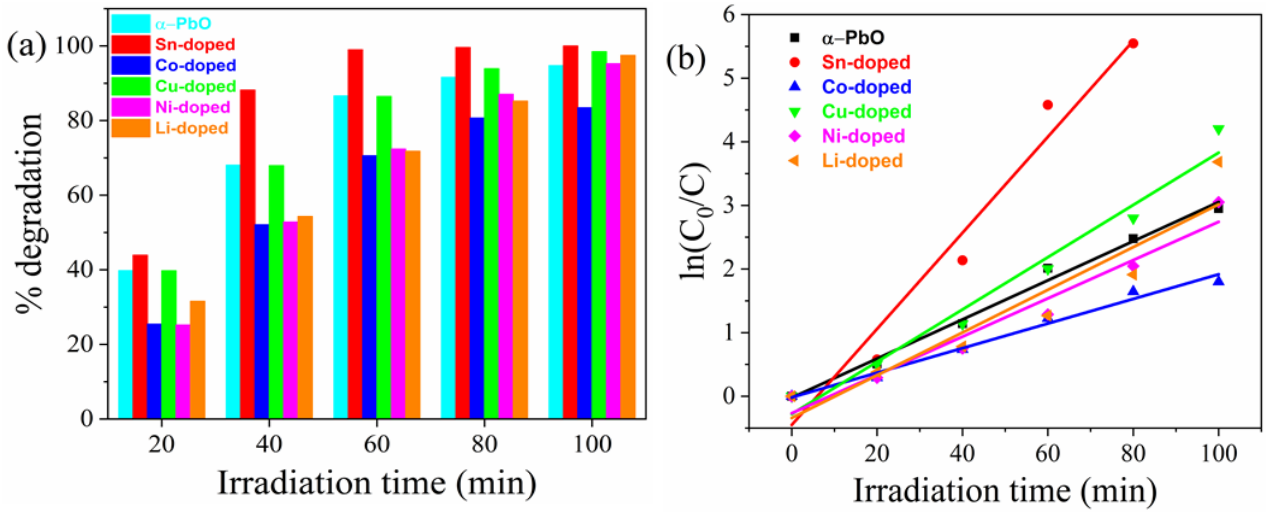

Figure 24: (a) Bar diagram of photodegradation percentage of MB dye with time under visible light irradiation using pristine α-PbO and Sn, Co, Cu, Ni and Li doped of α-PbO catalysts; and (b) pseudo-first-order kinetics plots of MB adsorption on with pristine α-PbO and different metal doped α-PbO.

The pseudo first order is used to study the photocatalytic degradation of MB dye. It is used to provide the information about the adsorption mechanisms. Thus, the rate constant is calculated by using pseudo first order kinetic expression given in Equation (10) (Pang et al., 2022). The value of rate constant k was obtained from the slope of the plot of $\ln C_0/C$ versus irradiation time. The plot of $\ln C_0/C$ vs. time is presented in Figure 24b. This plot is linear, which indicates

that the photocatalytic degradation of MB dye follows the pseudo-first-order condition of reaction. The higher rate constant means a better degradation rate when compared to the lower rate of constant. The correlation coefficient for the fitted line and rate constant of pristine α-PbO and different metal-doped α-PbO is presented in Table 3. Among all photocatalysts, the Sn-doped α-PbO possessed the highest rate of constant, whereas the Co-doped α-PbO possessed the least rate of constant. Thus, the highest rate constant value of Sn-doped α-PbO confirms the highest degradation efficiency within a short time of irradiation. The half-life time of the MB dye, while it was experienced to light in the presence of pristine α-PbO and different metal doped α-PbO, is given in Table 3.

Table 3: Rate constant and correlation coefficient for the degradation of MB dye with various catalysts and half-life time.

Catalyst	Rate constant k (min^{-1})	Correlation coefficient (R^2)	Half time (min)
Pristine α-PbO	0.03075 ± 0.00147	0.99	22.57
Sn-doped α-PbO	0.07547 ± 0.00854	0.96	9.20
Co-doped α-PbO	0.01934 ± 0.00119	0.98	35.88
Cu-doped α-PbO	0.04107 ± 0.00352	0.97	16.90
Ni-doped α-PbO	0.03008 ± 0.00313	0.96	23.07
Li-doped α-PbO	0.03357 ± 0.00587	0.89	20.67

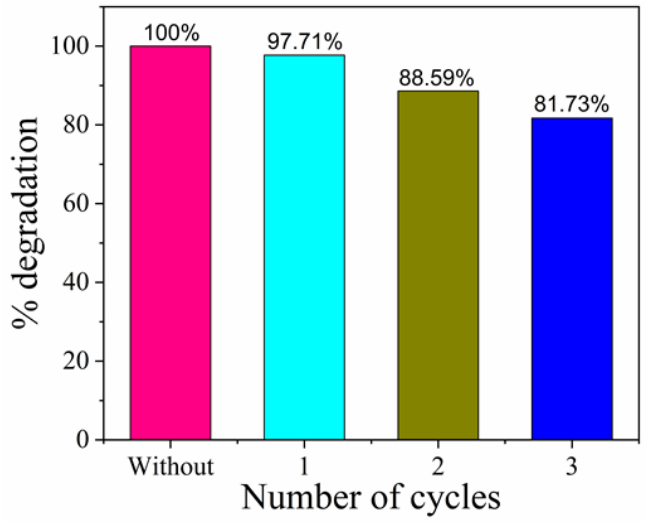

Figure 25: The cycling measurements of Sn-doped α-PbO photocatalyst for the degradation of MB dye.

Figure 25 presents the repeatability of the photocatalysts for the degradation of MB dye by recycling the catalyst three times. Sn-doped α-PbO photocatalyst was selected for repeatable experiment due to its best photodegradation efficiency compared to other doped photocatalysts. The recycling of the powder of the photocatalyst was carried out by filtration and washing with distilled water and ethanol followed by gentle drying. As mentioned earlier, Sn-doped α-PbO achieved 100% degradation efficiency without recycling. After recycling, its photodegradation efficiency was decreased due to the loss of some amounts of photocatalyst during the recycling process of catalyst powder. Despite this, even after the third cycle of the photocatalytic process no significant loss of degradation efficiency. Thus, the results unambiguously show the Sn-doped α-PbO photocatalyst is stable and can be reused.

4.1.7. MB photodegradation mechanisms

The schematic diagram of the bandgap of pristine α-PbO and different metal doped α-PbO and the MB dye photodegradation mechanism is shown in Figure 26a. When visible light with energy equal or beyond the photocatalysts bandgap was irradiated on the surface of photocatalysts, electrons in the valence band (VB) gets energy and excited to the conduction band (CB) and holes are occur in the valence band. The excited electrons were with strong reducibility, whereas holes formed on the valence band were with strong oxidability. Thus, the redox system was generated on the surface of pristine α-PbO and metal-doped α-PbO. Then the photogenerated electrons and holes separated and migrated to the surface of pristine α-PbO and metal-doped α-PbO photocatalysts. The excited electrons can also recombine with holes in the valence band. When pristine α-PbO and metal-doped α-PbO photocatalysts came into contact with organic pollutants, electrons (e−) in the conduction band of the photocatalyst surface react with O_2 and form reactive species superoxide (O_2•−). Meanwhile, holes (h^+) in the valence band of the surface of the photocatalysts react with moisture H_2O and produce reactive species free radicals •OH. On the other hand, the reactive species free radicals •OH can also be formed by the reaction between holes of the valence band of photocatalysts and OH^- in the aqueous solution. The obtained reactive species (O_2•− and •OH) oxidized MB to non-harmful products such as H_2O and CO_2.

Active species trapping experiments were conducted to capture the main active species generated in the photocatalytic process in order to determine the role of active species in the photodegradation of MB dye and to further investigate the mechanism of photocatalytic

degradation. The ascorbic acid (AA), isopropyl alcohol (IPA) and ethylenediaminetetraacetic acid (EDTA) were used to be the scavengers of superoxide radical ($\bullet O_2^-$), hydroxyl radical ($\bullet OH$) and holes (h^+), respectively (Alam et al., 2018; Mondol et al., 2021). Sn-doped α-PbO was chosen for the trapping experiment because it demonstrated excellent MB dye degradation among all the catalysts used in this study. Figure 26b shows the impact of these scavengers on the photodegradation of MB dye. With no scavengers present (blank), 100% photodegradation efficacy was achieved for Sn-doped α-PbO. However, in the AA, IPA, and EDTA trapping experiments, the rates of photodegradation were reduced to 82.65%, 47.82%, and 39.83%, respectively. As a result, the photodegradation of MB dye involves both h^+ and $\bullet OH$, with h^+ having a greater impact than the $\bullet OH$ radical. However, the $\bullet O_2^-$ radical only played a small part.

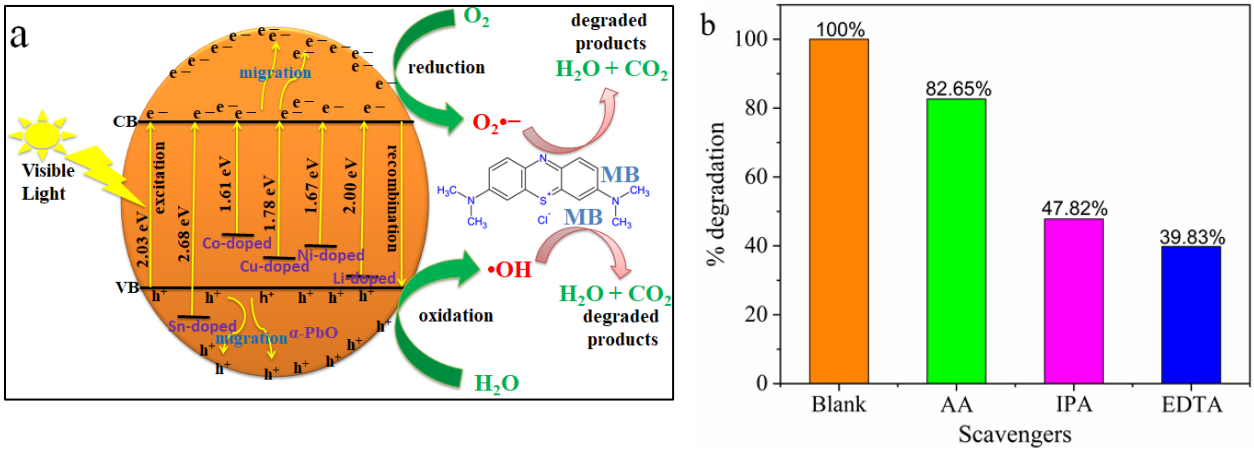

Figure 26: (a) Bandgap energy diagram of pristine α-PbO, Sn-doped α-PbO, Co-doped α-PbO, Cu-doped α-PbO, Ni-doped α-PbO and Li-doped α-PbO catalysts and photodegradation mechanism of MB dye; (b) effects of scavengers namely, ascorbic acid (AA), isopropyl alcohol (IPA) and ethylenediaminetetraacetic acid (EDTA) on the photodegradation of MB dye using Sn-doped α-PbO photocatalyst.

The photocatalytic reaction process can be proposed as follows:

$$\alpha\text{–PbO} + h\upsilon \rightarrow \alpha\text{–PbO}[(h^+)_{VB} + (e^-)_{CB}] \quad (72)$$

$$(h^+)_{VB} + H_2O \rightarrow \bullet OH \quad (73)$$

$$(e^-)_{CB} + O_2 \rightarrow O_2\bullet- \quad (74)$$

$$MB + [h^+ + \bullet OH + O_2\bullet-] \rightarrow \text{degraded products.} \quad (75)$$

All the prepared photocatalysts acquired the visible light region active because their optical bandgap was found in the visible region. However, in the doped photocatalysts, the impurity level was introduced in between bandgap for all doped catalysts except Sn-doped introduced impurity level outside of the bandgap. When impurity level was introduced in between the bandgap, it allowed electrons in the valence band to absorb less energy and excited. On the other hand, the Sn-doped α-PbO photocatalyst introduced the impurity level by increasing the bandgap, which abled it to absorb a wide range of visible light. Thus, the introduced impurity level increased the concentration of electrons and holes, thereby enhancing the photocatalytic activity of Sn-doped α-PbO. Cu and Li are with one oxidation number. Consequently, they can be used for electron trapping while doped into α-PbO, which reduces the recombination rate of photogenerated electron-hole pairs.

4.2. Experimental Results of β-PbO nanoparticles

4.2.1. XRD analysis

The XRD patterns of high purity and different metal doped β-PbO are presented in Figure 27a. The XRD patterns of these materials revealed the polycrystallinity nature. The diffraction peaks are indexed as (010), (111), (020), (200), (201), (220), (022), (131), (311), (222) and (040). The obtained phase is the β-PbO phase which is confirmed from the matching well with JCPDS PDF #38-1477. There is no unknown emerged peak for pristine β-PbO which indicates the high purity of this phase. The pristine and different metals doped β-PbO peaks are strong and sharp, which specify the crystalline nature of the prepared nanoparticles. Among the indexed peaks, the (111) and (020) are the highest intensities of characterized peaks of pristine and different metal doped β-PbO, and the rest indexed peaks are with lower intensities. The characterized (020) indexed plane is the predominance peak for pristine β-PbO and Li-doped β-PbO, which shows the orientation of phase is along the <020> whereas (111) is the dominant diffraction peak for other doped materials showing the orientation of phase is along the <111>.

As shown in the enlarged Figure 27b the different metal doped β-PbO shows shifts relative to the dominant diffraction peaks of pristine β-PbO at positions 29.12º, 30.34º, and 32.62º. All doped materials showed shifts to the highest angles, which can be attributed to the dopant impurities. The higher or lower angle shifts of diffractions are also may be due to the non-similar ionic radii between the pristine and dopant ions. This can causes the increase or decrease in crystallite size

of the samples. To the higher shift shows the lattice strain while to the lower angle shift shows the lattice relaxation. In terms of diffraction intensity peaks, the reduction after dopants incorporation indicates the introduction of some perturbation in the crystal structure of β-PbO (Sood et al., 2015).

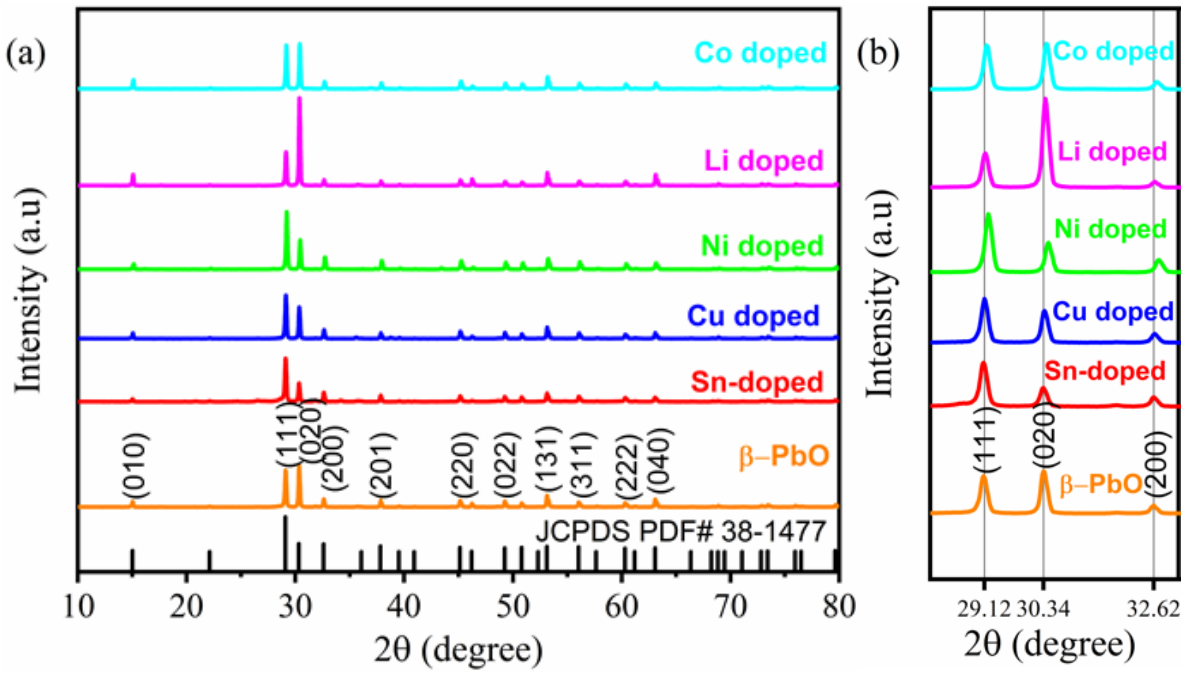

Figure 27: (a) XRD patterns of pristine and different metal doped β-PbO nanoparticles and (b) enlarged XRD patterns of the diffraction line of (111), (020) and (200) crystal plane.

From XRD data the d-spacing and lattice parameters can be calculated. The lattice parameters and d-spacing of β-PbO nanoparticles can be estimated by using the Bragg's expression given in Equation (62). Since the crystal structure of β-PbO is orthorhombic we can find lattice parameters from the d-spacing relations. For orthorhombic structure, all lattice parameters are not equal. Therefore we used Equation (76), for lattice parameters calculations.

$$\frac{1}{d_{hkl}^2} = \frac{h^2}{a^2} + \frac{k^2}{b^2} + \frac{l^2}{c^2} \tag{76}$$

The calculated lattice parameters of pristine and different metal-doped orthorhombic β-PbO are presented in Table 4. The obtained lattice parameters for pristine β-PbO is 5.8873 Å, 5.4858 Å, and 4.7519 Å for *a*, *b*, and *c*, respectively. These results are in the best agreement with the previous report (Aliakbari et al., 2014). After doping, the lattice parameters are decreased in all doped materials, which confirm that the diffraction peak shifts to the highest angle positions.

Table 4: The calculated d-spacing, lattice parameters, crystallite size, dislocation density and strain

Materials	hkl	d-spacing (Å)		Lattice constants (Å)					
		Standard	calculated	Standard			Calculated		
				a	*b*	*c*	*a*	*b*	*c*
Pristine β-PbO	200	2.7413	2.7429	5.8931	5.4904	4.7528	5.8873	5.4858	4.7519
	020	2.9403	2.9436						
	111	3.0631	3.0662						
Sn: β-PbO	200	2.7406	2.7429	_	_	_	5.8873	5.4858	4.7519
	020	2.9413	2.9436						
	111	3.0634	3.0662						
Co:β-PbO	200	2.7354	2.7380	_	_	_	5.8759	5.4760	4.7413
	020	2.9348	2.9380						
	111	3.0561	3.0600						
Cu:β-PbO	200	2.7394	2.7413	_	_	_	5.8835	5.4825	4.7488
	020	2.9388	2.9417						
	111	3.0612	3.0641						
Ni:β-PbO	200	2.7325	2.7331	_	_	_	5.8684	5.4662	4.7363
	020	2.9317	2.9342						
	111	3.0529	3.0559						
Li:β-PbO	200	2.7391	2.7413	_	_	_	5.8796	5.4825	4.7427
	020	2.9371	2.9399						
	111	3.0599	3.0621						

The crystallite size of pristine and different metals doped β-PbO nanoparticles is calculated by using Scherrer's equation. The calculated crystallite sizes of pristine and different metal doped β-PbO are presented in Table 5. The crystallite size of pristine β-PbO is 57.39 nm and then decreases for all doped samples except Li-doped β-PbO. The increased crystallite size of Li-doped β-PbO is attributed to the high shifts to the highest angle position and to its different preferred orientation growth compared to pristine and other doped materials. The size mismatch of the hosts Pb^{2+} or O^{2-} and dopants distort the crystallinity of the materials. Thus, the induced strain and distortion of the lattice can be caused by the size mismatch of Pb and dopants.

The strain is calculated by using Stokes-Wilson equations. The calculated values of induced strain for pristine β-PbO and different metal doped β-PbO are presented in Table 5. It is clear that the calculated values of induced strain increase for Sn, Cu, and Ni-doped β-PbO, which may attribute to the lattice mismatch of these dopants with pristine β-PbO. As explained earlier, the increasing induced strain confirms the crystalline quality deterioration of the doped β-PbO.

Specifically, for the Ni-doped β-PbO, the induced strain increases more when compared with other dopants. For Co-doped β-PbO, the induced strain is almost equal with pristine β-PbO, whereas it decreases for Li-doped. The increased induced strain in Ni-doped β-PbO shows the substantial ionic radii difference between Ni and β-PbO. This causes the lattice distortion, which can lead to XRD peaks shifting to the highest angle position, as one can observe from Figure 27b. The Li-doped induces a small strain relative to other dopants.

Table 5: The calculated crystallite sizes, dislocation density, and strain pristine and metals doped β-PbO.

Materials	D (nm)	ε [$(line^{-2}(nm)^{-4}) \times 10^{-4}$]	δ [$lines/(nm)^{2}) \times 10^{-4}$]
Pristine β-PbO	57.39	5.88	3.06
Sn: β-PbO	50.93	6.62	3.87
Co:β-PbO	57.36	5.88	3.05
Cu: β-PbO	56.09	6.01	3.20
Ni:β-PbO	54.94	6.13	3.33
Li:β-PbO	58.54	5.76	2.93

The amount of defects can firmly explain the optical properties. The amount of defect can be known by calculating the dislocation density (δ). It can be observed from Table 5 that the calculated dislocation density is increased for the Sn, Cu, and Ni-doped β-PbO compared to the pristine β-PbO. Thus, the increase of the dislocation density for the doped β-PbO shows the disorder and the crystalline quality degradation of β-PbO. The size mismatch of the dopants and Pb makes the atom of dopants to occupy position out of the sites of host materials. The calculated dislocation density for other doped materials is decreased, which is attributed to the high crystallinity of these materials.

Moreover, for further identification of phases the Rietveld refinement of XRD data of pristine and different metal-doped β-PbO by using GSAS-II software has been done. The Rietveld refinement plot of pristine and different metals doped β-PbO is presented in Figure 28a-f. The dot and black solid line show the experimentally observed data and calculated for the Rietveld refinement fit. The pink solid line shows the difference between the observed and calculated at each step. From the Rietveld refinement, the obtained results are given in Appendix Tables A22 and A23. In the Appendix of Tables A22 and A23, the obtained lattice parameters, cell volumes, hkl, 2-theta position, d-space, and FWHM are mentioned. The obtained lattice parameters from the Rietveld refinement are in a well agreement with the calculated one.

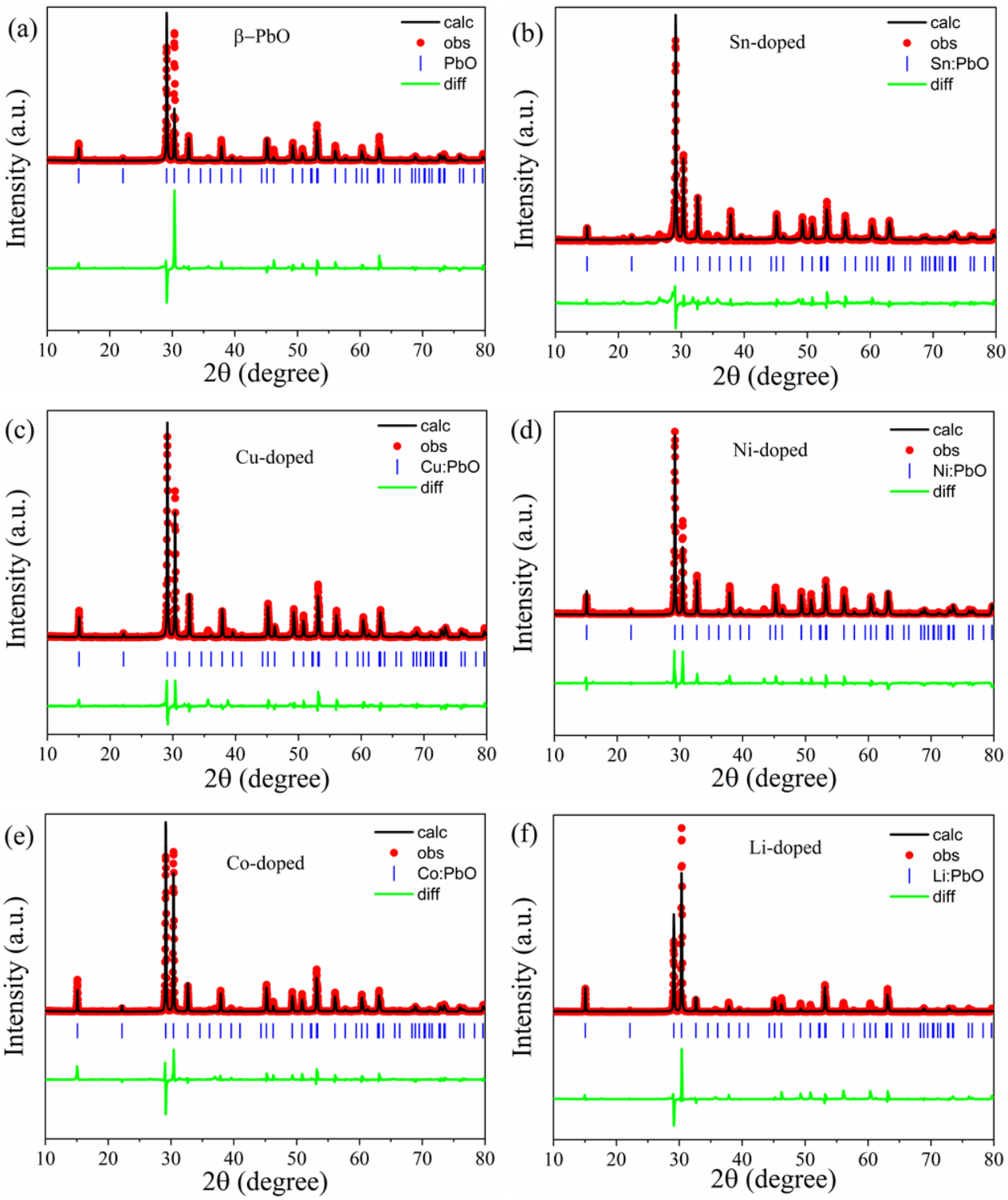

Figure 28: Rietveld refinement pattern of powder XRD data for (a) pristine β-PbO, (b) Sn-doped β-PbO, (c) Cu-doped β-PbO, (d) Ni-doped β-PbO, (e) Co-doped β-PbO, and (f) Li-doped β-PbO with the experimental data (red dots), calculated pattern (black line), difference curve (green line), and Bragg diffraction positions (blue ticks for *Pcam* space group).

4.2.2. UV-Vis DRS

The UV-Vis diffuse reflectance spectra of pristine β-PbO and different metal doped β-PbO are presented in Figure 29. It can be seen that the absorption edge for pristine β-PbO is near 420 nm, while Li and Ni-doped β-PbO the characteristic absorption edge is revealed near 430 nm, 418 nm, respectively. However, it shows a substantial variation for Co and Cu-doped β-PbO. Besides, pristine β-PbO, Li, Sn, and Ni-doped show similar characteristics of reflectance. For pristine β-PbO, the reflectance decreases up to 420 nm but from 420 nm, it increases. It possessed the greatest reflectance of greater than 98% in the visible light region above 566 nm. In the range between 320 nm to 566 nm, the Li-doped β-PbO owns the largest reflectance than pristine β-PbO and other metal-doped β-PbO. The absorption edge for Sn-doped β-PbO is near 396 nm, which showed shifts to the lowest wavelength. Starting from 396 nm, the reflectance of Sn-doped β-PbO increases and becomes greater than all doped materials for wavelength above 620 nm. Cu, Ni, and Co-doped β-PbO showed the lowest reflectance compared to pristine β-PbO, Sn, and Li-doped β-PbO in the spectral region 320-800 nm. For the Ni-doped, the reflectance slowly decreases in ultraviolet until 418 nm and gradually increases in the visible light region. The Li-doped β-PbO has the highest reflectance in the region 320 to 566 nm. For Co-doped, the reflectance decreases as wavelength increases from the ultraviolet to the visible region. In the highest wavelength starting from 566 to 800 nm, all doped materials have lower reflectance than pristine β-PbO. The range of lowest reflectance is due to charge transfers from the valence band to the conduction band. In general, when we compare the reflectance of all samples, Co-doped has lower reflectance. The lowest reflectance of the doped materials shows improved absorption, which may be attributed to the defect introduced due to dopants' impurity levels.

The optical bandgap is estimated by using the Kubelka-Munk relation given in Equation (71). The plots of $(F(R)h\nu)^2$ as a function of photon energy for pristine and different metal doped β-PbO are presented in Figure 30a-f. The bandgap is estimated from the intercept obtained by extrapolating the linear part of the curves. Except Sn-doped, other doped materials showed redshifts in their bandgap, which can be attributed to impurity levels due to doping. Thus, the obtained optical bandgap of pristine β-PbO, Co, Cu, Ni, Li, and Sn doped β-PbO is 2.68 eV, 1.88 eV, 2.01 eV, 2.65 eV, 2.64 eV, and 2.70 eV respectively. In the doped materials, the value of the bandgap is decreased, thereby improving the absorbance. However, in Sn-doped β-PbO, the

bandgap is slightly increased. The bandgap increasing while doping metal in metal oxide was reported in Ga-doped ZnO (Saha et al., 2015). The bandgap variation is attributed to the difference in the ionic radius of the host and dopant elements. The ionic radius of Co^{2+}, Cu^{2+}, Ni^{2+}, Li^{+}, and Sn^{2+} is 0.065 nm, 0.069 nm, 0.073 nm, 0.076 nm, and 0.118 nm, respectively. Among all dopants Co^{2+} possessed the smallest ionic radius; hence Co-doped β-PbO also possessed the lowest bandgap. However, Sn has a large ionic radius and the Sn-doped β-PbO also possessed the largest bandgap.

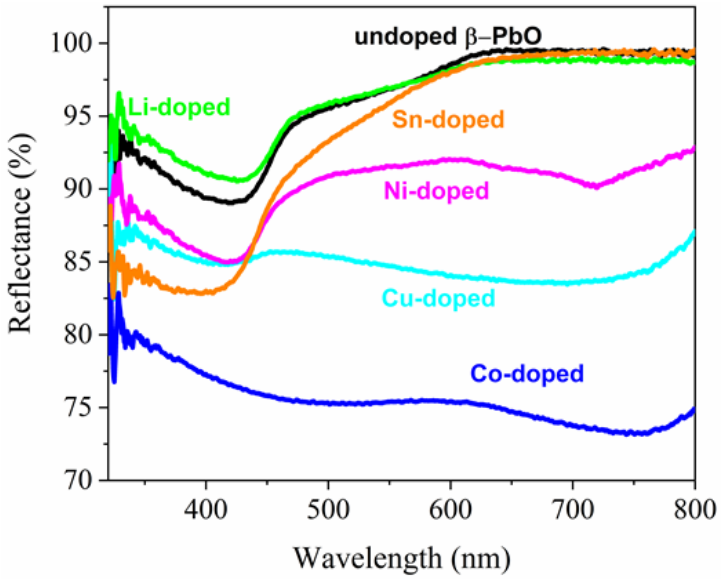

Figure 29: UV-Vis diffusion reflectance spectra of pristine and different metal doped β-PbO

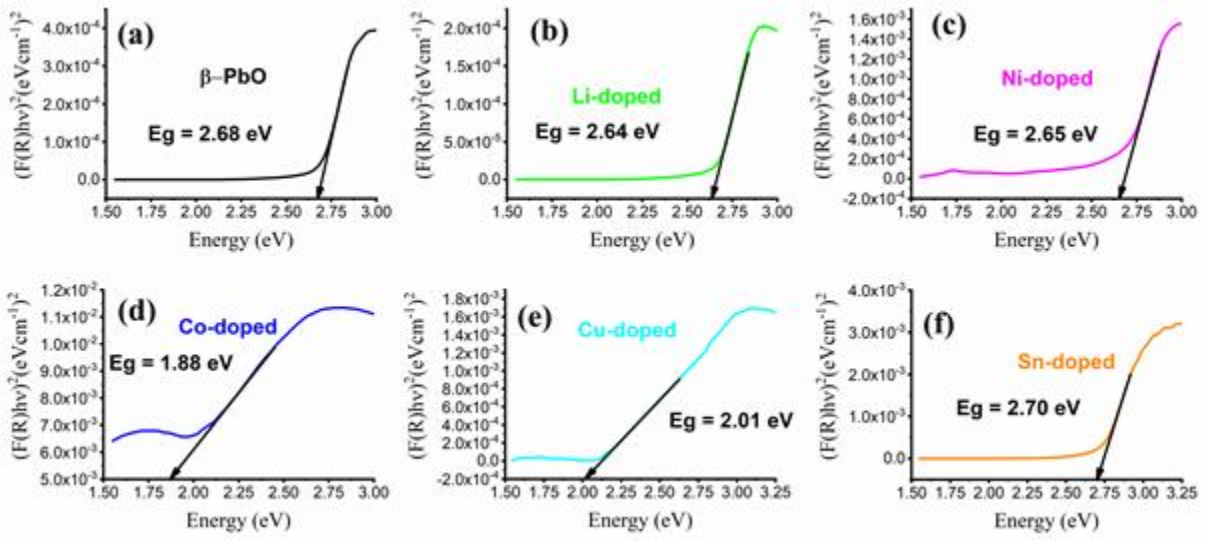

Figure 30: Curves for determination of bandgap of (a) pristine β-PbO, (b) Li-doped, (c) Ni-doped, (d) Co-doped, (e) Cu, and (f) Sn-doped β-PbO.

4.2.3. PL emissions analysis

Photoluminescence (PL) emission spectra of pristine β-PbO and different metal-doped β-PbO nanoparticles under the excitation wavelength of 352 nm are presented in Figure 31. The strong green emission band of pristine β-PbO, Ni, Co, and Cu-doped β-PbO are almost found at 523 nm but with different emission intensities which can be attributed to Pb^{2+} interstitial, oxygen vacancies, and dopant impurity ions formed due to creation of defect energy level. However, in Li and Sn doped, the intense green emission band shows a redshift which is 524 nm. In this case, the visible region green band emission can be attributed to several structural defects like O vacancies and interstitial defects. The intense green band emission of 523 nm is also attributed to the Pb^{2+} vacancy (Gandhi & Wu, 2017). The weak bands observed for pristine β-PbO are 536 nm, 547 nm, and 623 nm. For Li-doped β-PbO, the weak bands are 537 nm, 547 nm, and 622 nm. For Sn-doped, the weak bands are 537 nm, 547 nm, and 621 nm. For Cu-doped, the weak band 633 nm shows the redshifts. From these results, the blue and red shifts are observed. The weak broad red band observed at 623 nm can be attributed to an interstitial atomic defect. The observed shifts are due to the presence of defects from the dopant's impurity ion. The green emission is also attributed to the charge transfer from the conduction band edge to the acceptor level of singly ionized O_2 vacancies (Mythili & Arulmozhi, 2014). There is no excitonic recombination due to the nonexistence of near-band edge transition, which causes ultraviolet emission. Arulmozhi and Mythili have reported the ultraviolet emission of lead oxide nanoparticles by using oleic acid as a capping agent (Arulmozhi & Mythili, 2013).

The higher intensity peaks of Sn-doped compared to the undoped and other doped shows the low interaction of the Sn-O bond, and the increasing of PL intensity increases the capacity of free carriers within the trap center (Mebed et al., 2022). The Co-doped has lower intensity compared to others which can be attributed to the strong interaction Co-O bond (Rahmati et al., 2014). The PL emission intensity decrease might also be attributed to the transfer of electrons from the valence band to the donor level introduced by dopants. The PL intensity decrease is also attributed to oxygen vacancy or defects caused by dopant metals (Ndabankulu et al., 2019). The lower the PL intensity, the less the recombination rate of charge carriers, which has advantages in photocatalytic and solar cell applications (Ndabankulu et al., 2019; Shanmugam et al., 2016). The defect formation decreases the rate of recombination of charge carriers. Thus, the oxygen vacancy traps the excited electrons, while the dopants ion traps the hole (Shanmugam et al.,

2016). Therefore, a decrease in PL intensity indicates a reduction in the recombination of photoinduced electrons and holes; hence, enhanced photocatalytic activity is expected. From PL emission peak broadness, we can determine the crystalline quality of the synthesized material depending on FHWM. Thus, the smaller the FHWM better the optical quality, which indicates higher crystalline quality.

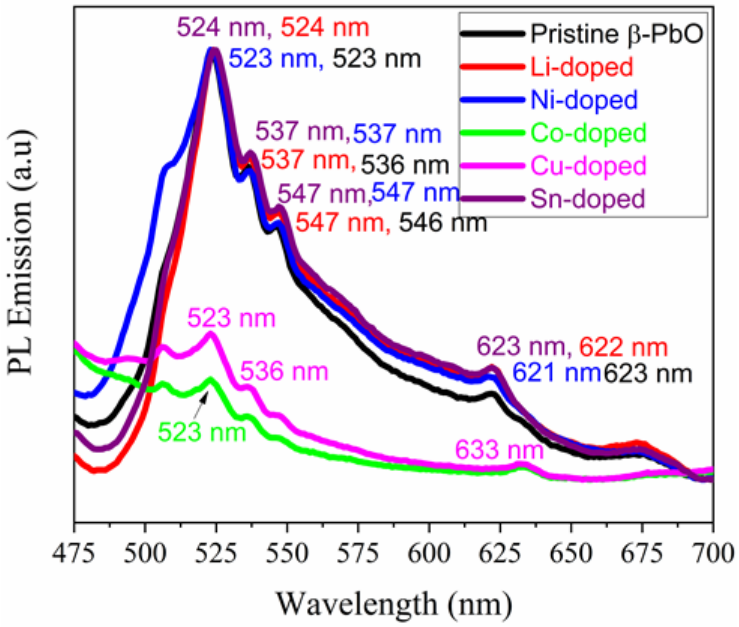

Figure 31: PL emission of pristine and different metal doped β-PbO nanoparticle.

4.2.4. SEM analysis

The SEM micrograph image of pristine β-PbO and different metal doped β-PbO is presented in Figure 32. As shown in Figure 32a, pristine β-PbO nanoparticles are agglomerated and formed interconnected flake-like morphologies. The aggregated particles have layered flake-like orthorhombic, which are deposited on top of each other by forming interconnected branches. Gaussian distribution is used to estimate the average particle size of the synthesized nanoparticles. The average particle size for pristine β-PbO nanoparticles is estimated to be 0.52 µm. The SEM micrograph morphology of Co-doped β-PbO is shown in Figure 32b. In this case, very tiny particle distributions with different morphological shapes such as an irregular morphology and nanorod-like shape are observed. Each particle is agglomerated with inter-particle distance. Thus, it has formed a void-like at the interface of agglomerated particles. The average particle size of Co-doped β-PbO is 0.08 µm which is the smallest particle size compared to pristine β-PbO and other metals doped β-PbO. As presented in Figure 32c, the Cu-doped β-

PbO nanoparticle has an irregularly shaped and flake-like morphology of agglomerated particles with 0.13 μm average particle size. The Ni-doped β-PbO has nanorods and orthorhombic morphological shapes as shown in Figure 32d. The hexagonal rod-like shapes are also observed. The average particle size of Ni-doped β-PbO is 0.1 μm. The Li-doped β-PbO has almost similar particle distributions to the pristine β-PbO as presented in Figure 32e. The plate-like flake shapes are deposited on top of each other and form agglomerated morphological distribution with 0.3 μm average particle size. Generally, the average particle size of the doped nanoparticles decreased compared to the undoped β-PbO.

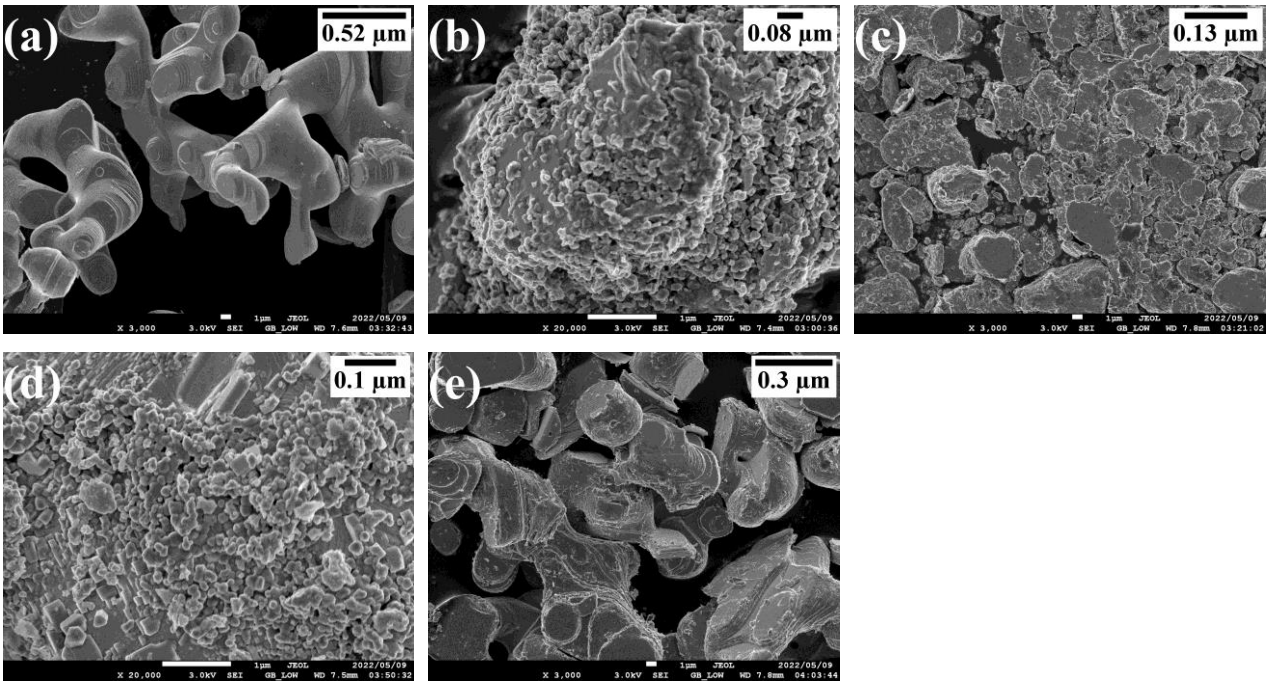

Figure 32: SEM micrograph image of (a) pristine, (b) Co-doped, (c) Cu-doped, (d) Ni-doped, and (e) Li-dope β-PbO.

4.2.5. EDX analysis

The EDX spectra of pristine β-PbO and different metal-doped β-PbO nanoparticles are presented in Figure 33a-d. These spectra confirmed the existence of the required elements in the synthesized β-PbO and different metal-doped β-PbO nanoparticles. The inset tables of Figure 33a-d presents the weight and atom percentage of elements in the composition. In all compositions except the existence of a small Al percentage, the required elements are observed. The Al impurity may be from the composition of crucible used during the annealing samples. During Li-doped β-PbO, due to the small atomic number of Li, the EDX spectrum of Li was not

revealed. Thus, EDX cannot measure the elements with small atomic numbers. However, as mentioned in the XRD and UV-Vis analysis, the incorporation of Li into the β-PbO nanoparticles can be confirmed by its influence on the pristine β-PbO properties. In the pristine Figure 33a, the atom percentage of a lead atom is greater than the oxygen atom percentage.

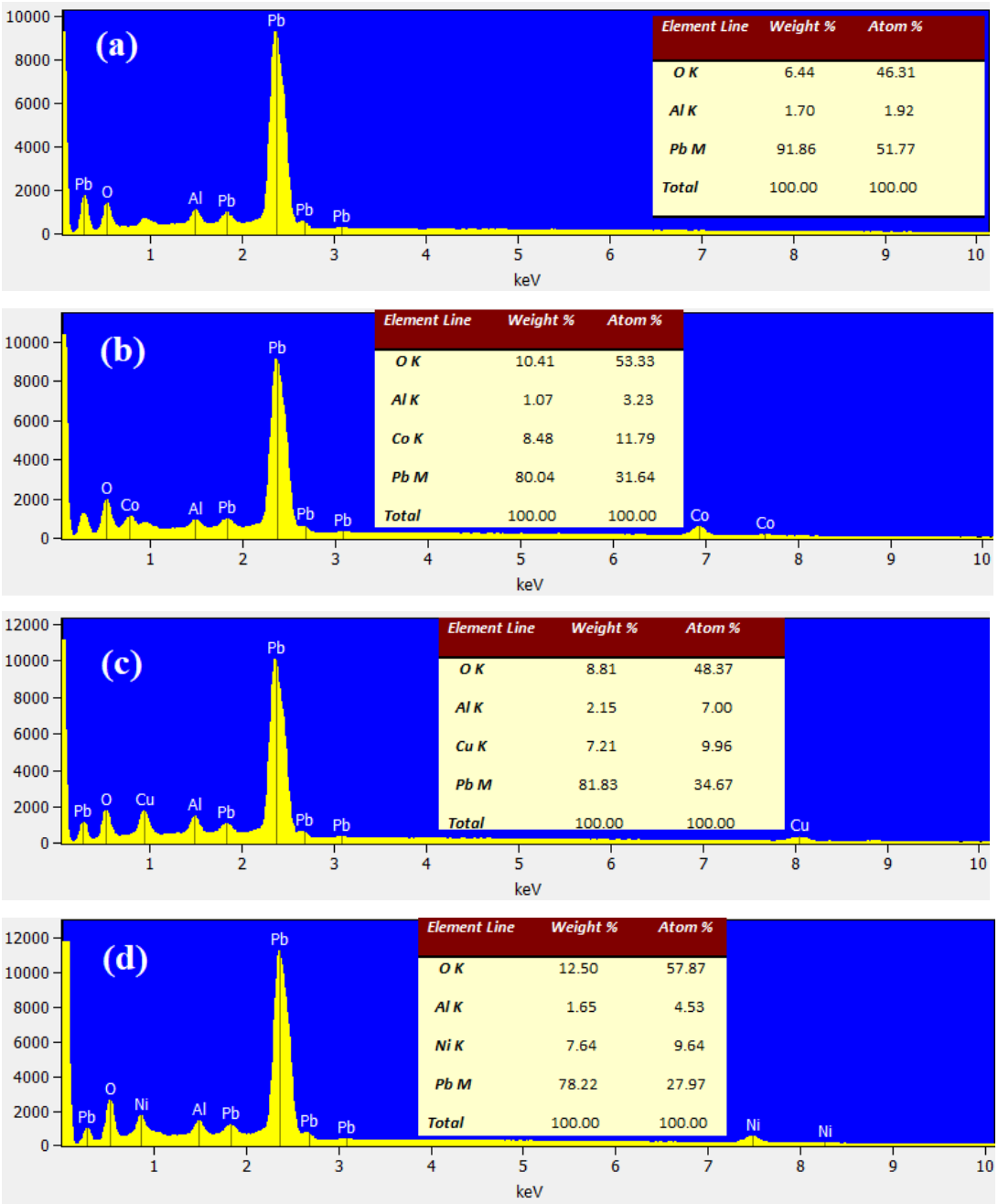

Figure 33: EDX spectrum of (a) pristine β-PbO, (b) Co doped, (c) Cu doped, and (d) Ni doped β-PbO nanoparticles.

4.2.6. Photocatalytic degradation of MB

The photocatalytic degradation of methylene blue (MB) dye by using pristine β-PbO and different metal doped β-PbO as photocatalysts is carried out under visible light irradiation. The photocatalytic activity of pristine β-PbO and metals doped β-PbO was investigated under the same condition. Figure 34 shows the absorption spectra of MB dye at different time intervals while the presence of photocatalysts under visible light irradiation. The absorption characteristics peaks of MB dye at 664 nm were considered to monitor the photocatalytic degradation efficiency of pristine and metals doped β-PbO nanoparticles. The absorption revealed around 300 nm corresponds to benzene ring absorption, and the peaks at 664 nm absorption correspond to the heteropoly aromatic linkage of MB dye (Kim et al., 2016). It can be observed that at a maximum wavelength of 664 nm, the absorbance progressively decreases as irradiation time increases. This shows that the MB dye is successfully decolorizing on the surfaces of photocatalysts with increasing time in 20 min intervals until 80 min reached. Figure 35 shows the decolorization of MB dye in the presence of Cu-doped β-PbO at different irradiation times. The decrease in absorption intensity of MB dye centered at 664 nm in the presence of photocatalysts is due to the loss of chromophoric groups, which are responsible for its color (Alam et al., 2018). It is evident from Figure 34a-f that all metal doped β-PbO showed enhanced photocatalytic activity toward the degradation of MB dye compared to pristine β-PbO. Due to the formation of impurity levels in the doped β-PbO the concentration of photogenerated electrons and holes increases, thereby enhancing the photocatalytic activity of β-PbO. The percentage degradation efficiency is calculated according to the Beer-Lambert law given by Equation (8).

After doping, the photocatalytic activity is enhanced in all doped photocatalysts. The photodegradation efficiency of pristine β-PbO and different metals doped β-PbO at different irradiation time intervals is presented in Figure 36a. The photocatalytic activity trend for metals doped β-PbO for the degradation of MB dye lies in the order: Cu:β-PbO > Co:β-PbO > Ni:β-PbO > Sn:β-PbO > Li:β-PbO, respectively, showing Cu-doped β-PbO with highest photocatalytic activity. The photocatalytic degradation efficiency of pristine β-PbO and different metals doped β-PbO is given in Table 6. Pristine β-PbO affords 75.13% degradation after 80 min of irradiation, while all doped β-PbO with similar doping content (0.1 M) showed enhanced photocatalytic activity under similar conditions. The enhanced photocatalytic activity after doping may be attributed to bandgap narrowing, higher carrier concentrations, reduction of

carrier recombination rate, and higher surface area than pristine β-PbO. Doping of β-PbO nanoparticles with different metals leads to the creation of intermediate energy states, which reduces the recombination of photogenerated charge carriers due to enhancing the charge separation sufficiently, thereby improving photocatalytic activity. Thus, dopants present in β-PbO can act as electron and hole trapping to reduce the recombination of photogenerated electrons and holes. The reduction of dopant ions on the surface of β-PbO can also be attributed to the enhanced photocatalytic activity of metals doped β-PbO. Consequently, when dopants are absorbed on the surface of β-PbO, they can absorb or release electrons which can support charge separation and shows enhanced photocatalytic activity by scavenging electrons by oxygen at the surface. For instance, Li is monovalent, and it accepts one electron to be reduced to a Li atom which supports the charge separation and acts as a reduction site. The enhanced photocatalytic activity of metal-doped β-PbO compared to pristine β-PbO can also be due to lighter harvesting in the visible region, which facilitated sufficient energy for the degradation of MB dye.

Morphology of the synthesized nanoparticles may also have effects on the photocatalytic performance of β-PbO. After metal doping the morphology of pristine β-PbO is changed specifically in Co, Ni, and Cu doped β-PbO. Particle size distribution is also reduced in the doped nanoparticles. The pristine β-PbO nanoparticles are agglomerated and formed interconnected flake-like morphologies and its surface is smooth, which decreases the amount of dye adsorbed onto its surface. If the MB dye adsorbed onto the photocatalyst surface reduced the photodegradation efficiency is low. In metals doped the surface of nanoparticles is rough with porosity and small size particle distribution is observed. Thus, the MB dye sufficiently adsorbed on the surface of photocatalysts, thereby enhanced photocatalytic performance. In Li doped β-PbO the particles morphology is almost similar to pristine β-PbO, but unlike pristine β-PbO the surface of particles is rough and able to adsorb MB dye in larger amount.

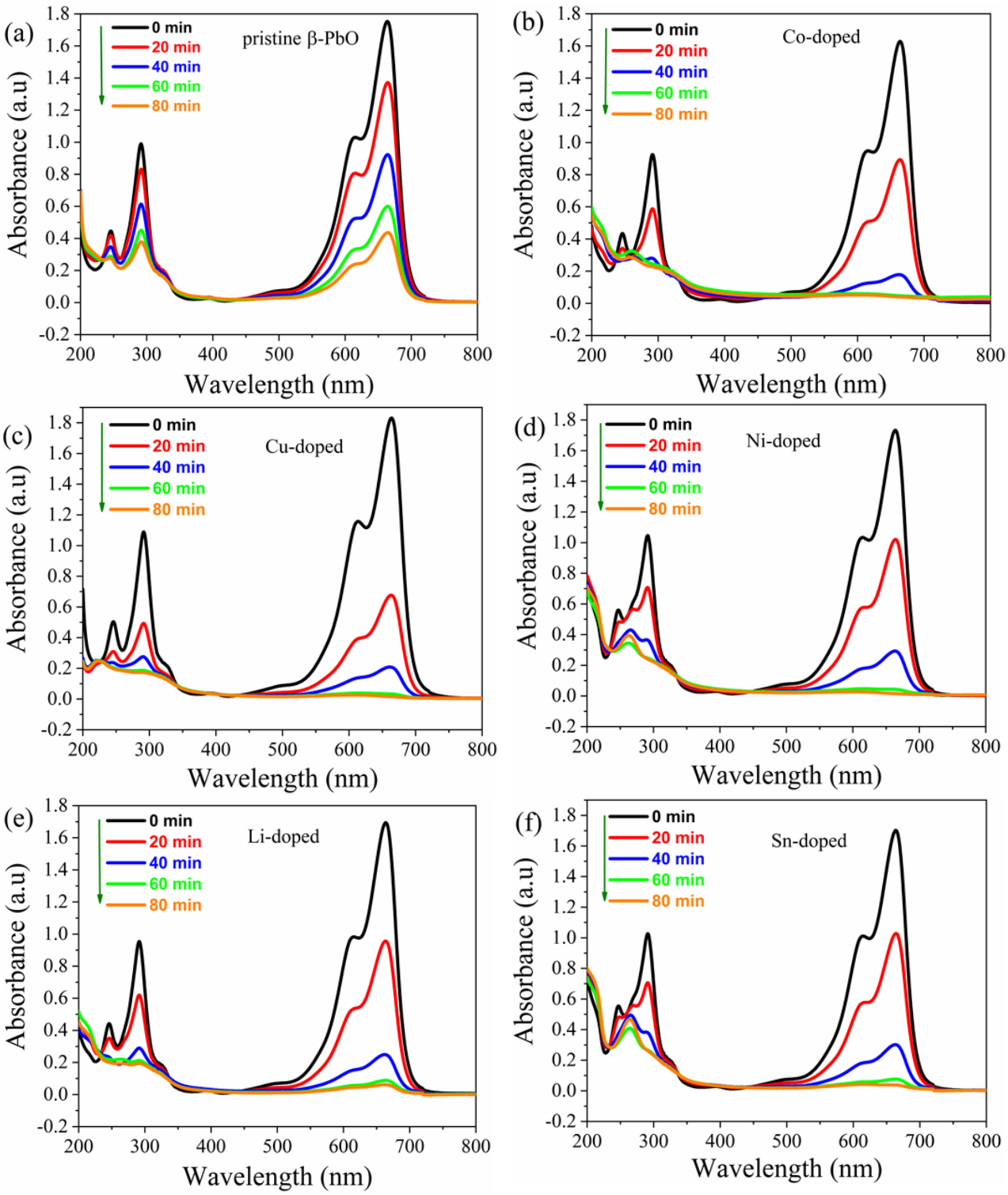

Figure 34: UV-Vis absorption spectra of MB dye at different time duration in the presence of (a) pristine β-PbO; (b) Co-doped β-PbO; (c) Cu-doped β-PbO; (d) Ni-doped β-PbO; (e) Li-doped β-PbO and (f) Sn-doped β-PbO.

The photocatalytic degradation of MB dye could be fitted well suggesting pseudo-first-order kinetics. The degradation rate constant MB dye was determined by using Equation (10). The slope of the plot of $\ln C_0/C$ versus irradiation time gives us the rate constant *k*. Figure 36b illustrates the linear regression curve fit of the natural logarithm for the concentration of MB dye at different irradiation times. The correlation coefficient for the fitted line and rate constants for pristine β-PbO and metals doped β-PbO are present in Table 7. It can be observed that the rate constants of different metals doped β-PbO was higher than that of pristine β-PbO nanoparticles and followed the photocatalytic activity trend as mentioned above, with the highest value for Cu-doped β-PbO nanoparticles. The higher the rate constant is, the higher the degradation rate compared to the lower rate constant. The half-life of the MB dye, while it was experienced to light in the presence of pristine β-PbO and different metal doped β-PbO, is also given in Table 7.

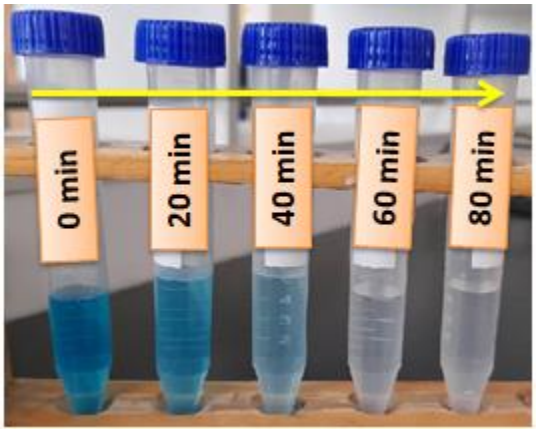

Figure 35: MB decoloration in the presence of Cu-doped β-PbO.

Table 6: photodegradation efficiency of pristine α-PbO and different metal doped β-PbO.

Time (min)	Degradation (%) of MB dye by different photocatalysts					
	Pristine β-PbO	Co-doped β-PbO	Cu-doped β-PbO	Ni-doped β-PbO	Li-doped β-PbO	Sn-doped β-PbO
0	0	0	0	0	0	0
20	21.73	45.15	63.03	41.08	43.57	39.60
40	47.40	89.07	88.59	83.09	85.30	82.26
60	65.77	96.31	97.87	97.23	94.75	95.48
80	75.13	99.39	99.45	98.44	96.34	97.71

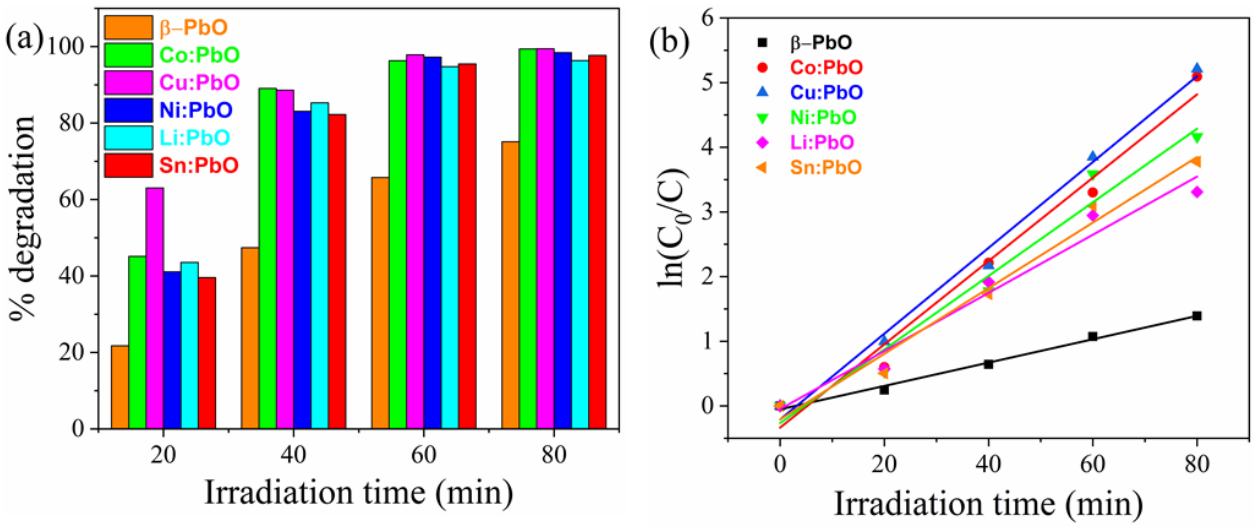

Figure 36: (a) Bar diagram of percentage photodegradation of MB dye with different time intervals under visible light irradiation using pristine, Co, Cu, Ni, Li and Sn doped of β-PbO photocatalysts; (b) pseudo-first-order kinetics plots of MB adsorption on with pristine β-PbO and different metal doped β-PbO.

Table 7: Rate constant and correlation coefficient for the degradation of MB dye with various catalysts and half-life time.

Catalyst	Rate constant k (min^{-1})	Correlation coefficient (R^2)	Half time (min)
Pristine β-PbO	0.01805 ± 8.77509E-4	0.99	38.45
Co-doped β-PbO	0.06443 ± 0.00552	0.98	10.77
Cu-doped β-PbO	0.06637 ± 0.00357	0.99	10.46
Ni-doped β-PbO	0.0569 ± 0.00612	0.97	12.20
Li-doped β-PbO	0.04495 ± 0.0046	0.97	15.44
Sn-doped β-PbO	0.05072 ± 0.00425	0.98	13.68

4.2.6.1. Effect of pH on the degradation of MB and reusability

In heterogeneous photocatalysts, the pH of the reaction mixture plays a great role because the surface charge properties of photocatalysts and the adsorption properties of organic pollutants on the surface of photocatalysts can be dictated (Alam et al., 2018). The effect of pH on the degradation of MB dyes in the presence of pristine β-PbO was examined in pH 4, 6, 8, and 10, as shown in Figure 37a. The degradation efficiency increases with increasing pH values, and the highest degradation efficiency is attained at pH 10. It is why we carried out the pH of the suspension to 10 throughout all photocatalysis experiments. The increased degradation efficiency under alkaline pH could be expressed based on electrostatic attraction between the cation MB

dye and anion photocatalysts, which facilitates the adsorption of MB dye on the surface of photocatalysts.

The reusability of the photocatalysts experiment was carried out by selecting Cu-doped β-PbO by reusing the photocatalyst for three consecutive cycles. Before applying for the next cycle, the photocatalyst was washed with distilled water and ethanol thoroughly to remove impurities and dried in an oven at 100 ^{o}C for 5 hr. As shown in Figure 37b, even after three cycles, it showed degradation efficiency greater than pristine β-PbO. The loss of the original degradation efficiency during recycling is due to the loss of some amount of photocatalyst while washing and drying.

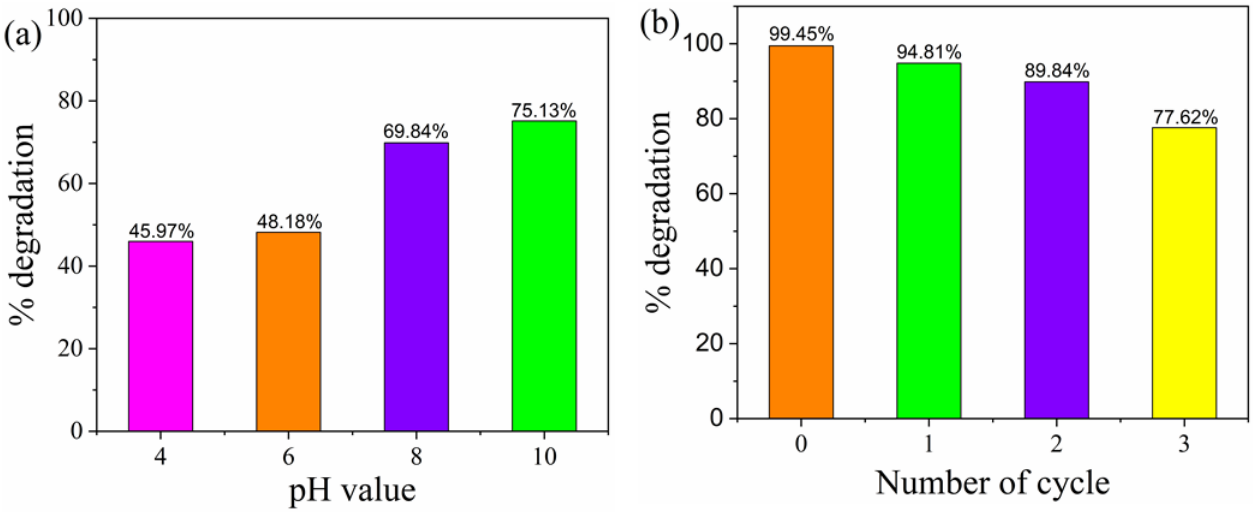

Figure 37: (a) effect of pH on the photodegradation of MB dye in the presence of pristine β-PbO; (b) the cycling measurements of Cu-doped β-PbO photocatalyst for the photodegradation of MB dye.

4.2.6.2. Trapping experiment and MB photodegradation mechanisms

To ascertain the major reactive species involved in the degradation of MB dye using Cu-doped β-PbO nanoparticles, a series of radical species trapping experiments have been employed. Scavengers such as disodium ethylenediaminetetraacetate (EDTA-2Na), isopropyl alcohol (IPA), and ascorbic acid (AA) have been used to trap holes (h^+), hydroxyl radical (•OH), and superoxide anion radical (O_2•−), respectively. Figure 38a presents the percent degradation of MB dye in the presence of different scavengers using Cu-doped β-PbO nanoparticles under visible light irradiation within 80 min. The figure indicates that the scavengers-free photodegradation process exhibited maximum degradation efficiency, whereas the photodegradation in the

presence of scavengers shows a decreased degradation percentage. The result indicates that the EDTA-2Na and IPA-assisted photocatalytic system exhibits a low percent of degradation with the EDTA-2Na assisted shows much more low percent of degradation than IPA. Thus, hydroxyl radicals and holes play a great role in the degradation of MB dye with holes being actively involved in the degradation process. However, the photodegradation of MB dye is slightly reduced, while the addition of AA indicates that O_2•− involves a minor role in the degradation of MB dye.

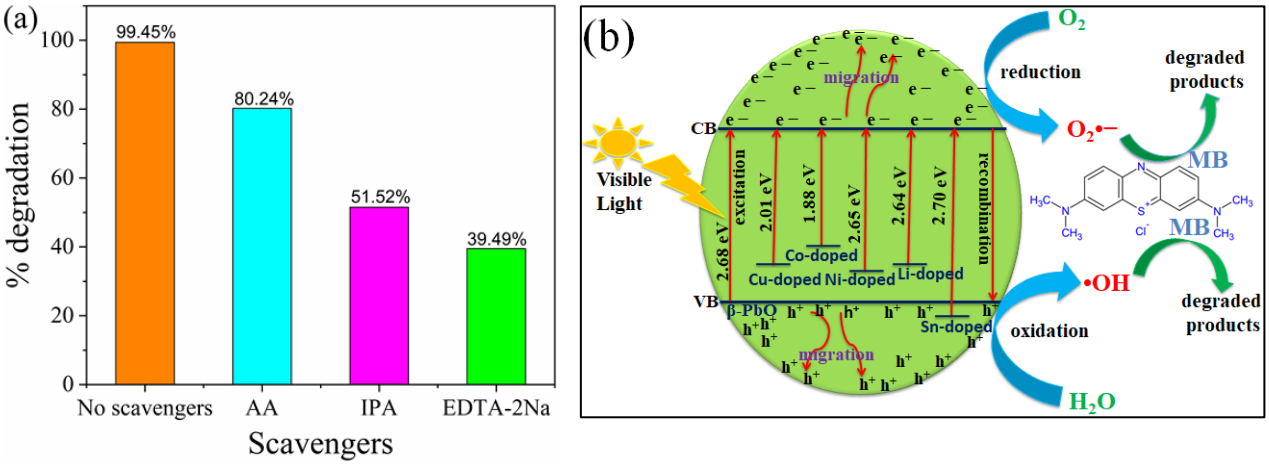

Figure 38: (a) effects of scavengers namely, ascorbic acid (AA), isopropyl alcohol (IPA) and disodium ethylenediaminetetraacetic acid (EDTA-2Na) on the photodegradation of MB dye using Cu-doped β-PbO photocatalyst; (b) Bandgap energy diagram of pristine β-PbO, Co-doped β-PbO, Cu-doped β-PbO, Ni-doped β-PbO, Li-doped β-PbO and Sn-doped β-PbO catalysts and photodegradation mechanism of MB dye.

Based on the abovementioned results and reported literature, a possible photocatalytic mechanism for MB dye degradation over pristine β-PbO and different metals doped β-PbO photocatalysts under the irradiation of visible light is proposed and presented in Figure 38b. The bandgap of pristine β-PbO and metals doped β-PbO nanoparticles lies in the visible region which can response the visible light irradiations. However, the bandgap of different metals doped β-PbO decreased compared to pristine β-PbO except slight increase in Sn-doped β-PbO. This is due to the impurity level of dopants that were introduced to narrow the bandgap of pristine β-PbO, which contributed to enhancing the photocatalytic activity of β-PbO nanoparticles. When the prepared photocatalyst absorbs energy equal to or greater than its bandgap, the electron gets sufficient energy to be excited from the valence band (VB) of the prepared photocatalysts to the

conduction band (CB) of the photocatalyst and simultaneously leaving holes (vacancy) in the VB of photocatalysts. Thus, photogenerated electrons and holes are created. In the pristine β-PbO, the photogenerated electron-hole pairs recombine rapidly, hence decreasing the photocatalytic activity of pure β-PbO nanoparticles. In metal doping β-PbO, the photogenerated electrons can be trapped by the dopant that serves as electron trapping, and the photogenerated electrons and holes are separated well. The photogenerated electrons (e^-) would produce O_2•− by reacting with oxygen. Meanwhile, holes (h^+) in the VB would undergo charge transfer to the water molecules or hydroxyl group adsorbed on the surfaces of photocatalysts and produces •OH. The generated radicals and holes during the photocatalysis process would react with MB dye molecules adsorbed on the surfaces of photocatalysts, and the MB dye could be successfully degraded. The degraded byproducts such as H_2O and CO_2 formed during the reaction between active species and MB dyes are non-harmful. The photocatalytic reaction process can be proposed as follows:

$$\beta\text{−PbO} + \text{dopants} + h\upsilon \rightarrow \beta\text{−PbO(dopants)}[(h^+)_{VB} + (e^-)_{CB}] \quad (77)$$

$$(h^+)_{VB} + OH^- \text{or } H_2O \rightarrow \bullet OH \quad (78)$$

$$(e^-)_{CB} + O_2 \rightarrow O_2\bullet- \quad (79)$$

$$MB + [h^+ + \bullet OH + O_2\bullet-] \rightarrow \text{degraded products.} \quad (80)$$

From sections 4.1 to 4.2, the experimentally obtained different metals doped α-PbO and β-PbO nanoparticles are discussed. As explained earlier, PbO can also be synthesized as a thin film. In the next section, the PbO thin film prepared by the chemical bath deposition method is analyzed and discussed.

4.3. PbO thin film

Pure α-PbO and β-PbO nanoparticles were synthesized successfully by the chemical precipitation method. However, the deposited PbO thin film by chemical bath deposition possessed both α-PbO and β-PbO phases. It is tried to synthesize high purity α-PbO phase or β-PbO phase by varying molar concentration, but the two phases co-exist at each concetrations with the majorly β-PbO phase domination.

4.3.1. XRD Structural Analysis

The XRD patterns of PbO thin film prepared at different molar concentrations are shown in

Figure 39a. The XRD analysis shows that the deposited PbO thin film has a polycrystalline nature that can be confirmed from the existence of many peaks for all molar concentrations. The Miller indices (100), (001), (111), (200), (020), (021), (220), (112), (311), (131), and (113) are indexed for the crystal structure of the deposited PbO thin films which matches with the Joint Committee on Powder Diffraction Standard (JCPDS) PDF# 38-1477. The two phases of PbO were revealed in the deposited thin film with the domination of the β-PbO phase. However, the α-PbO phase is rarely presented. Among the indexed peaks, (001), (020), and (112) are for the α-PbO phases, and the rest are for β-PbO phases. The characteristic peaks with high intensities are (200), (111), (100), (001), and (020), whereas the rest indexed peaks possessed the lowest intensities. The magnified XRD peaks for (111), (200) for the β-PbO phase, and the (020) for α-PbO phases are shown in Figure 39b, and there is a shift with the varying concentrations, which resulted in small crystal change. Shifts in the diffraction peak are observed by varying molar concentrations, as shown in Figure 39b, which shows that in the lattice of PbO, no structural deformation is caused (Soylu & Coskun, 2018).

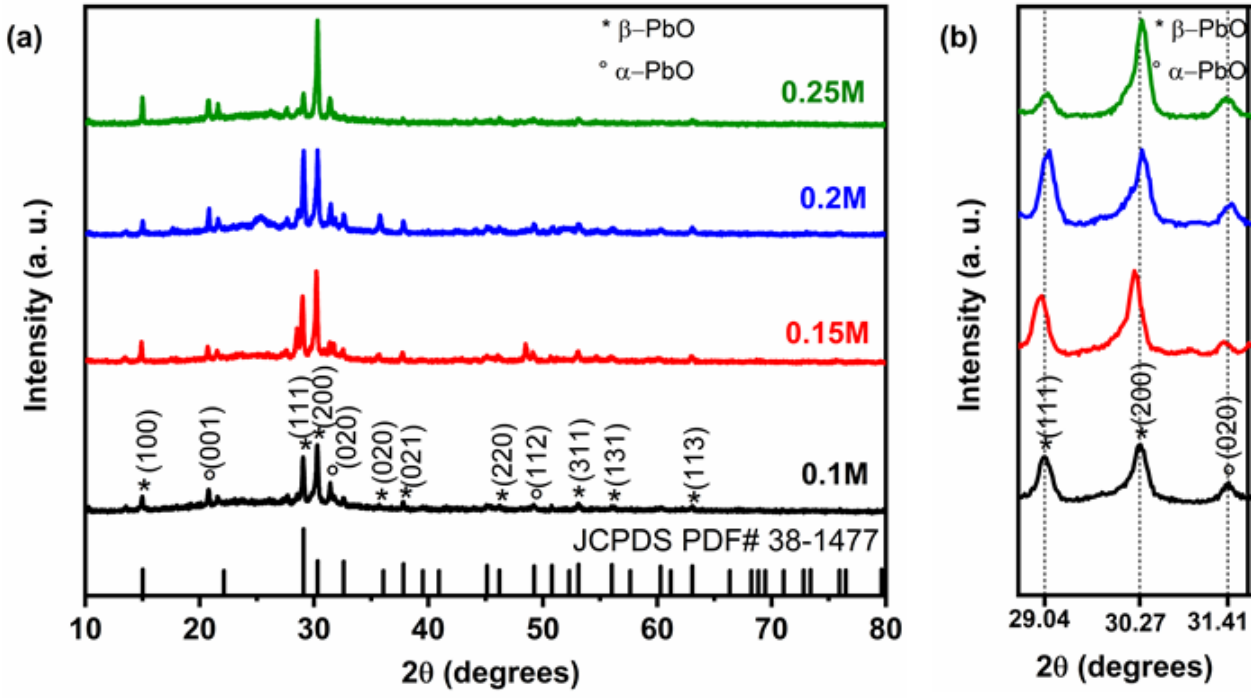

Figure 39: The XRD patterns of 0.1 M, 0.15 M, 0.2 M, and 0.25 M molar concentrations of PbO thin films; (b) The Magnified XRD patterns in (111), (200) and (020) directions.

Among the indexed peaks for the β-PbO phase, the (200) is the predominance peak, which shows

that the growth of the crystal is such that the a-axis is perpendicular to the surface of the substrate. For the calculation of the lattice parameter *a* the strongest peak of a plane (200) was used. The (200) indexed plane is the predominance peak which shows the orientation of the phase is along the [200] direction. Therefore, the growth of the crystal orientation and substrate was perpendicular. From the diffraction patterns, both β-PbO and α-PbO phases coexist. The (111) and (200) are the two maximum intensity peaks of β-PbO that showed variation with lead oxide precursor concentration. Initially, with the increase of the concentration from 0.1 M, the (111) peaks increased and were almost equal with the predominance (200) peak at 0.2 M; however, decreases for a further increment of the concentration to 0.25 M. This may show that the effect of molar concentrations on the crystal structure of PbO thin films. This may also be concerned with the crystalline quality degradation with increasing cations concentrations. From XRD patterns, it is observed that degradation of crystalline quality due to the increasing cation concentrations, which can cause defects and strain was observed. When the cation concentration increases, the two phases coexisted for all concentrations, which indicate that the deposited film is only PbO.

Table 8: Comparison of calculated and standard values of interplanar distance (d) and lattice parameters (*a*, b, and c).

Cation concentration	hkl	d-spacing (Å)		Lattice constants (Å)					
		standard	Calculated	standard			calculated		
				a	b	c	*a*	b	c
0.1M	200	2.948	2.949	5.893			5.898		
	020	2.745	2.746		5.490			5.492	
	111	3.070	3.073			4.752			4.767
0.15M	200	2.954	2.956	5.893			5.913		
	202	1.875	1.875		5.490			5.385	
	111	3.076	3.078			4.752			4.852
0.2M	200	2.945	2.946	5.893			5.892		
	020	2.742	2.743		5.490			5.487	
	111	3.066	3.069			4.752			4.758
0.25M	200	2.946	2.948	5.893			5.895		
	202	1.850	1.851		5.490			5.493	
	111	3.068	3.069			4.752			4.755

By using similar mathematical expressions given for α-PbO and β-PbO nanoparticles in sections 4.1 and 4.2, the d-spacing, lattice parameters, crystallite size, lattice strain and dislocation

density can be calculated. The calculated d-spacing and lattice parameters are given in Table 8 and compared with the standard values. The obtained lattice parameters are well agreed with the reported value (Samberg et al., 2014). The obtained crystallite size, strain, and dislocation density of different molar concentrations of the deposited PbO thin film are given in Table 9. The crystallite size for all concentrations is found in the range of 34.05 nm to 45.80 nm. The average crystallite size for 0.1 M, 0.15 M, 0.2 M, and 0.25 M concentrations were 36.51 nm, 41.22 nm, 37.28 nm, and 40.38 nm, respectively. Thus, initially, as the cation concentration increased from 0.1 M to 0.15 M, the crystallite size increased; however, it becomes decreased for 0.2 M and again its crystallite size increased as the cation concentration becomes increased to 0.25 M. The decrease in crystallite size shows the deterioration crystalline quality of the PbO thin film. Hence, 0.15 M has the larger crystallite size among others, and its value decreased for the given peaks (200), (202), and (111). This concentration may be the optimal concentration among the deposited PbO thin film. Generally, all the calculated values are approaching each other approximately, which indicates a slight deterioration in the crystal structure.

Table 9: Calculated average crystallite size, strain and dislocations density of PbO thin films with various molar concentrations.

Pb-cation concentrations	hkl	Calculated average crystallite size (nm)	Calculated strain (ε) ($line^{-2}(nm)^{-4}$) ($\times 10^{-4}$)	Calculated dislocation density (δ) ($lines/(nm)^2$) ($\times 10^{-4}$)
0.1M	200 020 111	36.50	9.23	7.50
0.15M	200 202 111	41.22	8.07	5.89
0.2M	200 020 111	37.28	9.07	7.20
0.25M	200 020 111	40.38	8.06	6.13

As presented in Figure 39b, there are small peak shifts as we vary the molar concentrations, which may be related to defects and strains. Due to the increase of the molar concentration, the crystal size varies and it may create lattice disorder and strain in the PbO lattice. The calculated values of induced strains are present in Table 9. From the obtained values, it can be observed that

there are little variations for each cation concentration at given peaks, which indicates that a slight crystallite deterioration confirming the crystal quality of the deposited PbO thin film is good. The decrease in the crystallite size after 0.15 M may be due to the existence of the strain in the PbO film crystal. The greatest induced strain is found in 0.1 M because its crystallite size is the smallest compared to others. From Table 9, it can be observed that the dislocation density was calculated for the indexed peaks, and it was random. For 0.1 M, the dislocation density is decreased for the given (hkl) peak, but for 0.15 M, it is increased. For 0.2 M, it decreased for the (020) peak and then increased for the (111) peak, however, for 0.25 M, it increased and then decreased with a value greater than the initial (200) peak. 0.1 M has a higher average dislocation density than all other concentrations. Hence, there is a high defect in the PbO film deposited with 0.1 M. On the other hand, 0.25 M has the least dislocation density, meaning that it has a low defect. The 0.15 M has a linear increase of dislocation densities for the given (hkl).

4.3.2. UV-Vis spectroscopy studies

The optical properties of semiconductors can be probed by using absorption spectra. The UV-Vis spectra of the deposited PbO thin films at different cation concentrations are shown in Figure 40. Figure 40a represents the optical absorbance of the PbO film for 0.1 M, 0.15 M, 0.2 M, and 0.25 M and Figure 40b shows the corresponding bandgap. The absorption maxima were found near 284 nm, 288 nm, 284 nm, and 283 nm for 0.1 M, 0.15 M, 0.2M, and 0.25 M, respectively. These values agree with the previously reported values and show the existence of the two phases (Mythili & Arulmozhi, 2014). The absorption peak becomes broad as the cation concentration is increased to 0.25 M. The maximum absorption intensity is observed at 0.15 M. Initially, the absorption intensity increased as concentration increased to 0.15 M, but decreased below the absorption intensity of the lowest concentration as concentration further increased to 0.2 M and 0.25 M. The intensity of the 0.1 M PbO film becomes greater than the 0.2 M after annealing to 400 ^{o}C. For 0.25 M the absorption becomes sharper after annealing, which shows perfect absorption at 283 nm. It is shown that the absorption edge is shifted to a shorter wavelength as concentration increased to 0.2 M and 0.25 M. This small shift can be correlated to a change in optical bandgap values. It is clear that the optical bandgap and wavelength have inverse proportional relation.

From absorption spectra, the optical bandgap of the PbO thin films can be calculated by using the Stern relation (Hone & Dejene, 2019),

$$\left(A\frac{hc}{\lambda}\right)^2 = K\left(\frac{hc}{\lambda} - E_g)\right)^n \quad (81)$$

where A is absorbance, h is plank's constant which is 6.62 × 10^{-34} Js, ν is frequency, c is the speed of light which is 2.998 × 10^8 m/s, is the incident photon energy, K is constant, E_g is band gap of the material, and n is either direct or indirect bandgap depending on the transitions: if n = 4 it is indirect band gap and if n = 1 it is direct band gap. Here we have got that the deposited PbO thin film is a direct bandgap. The plot of $\left(A\frac{hc}{\lambda}\right)^2$ versus reciprocal wavelength is presented in Figure 40b for the annealed PbO thin films at 400 °C for various molar concentrations. Once we obtained by extrapolating the linear region of the plot onto the x-axis for reciprocal wavelength, Equation (81) is used for the bandgap calculations.

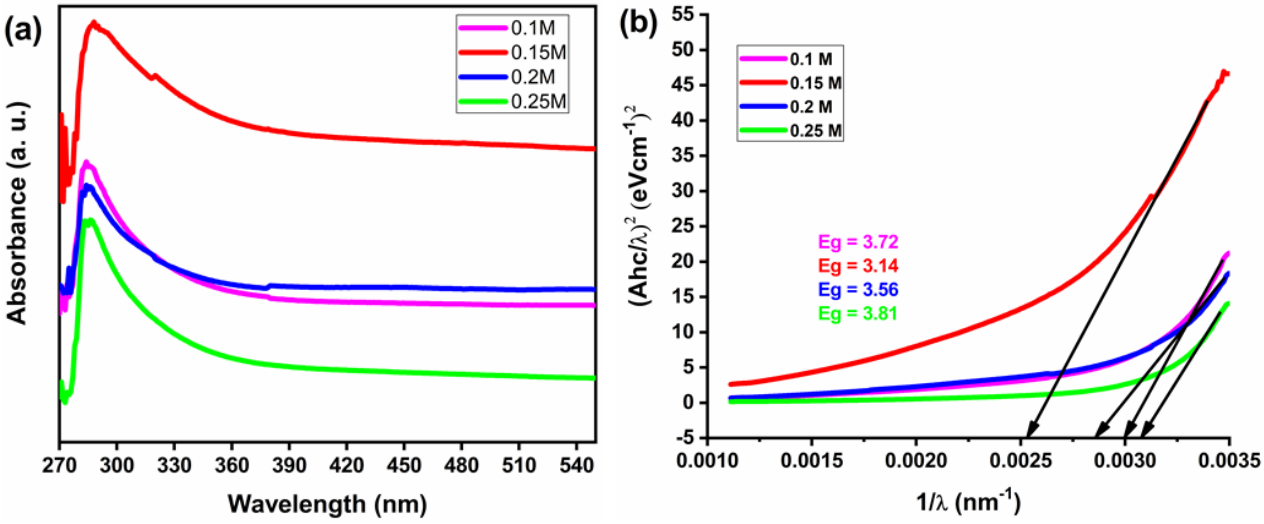

Figure 40: a) Optical absorbance of PbO thin films and b) Optical band gap of PbO thin film annealed at 400 °C for various molar concentrations.

Band gap values of the deposited films at 0.1 M, 0.15 M, 0.2 M, and 0.25 M are 3.72, 3.14, 3.56, and 3.81 eV, respectively. Thus, the band gap initially decreased for the 0.15 M and then increased. The bandgap for 0.1 M is higher than 0.15 M, and then when the cation concentration increased to 0.2 M and 0.25 M, the band gap value increased. We can observe from the optical absorption as the band gap increases the absorption is shifted to a smaller wavelength. The relationship between the bandgap of PbO, concentration, and annealing effect is presented in Figure 41. The band gap increased when the film was annealed, which tells us particle size decreases as temperature increases (Jang & Jeong, 1995). The increased band gap after annealing is also attributed to the coexistence of the two phases of PbO because α-PbO is stable at lower

temperatures, and it is gradually transformed to β-PbO as temperature increases. An optical band gap up to 5.5 eV has also been reported (Bapitha & Alagar, 2017). We have compared our calculated optical band gap values with the previously reported values. Our result is found in the range of reported values with small variations.

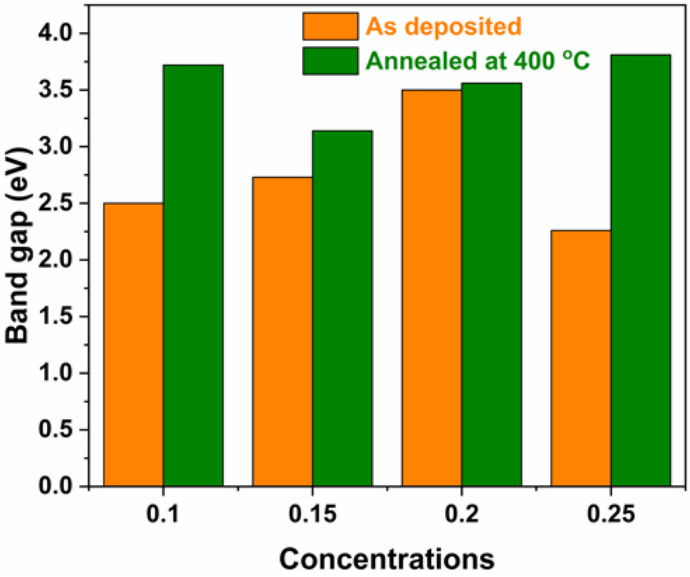

Figure 41: Molar concentrations versus energy band gap of the PbO thin films for as a deposited and annealed to 400 ^{0}C.

4.3.3. PL-emission Spectroscopy

It is important to study the luminescent properties of PbO nanostructure since it helps to find PbO film applications in optoelectronics. From the emission peaks, we can analyze the existence of defects and their dislocation density. Since we have used the CBD method for PbO thin film preparation, oxygen vacancy and Pb^{2+} interstitial defects which form trap states may be expected (Mythili & Arulmozhi, 2014). The PL spectra of the PbO thin film deposited at different molar concentrations were recorded under 352 nm excitation wavelengths and are presented in Figure 42. The deposited PbO thin film shows almost small intense blue emission at 441 nm for 0.1 M; 444 nm for 0.15 M, and 442 nm for 0.25 M. This can be attributed to the recombination of electrons in the excited conduction band edge and the doubly ionized oxygen vacancies and can also be attributed to the excitonic recombination (Mythili & Arulmozhi, 2014).

The band appeared in the regions 506 nm, 523 nm, and 536 nm with very small shifts for all molar concentrations found in the green emission. This can be attributed to the surface defect and

specifically the 523 nm band is the band with high-intensity green emission which can be attributed to the transition from the edge of the conduction band to the singly ionized oxygen vacancy (Yanjie Wang et al., 2023). The PL peak in the regions of 545 nm and 633 nm with a very small range of shifts for all molar concentrations are the orange and negligible red emissions respectively which are associated with electrons transition from conduction band edge to holes valence trapped at Pb^{2+} interstitial (Cheraghizade et al., 2017). The full width at half maximum (FWHM) of 0.15 M and 0.2 M is smaller than the 0.1 M and 0.25 M concentrations which indicates the best optical quality of PbO thin films at 0.15 M and 0.2 M molar concentrations. This could indicate, the film at these concentrations has higher crystalline quality as indicated in XRD results. There was only a small shift in emission wavelength in varying molar concentrations. This may be attributed to the deposited PbO thin film having no impurities like doped films. Moreover, in terms of their intensity as molar concentration increased the intensity increased for 0.15 M then decreased for 0.2 M, and again increased for 0.25 M with the domination of the 0.15 M concentration. Generally, the intensity increased in the order of 0.2 M, 0.1 M, 0.25 M, and 0.15 M cation concentrations and each cation concentration have high-intensity values as we can observe from the y-axis of Figure 42.

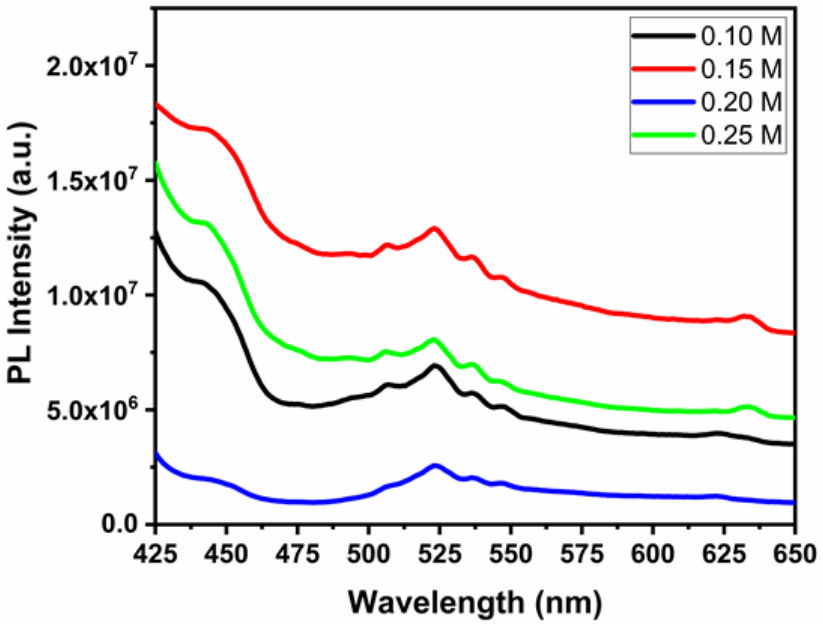

Figure 42: PL emission spectra of different molar concentrations of PbO thin films

4.3.4. SEM and EDX analysis

The SEM surface morphology images of PbO thin film deposited at 0.1, 0.15 as deposited, 0.15, 0.2, and 0.25 molar concentrations of lead ion (Pb^{2+}) are presented in Figure 43. The micrographs of the deposited films are a mixture of different nanostructures and are covered in a heterogeneous distribution. Thus, the coexistence of nanorods and cauliflower structure is observed which are formed in an agglomeration rather than creating individual particles. In all annealed molar concentrations the grains are interconnected. The formation of irregular grains shows the nonuniform nucleation on the surface of the substrate. The nanorods coating the surface of the substrate have a hexagonal structure; this may be due to the existence of the two phases in the deposited thin films. The existence of different shapes coating the substrate may be correlated with the result of the XRD preferential growth orientation. The formation of a regular shape decreases the dislocation density.

Figure 43a illustrates the as deposited 0.15 M PbO thin film, which has been covered by networked nanosheets and nanoflower-like structures. This film is deposited as $Pb(OH)_2$ thus, there exist wet before annealing. For the 0.1 M cation concentration, as illustrated in Figure 43b the agglomerated cauliflower structure with nanorods on the surface of films distributed heterogeneously. The heterogeneous coated nanoparticle shows that there was nonuniform nucleation for the growth of particles throughout the surface of the substrate. In addition to cauliflower and nanorods shape, very tiny particles are also seen in this cation concentration. The nanorods are revealed crossing each other forming a twin-like structure. On the surface of the nanorods, there are irregularly shaped and cauliflower-like structures. As shown in Figure 43c when the PbO film coated with 0.15 M concentration is annealed to 400 ^{o}C the mixture of nanorods and networked nanosheets-like structure is revealed. In this case, the cauliflower-like structure revealed in 0.1 M concentration is not observed rather the networked nanosheets and nanorods are found in aggregation. Thus, the XRD preferential growth orientation confirms the change in the shape of coated PbO thin film. For the 0.2 M concentration PbO film micrograph as shown in Figure 43d is covered by the domination of hexagonal nanorods with very few cauliflower structures. These nanorods are found in the agglomerated form which are tick together and interconnected. In this case, the rest of the film surface is covered with tinny distributed nanoparticles. The observed small pores and voids like on the surface of the films are the uncoated surfaces.

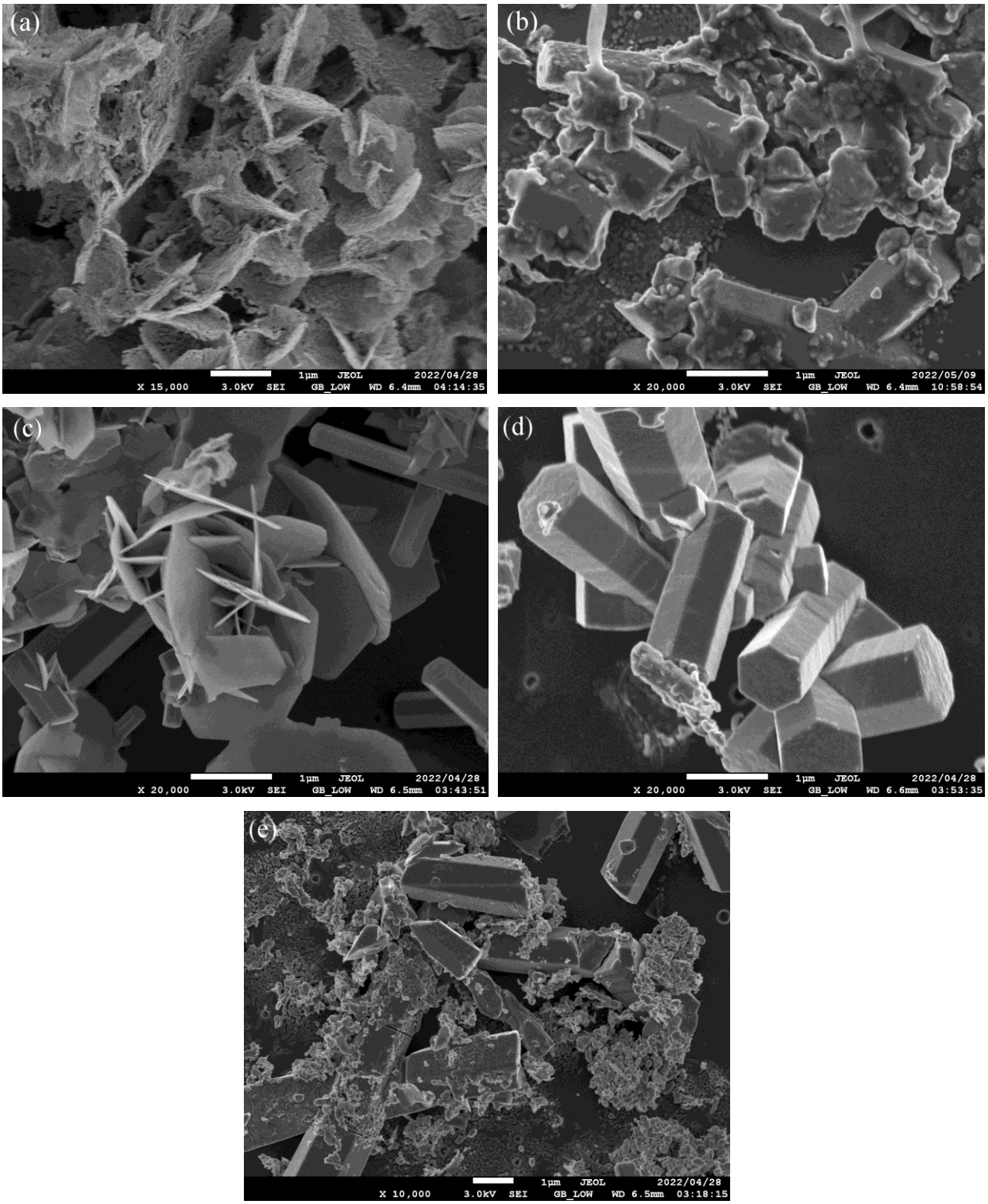

Figure 43: SEM images of (a) 0.15 M concentration as deposited, (b) 0.1 M, (c) 0.15 M, (d) 0.2 M, and (e) 0.25 M.

Moreover, the micrograph of 0.25 M concentration of PbO film shows nanorods and cauliflower like shape connected to the surface of the nanorods as presented in Figure 43e. It can be observed that the nanorods are fractured. Among the deposited PbO films this is the highest cation concentration which may cause particles fractures. As we have observed in the XRD results the 0.25 M has a high strain and dislocation density which result in structural changes. Thus, the SEM image of Figure 43e also confirms the particle fracture, which can be due to the volume change as cation concentrations increase. From the above discussion we can understand that after annealing the deposited PbO films, their shapes and structures were changed. Thus, temperature has influenced the as deposited $Pb(OH)_2$ film to have different shapes. As cation concentrations increased until 0.2 M the cauliflower-like structure property decreases. However, the nanorods are covering a large area of the substrate at 0.2 M concentration. In the highest 0.25 M concentrations, the nanorods exist in fractured with a very small size of cauliflower grains. In this case, the cauliflowers like grains are covering a large area of the substrate. As concentration increased the deposited particles get more agglomerated and finally the nanorods shape was broken at the highest molar concentration as shown in Figure 43e. Thus, the surface morphology of PbO thin film deteriorates with increasing molar concentration. At 0.15 M the morphology change is manifested specifically the cauliflower-like are almost not seen. Moreover, the nanorods with the smallest diameter compared to the 0.1 M cation concentrations with networked nanosheets-like morphology were seen. As the cation concentration of the precursor was increased to 0.2 M the nanorods shape was dominating and the film is deposited slightly. The SEM results revealed that altering the molar concentrations of lead acetate allowed for the synthesis of PbO nanomaterials with varied surface morphologies.

EDX is applied to know the elemental composition of the deposited PbO thin films at different molar concentrations. The existence of Pb and O is confirmed from the EDX spectrum representative of Figure 44 and Table 10. As it can be observed from the spectrum an impurity peaks are revealed. Specifically, the Si impurity is seen with a high atom percentage compared to other impurities in all samples which is from the composition of glass substrate used in depositing film. Table 10 lists the weight and atom percentages of PbO films deposited at 0.15 M concentration. The atom percentage of oxygen dominates in all molar concentrations, which results in the oxygen richness of the stoichiometry. Among all cation concentrations, the 0.15 M

has a high percentage which confirms the result from SEM as this concentration is the optimum concentration.

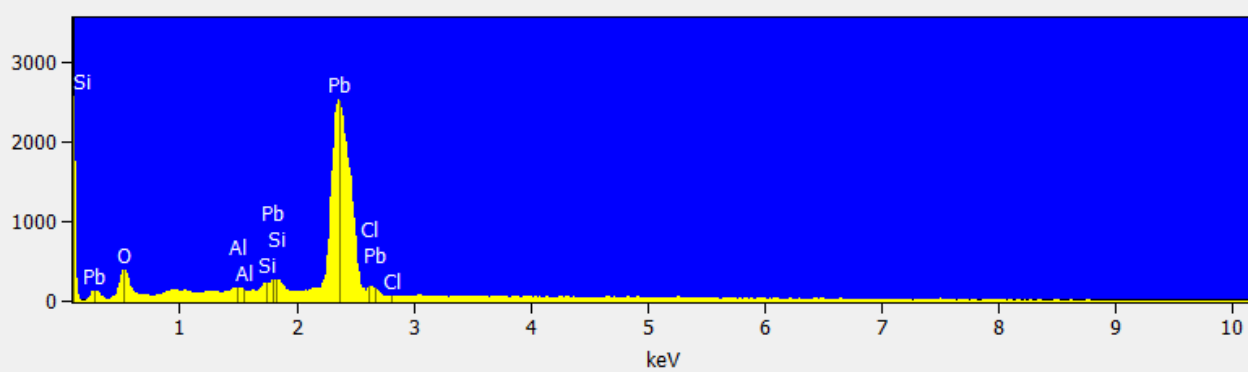

Figure 44: EDX spectrum representative of PbO thin film deposited at 0.15 M concentration.

Table 10: The elemental weight and atom percentages representative of PbO film deposited at 0.15 M.

Element Line	*Weight %*	*Weight % Error*	*Atom %*	*Atom % Error*
O K	9.18	± 0.31	53.89	± 1.82
Al K	0.57	± 0.06	1.98	± 0.20
Si K	0.65	± 0.07	2.16	± 0.22
Si L	---	---	---	---
Cl K	0.61	± 0.18	1.62	± 0.49
Cl L	---	---	---	---
Pb L	---	---	---	---
Pb M	89.00	± 0.92	40.35	± 0.42
Total	100.00		100.00	

In the next section 4.4 and 4.5, the computational DFT results for different metals doped β-PbO and α-PbO are presented. In these sections, in addition to structural, electrical, and optical properties, the photocatalytic activity of these materials is also analyzed based on the obtained results from the structural, band structures, optical, and effective masses.

4.4. DFT analysis of β-PbO

4.4.1. Structural study

The bulk β-PbO crystal structure is shown in Figure 45a. Before optimization, the cell geometry has the lattice parameters a = 5.89 Å, b = 5.49 Å, c = 4.75 Å, and bond angle parameters α = β = γ = 90° which is taken from American Mineralogist Crystal Structure Database (AMCSD) (Hill, 1985). This material has an orthorhombic structure with a *pbcm* space group. When it is extended in an a-axis direction, it will have the layered structure stacking with interlayer distances 4.21 Å and 5.11 Å for Pb-Pb and O-O respectively (Figure 45b). This phase is

characterized by its zigzag chains in which Pb^{2+} ions exist as pyramidally formed coordinates by O atoms. The zigzag chains are stacked by forming the layered structure as shown in Figure 45c. The total energy versus lattice parameters of pristine β-PbO is presented in Figure 45(d-f) for lattice parameters *a*, *b*, and *c*, respectively. From the equilibrium, the obtained lattice parameters were 6.07 Å, 5.64 Å, and 4.78 Å for *a*, *b*, and *c* correspondingly. The convergence for kinetic energy cutoff and k-points are presented in Figure 45g and Figure 45h, respectively. Also, the geometric lattice parameters of the fully optimized parameters are presented in Table 11. The obtained lattice parameters of β-PbO are slightly greater than the experimental values. The increase in the lattice parameter may be due to the displacement of atoms, which might cause significant lattice distortion. Comparing the lattice parameters of pristine and different metal-doped β-PbO, the *a* lattice parameter of all doped materials is decreased except Li-doped β-PbO which may also be related to the displacement of atoms due to the atomic radius. Thus, a smaller radius has smaller atomic movement which decreases the lattice parameters. The lattice parameters *b* increase for all doped materials except Sn-doped β-PbO, and lattice parameters *c* decrease for all doped materials compared to pristine β-PbO. The increase and decrease in lattice parameters may be due to the ionic radius of dopants (Muhammady et al., 2020). The dopant with a smaller ionic radius will have decreased lattice parameters comparing its ionic radius with the host atom (Pb^{2+}) (Kabbur et al., 2018). The ionic radius of O^{2-}, Pb^{2+}, Co^{2+}, Ni^{2+}, Cu^{2+}, Li^{+}, and Sn^{2+} are 0.135 nm, 0.119 nm, 0.072 nm, 0.078 nm, 0.073 nm, 0.060 nm, and 0.118 nm respectively. Hence, the ionic radii of dopants are less than the host ionic radius except for Li ionic radius. If the system gets distorted, it can cause the negative and positive centers of charges to get separated.

Table 11: Lattice parameters of fully optimized geometry of pristine and different metal doped β-PbO.

Parameters	Systems							
	β-PbO			Co:PbO	Ni:PbO	Cu:PbO	Li:PbO	Sn:PbO
	Present work	Other DFT[a]	Exp.[b]					
a (Å)	5.998	5.900	5.895	5.993	5.962	5.951	6.020	5.986
b (Å)	5.714	5.512	5.493	5.871	5.890	5.905	5.854	5.703
c (Å)	4.901	4.719	4.754	4.535	4.557	4.641	4.750	4.804

Note: Other DFT study and Experimental results [a], [b] taken from Ref. (Grimes et al., 2021)

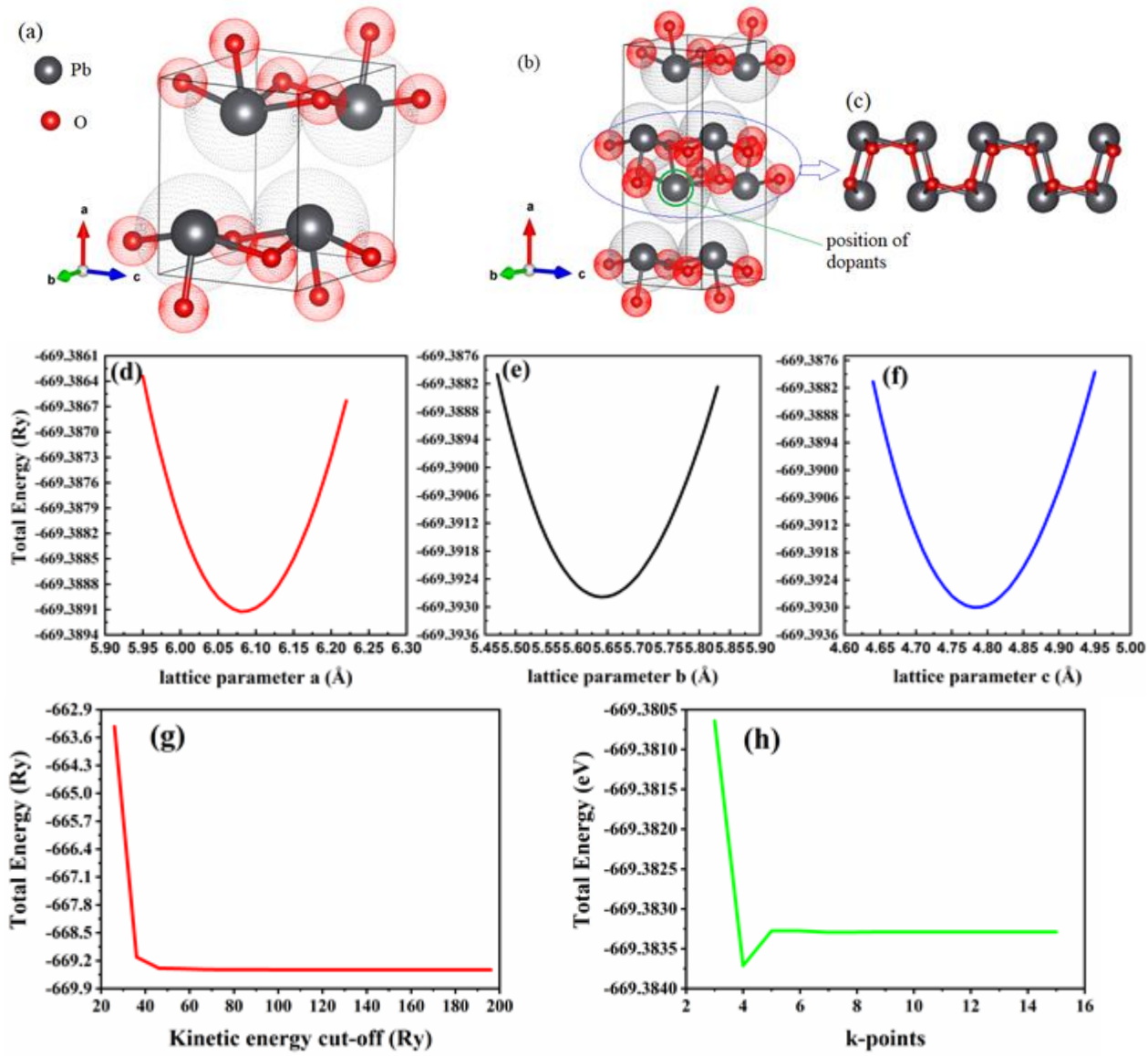

Figure 45: (a) Crystal structure of bulk β-PbO; (b) extended β-PbO in a-axis; (c) single monolayer of extended β-PbO; lattice parameters *a* (d), *b* (e) and *c* (f) versus total energy; (g) kinetic cut-off energy convergence and (h) k-points convergence.

As illustrated in Figure 46a, the Pb^{2+} is bonded to four equivalent O^{2-} atoms in a distorted rectangular geometry with one side Pb-O bond length represented by L1 and the other side bond length represented by L2. The bond geometry between Pb^{2+} and O^{2-} is in a distorted seesaw-like shape. Bond length and bond angles are given in Table 12. Distance between in layer and across the layer of Pb-Pb, Pb-dopants, O-dopants, and O-O are also given in Table 12, and its geometry representation is illustrated in Figure 46b. Comparing the bond length between Pb-O in doped and pristine β-PbO, the Pb-O bond length increased for doped β-PbO. This indicates that before

doping the electrons were tightly bound to the atom and it needs more energy to remove, whereas the increasing of bond length for doped β-PbO indicates the electrons need less energy to be removed. In addition to this, the atomic radius also affects the bond length between dopant and host atoms. Thus, each dopant and host atoms have a different radius in which the smaller the radius of the dopants may be increase in bond length.

Table 12: Bond length and bond angles of pristine and different metal doped β-PbO.

Systems	**Bond length (Å)**		**Distance between across or in layer atoms (Å)**		**Bond angles (°)**	
β-PbO	Pb-O (along L1)	2.329	Pb-Pb (in layer)	3.648	Pb-O-Pb	96.785
	Pb-O (along L2)	2.546	Pb-Pb (across layer)	4.345	O-Pb-O	77.578
			O-O (in layer)	3.058		
			O-O (across layer)	5.201		
Co:PbO	Pb-O (along L1)	2.458	Pb-Pb (in layer)	3.640	Co-O-Pb	107.839
	Co-O (along L2)	1.785	Co-Pb (in layer)	3.390	O-Co-O	88.534
	Co-O (along L1)	2.274	Co-Pb (across layer)	4.692	O-Pb-O	72.207
			O-O (in layer)	3.058		
			O-O (across layer)	5.201		
Ni:PbO	Pb-O (along L1)	2.387	Pb-Pb (in layer)	3.604	Ni-O-Pb	106.243
	Ni-O (along L2)	1.815	Ni-Pb (in layer)	3.379	O-Ni-O	87.965
	Ni-O (along L1)	2.285	Ni-Pb (across layer)	4.795	O-Pb-O	73.524
			O-O (in layer)	2.867		
			O-O (across layer)	5.437		
Cu:PbO	Pb-O (along L1)	2.3600	Pb-Pb (in layer)	3.5794	Cu-O-Pb	103.875
	Cu-O (along L2)	1.8583	Cu-Pb (in layer)	3.3797	O-Cu-O	87.879
	Cu-O (along L1)	2.3245	Cu-Pb (across layer)	4.8096	O-Pb-O	75.492
			O-O (in layer)	2.9217		
			O-O (across layer)	4.9747		
Li:PbO	Pb-O (along L1)	2.3220	Pb-Pb (in layer)	3.5970	Li-O-Pb	93.775
	Li-O (along L2)	2.0612	Li-Pb (in layer)	3.3315	O-Li-O	90.225
	Li-O (along L1)	2.3762	Li-Pb (across layer)	4.5441	O-Pb-O	81.859
			O-O (in layer)	3.1517		
			O-O (across layer)	5.0565		
Sn:PbO	Pb-O (along L1)	2.3454	Pb-Pb (in layer)	3.6156	Sn-O-Pb	99.133
	Sn-O (along L2)	2.1623	Sn-Pb (in layer)	3.5855	O-Sn-O	78.975
	Sn-O (along L1)	2.4734	Sn-Pb (across layer)	4.3421	O-Pb-O	74.444
			O-O (in layer)	2.9576		
			O-O (across layer)	2.9576		

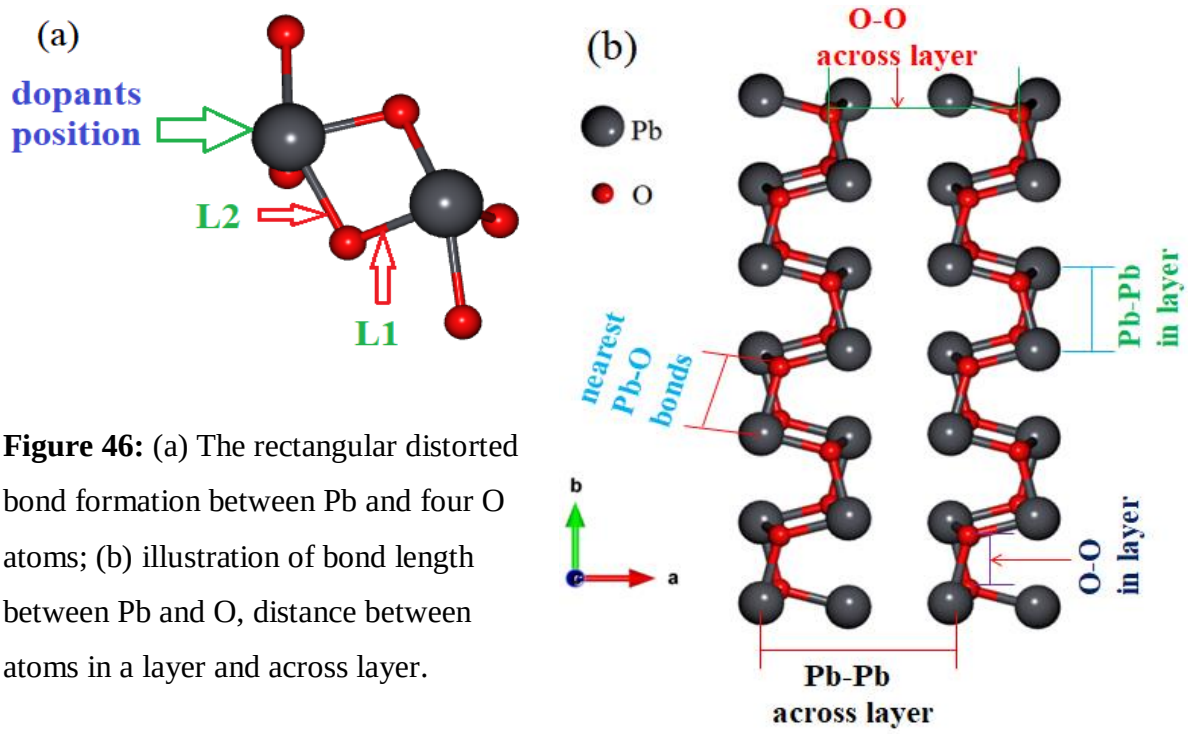

Figure 46: (a) The rectangular distorted bond formation between Pb and four O atoms; (b) illustration of bond length between Pb and O, distance between atoms in a layer and across layer.

4.4.2. Electronic properties

4.4.2.1. Band structure

In solid crystalline, the interaction between atoms produces electronic structures. The electronic band structure of pristine β-PbO and different metal doped β-PbO is presented in Figure 47. The path along the Γ—X—S—Y—Γ—Z—U—R—T—Z|X—U|Y—X|S—R in the irreducible Brillion zone were used for the band structures calculations. The spin-polarized calculation is applied, however, only spin-up band structures are plotted. For spin-down electronic properties, we can easily identify them in the plot of PDOS calculations. The band structure for pristine β-PbO is presented in Figure 47a. In this band structure, the valence band maximum (VBM) is found at X, Γ, and X|S points, while its conduction band minimum (CBM) is found between X|S and R points, which indicates that this material is an indirect bandgap material. The calculated bandgap for pristine and different metal doped β-PbO is presented in Table 13. For comparison of pristine β-PbO bandgap, the experimental and other DFT study results are also included in Table 13. The obtained energy bandgap for both spin up and spin down of pristine β-PbO is 2.28 eV which is underestimated compared to the experimental result due to the limitation of PBE functional for bandgap describing (Y Kurniawan, Sh Muhammady, 2018). However, it is found in the range of reported DFT calculations. For semiconductors, if the bandgap value is found in

the visible region it has a suitable application in different optoelectronic devices. Here, the obtained bandgap is found in the visible range with a wavelength of 544 nm.

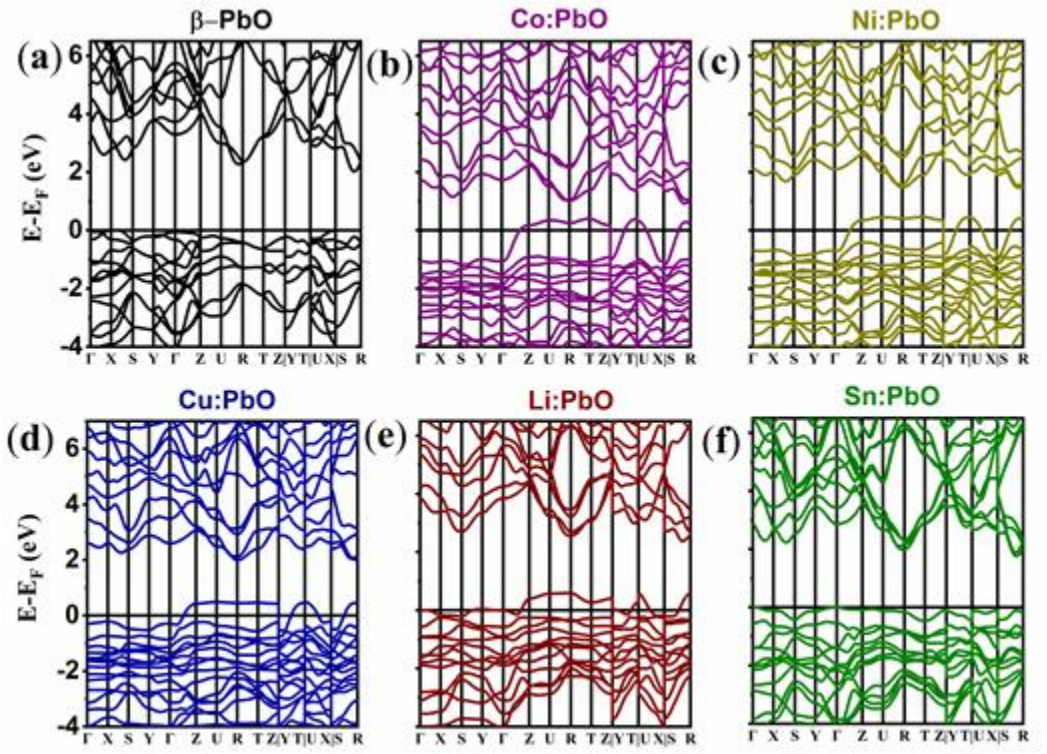

Figure 47: Electronic band structures of (a) pristine β-PbO, (b) Co doped, (c) Ni doped, (d) Cu doped, (e) Li doped and (f) Sn doped β-PbO.

For the doped materials, the dopant defect arises around the Fermi level and intersects the Fermi level. When the Fermi level is nearest to VBM, the material is called p-type conductivity, i.e., due to hole doping. However, when the Fermi level is nearest to CBM, it is n-type conductivity, i.e., because of electron doping. The Co-doped β-PbO band structure is presented in Figure 47b. Cobalt is a spin-polarized material, hence, the spin-up and spin-down band structures of Co-doped β-PbO is asymmetric. As it can be seen from the plot of spin-up the valence band is pushed up causing the bandgap to shrink. In this case, the Fermi level lies in the valence band which corroborates the p-type conductivity. The CBM is found at R point with 1.03 eV and the VBM is found at U point with 0.35 eV. Thus, the Co-doped system is an indirect bandgap like the pristine β-PbO, however, the CBM and VBM is found at different high symmetry points. Due to the effects of Co-doping, the bandgap value shrinks to 0.68 eV in spin-up and decreases more to 0.1 eV in spin-down states. In the case of Ni-doped, in the same manner, the spin-up and spin-down band structures are asymmetrical with different bandgap values. Figure 47c shows the

calculated spin-up electronic band structure of Ni-doped β-PbO. CBM is found at R point with 1.47 eV and VBM is found at T point with 0.46 eV. Thus, the band gap is reduced to 1.01 eV for spin up and 0.32 eV for spin down. In this case, the Fermi level lies inside the valence band state that emerged due to dopant defects, which indicates the p-type conductivity of Ni-doped β-PbO. Compared to the Co-doped system, the Ni-doped valence states are more nearest to the Fermi level relatively.

In the rest of the dopants cases, unlike Co and Ni doped systems the spin-up and spin-down band structures are not asymmetric due to their non-magnetic properties. Thus, the spin-up and spin-down band structures have the same Fermi level position and the same bandgap values. The spin-up electronic band structure of Cu-doped β-PbO is shown in Figure 47d. The position of CBM is at R point with 2.00 eV, and the position of VBM is at U and T|U points with 0.49 eV. Therefore, the energy band gap is reduced to 1.51 eV, i.e., the band gap shrinks by 0.51 eV compared to the pristine β-PbO. The Cu-doped β-PbO also confirms the p-type conductivity, and compared to Co and Ni-doped β-PbO the valence band states, which are found below the Fermi level are more nearest to the Fermi level. The lithium-doped β-PbO spin-up band structure is presented in Figure 47e. The defect states that emerged due to Li doping are found around the Fermi level, and the Fermi level lies inside these states leaving this system having p-type conductivity properties. Its CBM is found between X|S and R points with a minimum energy of 2.38 eV, and its VBM is found between U and R points with maximum energy of 0.59 eV by narrowing the band gap of pristine β-PbO to 1.79 eV, i.e., the band gap shrinks by only 0.49 eV which is small compared to other dopant effects. The valence band states found below the Fermi level are very nearest to the Fermi level relative to the aforementioned dopants. The spin-up band structure of Sn-doped β-PbO is illustrated in Figure 47f. In this case, the band structure has a similarity with the pristine β-PbO. Thus, like other dopants, there are no defect states above the Fermi level. Its CBM is found between X|S and R points whereas the VBM is the same as pristine β-PbO. For this system, the bandgap value is decreased to 1.76 eV. The bandgap calculated by using LDA functional is also given in Table 13. Compared to GGA functional, the calculated bandgap is underestimated. However, in the same manner as GGA results the spin up and spin down band gap values are equal for pristine, Cu, Li, and Sn doped β-PbO, whereas the Co-doped β-PbO and Ni-doped β-PbO have unequal values.

Generally, the doped band structures showed us the redshift effects on the pristine β-PbO. Thus, it shows the situation of narrowing the band gap of pristine β-PbO and increasing the visible light response, which is applicable as a photocatalyst under the irradiation of visible light. On the other hand, the induced impurity levels due to doping suppress the fast recombination of photogenerated electrons and holes, which improves photocatalytic activity. In addition to these, the indirect bandgap character of different metals doped β-PbO can reduce the recombination of photoinduced electrons and holes because the electrons that excited to the conduction band must travel some distances across the k-space before recombining with holes in the valence band (W. Yao et al., 2022).

Table 13: The calculated band gap of pristine and different metal doped β-PbO using PBE and LDA functional.

Systems		β-PbO			Co: β-PbO	Ni: β-PbO	Cu: β-PbO	Li: β-PbO	Sn: β-PbO
		This work	Other DFT	Exp.					
PBE: Band gap (eV)	Spin up	2.28	2.20[a] 1.97[b]	2.7[a]	0.68	1.01	1.57	1.79	1.76
	Spin down	2.28	----	----	0.1	0.32	1.57	1.79	1.76
LDA: Band gap (eV)	Spin up	1.95	----	----	0.81	0.89	1.51	1.72	1.66
	Spin down	1.95	----	----	0.36	0.39	1.51	1.72	1.66

Note: band gap values [a, b] are taken from Ref. (Liao et al., 2016) and (Grimes et al., 2021)

4.4.2.2. Density of states

The partial densities of states (PDOS) are with wider energy range than the band structure in the previous subsection. The PDOS of pristine and different metal doped β-PbO are presented in Figure 48. The total density of states (TDOS) is also included in the plot. The PDOS of each system has two separated valence band states and one conduction band state. Thus, the two valence band states are the deep valence band states and shallow valence band states. The PDOS of pristine β-PbO is shown in Figure 48a. The deep level of the valence band state of pristine β-PbO is due to the major contribution of Pb 6s orbital hybridized with a small contribution of O 2p orbital, which indicate that the Pb-O bond shows partially covalent bond behavior (Muhammady et al., 2020). In this level, the two highest peaks at -7.14 eV and -6.41 eV for both spin up and spin down are revealed from the TDOS, which indicates the localized states. The

antibonding interaction between Pb 6s and O 2p orbital is weak at this level. If the antibonding interaction between states is strong the VBM raises to a higher level causing the vacancy states to exist slightly above the VBM, which improves the transition of carriers and enhances the photocatalytic performance. The shallow level of the valence band mainly originated from the O 2p orbital with the small contribution of the Pb 6p orbital. In the pristine β-PbO, the major contribution of O 2p orbital indicates the fully occupied states of O 2p, which can be observed from the electron valence configuration of $2s^2$ $2p^6$ O positions. This level shows two highest peaks located at -1.40 eV and -0.28 eV which can be observed from TDOS peak. The conduction band near to E_F is dominated by Pb 6p orbital which shows that the unoccupied states of Pb 6p orbital. This result shows that 2+ is the oxidation states of Pb ions. The symmetric behavior of PDOS and TDOS indicates the non-magnetic properties of this system. The highest three peaks in pristine β-PbO are located at 3.23 eV, 6.16 eV, and 7.58 eV. The major contribution of O 2p orbital in the shallow level of the valence band and the major contribution of Pb 6p orbital in the conduction band indicates that only Pb 6p and O $2p^4$ are found around the bandgap edges which shows that their significant role to form an ionic bond.

Figure 48b shows the PDOS and TDOS of Co-doped β-PbO. The deep level of the valence band shows the highest peaks at -8.76 eV and -7.90 with originating from Pb 6s orbital hybridized with a small contribution of O 2p orbital. In this deep level, there is no contribution of any Co orbitals, which shows the same property as the pristine deep-level valence band. However, in the shallow level of the valence band, the major contribution of the hybridizing of Co 3d orbital and O 2p orbital is observed. From the TDOS, the shallow valence band shows four peaks at -5.79 eV, -5.03 eV, -3.47 eV, -2.10 eV, and -1.49 eV for the spin-up states and -5.42 eV, -4.17 eV, -3.53 eV, -2.45 eV and -1.88 for spin down states, which indicates the contribution of the ferromagnetic properties of Co dopant. The TDOS peak nearest to the Fermi level is related to a Van Hove singularity (Y Kurniawan, Sh Muhammady, 2018). In the spin-up of the shallow valence band, the Fermi level lies in the valence band states with small peaks, and the van Hove Singularity is located at 0.24 eV. Thus, the dopant pushes the valence band to the conduction band compared to the pristine β-PbO, which improves the photocatalytic activity of β-PbO. The conduction band of Co-doped β-PbO shows the highest peaks at 1.85 eV, 2.48 eV, and 5.59 eV for spin up state and at -0.58 eV, -0.10 eV, 0.69 eV, 2.56 eV, and 5.69 eV for spin down states, which also corroborates the magnetic property of this material. The spin-down conduction band

is found in the negative energy position below the Fermi level. If the conduction band is overlapped with E_F it indicates the partially occupied states of the conduction band states of the element. That is the dopant receives electrons from the host system and reduces the recombination of photogenerated charge carriers for photocatalysis applications.

The PDOS and TDOS of Ni-doped β-PbO is presented in Figure 48c. Like Co-doped, Ni-doped β-PbO also shows ferromagnetic properties due to the highest ferromagnetic property of Ni. The deep valence band shows the peaks located at -8.38 eV and -7.48 eV, which is a blue shift compared to pristine β-PbO. In this valence band state, the contribution of Ni orbitals is not seen in which the Pb 6s orbital dominates hybridizing with a minor contribution of O 2p orbitals. Furthermore, the shallow valence band consists of the contribution of Ni 3d orbital hybrid with O 2p orbital, and also a small contribution Pb 6p orbital hybridized with O 2p states is revealed. The shallow level valence band shows peaks at -5.27 eV, -4.55 eV, -1.14 eV, and 0.36 eV in the spin-up states and at -5.08 eV, -4.05eV, -3.13 eV, -2.18 eV, -1.52 eV, -0.83 eV, 0.045 eV and 1.1 eV for spin down states. The peaks at 0.36 eV of spin up and 1.1 eV of spin down state show the van Hove singularity point, which is mainly originated from the hybridization of Ni 3d and O 2p orbitals. The conduction band is originated from Pb 6p orbital, which indicates unoccupied states. The conduction band shows peaks at 2.28 eV, 2.95 eV, and 6.59 eV for spin-up states and at 2.34 eV, 2.97 eV, and 6.68 eV for spin-down states. Unlike Co and Ni doped β-PbO the Cu, Li, and Sn doped materials shows symmetrical for spin-up and spin-down states. Thus, they have no contribution to host material to have magnetic properties as it was expected. The PDOS and TDOS of Cu-doped β-PbO is shown in Figure 48d. The deep valence states are mainly composed of Pb 6s hybridizing with O 2p orbital, which shows two peaks at -7.76 eV and -6.94 eV. The Cu states did not contribute for the deep valence states. The shallow valence states are mainly originated from the hybridization of O 2p and Cu 3d orbitals with less contribution of Pb 6p orbital. The shallow valence states showed the symmetrical shape of PDOS and TDOS indicating the non-magnetic properties of this dopant. In the same manner, the conduction band showed a symmetrical shape of PDOS and TDOS located at 2.68 eV and 6.94 eV.

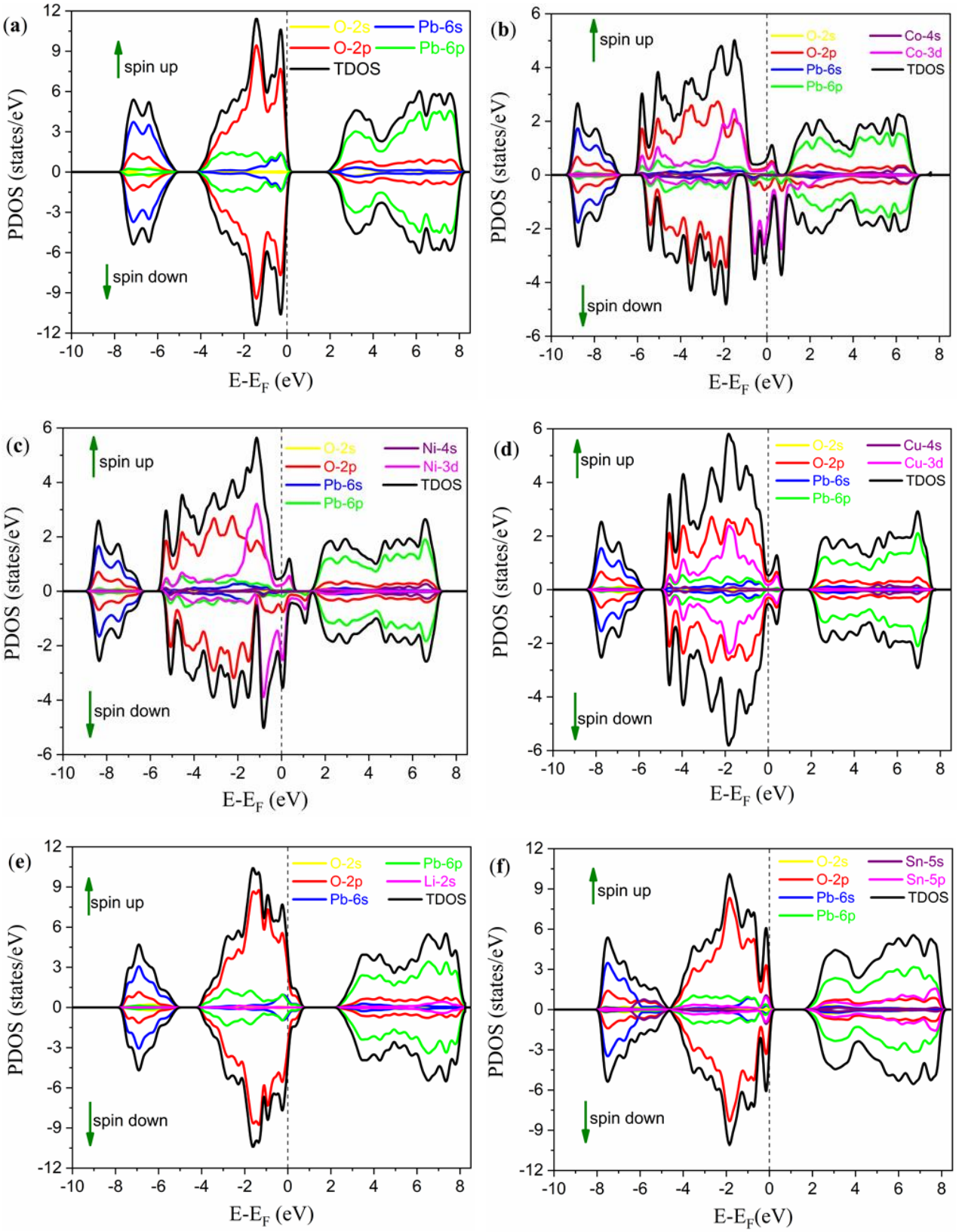

Figure 48: PDOS of (a) pristine β-PbO, (b) Co:β-PbO (c) Ni:β-PbO (d) Cu: β-PbO (e) Li:β-PbO and (f) Sn:β-PbO.

The PDOS and TDOS plot of Li-doped β-PbO is presented in Figure 48e. In this case, the deep valence band state shows only a single peak at -6.91 eV, which is mainly, composed of the hybridization of Pb 6s and O 2p orbitals. The shallow valence state is dominated by O 2p by hybridizing with Pb 6p orbital showing peaks at -1.60 eV, -0.93 eV, and -0.25 eV which can be seen from TDOS peaks. The contribution of Li 2s is not clearly seen in shallow valence states, however, its contribution is observed in the conduction band with a very small contribution. The Fermi level lies inside the valence band near to VBM and its VBM is found above the Fermi level in which the Li defect pushes the VBM towards the conduction and shrinks the band gap which enhances the photocatalytic performance of β-PbO.

Figure 48f shows the PDOS and TDOS of Sn-doped β-PbO. The deep valence band state shows a single highest peak at -7.50 eV with a major contribution of Pb 6s hybridized with O 2p orbital. In this case, the deep valence state is extended due to the contribution from Sn 5s orbital. The shallow valence states show peaks at -1.85 eV, -0.99 eV, and -0.15 eV. The O 2p orbital dominates the shallow valence band with the hybridization of Pb 6p and Sn 5p orbitals. The conduction band is originated from the major contribution of Pb 6p with less contribution of Sn 5p orbital, which indicates that the Sn dopant also contributes for the existence of unoccupied states. The conduction band states show three highest peaks at 3.09 eV, 6.70 eV, and 7.51 eV which can be seen from TDOS. It can be concluded that compared to the pristine β-PbO, the TDOS and PDOS of Co, Ni, and Cu doped β-PbO have a lower density of states (DOS), which indicates that the electronic state becomes more delocalized due to the decrease in peak magnitude of DOS. Thus, the charge carriers can reach the reactive sites for the process of photocatalytic activity. The newly emerged DOS peak corresponds to a defect state due to dopants which can trap the photogenerated electrons and holes and reduce the fast recombination of electrons and holes, thereby improving the photocatalytic performance. The DOS peak of pristine β-PbO is greater than all doped systems, which is attributed to the localized electronic states, thus it might have low photocatalytic performance compared to doped materials. In Li and Sn doped the peak is decreased relative to the pristine β-PbO. However, they have greater peaks than Co, Ni, and Cu dopants. Thus, in the doped β-PbO the electronic state becomes more delocalized than Li and Sn doped β-PbO.

4.4.3. Optical properties

In this section, the optical properties of pristine β-PbO and the effects of different metal doping are analyzed. For optical property analysis, the momentum matrix element and Kramers-Kronig-relation to get imaginary and real parts of dielectric functions, respectively is used (W. Jia et al., 2019). The real and imaginary parts of dielectric function are given by Equation 53 and 54, respectively. To investigate the optical properties, we have calculated the dielectric function having three components $\varepsilon_{xx}(E)$, $\varepsilon_{yy}(E)$, and $\varepsilon_{zz}(E)$. For all optical calculations, we have taken the average of these three components. Since our calculation is including spin-polarized calculations, for pristine and different metal doped β-PbO both spin-up and spin-down state data were added up (total spectra) to get a single optical plot for each system. The peaks observed in the optical spectra were determined based on the transition from occupied to unoccupied in the band structure, particularly at high symmetry points in the BZ. The oscillatory trend corroborates the existence of many-body interactions.

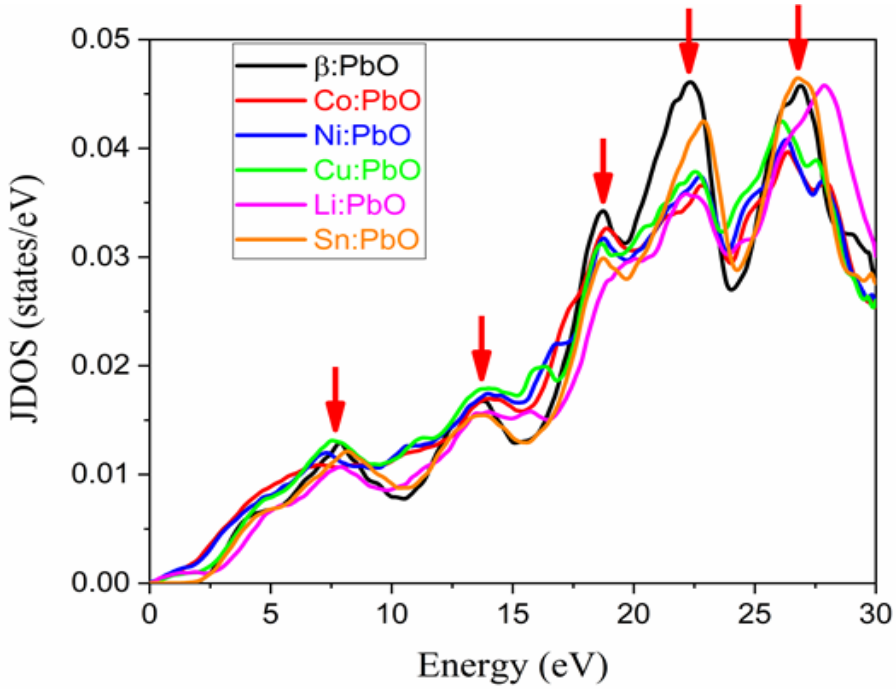

Figure 49: The joint density of states (JDOS) of pristine, Co, Ni, Cu, Li and Sn doped β-PbO.

The joint density of states (JDOS) of pristine and different metal doped β-PbO is presented in Figure 49. The calculated JDOS tells us the number of states available for the photon energy to interact with either for absorption or emission processes of photons. The pristine β-PbO and different metal doped β-PbO have five defined peaks. These peaks are found in the photon

energy classification ranges 6-9 eV, 12-14 eV, 18-19 eV, 20-23 eV, and 25-30 eV. At the photon energy below around 2 eV, the pristine and Sn-doped β-PbO has no states available to interact with photons. However, other dopants have available states in this region, which indicates that there are possible transitions. In the first range of 6-9 eV, the peaks of Co, Ni, Cu, and Li doped shift to the lowest energy, whereas the Sn-doped shifts to the highest energy. This may be due to the different band gap values of each doped materials, and also compared to other doped, Sn doped has similar band structure properties with the pristine as shown in previous sections. In the second range of photon energy 12-14 eV, except for pristine and Sn-doped β-PbO, other doped have broad peaks. In the third range, all systems have narrowed and well-defined peaks except Li-doped have broad peaks. In the fourth range, 20-23 eV, the sharp with the highest JDOS peak for pristine β-PbO is presented. In this region, the doped systems shift to the highest energy with Sn having the highest JDOS relatively. In the fifth range, 25-30 eV, each doped system has got highest JDOS than all other regions with all shifts to the lowest energy except Li-doped β-PbO. This may be due to the increase of photon energy increases the existence of states that interact with photons. These peaks are narrow and sharp. The existence of many peaks indicates the availability of many states for photon interaction. For pristine β-PbO, the defined peaks are only found in the aforementioned ranges of energy. However, the doped systems have additional peaks in the unlisted ranges of photon energy, which is due to the defect states of dopants.

The real part of the dielectric function determines the amount of stored energy in the medium. It also describes the dispersive conduct of materials. The polarization effects and dynamical screening can also be described by the real part of the dielectric function (Edossa & Woldemariam, 2020). The real part of the dielectric function as a function of photon energy in the range between 0-28 eV is shown in Figure 50a. The real part attains its' maxima 11.48, 11.18, 9.23, 7.99, 6.79, and 5.59 for pristine, Sn, Co, Cu, Ni, and Li doped β-PbO systems at photon energy 2.30 eV, 2.25 eV, 1.15 eV, 2.15 eV, 0.55 eV, and 2.45 eV respectively. They attained their minima -1.34, -1.13 -1.12, -0.51, -0.82, and -0.76 for pristine, Sn, Co, Cu, Ni, and Li doped β-PbO at photon energy 8.11 eV, 8.36 eV, 6.06 eV, 7.36 eV, 5.81 eV and 5.91 eV for each system respectively. The decreasing of the real part of the dielectric function is attributed to the reduction of dispersion and booting of the amount of transmittance (Ramaswamy et al., 2019).

The imaginary part of the dielectric function determines the amount of dissipated energy in the medium. Thus, it determines the characteristics of materials absorption, i.e., it describes the absorptive conduct of materials. In simple words, it illustrates the optical photon absorption for the charge excitation from occupied states to empty states (W. Jia et al., 2019; Pakizeh et al., 2019). Figure 50b illustrates the imaginary part of dielectric function as a function of photon energy. The maximum absorption peaks are 10.15, 9.57, 8.45, 7.93, 7.38 and 7.11 at photon energy 3.56 eV, 3.66 eV, 3.56 eV, 3.56 eV, 3.91 eV and 3.16 eV for pristine, Sn, Co, Ni, Cu and Li doped β-PbO respectively. The dominant peaks at each photon energy values originated from either transition between O 2p states valence band or excitation from occupied O 2p state at VBM to the unoccupied Pb 6p states at CBM (Bakhtatou & Ersan, 2019). The greater values of the imaginary part are the poorer insulating properties of materials indicating the higher the conductivity of electricity. Among the dopants Sn and Cu doped shows shifts to higher photon energy absorption, whereas the Li-doped shows the lowest photon energy absorption. In addition to main peak in Ni and Cu doped materials there are emerged peaks at 1 eV and 0.75 eV respectively. In the highest energy for all system the broad with small imaginary dielectric are emerged, which is attributed to enhanced insulation of materials due to the disappearance of sharp peaks. Except for pristine β-PbO and Sn-doped β-PbO, at 0 eV (static) for other doped materials, the imaginary dielectric function is not zero. Thus, Co, Ni, Cu and Li doped β-PbO system conducts electricity at zero photon energy and can act as absorptive conduct.

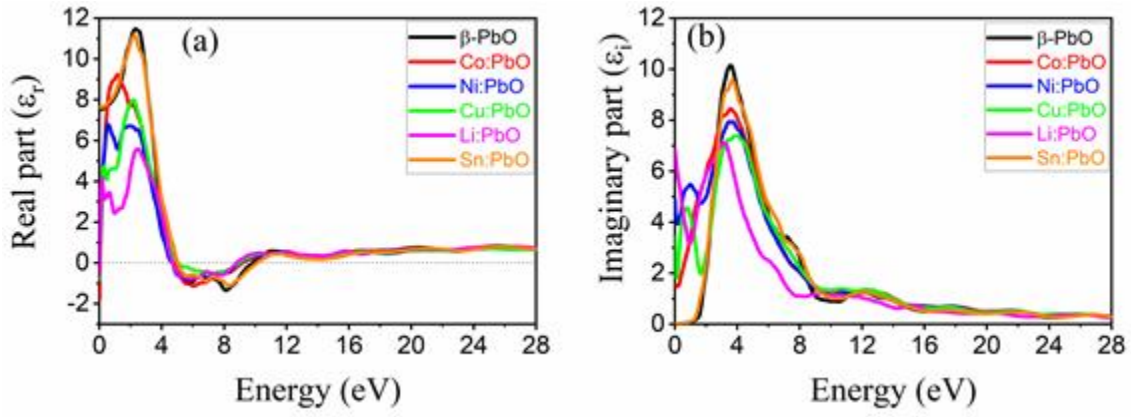

Figure 50: (a) Real and (b) imaginary parts dielectric function against photon energy.

Other optical properties such as refractive index (n), extinction coefficient (k), absorption coefficient (α), reflectivity (R), electron energy loss spectrum (L), and optical conductivity (σ) are calculated according to Equations 56 to 61, respectively. The refractive index as a function of

photon energy is presented in Figure 51a. The refractive index is found in the range of 0.56 to 3.48. The highest refractive index for pristine, Sn, Co, Cu Ni, and Li doped β-PbO were 3.48, 3.40, 3.11, 2.89, 2.77, 2.78, and 2.65 at 2.60 eV, 2.25 eV, 1.20 eV, 2.20 eV, 2.50 eV, and 0.15 eV photon energy respectively. Doping the material with different metal shifts the position of the highest refractive index to lower photon energy. The refractive indices are found in the range of visible regions. The larger refractive indices in the visible region make the materials suitable for photovoltaic applications, because the larger the refractive index means the retarded photon radiations in the medium, hence, to transverse the medium photon radiations takes a long time which results in a great possibility to interact with electrons leading to electron excitations (Nwanya et al., 2013). The static magnitude of the refractive index was 2.74, 2.76, 0.52, 1.16, 1.53, and 2.38 for pristine β-PbO, Sn, Co, Cu Ni, and Li-doped β-PbO, respectively. The obtained results revealed that as photon energy increases the magnitude of refractive index decreases. The extinction coefficient provides information about absorption at the band edges. The graph of the extinction coefficient as a function of photon energy is illustrated in Figure 51b. The extinction coefficient was found in the range of 0 to 1.91. The pristine β-PbO and Sn-doped β-PbO have zero extinction coefficients at zero photon energy and attained their maximum extinction coefficient 1.91 and 1.88 at 4.71 eV and 4.91 eV correspondingly. However, the other doped materials do not have zero extinction coefficients at zero photon energy. Thus, the Co^{2+}, Cu^{2+}, Ni^{2+}, and Li^{+} doped β-PbO attained their maximum extinction coefficient at 4.36 eV, 4.61 eV, 4.46 eV, and 3.51 eV, respectively. Except for the Sn-doped is shifted to the highest photon energy, all other doped systems are shifted to lower photon energy.

Figure 51c shows the optical reflectivity graph as a function of photon energy. The static values of reflectivity of pristine, Co^{2+}, Ni^{2+}, Cu^{2+}, Li^{+}, and Sn^{2+} doped β-PbO are 0.21, 0.14, 0.24, 0.12, 0.30, and 0.22, respectively. The reflectivity of these systems increased to its maximum at 8.31 eV, 5.41 eV, 4.91 eV, 4.61 eV, 3.61 eV, and 5.06 eV correspondingly. The pristine β-PbO and Sn-doped have two maximum peaks of reflectivity relative to other doped materials. This is due to the similar and highest values of refractive indices of the pristine and Sn-doped β-PbO as mentioned above (Holmes et al., 1998). Thus, pristine β-PbO and Sn-doped may have small transmittance compared to other doped materials. In other doped materials, the reflectivity decreases. In all materials, the reflectivity decreases as photon energy increases more. Due to the

reflectance peaks shifts in each doped material either to the highest or lowest photon energy the existence of dopant effects can be easily understood.

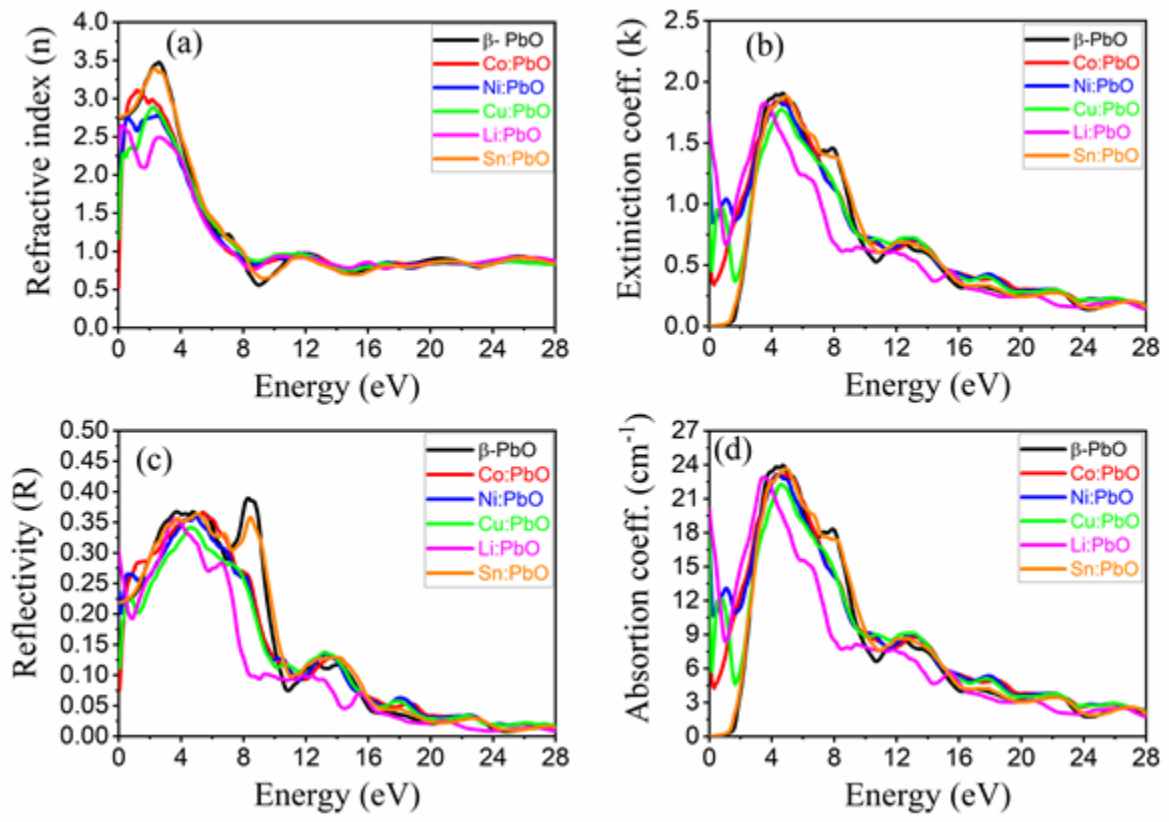

Figure 51: (a) Refractive index, (b) extinction coefficient, (c) reflectivity and (d) absorption coefficient as a function of photon energy.

The absorption coefficient describes the light intensity attenuation of the materials during the light travels some distances in a medium. The absorption coefficient as a function of the photon energy of pristine β-PbO and different metal doped is presented in Figure 51d. Compared to the undoped β-PbO except for Sn-doped materials; the other doped materials possessed a non-zero absorption coefficient at zero photon energy. The maximum absorption coefficient of pristine β-PbO and different metal doped is attained at different photon energy. The position where the degree of weak attenuation is observed, the systems have a high photon absorption effect. The materials with high optical absorption coefficients can be used in optoelectronics due to their sufficient optical absorbing properties. After attaining their maximum absorption coefficients in all systems the absorption coefficient decreases with increasing photon energy.

Energy loss electron spectrum (EELS) describes the energy loss of electrons propagating (fast-moving electrons) through the materials. When materials interact with photons, the electron cannot be simply sat at their lattice site; hence they start to perform the motion. The EELS against photon energy of pristine and doped β-PbO is shown in Figure 52a. The observed peaks in the EELS are the representation of Plasmon energy (Ghazanfar et al., 2021). The maximum peaks are the place where the fast-moving electron loses more energy. Figure 52b shows the optical conductivity against the photon energy of pristine and different metal doped β-PbO. Initially, the optical conductivity of Sn, Li, Cu, and Ni-doped β-PbO increases starting from zero and attained their maximum at 3.36 eV, 4.56 eV, 4.31 eV, and 4.31 eV respectively according to their optical conductivity increasing order. However, pristine and Co-doped β-PbO optical conductivity starts from 1.25 eV and attained the maximum optical conductivity at 3.66 eV and 3.81 eV, respectively. The doped systems have greater optical conductivity than the pristine β-PbO. Among all doped systems, the Co-doped system has the greatest optical conductivity, whereas the Sn-doped system has the lowest optical conductivity. After the maximum optical conductivity, all system obtains decreasing in their optical conductivity while photon energy increases.

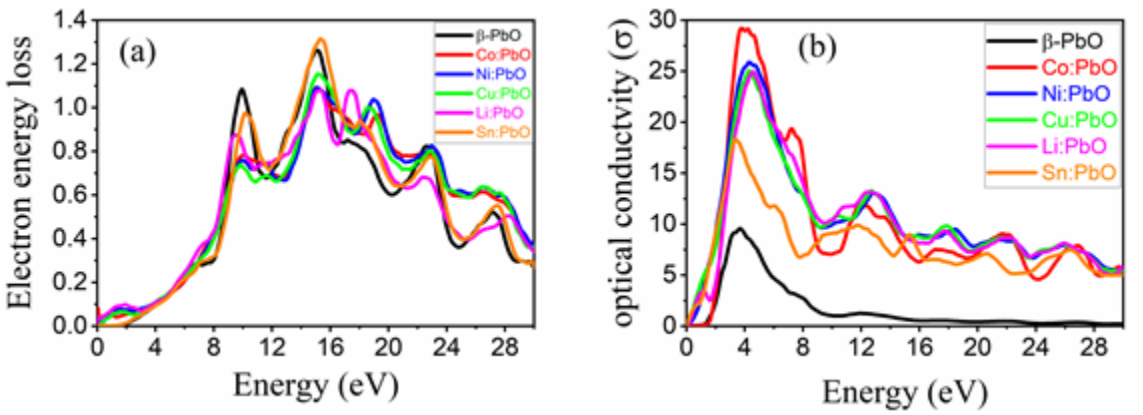

Figure 52: (a) The electron energy loss spectrum and (b) the optical conductivity of pristine, Co, Ni, Cu, Li and Sn doped β-PbO.

4.4.4. Effective mass of electrons and holes

It is clear that the carrier's effective mass can describe the ability of electrons and holes transfer along special directions. Migration and separation of charge carriers significantly influence the quantum efficiency of photocatalytic reactions. For the photocatalytic reactions

to take place the charge carriers must reach the active sites of photocatalyst surfaces. The transfer rate and mobility of photogenerated electrons and holes are determined by their effective masses (Opoku et al., 2017c). In determining the photocatalytic performance of materials, electrons' effective mass (m_e^*) and holes' effective mass (m_h^*) play a great role. If the photogenerated charge carriers possess lighter effective mass the carriers will reach the sites of surface reaction within their lifetime, thus enhancing the photocatalytic performance. In principle, the electron and hole effective masses are determined by the curvatures of the bottom of the conduction band and the top of the valence band, respectively.

Computationally the effective masses of electrons and holes can be calculated by fitting the parabolic functions to the conduction band minimum and valence band maximum of pristine and different metals doped α-PbO according to Eq. (81) (Opoku et al., 2017d):

$$m^* = \pm \frac{\hbar^2}{d^2E/dk^2} \tag{82}$$

where, m^* is the carriers' effective mass and d^2E/dk^2 is the second order term the curvature of band structures, $\pm$ denotes: $(-)$for holes in the valence band and $(+)$for electrons in the conduction band.

If the conduction band minimum is quite dispersive compared to the valence band maximum, the photoinduced electron will possess a lighter effective mass and can reach surface reaction sites within its lifetime, then it becomes a good photocatalyst material (Opoku et al., 2017a). A larger effective mass shows a low probability of charge carriers reaching the surface reaction sites, thereby decreasing the photocatalytic activity. The electron and hole effective masses of pristine and different metal doped β-PbO are summarized in Table 14. The larger hole effective masses of pristine β-PbO and Sn doped β-PbO shows that the diffusion rate of photogenerated holes is low, hence reducing the photocatalytic performance compared to other doped materials. However, Sn-doped β-PbO possesses lower electron effective mass than pristine β-PbO, which indicates faster electrons transfer to reach the surface reaction site than pristine β-PbO. Thus, the mobility of photogenerated electrons is enhanced in Sn-doped β-PbO. The largest effective masses of electrons and holes of pristine β-PbO indicate that the diffusion rate of photogenerated electrons and hole is low, which accounts for its low photocatalytic performance. The large difference between electron and hole effective masses (m_h^*/m_e^*) indicates significant variations in the mobility of charge carriers which suppresses the recombination rates

of electron-hole pairs. Because of the large difference between effective masses of electrons and holes in Sn doped β-PbO compared to pristine β-PbO, there may be good charge carriers separation and the recombination rate decreases, hence the photocatalytic performance is enhanced. Ni-doped β-PbO possesses a large difference between effective masses of electrons and holes, thereby it will have the highest photocatalytic performance compared to pristine β-PbO and other doped materials. The effective mass of electrons decreases after doping as one can see from Table 14. In the effective masses of holes, all doped materials decrease except Sn doped β-PbO is increased. Moreover, the difference in effective masses of all doped materials is larger than that of pristine β-PbO which shows that enhances of photocatalytic performance.

Table 14: Effective masses of electrons and holes of pristine and metals doped β-PbO.

Materials	m_h^*/m_o	m_e^*/m_o	m_h^*/m_e^*
pristine β-PbO	-2.25	1.18	1.91
Co-doped β-PbO	-2.10	1.01	2.08
Cu-doped β-PbO	-1.87	0.93	2.06
Ni-doped β-PbO	-2.16	0.79	2.74
Li-doped β-PbO	-1.85	0.86	2.16
Sn-doped β-PbO	-2.90	1.13	2.58

4.5. DFT analysis of α-PbO

4.5.1. Structural properties

Figure 53a, shows the crystal structure of pure bulk α-PbO. It has a tetragonal structure and belongs to the P4/nmm, 129 space groups in which oxygen atoms are bonded in between the two Pb atoms forming a layered structure. On the other hand, when four oxygen atoms are bonded to a single Pb atom it forms a pyramidal shape. When it is extended in the b and c-axes direction it will have the layered structure stacking with interlayer distances 2.313 Å, 3.974 Å and 2.811 Å for O-Pb, Pb-Pb, and O-O respectively (Figure 53b). This phase is characterized by its zigzag chains in which Pb^{2+} ions existed as pyramidally formed coordinates by O atoms. The zigzag chains are stacked by forming the layered structure as shown in Figure 53c. In this layered structure, the oxygen atoms are sandwiched between lead atoms in a monolayer. Before optimization, the cell geometry has the lattice parameters $a = b = 3.974$ Å, $c = 5.022$ Å and bond angle parameters $\alpha = \beta = \gamma = 90°$ which is taken from American Mineralogist Crystal Structure

Database (AMCSD) (Hill, 1985). The lead atoms are in placed (0, 0.5, 0.7756) and (0.5, 0, 0.2244), whereas the oxygen atoms are in positions (0, 0, 0) and (0.5, 0.5, 0). All of the pseudopotentials employed in this study are to perform structural relaxation for geometry optimizations.

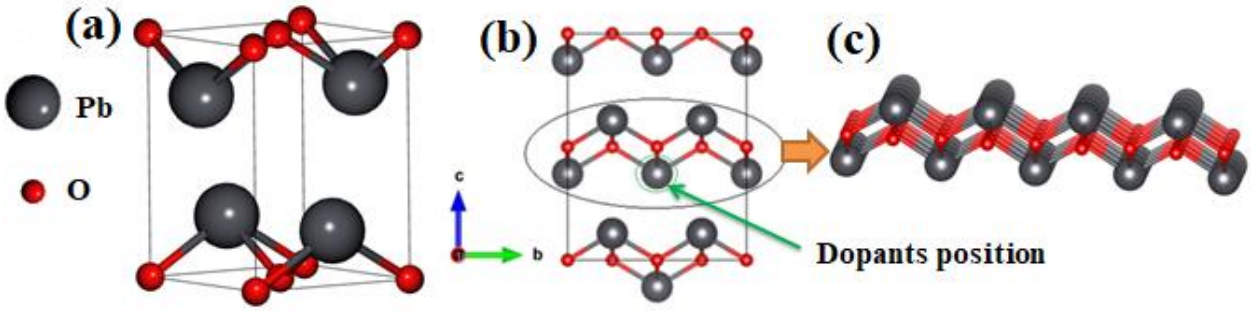

Figure 53: (a) Crystal structure of bulk α-PbO (tetragonal), (b) in b and c axes extended α-PbO and (c) single monolayer structure of α-PbO.

Table 15: Comparison between vc-relaxed with different pseudopotentials, other DFT studies and experimental values.

Parameters	Types of pseudopotentials				Other DFT study	Exp.
	PZ-USPP	PBEsol-PAW	PBE-PAW	PBE-USPP	GBRV-USPP	
Lattice constant *a* (Å)	3.958	3.997	3.997	4.07	3.989	3.972
Lattice constant *c* (Å)	4.713	5.22	4.952	5.52	5.028	5.023
Bang gap (eV)	1.08	1.16	1.30	1.75	1.16	1.9

After optimizations, the lead atom's positions were modified to (0, 0.5, 0.7842) and (0.5, 0, 0.2158), whereas oxygen atoms remained in their original places (0, 0, 0) and (0.5, 0.5, 0) while employing GGA of PBE within USPP. Since the values of the lattice constants were altered during the calculation of vc-relax, the unit cell volume varied. In the case of PBE-USPP, a modest increase in lattice constants is seen after vc-relaxation calculations. However, this value agrees with the experimental value with just minor differences. Table 15 compares estimated lattice constants $a = b$ and lattice constant c for different pseudopotentials to other DFT studies and experimental data. The result determined by utilizing PBEsol agrees well with experimental and other computational studies (Grimes et al., 2021). Furthermore, Figure 54a and Figure 54b show the total energy of pure α-PbO materials as a function of the lattice constants a and c, respectively. As indicated in Figure 54a, the minimum energy was obtained at a = 3.997 Å,

whereas the minimum energy was reached at 5.33 Å for lattice constant *c* as shown in Figure 54b. In this scenario, the lattice constant *c* was held constant while the value of the lattice constant *a* was varied until minimal energy was found. By altering lattice constant *c*, the value of the equilibrium lattice constant *a* was kept constant. The computed lattice constants closely match the experimental value with very minor deviations.

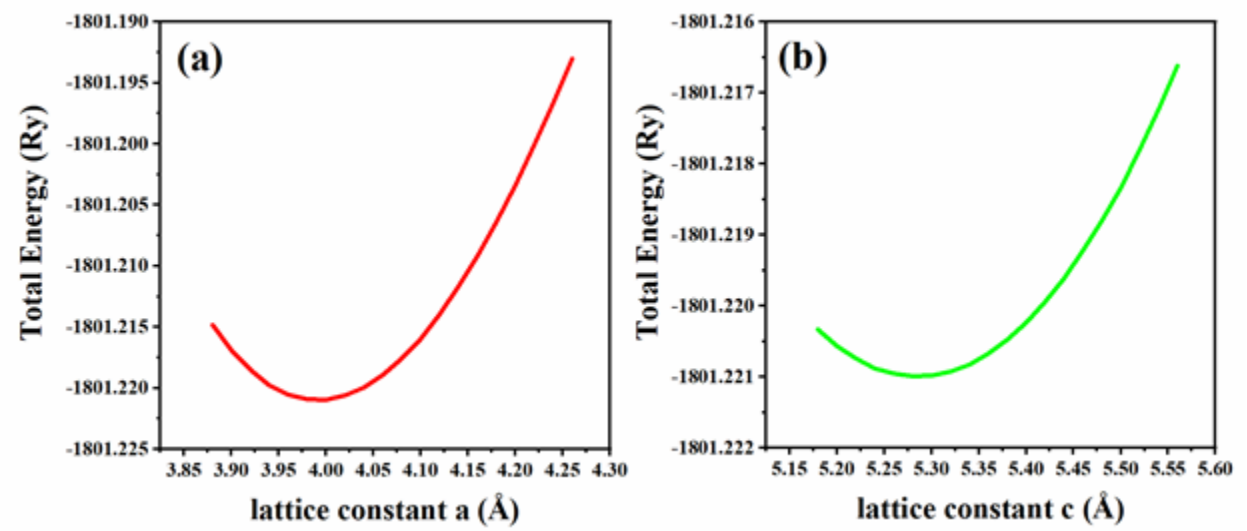

Figure 54: (a) Total energy versus lattice constant *a* and (b) Total energy versus lattice constant *c* by using PBEsol.

Table 16: Bond length and bond angles of pristine and different metal doped α-PbO.

Systems	Bond length (Å)		Bond angles (°)	
	Pb-O	2.359		
α-PbO	Pb-Pb	4.072		
	O-O	2.879	O-Pb-O	75.221
Co:PbO	Co-O	2.039	O-Co-O	81.380
Ni:PbO	Ni-O	2.072	O-Ni-O	80.265
Cu:PbO	Cu-O	2.157	Cu-O-Pb	80.175
Li:PbO	Li-O	2.137	Li-O-Pb	83.327
Sn:PbO	Sn-O	2.2694	Sn-O-Pb	76.065

As illustrated in Figure 55a, the Pb^{2+} is bonded to two equivalent O^{2-} atoms in a squared geometry. Bond length and bond angles are given in Table 16. Distance between in layer of Pb-Pb, O-dopant, and O-O are also given in Table 16, and its geometry representation is illustrated in Figure 55b. The distance across the layer or between the two layers was 5.022 Å. Comparing the bond length between Pb-O in doped and pristine α-PbO, the bond length decreased for doped α-PbO. This indicates that before doping the electrons were tightly bound to the atom and it

needs more energy to be removed, whereas the decreasing bond length for doped α-PbO indicates the electrons need less energy to be removed. In addition to this, the atomic radius also affects the bond length between dopant and host atoms. Thus, each dopant and host atom possesses a different radius in which the smaller the radius of the dopants may be increase in bond length. The structure of α-PbO deformed when dopant atoms were inserted into the host structure. This may also cause lattice distortion which can result in the centers of positive and negative charge separations.

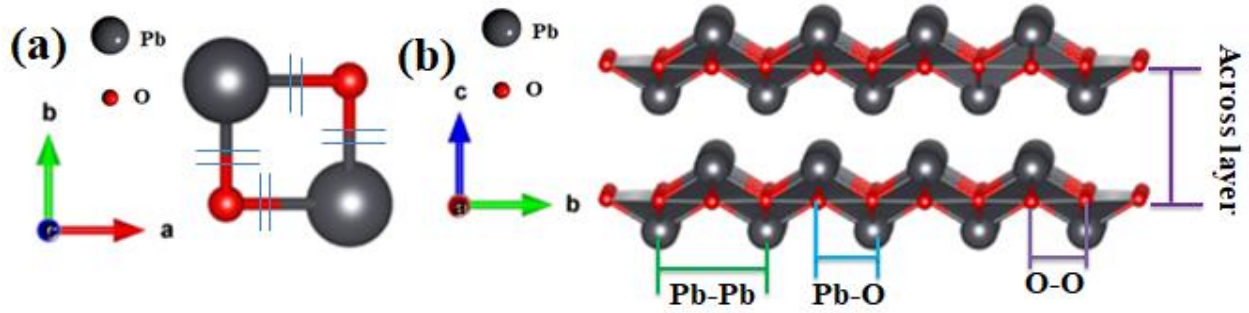

Figure 55: (a) The squared bond formation between Pb and O atoms; (b) illustration of bond length between Pb and O, distance between atoms in a layer and across layer.

Table 17: Lattice constant of pure and metals doped α-PbO.

Materials	Lattice constants (Å)		
	a	*b*	*c*
Pristine α-PbO	4.071	4.071	5.507
Sn:α-PbO	3.955	3.955	5.300
Ni:α-PbO	3.778	3.778	4.245
Cu:α-PbO	3.929	3.929	4.268
Li:α-PbO	4.017	4.017	3.411
Co:α-PbO	3.759	3.759	3.951

Table 17 shows the changes in lattice constants caused by doping different metals into α-PbO. These changes in lattice constants produce volume changes, which result in structural alterations in α-PbO. The lattice constant *a* changes slightly during doping. However, there is a significant change in the lattice constant *c* when Li and Co are doped. As a result, structural characteristics may alter dramatically, and deformation will occur in the α-PbO structure. In general, other dopants have little effect on structural properties. Because of the atomic size and electronegativity of the dopants, the bond lengths surrounding the dopants varied, resulting in

structural property changes (Tanko et al., 2021). This change in structural characteristics may enhance the system's structural stability.

4.5.2. Band structure and Density of states of bulk α-PbO

Figure 56-59 illustrates the electrical band structure and PDOS plot of pristine α-PbO using different pseudopotentials. It is critical to investigate the electronic structure of α-PbO for applications in optoelectronics and photocatalysis technology. For the electrical properties of pure α-PbO, we used several exchange correlations and pseudopotential types. The left Figure 56a-59a shows the calculated band structures by using different pseudopotentials. For bandgap estimation, the GGA of PBEsol exchange functional with PAW potential, GGA of PBE exchange functional with USPP and PAW potential, and LDA of PZ exchange functional with USPP potentials are used and compared with the experimental results as shown in Table 15. The α-PbO material can recognize to be an ionic bonding material. This ionic bonding can be explained by PDOS as shown on the right side in Figure 56b-59b. The orbital 2p of O and 6p of Pb are different above the Fermi level. PDOS has a bonding and anti-bonding character. According to the PDOS, the VBM is largely made of O 2p orbitals with minor contributions of Pb 6s and 6p orbitals. The CBM is mostly made of Pb 6p orbitals with very few contributions of Pb 6s and O 2p. Thus, based on the PDOS calculations in Figure 56b-59b, Pb of 6p dominated the states above the Fermi level, while O 2p dominated the states below the Fermi level. Electrons can be excited from O 2p orbital that is a fully occupied state to the empty state Pb 6p orbital when energy beyond the band gap is irradiated to the materials. The deep level is majorly made up of Pb 6s.

Different information can be extracted from the electrical band structures of pure α-PbO. The presence of a narrow band gap demonstrates that this is an oxide semiconductor. The valence band maximum (VBM) and conduction band minimum (CBM) are located at different high symmetry sites, confirming that this material is an indirect bandgap semiconductor that can suppress the rapid recombination of photogenerated electrons and holes for photocatalytic improvement. Thus, the indirect band gap enhances the transit time of charge carriers from VB to CB, thus increasing the separation lifetime of charges or reducing the recombination rate of photogenerated charge carriers (Singh & Sharma, 2018). The CBM is located at M-point and the VBM is found at Γ-point in the Brillouin zones (BZ), as can be seen in Figure 59a. Except for the

amount of the energy bandgap, the VBM and CBM positions are unchanged for all applied pseudopotentials. The reported experimental energy bandgap value of bulk α-PbO is 1.9 eV, while we calculated 1.08 eV, 1.16 eV, 1.30 eV, and 1.75 eV using LDA, PBEsol with PAW, PBE with PAW, and PBE with USPP potentials, respectively. Ryan T. Grimes (Grimes et al., 2021) employed the GBRV-type ultrasoft pseudopotentials to calculate the bandgap of bulk α-PbO and obtained the same 1.16 eV that we did from the PBEsol in Table 15. In this case, we used different exchange-correlation and pseudopotentials to get the optimum bandgap approximation. Among all of the results, the band gap obtained by GGA of PBE with USPP potential is quite close to the experimental value. As a result, we used the GGA of PBE with USPP type throughout the doping, and the findings obtained by utilizing GGA of PBE with USPP for pristine α-PbO are used as a reference to observe the dopant effects. In the plot of band structure and PDOS, the highest occupied energy level (Fermi energy, E_f) position has shown at zero values of energy $E-E_f$.

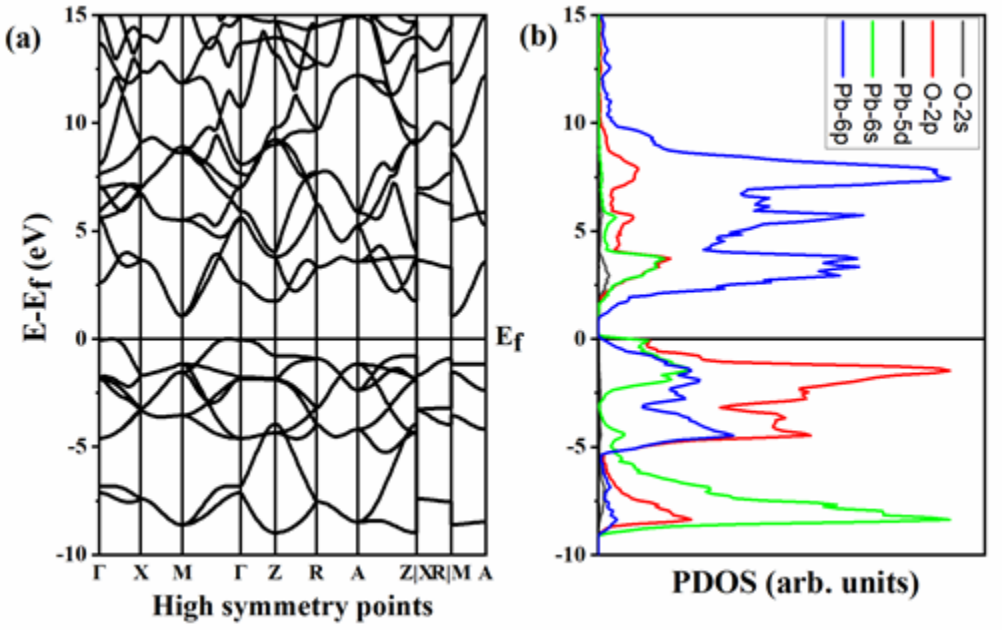

Figure 56: (a) Electronic Band structure diagram of bulk α-PbO and (b) PDOS of bulk α-PbO calculations by using LDA exchange correlation.

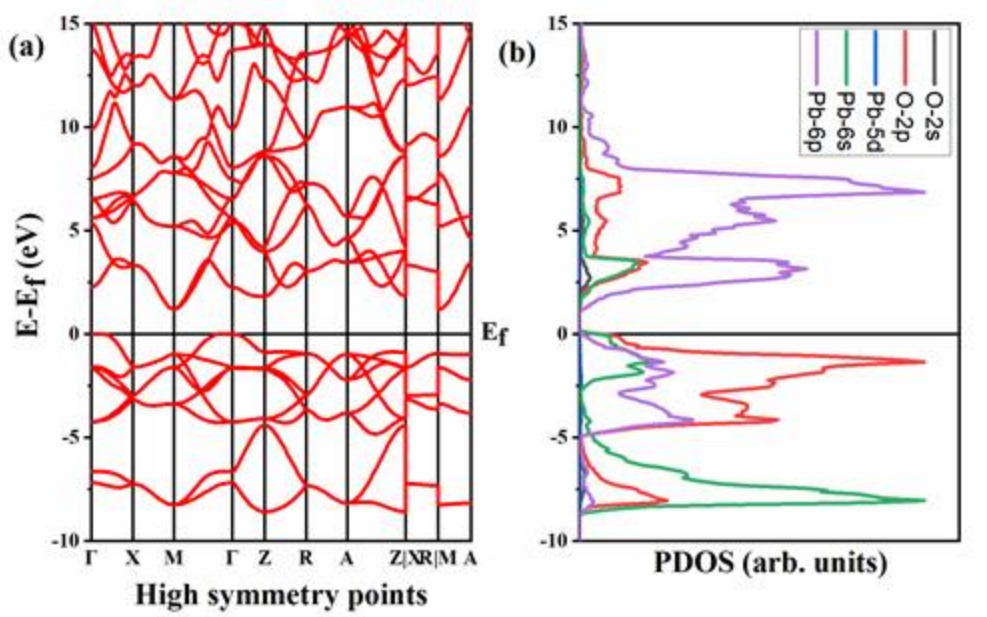

Figure 57: (a) Electronic Band structure diagram of bulk α-PbO and (b) PDOS of bulk α-PbO calculations by using PBEsol exchange correlation with PAW potential.

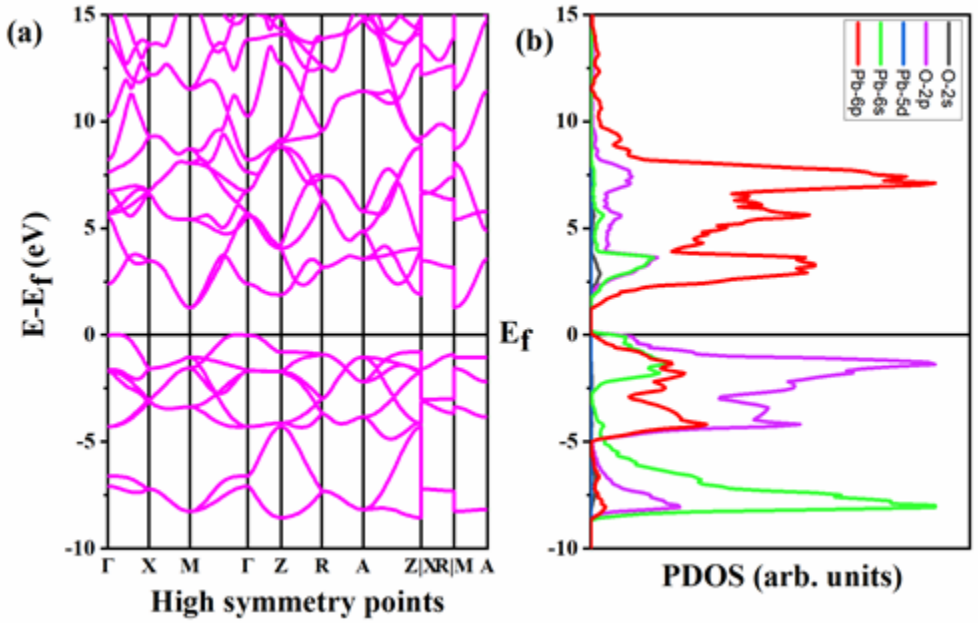

Figure 58: (a) Electronic Band structure diagram of bulk α-PbO and (b) PDOS of bulk α-PbO calculations by using PBE exchange correlation with PAW potential.

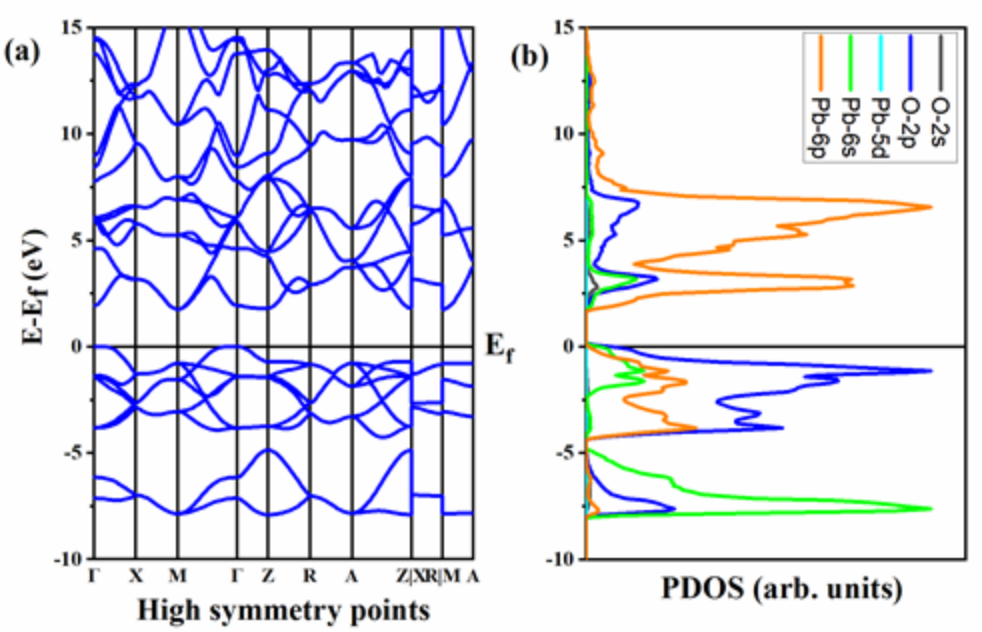

Figure 59: (a) Electronic Band structure diagram of bulk α-PbO and (b) PDOS of bulk α-PbO calculations by using PBE exchange correlation with USPP potential.

4.5.3. Effects of dopants on band structure and PDOS of α-PbO

It is important to explore the band structure and density of states of α-PbO to develop applications in electronics technology. The effect of several metals on the electronic properties of α-PbO has been investigated in this section. We employed the same k-point mesh for the Brillion zone sample and the same kinetic energy cut-off plane wave in doped α-PbO after the calculations of optimization and convergence. The PBE exchange functional with USPP pseudopotential is used throughout all doping. The energy band gap in different metal-doped α-PbO is narrowing compared to pristine α-PbO due to alteration of valence and conduction bands or insertion of impurity energy levels. The variation in the energy bandgap due to dopant is given in Table 18. The plots of energy band structure and PDOS show that either the valence and conduction bands have modified or an impurity energy level inserted. The appearance of the impurity energy level is cause by dopant state hybridization with O and Pb states. In transition metal doping, we employed dopants with 2+ oxidation states, and for convenience, we just performed spin-polarized calculations for magnetic dopants to include their spin-polarizing effects.

Table 18: Variation in energy band gap of α-PbO due to different metal doping using PBE functional

Materials	α-PbO	Sn:α-PbO	Ni:α-PbO	Cu:α-PbO	Li:α-PbO	Co:α-PbO
Band gap (eV)	1.75	1.53	1.36	1.30	1.57	1.14

4.5.3.1. Sn doped α-PbO

Group III, IV, and V periodic table of elements include both metal and nonmetal elements. In this research, we have used metals to incorporate into the pristine α-PbO. When these metals are doped into pristine α-PbO, the structural, electrical, and optical properties of α-PbO are changed. Due to their advantages in improving the properties of intrinsic and oxide semiconductors, these groups of metals have been used as dopants in different semiconductors. In this research, we took one element from each group to incorporate into the pristine α-PbO that may help to incorporate the rest metals into α-PbO.

Tin (Sn) is a fourth group element that is employed as a covering material due to its low cost. When it is doped with metal oxides, it improves electron transport and extraction, which is useful in solar cells and photocatalysis. Sn has four and two oxidation numbers. In our case, Sn^{2+} is introduced into the host α-PbO for the benefit of charge balancing, which avoids the formation of further impurity states. Figure 60a, depicts the electronic band structure of Sn-doped α-PbO. Compared to pristine α-PbO, the location of VBM and CBM does not change, resulting in an indirect band gap which may reduce the fast recombination rate of photogenerated charge carriers and enhance the photocatalytic activity. Sn doping in α-PbO causes impurity energy levels in both the valence and conduction bands resulting in the reduction of the energy band gap from 1.75 eV for pure α-PbO to 1.53 eV. The induced impurity level in both valence and conduction bands can trap the photogenerated holes and electrons. As a result, the recombination rates of charge carriers can be suppressed, thereby enhancing photocatalytic performance. The band gap narrowing due to the insertion of the impurity states of the dopants made the materials to be active under the irradiation of visible light. As seen in Figure 60, the Fermi level appears above the VBM in this instance, and electrons in the valence band can jump to the conduction band with low energy demand as compared to pristine α-PbO. The reduction of band gap during doping may lead to redshifts in optical properties. Moreover, the contribution of the Sn doped can also be observed from the PDOS shown in Figure 60b. The Sn 5p partial density of state contributes to the conduction band in addition to Pb 6p, while the Sn 5s and Pb 6s dominate the

deep level of the valence band. The shallow level of the valence band is majorly dominated by O 2p partial density of state with some contribution of Sn 5s. The existence of Sn 5p states near Fermi energy in CBM confirms the incorporation of Sn into the pure α-PbO, and electrons can transit from O 2p and Sn 5s to the empty states Pb 6p and Sn 5p.

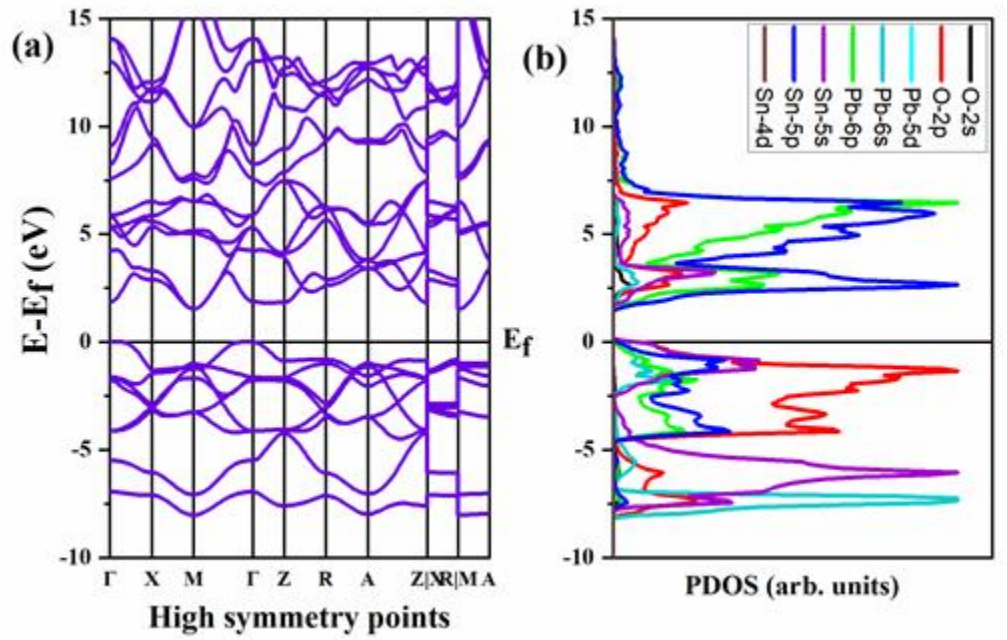

Figure 60: (a) Electronic Band structure diagram and (b) PDOS of Sn doped α-PbO.

4.5.3.2. Li doped α-PbO

Alkali metals are found in group IA of the periodic table, and they are very reactive species that can easily lose their single outermost valence electrons to form ionic compounds. Thus, they can easily react with the nonmetal elements. The catalytic properties of materials can be improved when they are used as dopants. In addition to this, the structural, electrical, and optical properties of metal oxide can be improved when they are incorporated into them. From this group, we incorporated Li metal into PbO and investigated its effects on the properties of the host material.

Lithium (Li) is one of the least electronegative alkali metals, and when added to α-PbO, it increases the electron transport properties of α-PbO. When Li is doped into α-PbO, it changes both the valence and conduction bands which results in changing the electrical and optical properties of the pure α-PbO. Figure 61a, depicts the electronic band structure of Li-doped α-PbO. As seen in the band structure of Li-doped α-PbO, an indirect band gap similar to pristine α-PbO was produced. However, when compared to pristine α-PbO, the VBM and CBM are

generated at distinct sites. VBM appears at the M-point, whereas CBM appears at the Z-point. In this case, the obtained band gap is 1.57 eV, which shows small decreases compared to the other doped system. An additional set of conduction bands is revealed, which may act as charge carriers trapping, thus enhancing the photocatalytic performance. Figure 61b depicts the contribution of the Li orbitals to the density of states. By mixing with Pb 6p orbital, the contribution of Li 2s is significantly detected in the conduction band which confirms the Pb site substitution. The Li 2s states found in the valence band near the Fermi energy shows its relation with O 2p states. The shallow valence band level is pushed up due to the Li 2s orbital, which contributes to the band gap narrowing.

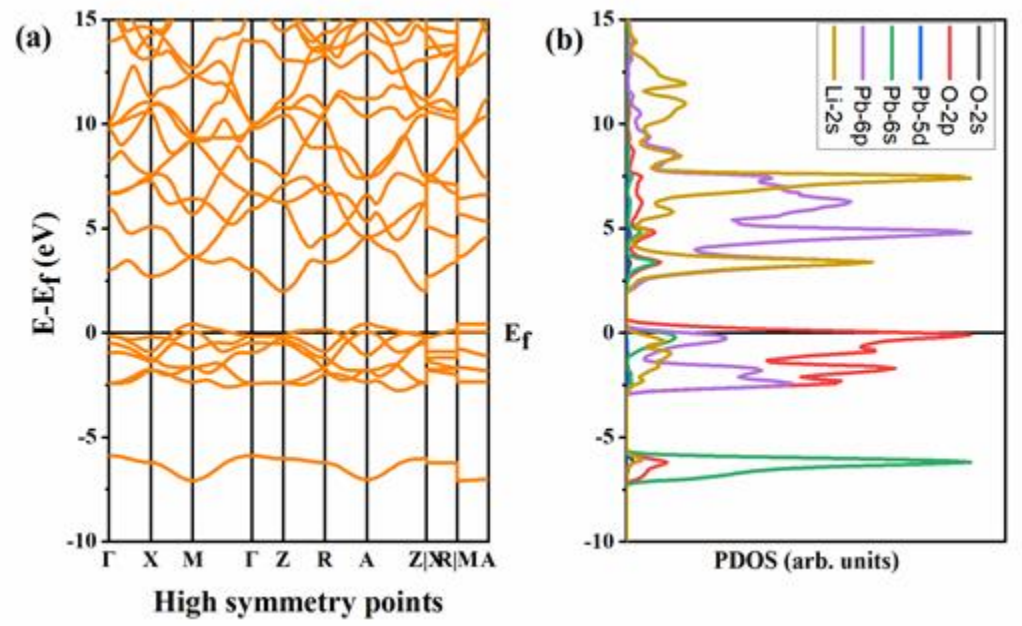

Figure 61: (a) Electronic Band structure diagram and (b) PDOS of Li doped α-PbO.

4.5.3.3. Ni doped α-PbO

For the investigation of the electronic structure of transition metal doped α-PbO we have performed the spin polarized calculations in order to include the influence of spin polarizing of these dopants on the electronic properties of α-PbO. Transition metals have good electron transporting characteristics, and when doped into metal oxides it improves the electronic properties of metal oxides. These elements have various valences and are partially or fully filled d orbitals, which can be classified as 3d, 4d, and 5d transition metals. Especially, in their oxide forms they have potential technological applications in solar cells, photoelectrochemistry, energy conversion devices, and photocatalysis due to their low-cost production and relatively abundant.

(Wenqing Li et al., 2013). Nickel (Ni), cobalt (Co), and Copper (Cu) are chosen among the transition metals to examine their effects when integrated into α-PbO. In order to investigate the influence of these dopants on the electronic properties, we have performed spin-polarized calculations for pristine α-PbO as a reference. Figure 62a and Figure 62b shows the electronic band structure diagram and PDOS of spin-polarized pristine α-PbO. Compared to the non-polarized calculation due to its non-magnetic properties its electronic structure is almost the same. The energy band gap value and contributions of orbital states also show the same properties as the non-polarized calculations.

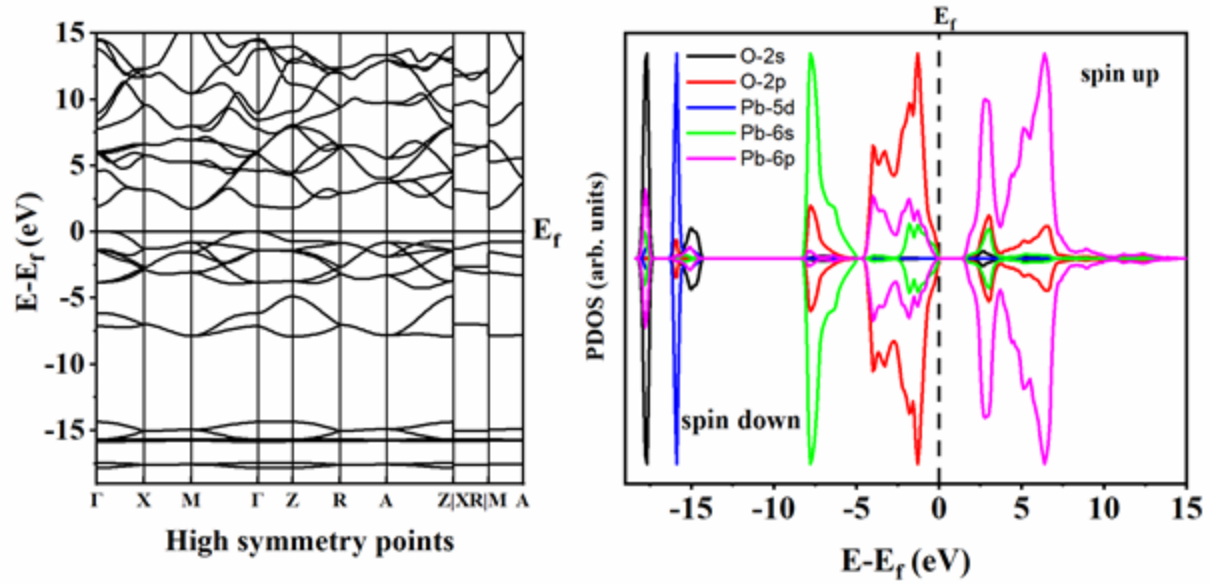

Figure 62: (a) Electronic Band structure diagram and (b) PDOS of spin polarized pristine α-PbO.

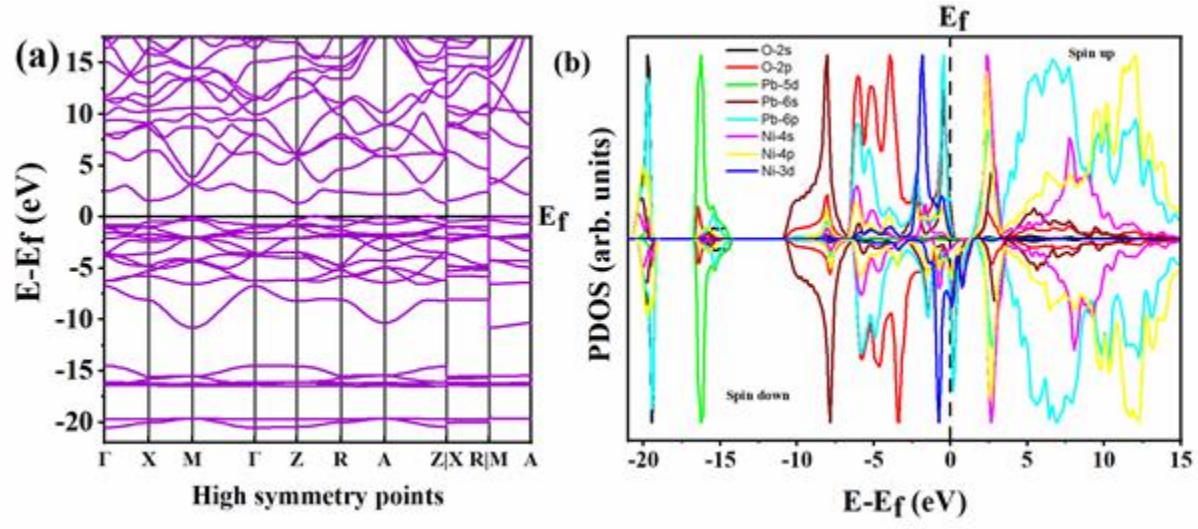

Figure 63: (a) Electronic Band structure diagram and (b) PDOS of Ni doped α-PbO.

Transition metals have noticeably high heat and electrical conductivity qualities. As a result of its incorporation into α-PbO, it improves the electrical and optical characteristics of α-PbO. Because several of these transition metals have multivalent, only the analogous chemical state with host substitution is used to avoid extra contaminants during charge balancing. A basic optimization of scf calculation was performed to determine their magnetic moment in order to estimate the oxidation state used. We can simply predict their oxidation states if we know their magnetic moment. In this case, the electronic configurations valence of Ni^{2+} is $3d^8$. As a result, Ni with a 2+ oxidation number was employed in doping into α-PbO. In the case of Ni-doped α-PbO, the valence and conduction bands are modified, as well as an impurity energy level formed in the midst of the VBM and CBM with contact with CBM and separated from the VBM by a gap, as shown in Figure 63a. As a result, there is no gap between the impurity energy level and the conduction band; instead, the impurity energy level produces a band gap with valence bands, resulting in a 1.36 eV band gap value. In actuality, this is a narrow band gap for electron excitation from the valence band to the conduction band, which requires little energy to leap to the conduction band. The PDOS in Figure 63b depicts the contributions of the Ni orbitals to the density of states. In the same conditions as other d-block doped α-PbO, the orbital Ni 3d states contribute more to the density of states below the Fermi level, whereas the orbital Ni 4p states contribute more to the density of states above the Fermi level. Compared to the undoped α-PbO the Ni-doped PDOS revealed many densities of states near to the Fermi level besides of the valence bands. The states found near to Fermi level are Ni 3d, Pb 6p, O 2p, and less density of Ni 4p states. The formation of Ni 3d states in this region shows the chemical reaction relations of Ni 3d with O 2p states (Ni-O). Generally, the existence of impurity states at conduction and valence band is used as charge carriers trapping, which results in reducing the rate of charge carriers' recombination. Including the indirect band gap narrowing the charge carriers trapping of impurity states due to Ni doping enhances the photocatalytic activity of α-PbO.

4.5.3.4. Co doped α-PbO

According to the pseudopotentials utilized, Co has an electronic configurations valence of 3d7. As a result, cobalt with a 2+ oxidation number was employed in doping to α-PbO. The valence band in Co^{2+} doped α-PbO has been modified by the introduction of impurity energy levels, and an extra impurity energy level has appeared between the VBM and CBM, as shown in Figure 64a. The upper impurity energy level that makes contact with the minimum of the conduction

band and forms a minimum on the Z-point, and the impurity level for valence band modification by overlapping with the lowest impurity level forms a maximum for valence band at A-point, reducing the energy band gap to 1.14 eV. The decreased band gap may be attributed to the strong correlation influences between the Co 3d states and the 6p of Pb (Tian et al., 2016). As a result, Co-doped α-PbO possesses a half-metallic property. It has p-type conductivity due to the relocation of the Fermi level position to the valence band. Except for the change in the position of the maximum and minimum of the valence and conduction bands, it retains its indirect band gap semiconducting behaviors as pristine α-PbO. Figure 64b shows the PDOS of Co-doped α-PbO. The orbital of Co 3d states and Pb 6p states dominate the density of states in the conduction band. The mixing of Co 3d, O 2p, Pb 6s, and Co 4s states dominates the partial density of state in the valence band. An additional impurity energy level overlaps with the Fermi level, as shown in the band structure and PDOS. As a result, these impurity states serve as acceptors to reduce the recombination of electron-hole pairs, thereby improving photocatalytic performance. In the same manner, as Ni-doped α-PbO, the Co-doped α-PbO 3d states in the spin up and spin downs are asymmetry which may be attributed to part of the 3d state electrons transmitted to the conduction band via Fermi level (Yang et al., 2014). In addition to this, Co and Ni have unpaired electrons according to crystal field theory from which we can estimate the magnetic moments.

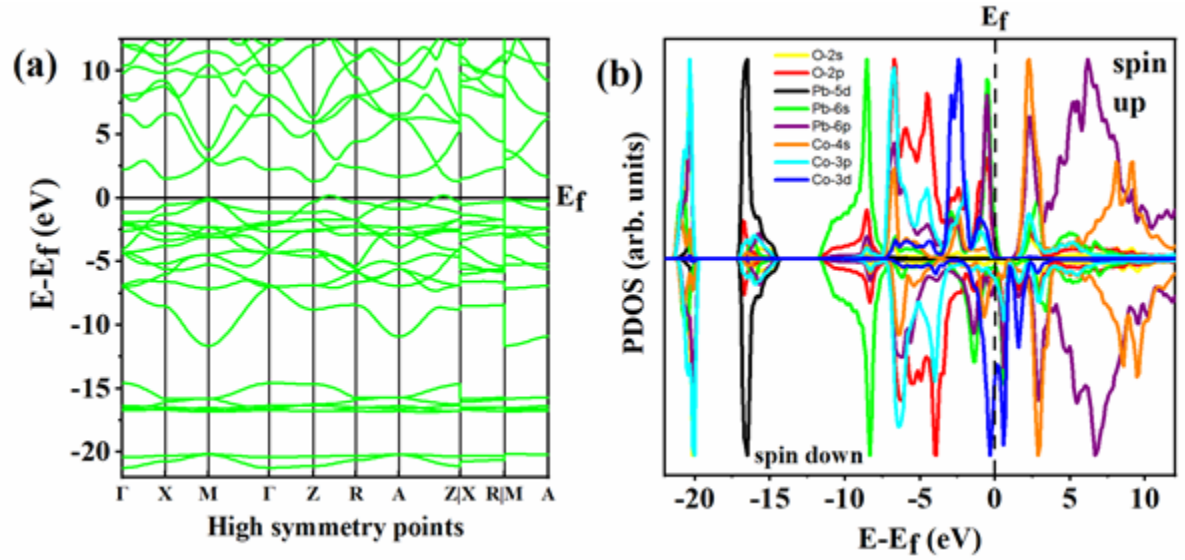

Figure 64: (a) Electronic Band structure diagram and (b) PDOS of Co doped α-PbO.

4.5.3.5. Cu doped α-PbO

Copper has a strong electrical conductivity quality, and when it is doped into α-PbO, it increases the material's electrical conductivity. Figure 65a, depicts the plot of the Cu-doped electronic band structure. The impurity energy level in Cu-doped α-PbO appears in the midst of VBM and CBM, is extremely connected to CBM, and by establishing an indirect gap with VBM at M- and A-points. As a result of pushing up the VBM and the contribution of Cu impurity, the band gap is lowered to 1.30 eV. The donor level is the impurity condition that appears closest to the conduction band. In this situation, the Fermi level enters the valence band due to the development of some electron-filled states. The impurity level appearing above the valence band makes the electrons to get sufficient energy to jump from the valence band to the impurity level then with small energy to the conduction band. As a result, some of the free electrons in the conduction band contribute to conductivity when it is in equilibrium. The PDOS data in Figure 65b also confirms that the Fermi level penetrates the valence band. The orbital state contributions of dopants are also disclosed, demonstrating the contribution of the partial density of states of orbitals Cu 3d and O 2p in the valence band. Other orbitals having partial densities of states in the conduction band include orbitals Cu 4p and Cu 4s, as well as the orbital Pb 6p. The contribution of Cu 3d states to the valence band shows its correlation with O 2p states and its strong correlation with Pb 6p in narrowing the band gap.

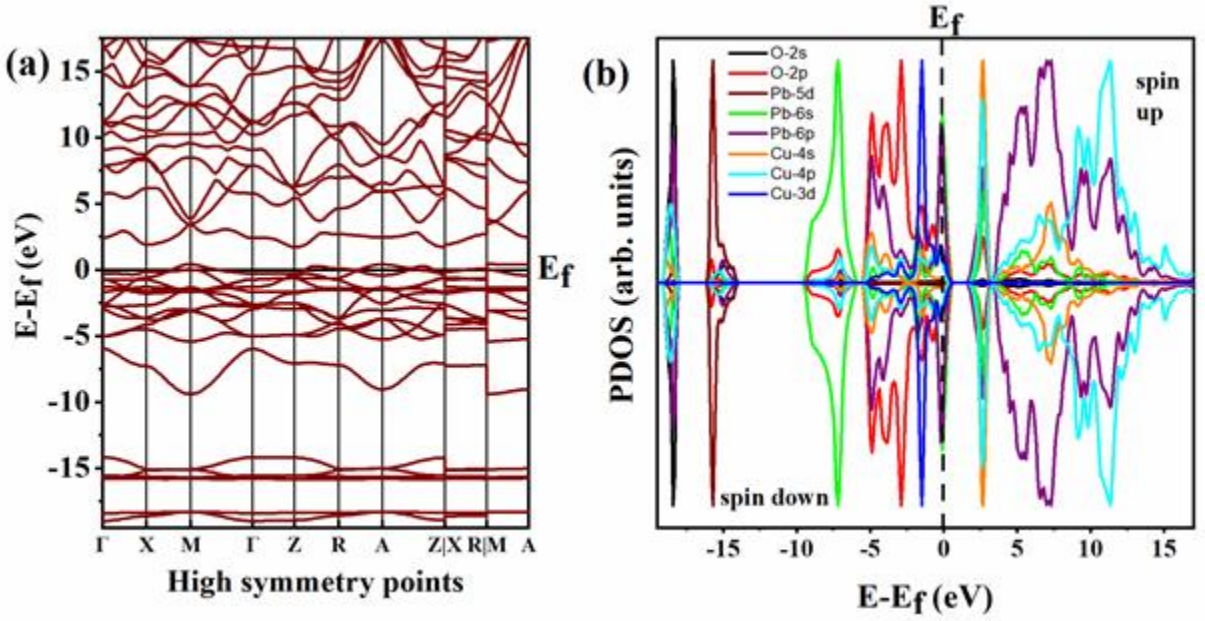

Figure 65: (a) Electronic Band structure diagram and (b) PDOS of Cu doped α-PbO.

4.5.4. n- or p-type conductivity

When intrinsic semiconductors are doped with electrons, they become n-type semiconductors, whereas when doped with holes, they become p-type semiconductors. For intrinsic semiconductors, the energy level appears in the middle, shifting downward as hole doping concentration increases and upward as electron doping concentration increases. According to the plots of electronic band structure, all doped α-PbO have p-type conductivity. It meant that the n- or p-type conductivity characteristic of pure α-PbO could be easily tuned for specific purposes by doping with different metal dopants. The energy level (Fermi level) can either penetrate the conduction or valence bands depending on the connections between carrier concentrations and the density of states. Thus, if the carrier concentration is greater than the density of states during doping into intrinsic semiconductors, the energy level penetrates the conduction band, which is known as the Burstein-Moss effect. The penetration of energy levels in the valence band may be attributed to a lack of electrons in the valence band, as opposed to the presence of surplus holes concentrations. The rising concentration of holes in the valence band is known as the inverse Burstein-Moss effect.

4.5.5. Optical properties

The light response of materials is described by their optical properties. Based on the electronic structure calculations, the optical properties of pristine α-PbO and different metals doped are calculated. In the same manner as calculated for different metals doped β-PbO, dielectric functions (real part ε_r and imaginary ε_i), refractive index (n), extinction coefficient (k), absorption coefficient (α), reflectivity (R), electron energy loss spectrum (L), and optical conductivity (σ) are calculated for different metals doped α-PbO.

The real part of the dielectric function (ε_r) helps to determine the dispersion and polarizations of light, while the imaginary part of the dielectric function (ε_i) describes the absorptive properties of different metals doped α-PbO. The real and imaginary parts of dielectric functions for pristine and different metals doped α-PbO is computed for the incident photon in the range from 0 eV to 28 eV as presented in Figure 66. Figure 66a shows the computed real part of the dielectric function (ε_r). The static real dielectric function for pristine, Co, Ni, and Sn doped α-PbO is 7.14, -5.62, -5.35, and 7.67. However, Cu and Li doped have no static real part of the dielectric function. The negative values of the real part of the dielectric function indicates that poor light

transmission and there will be a loss of energy in this region (Rouf et al., 2021). After decreasing to a negative region the value of the real part of the dielectric function for each material starts to increase and almost overlapped in energy above 10 eV, showing the presence of small amounts of dispersion and polarization of light.

The imaginary part of dielectric function behavior is presented in Figure 66b. There is an interband transition that can contribute to the imaginary part of the dielectric function of materials. The static imaginary part of the dielectric function value of pristine, Co, Ni, and Sn doped α-PbO is 0, 4.98, 3.83, and 0.000063, respectively. In the same condition as in the real part of dielectric function Cu and Li doped has no static imaginary part of dielectric functions. The maximum values of the imaginary part of the dielectric function is 10.95 at 3.60 eV, 13.53 at 1.65 eV, 11.46 at 1.90 eV, 11.04 at 2.40 eV, 6.60 at 2.46 eV, and 10.46 at 3.56 eV for pristine, Co, Ni, Cu, Li and Sn doped α-PbO respectively. The Li doped has the lowest value compared to other materials. All doped materials showed to the lower energy shifts compared to pristine α-PbO which may be due to the impurity states of dopants. Thus, it is the manner in which to enhance the visible light response of the doped materials compared to pure α-PbO. The slight fluctuation in the higher energy range indicates the nonuniform transition.

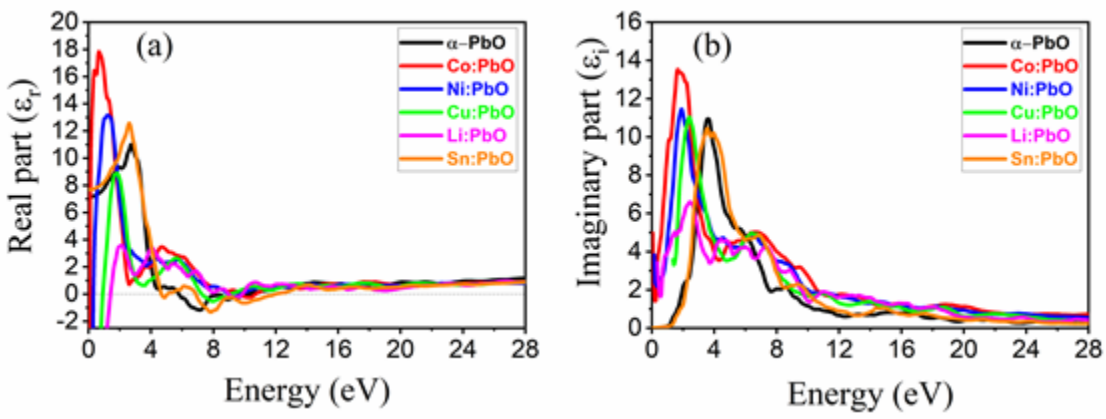

Figure 66: (a) Real and (b) imaginary parts dielectric function against photon energy for different metals doped α-PbO.

The refractive index of pristine and different metals doped α-PbO describes how light moves fast through them and is a dimensionless number. The refractive index as a function of photon energy is presented in Figure 67a. The refractive index is found in the range of 0.83 to 3.93. It is obvious that the static refractive index of pristine, Sn, Co, Cu, Ni, and Li doped α-PbO is 1.89, 1.96, 2.50, 2.16, 2.28, and 2.16 respectively. The maximum values of refractive index is 3.43 at 3.46 eV,

3.36 at 3.10 eV, 3.93 at 1.55 eV, 3.55 at 1.05 eV, 3.54 at 1.55 eV and 2.59 at 2.10 eV for pristine, Sn, Co, Cu Ni and Li doped α-PbO. The refractive index increases after doping due to a decrease in the band gap (Elazoumi et al., 2018). The increase of static refractive index value after doping may be related to the hybridizations of different orbitals of metal dopants with the pristine α-PbO orbitals as demonstrated in the PDOS of each material. In this research, the refractive index of pristine α-PbO compares with that of different metals doped, showing that different metals doped α-PbO is reasonable for optical materials coating applications either single or multilayered coating (Xue et al., 2019). The increase in refractive index after doping demonstrates that the retarded photon radiations in the medium which is suitable for photovoltaic and photocatalysis applications (Nwanya et al., 2013).

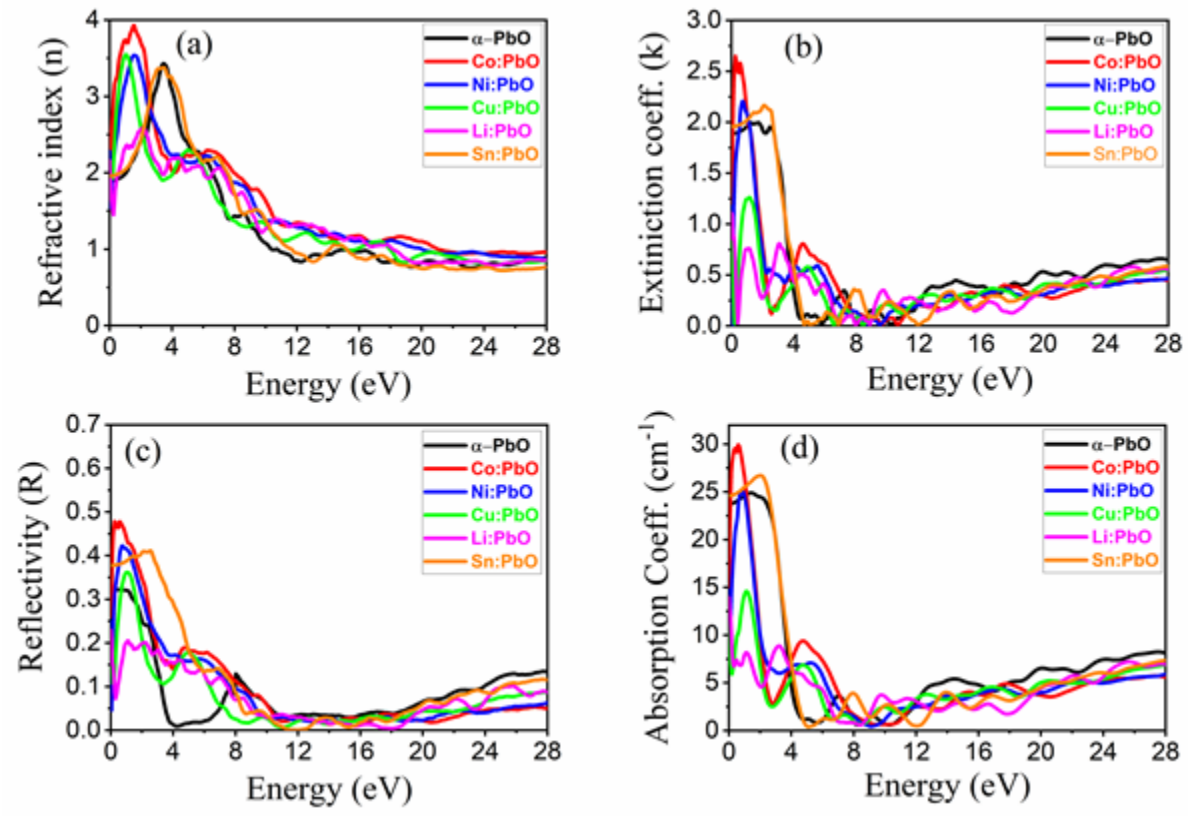

Figure 67: (a) Refractive index, (b) extinction coefficient, (c) reflectivity and (d) absorption coefficient as a function of photon energy for different metals doped α-PbO.

It is clear that the extinction coefficient provides information about absorption at the band edges. The graph of the extinction coefficient as a function of photon energy is presented in Figure 67b. The extinction coefficient was found in the range of 0 to 2.65. We can divide the extinction

coefficient into three parts including a first range from 0 eV to 4.43 eV, a second range from 4.43 eV to 12 eV, and a third range from 12 eV to 28 eV. The first range is due to the transition from CBM to VBM; the second and third ranges may be related to the shallow level. The curves of the extinction coefficient of different metals doped α-PbO from 4.43 eV to higher energy almost overlapped. As one can see from Figure 67b, different metal doping causes high absorption in visible light which may increase the concentrations of photogenerated electrons and holes, thereby improving the photocatalytic performance of α-PbO. It is obvious that the amplitude of incident light is affected by the interaction between photons and electrons, thus there is a high peak curves extinction coefficient of metals doped at lower energy. This is due to the narrowed bandgap after doping so that the doped materials can show enhanced photocatalytic activity in visible light situations (Xue et al., 2019).

Typically, the reflectivity calculation of different metals doped α-PbO depends on the dielectric functions and is presented in Figure 67c. At zero photon energy, the reflectivity of pristine, Co, Ni, Cu, Li, and Sn doped α-PbO is 32%, 26%, 24.8%, 21.9%, 22.9%, and 37.8% respectively. And the maximum values of reflectivity is 32.30% at 0.05 eV, 47.85% at 0.25 eV, 42.27% at 0.75 eV, 36.20% at 1.05 eV, 20.50% at 1.10 eV, and 41.16% at 2.55 eV for pristine, Co, Ni, Cu, Li and Sn doped α-PbO respectively. The minimum reflectivity shows the occurrence of the Plasmon resonance and in band absorption, the degree of overlap is enhanced. Factors such as the composition of the materials change in electron structure, and induced lattice distortion due to doping affected the reflectivity of pristine α-PbO due to photon scattering on charge carriers.

Absorption coefficient (α) is related to the ability of materials to absorb incident light in the form of photons with suitable energy. As shown in Figure 67d the absorption coefficient decreases as photon energy increases. It is clear that when a high amount of photon energy is absorbed by the medium, the attenuation of light will occur. Materials having low absorption coefficients weakly absorb light. The absorption coefficient is larger at lower energy which indicates that pristine and different metals doped α-PbO show better absorption of incident light at lower photon energy. Among all doped materials, Co-doped α-PbO shows the largest absorption coefficient at 0.60 eV. The higher values of absorption coefficients show the increase of absorption at a given photon energy. The shifts of absorption coefficients of doped materials compared to pristine α-PbO show shifts in absorption edge due to induced impurity levels after doping. The shift to the higher or lower energy is due to the different ionic radii of dopants and host materials. The

observed fluctuations in the absorption coefficient are revealed due to the nonuniform rate of absorption.

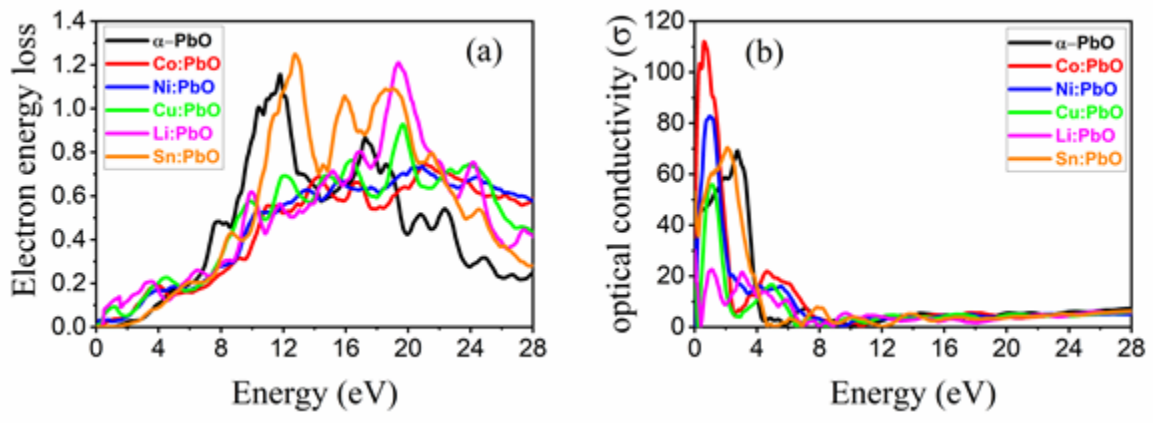

Figure 68: (a) The electron energy loss spectrum and (b) the optical conductivity of pristine, Co, Ni, Cu, Li and Sn doped α-PbO.

Electron energy loss describes the energy loss of electrons when the material interacts with incident photon energy. Dispersion of light, scattering of incident photons, and transmission of heat from the materials are factors for electrons to loss their energy. Figure 68a, shows the electron energy loss for pristine and different metals doped α-PbO in the energy range from 0 eV to 28 eV. The electron energy loss is zero at the origin, whereas it starts to increase as energy increases. Among all materials pristine, Sn and Li doped α-PbO showed large electron energy loss which may be related to the scattering of incident light. At the energy in the range from 6.78 eV to 11.95 eV pristine α-PbO has the highest electron loss energy. Sn and Li doped α-PbO attains maximum energy loss in the range of 12.33 eV to 18.90 eV and from 18.90 eV to 21.51 eV, respectively. At the maximum of electron loss energy a drop of absorption coefficient is observed, indicating that the scattering rate of light is higher in this region. After attaining their maximum, the electron energy loss becomes decrease at higher energy.

Optical conductivity (σ) is the conduction due to the existence of an alternating electric field. The optical conductivity in a material describes the conduction occurred by photoelectrons emitted through the photoelectric effect. Thus, it describes the bond breaking in the presence of electromagnetic radiation (Rouf et al., 2021). The optical conductivity properties of pristine and different metals doped α-PbO is presented in Figure 68b. The maximum optical conductivity of pristine, Co, Ni, Cu, Li and Sn doped α-PbO is 69.18 $(\Omega\ cm)^{-1}$ at 2.75 eV, 112.05 $(\Omega\ cm)^{-1}$ at

0.60 eV, 82.75 $(\Omega\ cm)^{-1}$ at 0.95 eV, 55.86$(\Omega\ cm)^{-1}$ at 1.15 eV, 22.63 $(\Omega\ cm)^{-1}$ at 1.10 eV, and 70.43 $(\Omega\ cm)^{-1}$ at 2.10 eV respectively. However, it decreased suddenly after reaching maximum values which may occur due to the inactivity of the photons incident on the surfaces of the materials. After doping different metals the highest conductivity is shifted to lower energy which may be related to the induced impurity level. At higher energy especially beyond 8.7 eV, the optical conductivity curves almost overlapped and decreases. In the range of energy where the largest absorption coefficient is obtained the largest optical conductivity is also obtained. The shifts and enhanced optical conductivity response after doping indicate the possible applications of the doped materials in photocatalysis.

Table 19: Effective masses of electrons and holes of different metals doped α-PbO in the unit of free electron mass.

Materials	m_h^*/m_o	m_e^*/m_o	m_h^*/m_e^*
pristine α-PbO	-2.54	1.42	1.79
Co-doped α-PbO	-0.89	0.79	1.13
Cu-doped α-PbO	-1.99	1.10	1.81
Li-doped α-PbO	-2.13	1.16	1.83
Ni-doped α-PbO	-1.70	0.80	2.10
Sn-doped α-PbO	-2.73	1.24	2.20

4.5.6. Effective masses of electrons and holes

For determining the effective masses of electrons and holes of different metals doped α-PbO, the description used in different metals doped β-PbO is employed. The effective masses of electrons and holes of different metals doped α-PbO are summarized in Table 19. The larger effective mass of holes of pristine α-PbO and Sn-doped α-PbO shows that the diffusion rate of photogenerated holes is low, hence reduces the photocatalytic performance compared to other doped materials. However, Sn doped α-PbO possesses lower electron effective mass than pristine α-PbO, which indicates faster electrons transfer to reach surface reaction site than pristine α-PbO. Thus, the mobility of photogenerated electrons is enhanced. Because of the large difference between effective masses of electron and holes in Sn doped α-PbO there may be good charge carriers' separation and the charge recombination rate decreases, which enhance the photocatalytic activity. Except Sn doped α-PbO has the largest effective mass of holes all other doped materials own smaller effective masses of electrons and holes compared to pristine α-PbO. Thus, there is an enhanced diffusion rate of photogenerated electrons and holes to reach surface reaction sites. In Co doped α-PbO both electrons and holes effective masses are much smaller

than all materials and the difference between its effective masses are also small indicating that there is no sufficient charge carriers separation which may result in fast recombination of charge carriers, hence reducing the photocatalytic performance of Co doped α-PbO.

5. CONCLUSIONS AND RECOMMENDATIONS

5.1. Conclusions

Photocatalytic degradation of organic pollutants by using semiconducting oxides has attracted great attention in current times. In the present work, undoped and different metals (Co, Cu, Ni, Li, and Sn) doped α-PbO and β-PbO nanoparticles were successfully synthesized through a chemical precipitation method. The prepared nanoparticles were utilized as photocatalysts for the degradation of MB dye under visible light irradiation. The XRD results confirmed that the synthesized pristine α-PbO and β-PbO nanoparticles were pure without the mixture of other phases of PbO. The XRD patterns showed shifts in doped materials compared to pristine β-PbO, which is attributed to the extension and shrinks of the lattice parameters. In metals doped α-PbO, there is a phase transition to β-PbO in Cu and Co-doped. However, in β-PbO, all doped materials showed only the β-PbO phases. This may be attributed to the phase stability of β-PbO at high temperatures and increasing annealing temperature enhances the crystallinity of materials.

From UV-Vis DRS analysis, the obtained band gap was 2.03 eV, 2.68 eV, 1.61 eV, 1.78 eV, 1.67 eV, and 2.00 eV for pristine α-PbO, Sn, Co, Cu, Ni and Li doped α-PbO, respectively. The obtained band gap for pristine β-PbO, Sn, Co, Cu, Ni, and Li doped β-PbO was 2.68 eV, 2.70 eV, 1.88 eV, 2.01 eV, 2.65 eV, and 2.64 eV, respectively. The PL emission analysis shows a strong green emission of 523 nm for pristine α-PbO, Co, Ni, and Li doped α-PbO whereas it shows a small shift to 524 nm for Sn and Cu doped. PL emission of pristine and different metals doped β-PbO nanoparticles showed similar characteristics as different metals doped α-PbO nanoparticles, but it possessed different intensities. The low PL emission intensity of the prepared catalysts showed the lowest recombination of the photogenerated electron-hole pairs. The SEM micrograph morphology analysis showed the non-uniformly distributed particles. The EDX study confirmed the existence of the expected elements in pristine and doped nanoparticles.

The photocatalytic experiments were employed under the same condition for both metals doped α-PbO and β-PbO except time of irradiation. The MB dye photocatalytic degradation efficiency of pristine α-PbO, Sn, Co, Cu, Ni, and Li doped α-PbO were 94.76%, 100%, 83.46%, 98.50%, 95.27%, and 97.49%, respectively, within 100 min. The highest pseudo-first-order kinetic reaction rate constant was the catalyst with the highest degradation efficiency. Among the doped α-PbO photocatalysts, Sn-doped α-PbO possessed the highest kinetic rate constant and complete

degradation of MB dye within 100 min. The photocatalytic degradation efficiency of pristine β-PbO, Sn, Co, Cu, Ni, and Li doped β-PbO towards the degradation of MB dye was 75.13%, 97.71%, 99.39%, 99.45%, 98.44%, and 96.34% respectively within 80 min. Among the doped β-PbO, Cu and Co-doped photocatalysts showed the maximum degradation efficiency and possessed high rate constants. After the incorporation of different metals into both α-PbO and β-PbO the photocatalytic performance is enhanced. The enhanced photocatalytic performance can be attributed to the broader light harvesting in the visible region, the band gap narrowing, formation of dopants impurity states, surface roughness, enhanced specific surface area, higher carrier concentration, reduced carriers recombination, the action of dopant ions and microstructural changes. Furthermore, the PbO thin film has also been prepared to identify the phases of PbO. However, unlike the enabled synthesizing of high purity α-PbO and β-PbO in nanoparticles, the PbO thin films prepared by chemical bath deposition resulted in the mixture of both α-PbO and β-PbO phases with the majorly existing β-PbO phase. The SEM surface morphology analysis of the prepared PbO thin film confirms the presence of nanorods, cauliflower, and nanosheets structure coated on the surface of the substrate.

On the other hand, the structural, electrical and optical properties of Co, Ni, Cu, Li, and Sn doped β-PbO and α-PbO were systematically studied by using density functional theory (DFT) under the implementation of Quantum espresso by replacing a single atom of each dopant in the site of Pb atom. From the structural property analyses, the obtained lattice parameters are well agreed with the previous studies. The electronic band structure calculation by using both GGA and LDA functional shows an indirect band gap for spin-up and spin-down states. The obtained spin-up band gap by using GGA for pristine, Co, Ni, Cu, Li, and Sn doped β-PbO was 2.28 eV, 0.68 eV, 1.01 eV, 1.57 eV, 1.79 eV, and 1.76 eV respectively. The obtained energy bandgap for pristine α-PbO and Sn, Cu, Li, Ni, and Co-doped α-PbO are 1.75 eV, 1.53 eV, 1.30 eV, 1.57 eV, 1.36 eV, and 1.31 eV, respectively. The resulting band gaps are slightly far from our experimental results. However, it is well agreed and the best results compared to different DFT studies. For both β-PbO and α-PbO and different metal incorporations, an indirect band gap was obtained, which shows the enhancing properties of photocatalytic activity because the charge recombination can be retarded. Based on the bandstructure calculations, the effective masses of photogenerated electrons and holes are calculated and it shows lower effective masses of carriers after the incorporation of different metals into β-PbO and α-PbO. This indicates that

the photogenerated electrons and holes can reach the surface reaction site within their lifetime, enhancing photocatalytic performance.

5.2. Recommendations

In this research, for metals doping α-PbO and β-PbO nanoparticles, the same concentrations (0.1M) of dopants were used. Due to financial constraints and a lack of chemicals, the effects of concentrations of dopants are not included in this research. However, based on the best degradation efficacy of Sn doped α-PbO and Cu or Co-doped β-PbO towards MB dye degradation, it should be investigated more by varying the concentrations of Sn, Cu, and Co to identify effects of dopant concentration on the photocatalytic activity of α-PbO and β-PbO nanoparticles. The photodegradation efficiency of metals doped α-PbO and β-PbO towards different organic dyes beyond MB dye also needs to be investigated. On the other hand, the ecotoxicity of photocatalysts and the clear separation of photocatalysts from the treated water need more attention. Generally, for organic pollutant degradation, an important concern that needs to be addressed is improving the response under the irradiation of visible solar light. Thus, for the degradation of organic contaminants efficiently, economically viable, greener, and faster approaches required a significant development in sustainable degradation of organic pollutants and creating a clean environment for living creatures. The lack of high supercomputing computer constrained our DFT study only to use LDA and GGA exchange-correlational functional. Still, it should be needed to go beyond LDA and GGA functionality for an accurate optical band gap. Finally, the density functional theory method can be used to understand and discover new materials for photocatalysis applications because it is a simple method to search for new materials in photocatalysis applications without using chemicals as raw materials that reduce cost. Therefore, DFT is recommended for searching for new materials that will be used as photocatalyst materials or predicting the way to improve the discovered metal oxides by understanding the properties of materials.

LIST OF PUBLICATIONS

1. Fikadu Takele Geldasa, Mesfin Abayneh Kebede, Megersa Wodajo Shura and Fekadu Gashaw Hone, Different metal dopants effects on the structural, electronic, and optical properties of β-PbO: a density functional theory study, *Eur. Phys. J. Plus*, vol. **138**, 165, 2023, https://doi.org/10.1140/epjp/s13360-023-03718-7.
2. F. T. Geldasa, M. A. Kebede, M. W. Shura, D. M. Andoshe, N. A. Tegegne, and F. G. Hone, Facile synthesis of different metals doped α-PbO nanoparticles for photocatalytic degradation of Methylene Blue dye, *Phys. Scr.* **98,** 2023, https://doi.org/10.1088/1402-4896/acd0e3.
3. F. T. Geldasa, M. A. Kebede, M. W. Shura, and F. G. Hone, Density functional theory study of different metal dopants influence on the structural and electronic properties of a tetragonal α-PbO, *AIP Adv.*, vol. **12**, no. 11, 115302, 2022, https://doi.org/10.1063/5.0121828
4. F. T. Geldasa, M. A. Kebede, M. W. Shura, and F. G. Hone, "Identifying surface degradation, mechanical failure, and thermal instability phenomena of high energy density Ni-rich NCM cathode materials for lithium ion batteries: A review," *RSC Adv.*, vol. **12**, no. 10, pp. 5891–5909, 2022, https://doi.org/10.1039/D1RA08401A.
5. F. T. Geldasa, M. A. Kebede, M. W. Shura, and F. G. Hone, Experimental and computational study of metal oxide nanoparticles for Photocatalysis applications: a review, *RSC Advances*, 2023, (under review).
6. F. T. Geldasa, M. A. Kebede, M. W. Shura, and F. G. Hone, One step chemical synthesis approach to produce three different morphologies of PbO thin films from different cation concentrations, *Materials Research Express*, 2023, (under review).
7. F. T. Geldasa, M. A. Kebede, M. W. Shura, and F. G. Hone, Effects of metal dopants on the structural, optical and photocatalytic activity of β-PbO nanoparticles, 2023, (under review).

REFERENCES

Abargues, R., Navarro, J., Rodríguez-Cantó, P. J., Maulu, A., Sánchez-Royo, J. F., & Martínez-Pastor, J. P. (2019). Enhancing the photocatalytic properties of PbS QD solids: The ligand exchange approach. *Nanoscale*, *11*(4), 1978–1987.

Abdel-Wahab, A. M., Al-Shirbini, A. S., Mohamed, O., & Nasr, O. (2017). Photocatalytic degradation of paracetamol over magnetic flower-like TiO_2/Fe_2O_3 core-shell nanostructures. *Journal of Photochemistry and Photobiology A: Chemistry*, *347*, 186–198.

Abhilash, M. R., Gangadhar, A., Krishnegowda, J., Chikkamadaiah, M., & Srikantaswamy, S. (2019). Hydrothermal synthesis, characterization and enhanced photocatalytic activity and toxicity studies of a rhombohedral Fe_2O_3 nanomaterial. *RSC Advances*, *9*(43), 25158–25169.

Adeel, M., Saeed, M., Khan, I., Muneer, M., & Akram, N. (2021). Synthesis and Characterization of Co–ZnO and Evaluation of Its Photocatalytic Activity for Photodegradation of Methyl Orange. *ACS Omega*, *6*(2), 1426–1435.

Ajmal, A., Majeed, I., Malik, R. N., Idriss, H., & Nadeem, M. A. (2014). Principles and mechanisms of photocatalytic dye degradation on TiO_2 based photocatalysts: A comparative overview. *RSC Advances*, *4*(70), 37003–37026.

Akbay, İ. K., Güngör, A., Genç, R., & Özdemir, T. (2019). Optimization of synthesis parameters for lead oxide nanoparticles using response surface methodology. *Selcuk University Journal of Engineering ,Science and Technology*, *7*(2), 298–308.

Al-Attiyah, K. H. H., Hashim, A., & Obaid, S. F. (2019). Fabrication of novel (carboxy methyl cellulose–polyvinylpyrrolidone–polyvinyl alcohol)/lead oxide nanoparticles: structural and optical properties for gamma rays shielding applications. *International Journal of Plastics Technology*, *23*(1), 39–45.

Al-Tohamy, R., Ali, S. S., Li, F., Okasha, K. M., Mahmoud, Y. A. G., Elsamahy, T., Jiao, H., Fu, Y., & Sun, J. (2022). A critical review on the treatment of dye-containing wastewater: Ecotoxicological and health concerns of textile dyes and possible remediation approaches for environmental safety. *Ecotoxicology and Environmental Safety*, 231, 113160.

Alam, U., Khan, A., Ali, D., Bahnemann, D., & Muneer, M. (2018). Comparative photocatalytic activity of sol-gel derived rare earth metal (La, Nd, Sm and Dy)-doped ZnO photocatalysts for degradation of dyes. *RSC Advances*, *8*(31), 17582–17594.

Ali Baig, A. B., Rathinam, V., & Ramya, V. (2021). Facile fabrication of Zn-doped SnO_2 nanoparticles for enhanced photocatalytic dye degradation performance under visible light exposure. *Advanced Composites and Hybrid Materials*, *4*(1), 114–126.

Ali, S. I., Das, A., Agrawal, A., Mukherjee, S., Ahmed, M., Nambissan, P. M. G., Mandal, S., & Mandal, A. C. (2021). Characterization, spectroscopic investigation of defects by positron annihilation, and possible application of synthesized PbO nanoparticles. *Chin. Phys. B*, 30(2), 026103.

Aliakbari, A., Najafi, E., Amini, M. M., & Ng, S. W. (2014). Structure and photoluminescence properties of lead(II) oxide nanoparticles synthesized from a new lead(II) coordination polymer. *Monatshefte Fur Chemie*, *145*(8), 1277–1285.

Andrade, X., Pemmaraju, C. Das, Kartsev, A., Xiao, J., Lindenberg, A., Rajpurohit, S., Tan, L. Z., Ogitsu, T., & Correa, A. A. (2021). Inq, a Modern GPU-Accelerated Computational Framework for (Time-Dependent) Density Functional Theory. *Journal of Chemical Theory and Computation*, *17*(12), 7447–7467.

Ansari, S. A., Khan, M. M., Ansari, M. O., Lee, J., & Cho, M. H. (2014). Visible light-driven photocatalytic and photoelectrochemical studies of Ag-SnO_2 nanocomposites synthesized using an electrochemically active biofilm. *RSC Advances*, *4*(49), 26013–26021.

Anwer, H., Mahmood, A., Lee, J., Kim, K. H., Park, J. W., & Yip, A. C. K. (2019). Photocatalysts for degradation of dyes in industrial effluents: Opportunities and challenges. *Nano Research*, *12*(5), 955–972.

Arularasu, M. V. (2019). Effect of organic capping agents on the optical and photocatalytic activity of mesoporous TiO_2 nanoparticles by sol–gel method. *SN Applied Sciences*, *1*(5).

Arulmozhi, K. T., & Mythili, N. (2013). Studies on the chemical synthesis and characterization of lead oxide nanoparticles with different organic capping agents. *AIP Advances*, *3*(12), 122122.

Arunadevi, R., Kavitha, B., Rajarajan, M., & Suganthi, A. (2019). Sonochemical synthesis and high-efficient solar-light-driven photocatalytic activity of novel cobalt and manganese codoped tungsten oxide nanoparticles. *Chemical Physics Letters*, *715*, 252–262.

Asenjo, N. G., Santamaría, R., Blanco, C., Granda, M., Álvarez, P., & Menéndez, R. (2013). Correct use of the Langmuir-Hinshelwood equation for proving the absence of a synergy effect in the photocatalytic degradation of phenol on a suspended mixture of titania and

activated carbon. *Carbon*, *55*, 62–69.

Ashok, A., Regmi, G., Romero-Núñez, A., Solis-López, M., Velumani, S., & Castaneda, H. (2020). Comparative studies of CdS thin films by chemical bath deposition techniques as a buffer layer for solar cell applications. *Journal of Materials Science: Materials in Electronics*, *31*(10), 7499–7518.

Ayodhya, D., & Veerabhadram, G. (2018). A review on recent advances in photodegradation of dyes using doped and heterojunction based semiconductor metal sulfide nanostructures for environmental protection. *Materials Today Energy*, *9*, 83–113.

Azarang, M., Aliahmad, M., Shiravizadeh, A. G., Azimi, H. R., Yousefi, R., Azarang, M., Aliahmad, M., Shiravizadeh, A. G., & Azimi, H. R. (2018). Zn-doped PbO nanoparticles (NPs)/fluorine-doped tin oxide (FTO) as photoanode for enhancement of visible-near-infrared (NIR) broad spectral photocurrent application of narrow bandgap nanostructures : SnSe NPs as a case study, *J. Appl. Phys. 124*, 123101.

Ba-Abbad, M. M., Kadhum, A. A. H., Mohamad, A. B., Takriff, M. S., & Sopian, K. (2013). Visible light photocatalytic activity of Fe^{3+}-doped ZnO nanoparticle prepared via sol-gel technique. *Chemosphere*, *91*(11), 1604–1611.

Bade, B. R., Rondiya, S. R., Hase, Y. V., Nasane, M. P., Jathar, S. B., Barma, S. V., Kore, K. B., Nilegave, D. S., Jadkar, S. R., & Funde, A. M. (2021). Hydrothermally synthesized CuO nanostructures and their application in humidity sensing. *AIP Conference Proceedings*, *2335*, 100001.

Baig, N., Kammakakam, I., Falath, W., & Kammakakam, I. (2021). Nanomaterials: A review of synthesis methods, properties, recent progress, and challenges. *Materials Advances*, *2*(6), 1821–1871.

Bakhtatou, A., & Ersan, F. (2019). Effects of the number of layers on the vibrational, electronic and optical properties of alpha lead oxide. *Physical Chemistry Chemical Physics*, *21*(7), 3868–3876.

Bangi, U. K. H., Han, W., Yoo, B., & Park, H. H. (2013). Effects of successive additions of two capping ligands on the structural properties of PbO nanoparticles. *Journal of Nanoparticle Research*, *15*(11), 1–8.

Bangi, U. K. H., Park, H.-H., Han, W., Prakshale, V. M., & Deshmukh, L. P. (2017). Ultrasonically assisted synthesis of lead oxide nanoflowers using ball milling. *International*

Nano Letters, *7*(2), 149–155.

Banu, R., Salvi, N., Gupta, S., Ameta, C., Ameta, R., & Punjabi, P. B. (2022). A Facile Synthesis of GO/CuO Nanocomposite with Enhancing Photocatalytic Activity for the Degradation of Azure-B Dye and Its Antimicrobial Behavior. *Arabian Journal for Science and Engineering*, *47*(1), 365–378.

Bapitha, R., & Alagar, M. (2017). Synthesis and Characterization of Bio-Template Assisted Lead Oxide Nanoparticles. *J. Adv. Chem. Sci.*, *3*(3), 499–501.

Basak, S., Nandi, N., Paul, S., Hamley, I. W., & Banerjee, A. (2017). A tripeptide-based self-shrinking hydrogel for waste-water treatment: Removal of toxic organic dyes and lead (Pb^{2+}) ions. *Chemical Communications*, *53*(43), 5910–5913.

Bayuo, J., Rwiza, M., & Mtei, K. (2022). A comprehensive review on the decontamination of lead(ii) from water and wastewater by low-cost biosorbents. *RSC Advances*, *12*(18), 11233–11254.

Bazzi, A., Nriagu, J. O., & Linder, A. M. (2008). Determination of toxic and essential elements in children's blood with inductively coupled plasma-mass spectrometry. *Journal of Environmental Monitoring*, *10*(10), 1226–1232.

Behzad, S. K., Najafi, E., Amini, M. M., Tadjarodi, A., Dehghani, A., & Notash, B. (2015). Synthesis, characterization, and optical properties of lead(II) coordination polymers and nanosize lead oxide core of polymer. *Monatshefte Fur Chemie*, *146*(1), 35–45.

Bhachu, D. S., Sathasivam, S., Carmalt, C. J., & Parkin, I. P. (2014). PbO-modified TiO_2 thin films: A route to visible light photocatalysts. *Langmuir*, *30*(2), 624–630.

Bhapkar, A. R., Geetha, M., Jaspal, D., Gheisari, K., Laad, M., Cabibihan, J. J., Sadasivuni, K. K., & Bhame, S. (2023). Aluminium doped ZnO nanostructures for efficient photodegradation of indigo carmine and azo carmine G in solar irradiation. *Applied Nanoscience*, 1–17.

Bokov, D., Turki Jalil, A., Chupradit, S., Suksatan, W., Javed Ansari, M., Shewael, I. H., Valiev, G. H., & Kianfar, E. (2021). Nanomaterial by Sol-Gel Method: Synthesis and Application. *Advances in Materials Science and Engineering*, *2021*,1–21

Borhade, A. V., Uphade, B. K., & Tope, D. R. (2013). PbO as an efficient and reusable catalyst for one-pot synthesis of tetrahydro benzo pyrans and benzylidene malonitriles. *Journal of Chemical Sciences*, *125*(3), 583–589.

Borhade, A. V, Tope, D. R., & Uphade, B. K. (2012). An Efficient Photocatalytic Degradation of Methyl Blue Dye by Using Synthesised PbO Nanoparticles. *E-Journal of Chemistry*, *9*(2), 705–715.

Boyjoo, Y., Sun, H., Liu, J., Pareek, V. K., & Wang, S. (2017). A review on photocatalysis for air treatment: From catalyst development to reactor design. *Chemical Engineering Journal*, *310*, 537–559.

Buraso, W., Lachom, V., Siriya, P., & Laokul, P. (2018). Synthesis of TiO_2 nanoparticles via a simple precipitation method and photocatalytic performance. *Materials Research Express*, *5*(11), 0–10.

Butler, M. A., Nasby, R. D., & Quinn, R. K. (1976). Tungsten trioxide as an electrode for photoelectrolysis of water. *Solid State Communications*, *19*(10), 1011–1014.

Capelle, K. (2006). A bird's-eye view of density-functional theory. *Brazilian Journal of Physics*, *36*(4 A), 1318–1341.

Chakhtouna, H., Benzeid, H., Zari, N., Qaiss, A. el kacem, & Bouhfid, R. (2021). Recent progress on Ag/TiO_2 photocatalysts: photocatalytic and bactericidal behaviors. *Environmental Science and Pollution Research*, *28*(33), 44638–44666.

Chavali, M. S., & Nikolova, M. P. (2019). Metal oxide nanoparticles and their applications in nanotechnology. *SN Applied Sciences*, *1*(6), 1–30.

Chen, K. C., Wang, C. W., Lee, Y. I., & Liu, H. G. (2011). Nanoplates and nanostars of β-PbO formed at the air/water interface. *Colloids and Surfaces A: Physicochemical and Engineering Aspects*, *373*(1–3), 124–129.

Chen, K., Wang, X., Xia, P., Xie, J., Wang, J., Li, X., Tang, Y., & Li, L. (2020). Efficient removal of 2,2′,4,4′-tetrabromodiphenyl ether with a Z-scheme Cu_2O-(rGO-TiO_2) photocatalyst under sunlight irradiation. *Chemosphere*, *254*, 126806.

Cheraghizade, M., Jamali-Sheini, F., & Yousefi, R. (2017). Optical, electrical, and photovoltaic properties of PbS thin films by anionic and cationic dopants. *Applied Physics A: Materials Science and Processing*, *123*(6), 1–9.

Danish, M. S. S., Estrella, L. L., Alemaida, I. M. A., Lisin, A., Moiseev, N., Ahmadi, M., Nazari, M., Wali, M., Zaheb, H., & Senjyu, T. (2021). Photocatalytic Applications of Metal Oxides for Sustainable Environmental Remediation. *Metals*, *11*(1), 1–25.

Dardouri, S., & Sghaier, J. (2017). Adsorptive removal of methylene blue from aqueous solution

using different agricultural wastes as adsorbents. *Korean Journal of Chemical Engineering*, *34*(4), 1037–1043.

De, A. K., Majumdar, S., Pal, S., Kumar, S., & Sinha, I. (2020). Zn doping induced band gap widening of Ag_2O nanoparticles. *Journal of Alloys and Compounds*, *832*, 154127.

Devi, L. G., & Shyamala, R. (2018). Photocatalytic activity of SnO_2-α-Fe_2O_3 composite mixtures: Exploration of number of active sites, turnover number and turnover frequency. *Materials Chemistry Frontiers*, *2*(4), 796–806.

Dheyab, M. A., Aziz, A. A., & Jameel, M. S. (2021). Recent advances in inorganic nanomaterials synthesis using sonochemistry: A comprehensive review on iron oxide, gold and iron oxide coated gold nanoparticles. *Molecules*, *26*(9), 1–19.

Djurišić, A. B., Leung, Y. H., & Ching Ng, A. M. (2014). Strategies for improving the efficiency of semiconductor metal oxide photocatalysis. *Materials Horizons*, *1*(4), 400–410.

Droessler, L. M., Assender, H. E., & Watt, A. A. R. (2012). Thermally deposited lead oxides for thin film photovoltaics. *Materials Letters*, *71*, 51–53.

Du, Y., Wang, W., Li, X., Zhao, J., Ma, J., Liu, Y., & Lu, G. (2012). Preparation of NiO nanoparticles in microemulsion and its gas sensing performance. *Materials Letters*, *68*, 168–170.

Dumková, J., Smutná, T., Vrlíková, L., Kotasová, H., Dočekal, B., Čapka, L., Tvrdoňová, M., Jakešová, V., Pelková, V., Křůmal, K., Coufalík, P., Mikuška, P., Večeřa, Z., Vaculovič, T., Husáková, Z., Kanický, V., Hampl, A., & Buchtová, M. (2020). Variability in the Clearance of Lead Oxide Nanoparticles Is Associated with Alteration of Specific Membrane Transporters. *ACS Nano*, *14*(3), 3096–3120.

Eddiouane, A., Chaib, H., Nafidi, A., Najjaoui, M., & Ait-Taleb, T. (2018). First principles investigation of electronic properties and high refractive index of rutile TiO_2 for photovoltaic applications. *AIP Conference Proceedings*, *2056*, 1–9.

Edossa, T. G., & Woldemariam, M. M. (2020). Electronic, Structural, and Optical Properties of Zinc Blende and Wurtzite Cadmium Sulfide (CdS) Using Density Functional Theory. *Advances in Condensed Matter Physics*, *2020*, 1–8.

Eisa, M. H. (2020). Effects of beta-ray irradiation on optical properties of PbO thin films. *Materials Science in Semiconductor Processing*, *110*, 1–6.

Elazoumi, S. H., Sidek, H. A. A., Rammah, Y. S., El-Mallawany, R., Halimah, M. K., Matori, K.

A., & Zaid, M. H. M. (2018). Effect of PbO on optical properties of tellurite glass. *Results in Physics*, *8*, 16–25.

Elsafi, M., Sayyed, M. I., Almuqrin, A. H., Gouda, M. M., & El-khatib, A. M. (2021). Analysis of particle size on mass dependent attenuation capability of bulk and nanoparticle PbO radiation shields. *Results in Physics*, *26*, 1–7.

Ernzerhof, M., & Scuseria, G. E. (1999). Assessment of the Perdew-Burke-Ernzerhof exchange-correlation functional. *Journal of Chemical Physics*, *110*(11), 5029–5036.

Esencan Türkaslan, B., Çelik, A. K., Dalbeyler, A., & Fantuzzi, N. (2022). The Effect of Different Morphologies of WO_3/GO Nanocomposite on Photocatalytic Performance. *Materials*, *15*(22), 1–12.

Fito, J., Abrham, S., & Angassa, K. (2020). Adsorption of Methylene Blue from Textile Industrial Wastewater onto Activated Carbon of Parthenium hysterophorus. *International Journal of Environmental Research*, *14*(5), 501–511.

Flick, J., Appel, H., Ruggenthaler, M., & Rubio, A. (2017). Cavity Born-Oppenheimer Approximation for Correlated Electron-Nuclear-Photon Systems. *Journal of Chemical Theory and Computation*, *13*(4), 1616–1625.

Frindy, S., & Sillanpää, M. (2020). Synthesis and application of novel α-Fe_2O_3/graphene for visible-light enhanced photocatalytic degradation of RhB. *Materials and Design*, *188*, 1–12.

Fu, H., Liu, G., Bao, H., Zhou, L., Zhang, H., Zhao, Q., Li, Y., & Cai, W. (2020). Ultrathin Hexagonal PbO Nanosheets Induced by Laser Ablation in Water for Chemically Trapping Surface-Enhanced Raman Spectroscopy Chips and Detection of Trace Gaseous H_2S. *ACS Applied Materials and Interfaces*, *12*(20), 23330–23339.

Fujishima, A., & Honda, K. (1972). Electrochemical Photolysis of Water at a Semiconductor Electrode. *Nature*, *238*(5358), 38–40.

Gahlawat, S., Singh, J., Yadav, A. K., & Ingole, P. P. (2019). Exploring Burstein-Moss type effects in nickel doped hematite dendrite nanostructures for enhanced photo-electrochemical water splitting. *Physical Chemistry Chemical Physics*, *21*(36), 20463–20477.

Galstyan, V., Bhandari, M. P., Sberveglieri, V., Sberveglieri, G., & Comini, E. (2018). Metal oxide nanostructures in food applications: Quality control and packaging. *Chemosensors*, *6*(2), 1–21.

Gan, Y. X., Jayatissa, A. H., Yu, Z., Chen, X., & Li, M. (2020). Hydrothermal Synthesis of Nanomaterials. *Journal of Nanomaterials*, *2020*, 1–3.

Gandhi, A., & Wu, S. (2017). Strong Deep-Level-Emission Photoluminescence in NiO Nanoparticles. *Nanomaterials*, *7*(8), 1–12.

Gao, H., Zhang, J., & Wang, M. (2013). Controllable growth and photocatalytic activity of Cu_2O solid microspheres. *Materials Research Bulletin*, *48*(9), 3431–3437.

Gao, P., Liu, Y., Bu, X., Hu, M., Dai, Y., Gao, X., & Lei, L. (2013). Solvothermal synthesis of α-PbO from lead dioxide and its electrochemical performance as a positive electrode material. *Journal of Power Sources*, *242*, 299–304.

Garza-Arévalo, J. I., García-Montes, I., Reyes, M. H., Guzmán-Mar, J. L., Rodríguez-González, V., & Reyes, L. H. (2016). Fe doped TiO_2 photocatalyst for the removal of As(III) under visible radiation and its potential application on the treatment of As-contaminated groundwater. *Materials Research Bulletin*, *73*, 145–152.

Geldasa, F. T., Kebede, M. A., Shura, M. W., & Hone, F. G. (2022). Density functional theory study of different metal dopants influence on the structural and electronic properties of a tetragonal α-PbO. *AIP Advances*, *12*(11), 115302.

George, A., Magimai Antoni Raj, D., Venci, X., Dhayal Raj, A., Albert Irudayaraj, A., Josephine, R. L., John Sundaram, S., Al-Mohaimeed, A. M., Al Farraj, D. A., Chen, T. W., & Kaviyarasu, K. (2022). Photocatalytic effect of CuO nanoparticles flower-like 3D nanostructures under visible light irradiation with the degradation of methylene blue (MB) dye for environmental application. *Environmental Research*, *203*, 1–6.

Ghazanfar, M., Azam, S., Farooq, M., & Khan, R. (2021). Effect of manganese on electronic and optical properties of Ba_2ZnS_3: A DFT study. *Journal of Solid State Chemistry*, *301*, 122335.

Ghoderao, K. P., Jamble, S. N., & Kale, R. B. (2018). Influence of pH on hydrothermally derived ZnO nanostructures. *Optik*, *156*, 758–771.

Giannozzi, P., Andreussi, O., Brumme, T., Bunau, O., Buongiorno Nardelli, M., Calandra, M., Car, R., Cavazzoni, C., Ceresoli, D., Cococcioni, M., Colonna, N., Carnimeo, I., Dal Corso, A., De Gironcoli, S., Delugas, P., Distasio, R. A., Ferretti, A., Floris, A., Fratesi, G., Baroni, S. (2017). Advanced capabilities for materials modelling with Quantum ESPRESSO. *Journal of Physics Condensed Matter*, *29*(46), 1–31.

Giannozzi, Paolo, Baroni, S., Bonini, N., Calandra, M., Car, R., Cavazzoni, C., Ceresoli, D.,

Chiarotti, G. L., Cococcioni, M., Dabo, I., Corso, A. D., Gironcoli, S. De, Fabris, S., Fratesi, G., Gebauer, R., Gerstmann, U., Gougoussis, C., Kokalj, A., Lazzeri, M., Umari, P. (2009). *QUANTUM ESPRESSO : a modular and open-source software project for quantum simulations of materials*. *395502*.

Gillman, P. K. (2006). Methylene blue implicated in potentially fatal serotonin toxicity. *Anaesthesia*, *61*(10), 1007–1019.

Godlaveeti, S. K., Somala, A. R., Sana, S. S., Ouladsmane, M., Ghfar, A. A., & Nagireddy, R. R. (2022). Evaluation of pH Effect of Tin Oxide (SnO_2) Nanoparticles on Photocatalytic Degradation, Dielectric and Supercapacitor Applications. *Journal of Cluster Science*, *33*(4), 1635–1644.

Grimes, R. T., Leginze, J. A., Zochowski, R., & Bennett, J. W. (2021). Surface Transformations of Lead Oxides and Carbonates Using First-Principles and Thermodynamics Calculations. *Inorganic Chemistry*, *60*(2), 1228–1240.

Güngör, A., Genç, R., & Özdemir, T. (2017). Facile Synthesis of Semiconducting Nanosized 0D and 2D Lead Oxides Using a Modified Co-Precipitation Method. *Journal of the Turkish Chemical Society, 4(3)*, 1017–1030.

Gunjakar, J. L., Jo, Y. K., Kim, I. Y., Lee, J. M., Patil, S. B., Pyun, J. C., & Hwang, S. J. (2016). A chemical bath deposition route to facet-controlled Ag_3PO_4 thin films with improved visible light photocatalytic activity. *Journal of Solid State Chemistry*, *240*, 115–121.

Guo, J., Zhu, S., Chen, Z., Li, Y., Yu, Z., Liu, Q., Li, J., Feng, C., & Zhang, D. (2011). Sonochemical synthesis of TiO_2 nanoparticles on graphene for use as photocatalyst. *Ultrasonics Sonochemistry*, *18*(5), 1082–1090.

Gyawali, G., Adhikari, R., Joshi, B., Kim, T. H., Rodríguez-González, V., & Lee, S. W. (2013). Sonochemical synthesis of solar-light-driven Ag̊-$PbMoO_4$ photocatalyst. *Journal of Hazardous Materials*, *263*, 45–51.

Hai, K., Tang, D., & Wang, X. G. (2013). Effect of an oxidizing environment on the phase structure of lead oxide nanowires. *AIP Advances*, *3*(2), 1–6.

Hanifehpour, Y., Mirtamizdoust, B., Farzam, A. R., & Joo, S. W. (2012). Synthesis and Crystal Structure of $[Pb(phen)(\mu\text{-}N_3)(\mu\text{-}NO_3)]_n$ and Its Thermal Decomposition to PbO Nanoparticles. *Journal of Inorganic and Organometallic Polymers and Materials*, *22*(5), 957–962.

Harjuoja, J., Kosola, A., Putkonen, M., & Niinisto, L. (2006). Atomic layer deposition and post-deposition annealing of $PbTiO_3$ thin films. *Thin Solid Films*, *496*, 346–352.

Hassanjani-Roshan, A., Vaezi, M. R., Shokuhfar, A., & Rajabali, Z. (2011). Synthesis of iron oxide nanoparticles via sonochemical method and their characterization. *Particuology*, *9*(1), 95–99.

He, X., & Zhang, C. (2019). Recent advances in structure design for enhancing photocatalysis. *Journal of Materials Science*, *54*(12), 8831–8851.

Helal, A., El-Sheikh, S. M., Yu, J., Eid, A. I., El-Haka, S. A., & Samra, S. E. (2020). Novel synthesis of $BiVO_4$ using homogeneous precipitation and its enhanced photocatalytic activity. *Journal of Nanoparticle Research*, *22*(6), 1–12.

Heshmatpour, F., & Aghakhanpour, R. B. (2011). Synthesis and characterization of nanocrystalline zirconia powder by simple sol-gel method with glucose and fructose as organic additives. *Powder Technology*, *205*(1–3), 193–200.

Hill, R. J. (1985). Refinement of the structure of orthorhombic PbO (massicot) by Rietveld analysis of neutron powder diffraction data. *Acta Crystallographica, C41*, 1281–1284.

Hitam, C. N. C., & Jalil, A. A. (2020). A review on exploration of Fe_2O_3 photocatalyst towards degradation of dyes and organic contaminants. *Journal of Environmental Management*, *258*, 1–19.

Hodes, G. (2007). Semiconductor and ceramic nanoparticle films deposited by chemical bath deposition. *Physical Chemistry Chemical Physics*, *9*(18), 2181–2196.

Holmes, A. L., Islam, M. R., Chelakara, R. V., Ciuba, F. J., & Dupuis, R. D. (1995). High-reflectivity visible-wavelength semiconductor native oxide Bragg reflectors grown by metalorganic chemical vapor deposition. *Appl. Phys. Lett. 66 (21)*, 2831, 1–4.

Hone, F. G., & Dejene, F. B. (2018). Synthesis and characterization of lead sulphide thin films from ethanolamine (ETA) complexing agent chemical bath. *Materials Research Express*, *5*(2), 026409.

Hone, F. G., & Dejene, F. B. (2019). Chemosynthesis of nanostructures lead sulphide thin films from triethylamin (Et_3N) complexing agent. *Inorganic Chemistry Communications, 111*, 107583.

Hoque, M. A., Ahmed, M. R., Rahman, G. T., Rahman, M. T., Islam, M. A., Khan, M. A., & Hossain, M. K. (2018). Fabrication and comparative study of magnetic Fe and α-Fe_2O_3

nanoparticles dispersed hybrid polymer (PVA+Chitosan) novel nanocomposite film. *Results in Physics, 10*, 434-443.

Hsieh, S. H., Manivel, A., Lee, G. J., & Wu, J. J. (2013). Synthesis of mesoporous Bi_2O_3/CeO_2 microsphere for photocatalytic degradation of Orange II dye. *Materials Research Bulletin*, *48*(10), 4174–4180.

Huang, B., & Hart, J. N. (2020). DFT study of various tungstates for photocatalytic water splitting. *Physical Chemistry Chemical Physics*, *22*(3), 1727–1737. https://doi.org/10.1039/c9cp05944j

Hyun-jun Shin, and B. M. (2013). Direct Synthesis of PbO Nanoparticles from a Lead(II) Nanoflower Coordination Polymer Precursor : Synthesis, Crystal Structure and DFT Calculations of $[Pb(pcih)N_3H_2O]_n$ with the Terminal Azide Unit. *J. Inorg. Organomet Polym. 10*, 1–8.

Ibrahim, I. A. M., & Chung, C. Y. (2022). Lead-free double perovskites: how divalent cations tune the electronic structure for photovoltaic applications. *Journal of Materials Chemistry C*, *10*(34), 12276–12285.

Islam, M. R., Saiduzzaman, M., Nishat, S. S., Kabir, A., & Farhad, S. F. U. (2021). Synthesis, characterization and visible light-responsive photocatalysis properties of Ce doped CuO nanoparticles: A combined experimental and DFT+U study. *Colloids and Surfaces A: Physicochemical and Engineering Aspects*, *617*, 126386.

Iwaszuk, A., & Nolan, M. (2013). Lead oxide-modified TiO_2 photocatalyst: Tuning light absorption and charge carrier separation by lead oxidation state. *Catalysis Science and Technology*, *3*(8), 2000–2008.

Jaafar, M., Fard, S., Hayati, P., Naraghi, H. S., & Tabeie, S. A. (2017). Synthesis and Characterization of a New Nano Lead(II) 0-D Coordination Supramolecular Compound: A Precursor to Produce Pure Phase Nano-sized Lead(II) Oxide. *Ultrasonics-Sonochemistry*, *39*, 129-136.

Jahnavi, V. S., Tripathy, S. K., & Ramalingeswara Rao, A. V. N. (2019). Structural, optical, magnetic and dielectric studies of SnO_2 nano particles in real time applications. *Physica B: Condensed Matter*, *565*, 61–72.

Jamil, S., Khan, S. R., Sultana, B., Hashmi, M., Haroon, M., & Janjua, M. R. S. A. (2018). Synthesis of Saucer Shaped Manganese Oxide Nanoparticles by Co-precipitation Method

and the Application as Fuel Additive. *Journal of Cluster Science*, *29*(6), 1099–1106.

Jang, H. D., & Jeong, J. (1995). The effects of temperature on particle size in the gas-phase production of TiO_2. *Aerosol Science and Technology*, *23*(4), 553–560.

Jeevitha, G., Abhinayaa, R., Mangalaraj, D., & Ponpandian, N. (2018). Tungsten oxide-graphene oxide (WO_3-GO) nanocomposite as an efficient photocatalyst, antibacterial and anticancer agent. *Journal of Physics and Chemistry of Solids*, *116*, 137–147.

Ji, Z., Luo, Z., Li, J., & Li, P. (2019). Enhanced Photocatalytic Activity of ZnO Toward the Degradation of Methylene Blue Dye: Effects of Fe^{3+} and Sn^{4+} Doping. *Physica Status Solidi (A) Applications and Materials Science*, *216*(7), 1–9.

Jia, B., & Gao, L. (2006). Synthesis and characterization of single crystalline PbO nanorods via a facile hydrothermal method. *Materials Chemistry and Physics*, *100*(2–3), 351–354.

Jia, W., Niu, Y., Zhou, M., Liu, R., Zhang, L., Wang, X., & Ji, W. (2019). Effects of vacancy defects on the electronic structure and optical properties of GaN:Fe. *Superlattices and Microstructures*, *133*, 1–9.

Kabbur, S. M., Waghmare, S. D., Ghodake, U. R., & Suryavanshi, S. S. (2018). Synthesis, morphology and electrical properties of Co^{2+} substituted NiCuZn ferrites for MLCI applications. *AIP Conference Proceedings*, *1942*(April 2018), 2–6.

Kale, A. J., Chaurasiya, R., & Dixit, A. (2021). Inorganic Lead-Free $Cs_2AuBiCl_6$ Perovskite Absorber and Cu_2O Hole Transport Material Based Single-Junction Solar Cells with 22.18% Power Conversion Efficiency. *Advanced Theory and Simulations*, *4*(3), 1–14.

Kamel, G. M., El-Nahass, M. N., El-Khouly, M. E., Fayed, T. A., & El-Kemary, M. (2019). Simple, selective detection and efficient removal of toxic lead and silver metal ions using Acid Red 94. *RSC Advances*, *9*(15), 8355–8363.

Kandasamy, M., Seetharaman, A., Sivasubramanian, D., Nithya, A., Jothivenkatachalam, K., Maheswari, N., Gopalan, M., Dillibabu, S., & Eftekhari, A. (2018). Ni-Doped SnO_2 Nanoparticles for Sensing and Photocatalysis. *ACS Applied Nano Materials*, *1*(10), 5823–5836.

Kangralkar, M. V., Kangralkar, V. A., Momin, N., & Manjanna, J. (2019). Cu_2O nanoparticles for removal of methylene blue dye from solution. *Environmental Nanotechnology, Monitoring & Management*, *12*, 100265.

Karami, H., Karimi, M. A., Haghdar, S., Sadeghi, A., Mir-Ghasemi, R., & Mahdi-Khani, S.

(2008). Synthesis of lead oxide nanoparticles by Sonochemical method and its application as cathode and anode of lead-acid batteries. *Materials Chemistry and Physics*, *108*(2–3), 337–344.

Karthikeyan, S., Ahmed, K., Osatiashtiani, A., Lee, A. F., Wilson, K., Sasaki, K., Coulson, B., Swansborough-Aston, W., Douthwaite, R. E., & Li, W. (2020). Pompon Dahlia-like Cu_2O/rGO Nanostructures for Visible Light Photocatalytic H_2 Production and 4-Chlorophenol Degradation. *ChemCatChem*, *12*(6), 1699–1709.

Karuppasamy, P., Ramzan Nilofar Nisha, N., Pugazhendhi, A., Kandasamy, S., & Pitchaimuthu, S. (2021). An investigation of transition metal doped TiO_2 photocatalysts for the enhanced photocatalytic decoloration of methylene blue dye under visible light irradiation. *Journal of Environmental Chemical Engineering*, *9*(4), 105254.

Kashani-Motlagh, M. M., & Mahmoudabad, M. K. (2011). Synthesis and characterization of lead oxide nano-powders by sol-gel method. *Journal of Sol-Gel Science and Technology*, *59*(1), 106–110.

Kerour, A., Boudjadar, S., Bourzami, R., & Allouche, B. (2018). Eco-friendly synthesis of cuprous oxide (Cu_2O) nanoparticles and improvement of their solar photocatalytic activities. *Journal of Solid State Chemistry*, *263*, 79–83.

Khalil, A. T., Ovais, M., Ullah, I., Ali, M., Jan, A., Shinwari, Z. K., & Maaza, M. (2017). Bioinspired synthesis of pure massicot phase lead oxide nanoparticles and assessment of their biocompatibility, cytotoxicity and in-vitro biological properties. *Arabian Journal of Chemistry*, *13*, 916-931.

Khan, I., Saeed, K., Zekker, I., Zhang, B., Hendi, A. H., Ahmad, A., Ahmad, S., Zada, N., Ahmad, H., Shah, L. A., Shah, T., & Khan, I. (2022). Review on Methylene Blue: Its Properties, Uses, Toxicity and Photodegradation. *Water*, *14*(2), 1–30.

Khashaei, M., Kafi-Ahmadi, L., Khademinia, S., Poursattar Marjani, A., & Nozad, E. (2022). A facile hydrothermal synthesis of high-efficient NiO nanocatalyst for preparation of 3,4-dihydropyrimidin-2(1H)-ones. *Scientific Reports*, *12*(1), 1–15.

Khlyustova, A., Sirotkin, N., Kusova, T., Kraev, A., Titov, V., & Agafonov, A. (2020). Doped TiO_2: The effect of doping elements on photocatalytic activity. *Materials Advances*, *1*(5), 1193–1201.

Khodaie, M., Ghasemi, N., Moradi, B., & Rahimi, M. (2013). Removal of methylene blue from

wastewater by adsorption onto znclactivated corn husk carbon equilibrium studies. *Journal of Chemistry*, *2013*, 1–7.

Kim, S. P., Choi, M. Y., & Choi, H. C. (2016). Photocatalytic activity of SnO_2 nanoparticles in methylene blue degradation. *Materials Research Bulletin*, *74*, 85–89.

King-Smith, R. D., & Vanderbilt, D. (1993). Theory of polarization of crystalline solids. *Physical Review B*, *47*(3), 1651–1654.

Kishor Kumar, M. J., & Kalathi, J. T. (2018). Low-temperature sonochemical synthesis of high dielectric Lanthanum doped Cerium oxide nanopowder. *Journal of Alloys and Compounds*, *748*, 348–354.

Kitchamsetti, N., Ramteke, M. S., Rondiya, S. R., Mulani, S. R., Patil, M. S., Cross, R. W., Dzade, N. Y., & Devan, R. S. (2021). DFT and experimental investigations on the photocatalytic activities of NiO nanobelts for removal of organic pollutants. *Journal of Alloys and Compounds*, *855*, 1–10.

Koe, W. S., Lee, J. W., Chong, W. C., Pang, Y. L., & Sim, L. C. (2020). An overview of photocatalytic degradation: photocatalysts, mechanisms, and development of photocatalytic membrane. *Environmental Science and Pollution Research*, *27*(3), 2522–2565.

Kohn, W., Becke, A. D., & Parr, R. G. (1996). Density functional theory of electronic structure. *Journal of Physical Chemistry*, *100*(31), 12974–12980.

Kokalj, A. (1999). XCrySDen-a new program for displaying crystalline structures and electron densities. *Journal of Molecular Graphics and Modelling*, *17*(3–4), 176–179.

Kotresh, M. G., Patil, M. K., & Inamdar, S. R. (2021). Reaction temperature based synthesis of ZnO nanoparticles using co-precipitation method: Detailed structural and optical characterization. *Optik*, *243*, 1–10.

Krishna Moorthy, A., Govindarajan Rathi, B., Shukla, S. P., Kumar, K., & Shree Bharti, V. (2021). Acute toxicity of textile dye Methylene blue on growth and metabolism of selected freshwater microalgae. *Environmental Toxicology and Pharmacology*, *82*, 1–10.

Kumar, A., Saxena, A., De, A., Shankar, R., & Mozumdar, S. (2013). Facile synthesis of size-tunable copper and copper oxide nanoparticles using reverse microemulsions. *RSC Advances*, *3*(15), 5015–5021.

Kumar, K. V., Porkodi, K., & Rocha, F. (2008). Langmuir-Hinshelwood kinetics - A theoretical study. *Catalysis Communications*, *9*(1), 82–84.

Kumar, P., Liu, J., Ranjan, P., Hu, Y., Yamijala, S. S. R. K. C., Pati, S. K., Irudayaraj, J., & Cheng, G. J. (2018). Alpha Lead Oxide (α-PbO): A New 2D Material with Visible Light Sensitivity. *Small*, *14*(12), 1–10.

Kushniarou, A., Garrido, I., Fenoll, J., Vela, N., Flores, P., Navarro, G., Hellín, P., & Navarro, S. (2019). Solar photocatalytic reclamation of agro-waste water polluted with twelve pesticides for agricultural reuse. *Chemosphere*, *214*, 839–845.

Lambat, T. L., Chaudhary, R. G., Abdala, A. A., Mishra, R. K., Mahmood, S. H., & Banerjee, S. (2019). Mesoporous PbO nanoparticle-catalyzed synthesis of arylbenzodioxy xanthenedione scaffolds under solvent-free conditions in a ball mill. *RSC Advances*, *9*(54), 31683–31690.

Leelavathi, A., Mukherjee, B., Nethravathi, C., Kundu, S., Dhivya, M., Ravishankar, N., & Madras, G. (2013). Highly photoactive heterostructures of PbO quantum dots on TiO_2. *RSC Advances*, *3*(43), 20970–20977.

Leijtens, T., Eperon, G. E., Barker, A. J., Grancini, G., Zhang, W., Ball, J. M., Kandada, A. R. S., Snaith, H. J., & Petrozza, A. (2016). Carrier trapping and recombination: The role of defect physics in enhancing the open circuit voltage of metal halide perovskite solar cells. *Energy and Environmental Science*, *9*(11), 3472–3481.

Lemecho, B. A., Sabir, F. K., Andoshe, D. M., Gultom, N. S., Kuo, D. H., Chen, X., Mulugeta, E., Desissa, T. D., & Zelekew, O. A. (2022). Biogenic Synthesis of Cu-Doped ZnO Photocatalyst for the Removal of Organic Dye. *Bioinorganic Chemistry and Applications*, *2022*, 1–10.

Li, J., Guo, M., Shao, Y., Yu, H., & Ni, K. (2021). Electrocatalytic Properties of a Novel β-PbO_2/Halloysite Nanotube Composite Electrode. *ACS Omega*, *6*(8), 5436–5444.

Li, N., Jiang, Y., He, Y. long, Gao, L., Yi, Z. zhou, Zhai, F. rui, & Chattopadhyay, K. (2021). Sustainable synthesis of multiple-metal-doped Fe_2O_3 nanoparticles with enhanced photocatalytic performance from Fe-bearing dust. *Journal of Materials Research and Technology*, *15*, 810–820.

Li, Q., Chen, Z., Wang, H., Yang, H., Wen, T., Wang, S., Hu, B., & Wang, X. (2021). Removal of organic compounds by nanoscale zero-valent iron and its composites. *Science of the Total Environment*, *792*, 148546.

Li, S., Yang, W., Chen, M., Gao, J., Kang, J., & Qi, Y. (2005). Preparation of PbO nanoparticles by microwave irradiation and their application to Pb(II)-selective electrode based on

cellulose acetate. *Materials Chemistry and Physics*, *90*, 262–269.

Li, T., Quan, S., Shi, X., Yang, L., & Liu, C. (2020). Fabrication of La-Doped Bi_2O_3 Nanoparticles with Oxygen Vacancies for Improving Photocatalytic Activity. *Catalysis Letters*, *150*(3), 640–651.

Li, Weidong, Yang, H., & Liu, Q. (2017). Hydrothermal Synthesis of PbO_2/RGO Nanocomposite for Electrocatalytic Degradation of Cationic Red X-GRL. *Journal of Nanomaterials*, *2017*, 1–8

Li, Wenqing, Walther, C. F. J., Kuc, A., & Heine, T. (2013). Density Functional Theory and Beyond for Band-Gap Screening: Performance for Transition-Metal Oxides and Dichalcogenides. *J. Chem. Theory Comput. 9*, 2950−2958.

Li, Yang, Zhao, J., Zhang, G., Zhang, L., Ding, S., Shang, E., & Xia, X. (2019). Visible-light-driven photocatalytic disinfection mechanism of Pb-$BiFeO_3$/rGO photocatalyst. *Water Research*, *161*, 251–261.

Li, Yuanyuan, Yang, Q., Wang, Z., Wang, G., Zhang, B., Zhang, Q., & Yang, D. (2018). Rapid fabrication of SnO_2 nanoparticle photocatalyst: Computational understanding and photocatalytic degradation of organic dye. *Inorganic Chemistry Frontiers*, *5*(12), 3005–3014.

Liang, D., Liu, S., Wang, Z., Guo, Y., Jiang, W., Liu, C., Wang, H., Wang, N., Ding, W., He, M., Wang, L., & Xu, S. (2019). Coprecipitation synthesis of N, Fe doped anatase TiO_2 nanoparticles and photocatalytic mechanism. *Journal of Materials Science: Materials in Electronics*, *30*(13), 12619–12629.

Liang, X., Li, W., Li, J., Niu, G., & Wang, L. (2016). High quality perovskite thin films induced by crystal seeds with lead monoxide interfacial engineering. *Journal of Materials Chemistry A*, *4*(43), 16913–16919.

Liao, M., Takemoto, S., Xiao, Z., Toda, Y., Tada, T., Ueda, S., Kamiya, T., & Hosono, H. (2016). Difficulty of carrier generation in orthorhombic PbO. *Journal of Applied Physics*, *119*(16), 1–8.

Lima, L. F. de S., Coelho, C. R., Gomes, G. H. M., & Mohallem, N. D. S. (2020). Nb_2O_5/SiO_2 mesoporous monoliths synthetized by sol–gel process using ammonium niobate oxalate hydrate as porogenic agent. *Journal of Sol-Gel Science and Technology*, *93*(1), 168–174.

Lin, J., Luo, Z., Liu, J., & Li, P. (2018). Photocatalytic degradation of methylene blue in aqueous

solution by using ZnO-SnO_2 nanocomposites. *Materials Science in Semiconductor Processing*, *87*(20), 24–31.

Lin, X., Fu, D., Hao, L., & Ding, Z. (2013). Synthesis and enhanced visible-light responsive of C,N,S-tridoped TiO2 hollow spheres. *Journal of Environmental Sciences (China)*, *25*(10), 2150–2156.

Liu, F. Y., Lin, J. H., Dai, Y. M., Chen, L. W., Huang, S. T., Yeh, T. W., Chang, J. L., & Chen, C. C. (2018). Preparation of perovskites $PbBiO_2I$/PbO exhibiting visible-light photocatalytic activity. *Catalysis Today*, *314*, 28–41.

Liu, N., Senthil, R. A., Zhang, X., Pan, J., & Sun, Y. (2020). A green and cost-effective process for recovery of high purity α-PbO from spent lead acid batteries. *Journal of Cleaner Production*, *267*, 122107. https://doi.org/10.1016/j.jclepro.2020.122107

Liu, S., Wei, X., Lin, S., & Guo, M. (2021). Preparation of aerogel $Mg(OH)_2$ nanosheets by a combined sol–gel-hydrothermal process and its calcined MgO towards enhanced degradation of paraoxon pollutants. *Journal of Sol-Gel Science and Technology*, *99*(1), 122–131.

Liu, W., Ma, B., Fu, Y., Zhang, K., Mezaal, M. A., Li, F., Zhao, X., & Lei, L. (2017). Electrochemical property of α-PbO prepared from the spent negative powders of lead acid batteries. *Journal of Solid State Electrochemistry*, *21*(1), 35–46.

Liu, Y., Wang, W., Xu, X., Marcel Veder, J. P., & Shao, Z. (2019). Recent advances in anion-doped metal oxides for catalytic applications. *Journal of Materials Chemistry A*, *7*(13), 7280–7300.

Luo, J., Zhang, S., Sun, M., Yang, L., Luo, S., & Crittenden, J. C. (2019). A Critical Review on Energy Conversion and Environmental Remediation of Photocatalysts with Remodeling Crystal Lattice, Surface, and Interface. *ACS Nano*, *13*(9), 9811–9840.

M., J. A., A., P., N., S., K., J., P., F. H. I., & J., J. prince. (2019). Flake-like $CuMn_2O_4$ nanoparticles synthesized via co-precipitation method for photocatalytic activity. *Physica B: Condensed Matter*, *572*(May), 117–124.

Machala, L., Tuček, J., & Zbořil, R. (2011). Polymorphous transformations of nanometric iron(III) oxide: A review. *Chemistry of Materials*, *23*(14), 3255–3272.

Mahdavi, R., & Talesh, S. S. A. (2017). Sol-gel synthesis, structural and enhanced photocatalytic performance of Al doped ZnO nanoparticles. *Advanced Powder Technology*, *28*(5), 1418–

1425.

Makkar, P., & Ghosh, N. N. (2021). A review on the use of DFT for the prediction of the properties of nanomaterials. *RSC Advances*, *11*(45), 27897–27924.

Makuła, P., Pacia, M., & Macyk, W. (2018). How To Correctly Determine the Band Gap Energy of Modified Semiconductor Photocatalysts Based on UV–Vis Spectra. *The Journal of Physical Chemistry Letters*, *9*(23), 6814–6817. https://doi.org/10.1021/acs.jpclett.8b02892

Malwal, D., & Gopinath, P. (2016). Enhanced photocatalytic activity of hierarchical three dimensional metal oxide@CuO nanostructures towards the degradation of Congo red dye under solar radiation. *Catalysis Science and Technology*, *6*(12), 4458–4472.

Manivel, A., Lee, G. J., Chen, C. Y., Chen, J. H., Ma, S. H., Horng, T. L., & Wu, J. J. (2015). Synthesis of MoO3 nanoparticles for azo dye degradation by catalytic ozonation. *Materials Research Bulletin*, *62*, 184–191.

Maraj, M., Raza, A., Wang, X., Chen, J., Riaz, K. N., & Sun, W. (2021). Mo-doped CuO nanomaterial for photocatalytic degradation of water pollutants under visible light. *Catalysts*, *11*(10), 1–10.

Martínez-Gil, M., Pintor-Monroy, M. I., Cota-Leal, M., Cabrera-German, D., Garzon-Fontecha, A., Quevedo-López, M. A., & Sotelo-Lerma, M. (2017). Influence of annealing temperature on nickel oxide thin films grown by chemical bath deposition. *Materials Science in Semiconductor Processing*, *72*, 37–45.

Masudy-Panah, S., Katal, R., Khiavi, N. D., Shekarian, E., Hu, J., & Gong, X. (2019). A high-performance cupric oxide photocatalyst with palladium light trapping nanostructures and a hole transporting layer for photoelectrochemical hydrogen evolution. *Journal of Materials Chemistry A*, *7*(39), 22332–22345.

McDonnell, A. M., Rybak, I., Wadleigh, M., & Fisher, D. C. (2012). Suspected serotonin syndrome in a patient being treated with methylene blue for ifosfamide encephalopathy. *Journal of Oncology Pharmacy Practice*, *18*(4), 436–439.

Mebed, A. M., Abd-Elnaiem, A. M., Alshammari, A. H., Taha, T. A., Rashad, M., & Hamad, D. (2022). Controlling the Structural Properties and Optical Bandgap of $PbO–Al_2O_3$ Nanocomposites for Enhanced Photodegradation of Methylene Blue. *Catalysts*, *12*(2), 1–16.

Medhi, R., Marquez, M. D., & Lee, T. R. (2020). Visible-Light-Active Doped Metal Oxide Nanoparticles: Review of their Synthesis, Properties, and Applications. *ACS Applied Nano*

Materials, *3*(7), 6156–6185.

Mehdi, M., & Mehdi, F. (2017). Graphene Oxide Doped with PbO Nanoparticles , Synthesis by Microwave Assistant Thermal Decomposition and Investigation of Optical Property. *Journal of Cluster Science*, 1–10.

Mehrjouei, M., Müller, S., & Möller, D. (2015). A review on photocatalytic ozonation used for the treatment of water and wastewater. *Chemical Engineering Journal*, *263*, 209–219.

Mehtab, A., Ahmed, J., Alshehri, S. M., Mao, Y., & Ahmad, T. (2022). Rare earth doped metal oxide nanoparticles for photocatalysis: A perspective. *Nanotechnology*, *33*(14), 1–33.

Mendiola-Alvarez, S. Y., Hernández-Ramírez, A., Guzmán-Mar, J. L., Maya-Treviño, M. L., Caballero-Quintero, A., & Hinojosa-Reyes, L. (2019). A novel P-doped Fe_2O_3-TiO_2 mixed oxide: Synthesis, characterization and photocatalytic activity under visible radiation. *Catalysis Today*, *328*, 91–98.

Mirzaeifard, Z., Shariatinia, Z., Jourshabani, M., & Rezaei Darvishi, S. M. (2020). ZnO Photocatalyst Revisited: Effective Photocatalytic Degradation of Emerging Contaminants Using S-Doped ZnO Nanoparticles under Visible Light Radiation. *Industrial and Engineering Chemistry Research*, *59*(36), 15894–15911.

Mirzajani, V., Farhadi, K., & Pourmortazavi, S. M. (2018). Catalytic effect of lead oxide nano- and microparticles on thermal decomposition kinetics of energetic compositions containing TEGDN/NC/DAG. *Journal of Thermal Analysis and Calorimetry*, *131*(2), 937–948.

Mishra, M., & Chun, D. M. (2015). α-Fe_2O_3 as a photocatalytic material: A review. *Applied Catalysis A: General*, *498*, 126–141. https://doi.org/10.1016/j.apcata.2015.03.023

Mochane, M. J., Motloung, M. T., Mokhena, T. C., & Mofokeng, T. G. (2022). Morphology and Photocatalytic Activity of Zinc Oxide Reinforced Polymer Composites: A Mini Review. *Catalysts*, *12*(11), 1–19.

Mohammed, A. M., Mohtar, S. S., Aziz, F., Mhamad, S. A., & Aziz, M. (2021). Review of various strategies to boost the photocatalytic activity of the cuprous oxide-based photocatalyst. *Journal of Environmental Chemical Engineering*, *9*(2), 1–16.

Momma, K., & Izumi, F. (2011). VESTA 3 for three-dimensional visualization of crystal, volumetric and morphology data. *Journal of Applied Crystallography*, *44*(6), 1272–1276.

Mondol, B., Sarker, A., Shareque, A. M., Dey, S. C., Islam, M. T., Das, A. K., Shamsuddin, S. M., Molla, M. A. I., & Sarker, M. (2021). Preparation of Activated Carbon/TiO_2

Nanohybrids for Photodegradation of Reactive Red-35 Dye Using Sunlight. *Photochem*, *1*(1), 54–66.

Mousavi-Kamazani, M., & Azizi, F. (2019). Facile sonochemical synthesis of Cu doped CeO_2 nanostructures as a novel dual-functional photocatalytic adsorbent. *Ultrasonics Sonochemistry*, *58*, 1–15.

Mugunthan, E., Saidutta, M. B., & Jagadeeshbabu, P. E. (2019). Photocatalytic activity of ZnO-WO_3 for diclofenac degradation under visible light irradiation. *Journal of Photochemistry and Photobiology A: Chemistry*, *383*, 1–15.

Muhammady, S., Noor, F. A., Widita, R., & Darma, Y. (2020). Ferromagnetism and structural deformation in monolayer alpha lead oxide induced by N and F doping: New insights from first principles. *International Journal of Quantum Chemistry*, *120*(16), 1–11.

Murata, H., Kataoka, Y., Kawamoto, T., Tanaka, I., & Taniguchi, T. (2014). Photocatalytic activity of α-PbO_2-type TiO_2. *Physica Status Solidi - Rapid Research Letters*, *8*(10), 822–826.

Muthukumaran, M., Gnanamoorthy, G., Varun Prasath, P., Abinaya, M., Dhinagaran, G., Sagadevan, S., Mohammad, F., Oh, W. C., & Venkatachalam, K. (2020). Enhanced photocatalytic activity of Cuprous Oxide nanoparticles for malachite green degradation under the visible light radiation. *Materials Research Express*, *7*(1), 015038.

Mythili, N., & Arulmozhi, K. T. (2014). Characterization Studies on the Chemically Synthesized alpha and beta Phase PbO Nanoparticles. *International Journal of Scientific & Engineering Research*, *5*(1), 412–416.

Mythili, N., & Arulmozhi, K. T. (2015). Studies on the electrical and dielectric properties of chemically synthesized α-PbO nanoparticles. *Applied Physics A*, *118*, 261–267.

Naeem, R., Yahya, R., Pandikumar, A., Ming, H. N., & Mazhar, M. (2017). Optical and optoelectronic properties of morphology and structure controlled ZnO, CdO and PbO thin films deposited by electric field directed aerosol assisted CVD. *Journal of Materials Science: Materials in Electronics*, *28*(1), 868–877.

Nafees, M., Ikram, M., & Ali, S. (2017). Thermal stability of lead sulfide and lead oxide nano-crystalline materials. *Applied Nanoscience (Switzerland)*, *7*(7), 399–406.

Najafi, E., Amini, M. M., Behmagham, F., Shaabani, N., & Shojaei, N. (2019). Crystal structure and luminescence properties of a new nanostructure lead(II) complex : a precursor for

preparation of pure phase nanosized PbO. *Chemical Review and Letters*, *2*, 13–20.

Napari, M., Huq, T. N., Hoye, R. L. Z., & MacManus-Driscoll, J. L. (2021). Nickel oxide thin films grown by chemical deposition techniques: Potential and challenges in next-generation rigid and flexible device applications. *InfoMat*, *3*(5), 536–576.

Narkbuakaew, T., & Sujaridworakun, P. (2019). Role of Ag (^{0}) deposited on TiO_2 nanoparticles for superior photocatalytic performance induced by calcination. *Optical Materials*, *98*, 1–7.

Nazim, M., Khan, A. A. P., Asiri, A. M., & Kim, J. H. (2021). Exploring Rapid Photocatalytic Degradation of Organic Pollutants with Porous CuO Nanosheets: Synthesis, Dye Removal, and Kinetic Studies at Room Temperature. *ACS Omega*, *6*(4), 2601–2612.

Ndabankulu, V. O., Maddila, S., & Jonnalagadda, S. B. (2019). Synthesis of lanthanide-doped TiO_2 nanoparticles and their photocatalytic activity under visible light. *Canadian Journal of Chemistry*, *00*(9), 1–10.

Ng, D. Q., Chu, Y., Tan, S. W., Wang, S. L., Lin, Y. P., Chu, C. H., Soo, Y. L., Song, Y. F., & Chen, P. J. (2019). In vivo evidence of intestinal lead dissolution from lead dioxide (PbO_2) nanoparticles and resulting bioaccumulation and toxicity in medaka fish. *Environmental Science: Nano*, *6*(2), 580–591.

Noman, M. T., Petru, M., Militkỳ, J., Azeem, M., & Ashraf, M. A. (2020). One-Pot sonochemical synthesis of ZnO nanoparticles for photocatalytic applications, modelling and optimization. *Materials*, *13*(1), 1–18.

Noukelag, S. K., Mohamed, H. E. A., Razanamahandry, L. C., Ntwampe, S. K. O., & Arendse, C. J. (2019). Bio-inspired synthesis of PbO nanoparticles (NPs) via an aqueous extract of Rosmarinus officinalis (rosemary) leaves. *Materials Today: Proceedings*, *36*, 421–426.

Nwanya, A. C., Ugwuoke, P. E., Ezekoye, B. A., Osuji, R. U., & Ezema, F. I. (2013). Structural and Optical Properties of Chemical Bath Deposited Silver Oxide Thin Films: Role of Deposition Time. *Advances in Materials Science and Engineering*, *2013*(14), 2–8.

Oktavianti, N. I., Anindika, G. R., Ivansyah, A. L., Juwono, H., & Kusumawati, Y. (2021). Computational study of methylene blue on nickel doped ZnO cluster. *AIP Conference Proceedings*, *2349*, 1–9.

Oladoye, P. O., Ajiboye, T. O., Omotola, E. O., & Oyewola, O. J. (2022). Methylene blue dye: Toxicity and potential elimination technology from wastewater. *Results in Engineering*, *16*, 1–17.

Olama, N., Dehghani, M., & Malakootian, M. (2018). The removal of amoxicillin from aquatic solutions using the TiO_2/UV-C nanophotocatalytic method doped with trivalent iron. *Applied Water Science*, *8*(4), 1–12.

Ong, S. A., Toorisaka, E., Hirata, M., & Hano, T. (2005). Biodegradation of redox dye Methylene Blue by up-flow anaerobic sludge blanket reactor. *Journal of Hazardous Materials*, *124*(1–3), 88–94.

Opoku, F., Govender, K. K., van Sittert, C. G. C. E., & Govender, P. P. (2017a). Enhancing photocatalytic activity for hydrogen production and pollutant degradation by modifying tetragonal ZrO_2 with monolayers slab surface of $BiVO_4$, Ag_3PO_4, $SrTiO_3$ and WO_3: A first-princ. *Computational Materials Science*, *138*, 462–473.

Opoku, F., Govender, K. K., van Sittert, C. G. C. E., & Govender, P. P. (2017b). Recent Progress in the Development of Semiconductor-Based Photocatalyst Materials for Applications in Photocatalytic Water Splitting and Degradation of Pollutants. *Advanced Sustainable Systems*, *1*(7), 1–24.

Opoku, F., Govender, K. K., van Sittert, C. G. C. E., & Govender, P. P. (2017c). Role of MoS_2 and WS_2 monolayers on photocatalytic hydrogen production and the pollutant degradation of monoclinic $BiVO_4$: A first-principles study. *New Journal of Chemistry*, *41*(20), 11701–11713.

Opoku, F., Govender, K. K., van Sittert, C. G. C. E., & Govender, P. P. (2017d). Understanding the mechanism of enhanced charge separation and visible light photocatalytic activity of modified wurtzite ZnO with nanoclusters of ZnS and graphene oxide: From a hybrid density functional study. *New Journal of Chemistry*, *41*(16), 8140–8155.

P. Hohenberg, & W. Kohn. (1994). Inhomogeneous Electron Gas. *PHYSICAL REVIEW*, *136*(3B), 391–402.

Pakizeh, E., Jalilian, J., & Mohammadi, M. (2019). Electronic, optical and thermoelectric properties of Fe2ZrP compound determined: Via first-principles calculations. *RSC Advances*, *9*(44), 25900–25911.

Palanivel, C., Prabhakaran, N. R., & Selvakumar, G. (2019). Morphological expedient flower like nanostructures WO_3–TiO_2 nanocomposite material and its multi applications. *OpenNano*, *4*, 1–21.

Pang, X., Sarvothaman, V. P., Skillen, N., Wang, Z., Rooney, D. W., Ranade, V. V., &

Robertson, P. K. J. (2022). Kinetic modelling of the photocatalytic degradation of Diisobutyl phthalate and coupling with acoustic cavitation. *Chemical Engineering Journal*, *444*, 1–21.

Parashar, M., Shukla, V. K., & Singh, R. (2020). Metal oxides nanoparticles via sol–gel method: a review on synthesis, characterization and applications. *Journal of Materials Science: Materials in Electronics*, *31*(5), 3729–3749.

Pasha, S., & Chidambaram, K. (2014). Synthesis, Characterization and electrical properties of nano β–PbO. *International Journal of ChemTech Research*, *6*(3), 2106–2109.

Patel, M., Mishra, S., Verma, R., & Shikha, D. (2022). Synthesis of ZnO and CuO nanoparticles via Sol gel method and its characterization by using various technique. *Discover Materials*, *2*(1), 1–11.

Peng, B., Meng, X., Tang, F., Ren, X., Chen, D., & Ren, J. (2009). General synthesis and optical properties of monodisperse multifunctional metal-ion-doped TiO_2 hollow particles. *Journal of Physical Chemistry C*, *113*(47), 20240–20245.

Perdew, J. P., Burke, K., & Ernzerhof, M. (1998). Perdew, Burke, and Ernzerhof Reply. *Physical Review Letters*, *80*(4), 891.

Perdew, John P., Burke, K., & Ernzerhof, M. (1996). Generalized gradient approximation made simple. *Physical Review Letters*, *77*(18), 3865–3868.

Perry, D. L., & Wilkinson, T. J. (2007). Synthesis of high-purity α- And β-PbO and possible applications to synthesis and processing of other lead oxide materials. In *Applied Physics A: Materials Science and Processing, 89(1)*, 77–80).

Polat, K. (2020). Cuprous oxide film sputtered on monolayer graphene for visible light sensitive heterogeneous photocatalysis. *Thin Solid Films*, *709*, 138254.

Poll, C. G., & Payne, D. J. (2014). Electrochemical synthesis of PbO_2, Pb_3O_4 and PbO films on a transparent conducting substrate. *Electrochimica Acta*, *156*(3), 283–288.

Pourmasoud, S., Eghbali-Arani, M., Ahmadi, F., & Rahimi-Nasrabadi, M. (2017). Synthesis, characterization, and morphological control of $PbWO_4$ nanostructures through precipitation method and its photocatalyst application. *Journal of Materials Science: Materials in Electronics*, *28*(22), 17089–17097.

Pradeev raj, K., Sadaiyandi, K., Kennedy, A., Sagadevan, S., Chowdhury, Z. Z., Johan, M. R. Bin, Aziz, F. A., Rafique, R. F., Thamiz Selvi, R., & Rathina bala, R. (2018). Influence of

Mg Doping on ZnO Nanoparticles for Enhanced Photocatalytic Evaluation and Antibacterial Analysis. *Nanoscale Research Letters*, *13*, *1–13*.

Prado-Chay, D. A., Cortés-Jácome, M. A., Angeles-Chávez, C., Oviedo-Roa, R., Martínez-Magadán, J. M., Zuriaga-Monroy, C., Hernández-Hernández, I. J., Mayoral, P. R., Gómora-Herrera, D. R., & Toledo-Antonio, J. A. (2020). Synthesis and Photocatalytic Activity of Cu_2O Microspheres upon Methyl Orange Degradation. *Topics in Catalysis*, *63*(5–6), 586–600.

Prashant, R. ., & Jyothi, S. . (2010). Methylene Blue:Revisited. *J Anaesth Clin Pharmacol*, *26*(4), 517–520.

Qi, K., Xing, X., Zada, A., Li, M., Wang, Q., Liu, S. yuan, Lin, H., & Wang, G. (2020). Transition metal doped ZnO nanoparticles with enhanced photocatalytic and antibacterial performances: Experimental and DFT studies. *Ceramics International*, *46*(2), 1494–1502.

Qumar, U., Hassan, J. Z., Bhatti, R. A., Raza, A., Nazir, G., Nabgan, W., & Ikram, M. (2022). Photocatalysis vs adsorption by metal oxide nanoparticles. *Journal of Materials Science and Technology*, *131*, 122–166.

Rahmati, A., Balouch Sirgani, A., Molaei, M., & Karimipour, M. (2014). Cu-doped ZnO nanoparticles synthesized by simple co-precipitation route. *The European Physical Journal Plus*, *129*(11), 250.

Ramandi, S., Entezari, M. H., & Ghows, N. (2017). Sono-synthesis of solar light responsive S–N–C–tri doped TiO_2 photo-catalyst under optimized conditions for degradation and mineralization of Diclofenac. *Ultrasonics Sonochemistry*, *38*, 234–245.

Ramasamy Raja, V., Rosaline, D. R., Suganthi, A., & Rajarajan, M. (2018). Facile sonochemical synthesis of Zn_2SnO_4-V_2O_5 nanocomposite as an effective photocatalyst for degradation of Eosin Yellow. *Ultrasonics Sonochemistry*, *44*, 310–318.

Ramaswamy, K. P. S., Shkir, M., Yahia, I. S., & Alfaify, M. S. H. S. (2019). Analysis of neodymium rare earth element doping in PbS films for opto-electronics applications. *Journal of Materials Science: Materials in Electronics*, *31*,1817–1827.

Ramkumar, S., & Rajarajan, G. (2017). A comparative study of humidity sensing and photocatalytic applications of pure and nickel (Ni)-doped WO_3 thin films. *Applied Physics A: Materials Science and Processing*, *123*(6), 1–8.

Ramsay, R. R., Dunford, C., & Gillman, P. K. (2007). Methylene blue and serotonin toxicity:

Inhibition of monoamine oxidase A (MAOA) confirms a theoretical prediction. *British Journal of Pharmacology*, *152*(6), 946–951.

Ran, L., Zhao, D., Gao, X., & Yin, L. (2015). Highly crystalline Ti-doped SnO_2 hollow structured photocatalyst with enhanced photocatalytic activity for degradation of organic dyes. *CrystEngComm*, *17*(22), 4225–4237.

Rangel, W. M., Boca Santa, R. A. A., & Riella, H. G. (2020). A facile method for synthesis of nanostructured copper (II) oxide by coprecipitation. *Journal of Materials Research and Technology*, *9*(1), 994–1004.

Rong, R., & Wang, L. (2021). Synthesis of hierarchical hollow nest-like WO_3 micro/nanostructures with enhanced visible light-driven photocatalytic activity. *Journal of Alloys and Compounds*, *850*, 156742.

Rouf, S. A., Hussain, M. I., Mumtaz, U., Majeed, A. M., & Masood, H. T. (2021). A density functional theory study of the structural, electronic, and optical properties of $XGaO_3$ (X = V, Nb) perovskites for optoelectronic applications. *Journal of Computational Electronics*, *20*(4), 1484–1495.

Saeed, M., Jamal, M. A., Haq, A. U., Ilyas, M., Younas, M., & Shahzad, M. A. (2016). Oxidative Degradation of Methylene Blue in Aqueous Medium Catalyzed by Lab Prepared Nickel Hydroxide. *International Journal of Chemical Reactor Engineering*, *14*(1), 45–51.

Saha, M., Ghosh, S., Ashok, V. D., & De, S. K. (2015). Carrier concentration dependent optical and electrical properties of Ga doped ZnO hexagonal nanocrystals. *Physical Chemistry Chemical Physics*, *17*(24), 16067–16079.

Sakaguchi Miyamoto, N., Miyamoto, R., Giamello, E., Kurisaki, T., & Wakita, H. (2018). Characterization and photocatalytic properties of lutetium ion-doped titanium dioxide photocatalyst. *Research on Chemical Intermediates*, *44*(7), 4577–4594.

Sakib, A. A. M., Masum, S. M., Hoinkis, J., Islam, R., & Molla, M. A. I. (2019). Synthesis of CuO/ZnO nanocomposites and their application in photodegradation of toxic textile dye. *Journal of Composites Science*, *3*(3), 1–13.

Salavati-Niasari, M., Mohandes, F., & Davar, F. (2009). Preparation of PbO nanocrystals via decomposition of lead oxalate. *Polyhedron*, *28*(11), 2263–2267.

Samberg, J. P., Kajbafvala, A., & Koolivand, A. (2014). PbO networks composed of single crystalline nanosheets synthesized by a facile chemical precipitation method. *Materials*

Research Bulletin, *51*, 356–360.

Sangpour, P., Hashemi, F., & Moshfegh, A. Z. (2010). Photoenhanced degradation of methylene blue on cosputtered M:TiO_2 (M = Au, Ag, Cu) nanocomposite systems: A comparative study. *Journal of Physical Chemistry C*, *114*(33), 13955–13961.

Saqib, N. U., Adnan, R., & Shah, I. (2019). Zeolite supported TiO_2 with enhanced degradation efficiency for organic dye under household compact fluorescent light. *Materials Research Express*, *6*(9), 2–14.

Saroj, S., Singh, L., & Singh, S. V. (2020). Solution-combustion synthesis of anion (iodine) doped TiO_2 nanoparticles for photocatalytic degradation of Direct Blue 199 dye and regeneration of used photocatalyst. *Journal of Photochemistry and Photobiology A: Chemistry*, *396*, 112532.

Schileo, G., & Grancini, G. (2021). Lead or no lead? Availability, toxicity, sustainability and environmental impact of lead-free perovskite solar cells. *Journal of Materials Chemistry C*, *9*(1), 67–76.

Senthil, R. A., Priya, A., Theerthagiri, J., Selvi, A., Nithyadharseni, P., & Madhavan, J. (2018). Facile synthesis of α-Fe_2O_3/WO_3 composite with an enhanced photocatalytic and photo-electrochemical performance. *Ionics*, *24*(11), 3673–3684.

Senvaitiene, J., Smirnova, J., Beganskiene, A., & Kareiva, A. (2007). XRD and FTIR characterisation of lead oxide-based pigments and glazes. *Acta Chimica Slovenica*, *54*(1), 185–193.

Shahat, A. M., El-Hossary, F. M., Ghitas, A., Abd El-Rahman, A. M., & Ebnalwaled, A. A. (2021). Low-temperature Hydrothermal Synthesis of Titanium Dioxide Nanoparticles for Photocatalytic Applications. *IOP Conference Series: Materials Science and Engineering*, *1171*(1), 012008.

Shaikh, S. K., Inamdar, S. I., Ganbavle, V. V., & Rajpure, K. Y. (2016). Chemical bath deposited ZnO thin film based UV photoconductive detector. *Journal of Alloys and Compounds*, *664*(December), 242–249.

Shakoor, S., & Nasar, A. (2017). Adsorptive treatment of hazardous methylene blue dye from artificially contaminated water using cucumis sativus peel waste as a low-cost adsorbent. *Groundwater for Sustainable Development*, *5*, 152–159.

Shanmugam, N., Sathya, T., Viruthagiri, G., Kalyanasundaram, C., Gobi, R., & Ragupathy, S.

(2016). Photocatalytic degradation of brilliant green using undoped and Zn doped SnO_2 nanoparticles under sunlight irradiation. *Applied Surface Science*, *360*, 283–290.

Sharda, D., Attri, K., Kaur, P., & Choudhury, D. (2021). Protection of lead-induced cytotoxicity using paramagnetic nickel-insulin quantum clusters. *RSC Advances*, *11*(40), 24656–24668.

Shimoni-Livny, L., Glusker, J. P., & Bock, C. W. (1998). Lone Pair Functionality in Divalent Lead Compounds. *Inorganic Chemistry*, *37*(8), 1853–1867.

Shlapa, Y., Sarnatskaya, V., Timashkov, I., Yushko, L., Antal, I., Gerashchenko, B., Nychyporenko, I., Belous, A., Nikolaev, V., & Timko, M. (2019). Synthesis of CeO_2 nanoparticles by precipitation in reversal microemulsions and their physical–chemical and biological properties. *Applied Physics A: Materials Science and Processing*, *125*(6), 1–10.

Siddiqui, H., Parra, M. R., Malik, M. M., & Haque, F. Z. (2018). Structural and optical properties of Li substituted CuO nanoparticles. *Optical and Quantum Electronics*, *50*, 1–13.

Singh, S., & Sharma, R. (2018). Bi_2O_3/Ni-Bi_2O_3 system obtained via Ni-doping for enhanced PEC and photocatalytic activity supported by DFT and experimental study. *Solar Energy Materials and Solar Cells*, *186*, 208–216.

Siriwong, C., Wetchakun, N., Inceesungvorn, B., Channei, D., Samerjai, T., & Phanichphant, S. (2012). Doped-metal oxide nanoparticles for use as photocatalysts. *Progress in Crystal Growth and Characterization of Materials*, *58*(2), 145–163.

Siva, N., Sakthi, D., Ragupathy, S., Arun, V., & Kannadasan, N. (2020). Synthesis, structural, optical and photocatalytic behavior of Sn doped ZnO nanoparticles. *Materials Science and Engineering B: Solid-State Materials for Advanced Technology*, *253*, 114497.

Slama, H. Ben, Bouket, A. C., Pourhassan, Z., Alenezi, F. N., Silini, A., Cherif-Silini, H., Oszako, T., Luptakova, L., Golińska, P., & Belbahri, L. (2021). Diversity of synthetic dyes from textile industries, discharge impacts and treatment methods. *Applied Sciences*, *11*(14), 1–21.

Song, L. N., Ding, F., Yang, Y. K., Ding, D., Chen, L., Au, C. T., & Yin, S. F. (2018). Synthesis of TiO_2/Bi_2MoO_6 Composite for Partial Oxidation of Aromatic Alkanes under Visible-Light Illumination. *ACS Sustainable Chemistry and Engineering*, *6*(12), 17044–17050.

Song, Y., You, K., Chen, Y., Zhao, J., Jiang, X., Ge, Y., Wang, Y., Zheng, J., Xing, C., & Zhang, H. (2019). Lead monoxide: A promising two-dimensional layered material for applications in nonlinear photonics in the infrared band. *Nanoscale*, *11*(26), 12595–12602.

Sood, S., Umar, A., Mehta, S. K., & Kansal, S. K. (2015). Highly effective Fe-doped TiO_2 nanoparticles photocatalysts for visible-light driven photocatalytic degradation of toxic organic compounds. *Journal of Colloid and Interface Science*, *450*, 213–223.

Soylu, M., & Coskun, M. (2018). Controlling the properties of ZnO thin films by varying precursor concentration. *Journal of Alloys and Compounds*, *741*, 957–968.

Srichai, K., Krataitong, C., & Tubtimtae, A. (2021). *Antimony-doped lead oxide nanoparticles synthesized via using chemical precipitation and annealing treatments : structural and optical properties*. *18*(10), 607–615.

Sriwong, C., Choojun, K., & Sriwong, S. (2019). High photocatalytic performance of 3D porous-structured TiO_2@natural rubber hybrid sheet on the removal of indigo carmine dye in water. *SN Applied Sciences*, *1*(8), 1–10.

Stankic, S., Suman, S., Haque, F., & Vidic, J. (2016). Pure and multi metal oxide nanoparticles: Synthesis, antibacterial and cytotoxic properties. *Journal of Nanobiotechnology*, *14*, 1–20.

Suganya, M., Balu, A. R., & Usharani, K. (2014). Role of substrate temperature on the growth mechanism and physical properties of spray deposited lead oxide thin films. *Materials Science- Poland*, *32*(3), 448–456.

Sukumar, S., Rudrasenan, A., & Padmanabhan Nambiar, D. (2020). Green-Synthesized Rice-Shaped Copper Oxide Nanoparticles Using Caesalpinia bonducella Seed Extract and Their Applications. *ACS Omega*, *5*(2), 1040–1051.

Suryawanshi, V. N., Varpe, A. S., & Deshpande, M. D. (2018). Band gap engineering in PbO nanostructured thin films by Mn doping. *Thin Solid Films*, *645*, 87–92.

Suthakaran, S., Dhanapandian, S., Krishnakumar, N., & Ponpandian, N. (2019). Hydrothermal synthesis of SnO_2 nanoparticles and its photocatalytic degradation of methyl violet and electrochemical performance. *Materials Research Express*, *6*(8), 1–19.

Takahashi, A. (2016). Fundamental of rate theory for CMNS. *Journal of Condensed Matter Nuclear Science*, *19*, 298–315.

Tanko, Y., Shuaibu, A., Abdulrahman, A., Olusola, O., Isa, M., & Yamusa, A. (2021). Effect of Doping Concentration on Structural Stability and Formation Energy of the Fluorine Doped Hexagonal Molybdenum Dioxide (MoO_2). A First Principle Study. *Physics Access*, *01*, 55–59.

Tayebee, R., Maleki, B., & sabeti, M. (2017). A new simple method for the preparation of PbO

nanoparticles and implementation of an efficient and reusable catalytic system for the synthesis of 1H-pyrazolo[1,2-b]phthalazine-5,10-diones. *Journal of the Iranian Chemical Society*, *14*(6), 1179–1188.

Temerov, F., Baghdadi, Y., Rattner, E., & Eslava, S. (2022). A Review on Halide Perovskite-Based Photocatalysts: Key Factors and Challenges. *ACS Applied Energy Materials*, *5*, 14605–14637.

Tian, D., Zeng, C., Fu, Y., Luo, H., Xiang, C., Li, K., & Zhu, X. (2016). A DFT study of the structural, electronic and optical properties of transition metal doped fluorite oxides:$Ce_{0.75}M_{0.25}O_2$ (M=Fe, Co, Ni). *Solid State Communications*, *2*, 0–20.

Tong, H., Ouyang, S., Bi, Y., Umezawa, N., Oshikiri, M., & Ye, J. (2012). Nano-photocatalytic materials: Possibilities and challenges. *Advanced Materials*, *24*(2), 229–251.

Touati, A., Hammedi, T., Najjar, W., Ksibi, Z., & Sayadi, S. (2016). Photocatalytic degradation of textile wastewater in presence of hydrogen peroxide: Effect of cerium doping titania. *Journal of Industrial and Engineering Chemistry*, *35*, 36–44.

Toulouse, J. (2019). Introduction to density-functional theory. *Paris, France,*1–81.

Tulinska, J., Krivosikova, Z., Liskova, A., Lehotska Mikusova, M., Masanova, V., Rollerova, E., Stefikova, K., Wsolova, L., Babelova, A., Tothova, L., Busova, M., Babickova, J., Uhnakova, I., Alacova, R., Dusinska, M., Horvathova, M., Szabova, M., Vecera, Z., Mikuska, P., … Docekal, B. (2022). Six-week inhalation of lead oxide nanoparticles in mice affects antioxidant defense, immune response, kidneys, intestine and bones. *Environmental Science: Nano*, *9*(2), 751–766.

Uddin, M. T., Hoque, M. E., & Chandra Bhoumick, M. (2020). Facile one-pot synthesis of heterostructure SnO_2/ZnO photocatalyst for enhanced photocatalytic degradation of organic dye. *RSC Advances*, *10*(40), 23554–23565.

Uma, B., Anantharaju, K. S., Renuka, L., Malini, S., More, S. S., Vidya, Y. S., & Meena, S. (2021). Synthesis of CuO samples by co-precipitation and green mediated combustion routes: Comparison of their structural, optical properties, photocatalytic, antibacterial, haemolytic and cytotoxic activities. *Ceramics International*, *47*(7), 10355–10369.

Urhan, B. K., Öznülüer, T., Demġr, Ü., & Doğan, H. Ö. (2019). One-Pot Electrochemical Synthesis of Lead Oxide-Electrochemically Reduced Graphene Oxide Nanostructures and Their Electrocatalytic Applications. *IEEE Sensors. 19*, 4781-4788.

Uribe-López, M. C., Hidalgo-López, M. C., López-González, R., Frías-Márquez, D. M., Núñez-Nogueira, G., Hernández-Castillo, D., & Alvarez-Lemus, M. A. (2021). Photocatalytic activity of ZnO nanoparticles and the role of the synthesis method on their physical and chemical properties. *Journal of Photochemistry and Photobiology A: Chemistry*, *404*, 2-10.

Velempini, T., Prabakaran, E., & Pillay, K. (2021). Recent developments in the use of metal oxides for photocatalytic degradation of pharmaceutical pollutants in water—a review. *Materials Today Chemistry*, *19*, 100380.

Wang, Changhua, Zhang, X., Yuan, B., Wang, Y., Sun, P., Wang, D., Wei, Y., & Liu, Y. (2014). Multi-heterojunction photocatalysts based on WO_3 nanorods: Structural design and optimization for enhanced photocatalytic activity under visible light. *Chemical Engineering Journal*, *237*, 29–37.

Wang, Chunlan, Guo, G., Zhu, C., Li, Y., Jin, Y., Zou, B., He, H., & Wang, A. (2022). Facile Synthesis, Characterization, and Photocatalytic Evaluation of In_2O_3/SnO_2 Microsphere Photocatalyst for Efficient Degradation of Rhodamine B. *Nanomaterials*, *12*, 2–13.

Wang, Congjun, Kwon, K. W., Odlyzko, M. L., Lee, B. H., & Shim, M. (2007). PbSe nanocrystal/TiO_x heterostructured films: A simple route to nanoscale heterointerfaces and photocatalysis. *Journal of Physical Chemistry C*, *111*(31), 11734–11741.

Wang, S., Wang, Z., & Zha, Z. (2009). Metal nanoparticles or metal oxide nanoparticles, an efficient and promising family of novel heterogeneous catalysts in organic synthesis. *Dalton Transactions*, *43*, 9363.

Wang, Y. C., Lee, A. H., & Chen, C. C. (2018). Perovskite-like photocatalyst, $PbBiO_2Br/PbO/g\text{-}C_3N_4$: Synthesis, characterization, and visible-light-driven photocatalytic activity. *Journal of the Taiwan Institute of Chemical Engineers*, *93*, 315–328.

Wang, Yanfen, Gao, J., Wang, X., Jin, L., Fang, L., Zhang, M., He, G., & Sun, Z. (2018). Facile synthesis of core-shell ZnO/Cu_2O heterojunction with enhanced visible light-driven photocatalytic performance. *Journal of Sol-Gel Science and Technology*, *88*(1), 172–180.

Wang, Yanjie, Gao, R., Zhao, H., Li, J., Zhang, R., Wang, Y., & Zhou, Y. (2023). Oxygen vacancy-rich ZnO nanorods-based MEMS sensors for swift trace ethanol recognition. *Journal of the American Ceramic Society*, *106*(2), 1050–1061.

Wang, Yonggang, Lin, X., Zhang, H., Wen, T., Huang, F., Li, G., Wang, Y., Liao, F., & Lin, J. (2013). Selected-control hydrothermal growths of α- And β-PbO crystals and orientated

pressure-induced phase transition. *CrystEngComm*, *15*(18), 3513–3516.

Wang, Yuan, Wang, S., Wu, Y., Wang, Z., Zhang, H., Cao, Z., He, J., Li, W., Yang, Z., Zheng, L., Feng, D., Pan, P., Bi, J., Li, H., Zhao, J., & Zhang, K. (2021). A α-Fe_2O_3/rGO magnetic photocatalyst: Enhanced photocatalytic performance regulated by magnetic field. *Journal of Alloys and Compounds*, *851*, 156733.

Wang, Yuliang, & Xia, Y. (2004). Bottom-Up and Top-Down Approaches to the Synthesis of Monodispersed Spherical Colloids of Low Melting-Point Metals. *Nano Letters*, *4*(10), 2047–2050.

Wang, Z., Deb, A., Srivastava, V., Iftekhar, S., Ambat, I., & Sillanpää, M. (2019). Investigation of textural properties and photocatalytic activity of PbO/TiO_2 and Sb_2O_3/TiO_2 towards the photocatalytic degradation Benzophenone-3 UV filter. *Separation and Purification Technology*, *228*, 1–13.

Wang, Z., Srivastava, V., Iftekhar, S., Ambat, I., & Sillanpää, M. (2018). Fabrication of Sb_2O_3/PbO photocatalyst for the UV/PMS assisted degradation of carbamazepine from synthetic wastewater. *Chemical Engineering Journal*, *354*, 663–671.

Wani, A. L., Ara, A., & Usmani, J. A. (2015). Lead toxicity: A review. *Interdisciplinary Toxicology*, *8*(2), 55–64.

Wei, W., Yue, X., Cui, H., Lü, X., & Xie, J. (2013). Hydrothermal synthesis and properties of $BiVO_4$ photocatalysts. *Journal of Materials Research*, *28*(24), 3408–3416.

Wongwailikhit, K., & Horwongsakul, S. (2011). The preparation of iron (III) oxide nanoparticles using W/O microemulsion. *Materials Letters*, *65*(17–18), 2820–2822.

Xiao, Q., Zhang, J., Xiao, C., Si, Z., & Tan, X. (2008). Solar photocatalytic degradation of methylene blue in carbon-doped TiO_2 nanoparticles suspension. *Solar Energy*, *82*(8), 706–713.

Xie, W., Li, R., & Xu, Q. (2018). Enhanced photocatalytic activity of Se-doped TiO_2 under visible light irradiation. *Scientific Reports*, *8*(1), 1–10.

Xue, Y., Tian, D., Zhang, D., Zeng, C., Fu, Y., Li, K., Wang, H., & Tian, Y. (2019). The mechanism of photocatalyst and the effects of co-doping CeO_2 on refractive index and reflectivity from DFT calculation. *Computational Materials Science*, *158*, 197–208.

Y Kurniawan, Sh Muhammady, R. W. and Y. D. (2018). Optical properties and plasmonic states in two-dimensional alpha lead oxide systems: A density-functional study. *Materials*

Research Express, *6*, 1–10.

Yadav, P., Saini, R., & Bhaduri, A. (2022). Facile synthesis of MgO nanoparticles for effective degradation of organic dyes. *Environmental Science and Pollution Research*, *0123456789*.

Yadav, Sapna, Shakya, K., Gupta, A., Singh, D., Chandran, A. R., Varayil Aanappalli, A., Goyal, K., Rani, N., & Saini, K. (2022). A review on degradation of organic dyes by using metal oxide semiconductors. *Environmental Science and Pollution Research*, *0123456789*.

Yadav, Sushma, Chauhan, M., Mathur, D., Jain, A., & Malhotra, P. (2021). Sugarcane bagasse-facilitated benign synthesis of Cu_2O nanoparticles and its role in photocatalytic degradation of toxic dyes: a trash to treasure approach. *Environment, Development and Sustainability*, *23*(2), 2071–2091.

Yang, J., Xiao, Z., Li, Z., Wen, Q., & Yang, F. (2014). First principles study on the structural , electronic and magnetic properties of Ni_4C. *Computational Condensed Matter*, *1*, 51–57.

Yao, S., Zhou, S., Wang, J., Li, W., & Li, Z. (2019). Optimizing the synthesis of SnO_2/TiO_2/RGO nanocomposites with excellent visible light photocatalytic and antibacterial activities. *Photochemical and Photobiological Sciences*, *18*(12), 2989–2999.

Yao, W., Li, D., Wei, S., Liu, X., Liu, X., & Wang, W. (2022). Density Functional Theory Study on the Enhancement Mechanism of the Photocatalytic Properties of the g-C_3N_4/BiOBr(001) Heterostructure. *ACS Omega*, *7*(41), 36479–36488.

Yazdani Darki, S., Eslami-Kalantari, M., Zare, H., & Shahedi, Z. (2021). Effects of PVP surfactant and different alkalis on the properties of PbO nanostructures. *Materials Chemistry and Physics*, *262*, 2–6.

Yildirim, Ö. A., & Durucan, C. (2010). Synthesis of zinc oxide nanoparticles elaborated by microemulsion method. *Journal of Alloys and Compounds*, *506*(2), 944–949.

Yousefi, R., Sheini, F. J., Sa´aedi, A., & Cheraghizade, M. (2015). Growth and Characterization of PbO Nanorods Grown using Facile Oxidation of Lead Sheet. *Sains Malaysiana*, *44*(2), 291–294.

Yu, N., Gao, L., Zhao, S., & Wang, Z. (2009). Electrodeposited PbO_2 thin film as positive electrode in PbO_2/AC hybrid capacitor. *Electrochimica Acta*, *54*(14), 3835–3841.

Zahid, A. H., & Han, Q. (2021). A review on the preparation, microstructure, and photocatalytic performance of Bi_2O_3 in polymorphs. *Nanoscale*, *13*(42), 17687–17724.

Zhan, L., Xiang, X., Xie, B., & Gao, B. (2017). Preparing lead oxide nanoparticles from waste

electric and electronic equipment by high temperature oxidation-evaporation and condensation. *Powder Technology*, *308*, 30–36.

Zhang, T., Liu, J., Zhou, F., Zhou, S., Wu, J., Chen, D., Xu, Q., & Lu, J. (2020). Polymer-Coated Fe_2O_3 Nanoparticles for Photocatalytic Degradation of Organic Materials and Antibiotics in Water. *ACS Applied Nano Materials*, *3*(9), 9200–9208.

Zhang, Z., Sun, L., Wu, Z., Liu, Y., & Li, S. (2020). Facile hydrothermal synthesis of CuO-Cu_2O/GO nanocomposites for the photocatalytic degradation of organic dye and tetracycline pollutants. *New Journal of Chemistry*, *44*(16), 6420–6427.

Zhou, M., Tian, X., Yu, H., Wang, Z., Ren, C., Zhou, L., Lin, Y. W., & Dou, L. (2021). WO_3/Ag_2CO_3 Mixed Photocatalyst with Enhanced Photocatalytic Activity for Organic Dye Degradation. *ACS Omega*, *6*(40), 26439–26453.

Zhu, D., & Zhou, Q. (2019). Action and mechanism of semiconductor photocatalysis on degradation of organic pollutants in water treatment: A review. *Environmental Nanotechnology, Monitoring and Management*, *12*, 1–12.

Zhu, J., & Zäch, M. (2009). Nanostructured materials for photocatalytic hydrogen production. *Current Opinion in Colloid and Interface Science*, *14*(4), 260–269.

Zori, M. H. (2011). Synthesis of TiO_2 Nanoparticles by Microemulsion/Heat Treated Method and Photodegradation of Methylene Blue. *Journal of Inorganic and Organometallic Polymers and Materials*, *21*, 81–90.

APPENDIX: Rietveld refinement using GSAS II software

Table A20: hkl plane, d-space, 2-theta position, and FWHM of pristine and different metal doped α-PbO nanoparticles obtained from Rietveld refinement by using GSAS-II software.

Pristine α-PbO						Li:α-PbO					
h	**k**	**l**	**d-space**	**2-theta**	**FWHM**	**h**	**k**	**l**	**d-space**	**2-theta**	**FWHM**
0	0	1	5.01702	17.605	0.13076	0	0	1	5.01768	17.643	0.14696
1	0	1	3.11379	28.586	0.17075	1	0	1	3.11463	28.619	0.18821
1	1	0	2.80807	31.783	0.18352	1	1	0	2.80907	31.812	0.20152
0	0	2	2.50851	35.706	0.1998	0	0	2	2.50884	35.742	0.21858
1	1	1	2.45036	36.584	0.20354	1	1	1	2.4511	36.614	0.22247
1	0	2	2.12083	42.534	0.22974	1	0	2	2.12124	42.566	0.24998
2	0	0	1.9856	45.592	0.24384	2	0	0	1.98631	45.616	0.26475
1	1	2	1.87076	48.569	0.25798	1	1	2	1.87119	48.598	0.27966
2	0	1	1.84626	49.257	0.26131	2	0	1	1.84687	49.281	0.28313
2	1	1	1.67418	54.726	0.28866	2	1	1	1.67473	54.747	0.31193
0	0	3	1.67234	54.792	0.289	0	0	3	1.67256	54.824	0.31235
2	0	2	1.55689	59.247	0.31254	2	0	2	1.55731	59.27	0.33711
1	0	3	1.54125	59.91	0.31614	1	0	3	1.54151	59.94	0.34096
2	1	2	1.44948	64.142	0.33985	2	1	2	1.44989	64.162	0.36592
1	1	3	1.43683	64.776	0.3435	1	1	3	1.43711	64.803	0.36981
2	2	0	1.40403	66.484	0.3535	2	2	0	1.40453	66.498	0.38029
2	2	1	1.35208	69.397	0.37107	2	2	1	1.35255	69.411	0.39885
3	0	1	1.27993	73.939	0.39986	3	0	1	1.28037	73.95	0.42926
2	0	3	1.27911	73.994	0.40023	2	0	3	1.2794	74.015	0.42971
3	1	0	1.2558	75.607	0.41091	3	1	0	1.25625	75.616	0.44092
0	0	4	1.25426	75.717	0.41165	0	0	4	1.25442	75.746	0.44184
2	2	2	1.22518	77.848	0.42618	2	2	2	1.22555	77.861	0.4571
3	1	1	1.21822	78.378	0.42987	3	1	1	1.21864	78.387	0.46097
2	1	3	1.21751	78.433	0.43025	2	1	3	1.2178	78.451	0.46144
Sn:α-PbO						**Cu:α-PbO**					
h	**k**	**l**	**d-space**	**2-theta**	**FWHM**	**h**	**k**	**l**	**d-space**	**2-theta**	**FWHM**
0	0	1	5.01536	17.613	0.15076	0	0	1	5.02017	17.646	0.15451
1	0	1	3.11356	28.59	0.19662	1	0	1	3.11341	28.641	0.21981
1	1	0	2.80832	31.782	0.21085	1	1	0	2.80641	31.854	0.24012
0	0	2	2.50768	35.72	0.22897	0	0	2	2.51009	35.734	0.26536
1	1	1	2.45033	36.587	0.23304	1	1	1	2.44962	36.648	0.27142
1	0	2	2.12038	42.545	0.26194	1	0	2	2.12142	42.573	0.31182
2	0	0	1.98578	45.59	0.27733	2	0	0	1.98443	45.672	0.33376
1	1	2	1.87049	48.579	0.2929	1	1	2	1.87092	48.617	0.35516
2	0	1	1.84632	49.258	0.29649	2	0	1	1.84548	49.332	0.36044
2	1	1	1.67425	54.726	0.32642	2	1	1	1.67342	54.805	0.4021

0	0	3	1.67179	54.813	0.32691	0	0	3	1.67339	54.806	0.40211
2	0	2	1.55678	59.253	0.35257	2	0	2	1.55671	59.306	0.4381
1	0	3	1.54084	59.929	0.3566	1	0	3	1.54194	59.932	0.44325
2	1	2	1.44941	64.148	0.38243	2	1	2	1.44921	64.207	0.47934
1	1	3	1.43652	64.794	0.38651	1	1	3	1.43728	64.805	0.48454
2	2	0	1.40416	66.479	0.3973	2	2	0	1.4032	66.58	0.50017
2	2	1	1.35216	69.395	0.41652	2	2	1	1.35141	69.489	0.52653
3	0	1	1.28001	73.935	0.44801	3	0	1	1.27928	74.035	0.56974
2	0	3	1.27891	74.009	0.44854	2	0	3	1.27927	74.035	0.56975
3	1	0	1.25592	75.601	0.46008	3	1	0	1.25506	75.711	0.58636
0	0	4	1.25384	75.748	0.46116	0	0	4	1.25504	75.712	0.58638
2	2	2	1.22517	77.851	0.47686	2	2	2	1.22481	77.928	0.60895
3	1	1	1.2183	78.374	0.48084	3	1	1	1.21759	78.479	0.61468
2	1	3	1.21735	78.447	0.4814	2	1	3	1.21758	78.479	0.61469
Ni:α-PbO						**Co:α-PbO**					
h	**k**	**l**	**d-space**	**2-theta**	**FWHM**	**h**	**k**	**l**	**d-space**	**2-theta**	**FWHM**
0	0	1	5.02372	17.581	0.18709	0	0	1	5.04285	17.21	0.40137
1	0	1	3.11398	28.584	0.2501	1	0	1	3.09401	28.469	0.66221
1	1	0	2.806	31.806	0.26961	1	1	0	2.77056	31.922	0.74499
0	0	2	2.51186	35.656	0.29356	0	0	2	2.52143	35.213	0.82533
1	1	1	2.44976	36.593	0.29951	1	1	1	2.42822	36.627	0.86031
1	0	2	2.1224	42.5	0.33805	1	0	2	2.12033	42.241	1.00228
2	0	0	1.98414	45.627	0.35925	2	0	0	1.95908	45.942	1.09889
1	1	2	1.87153	48.548	0.37961	1	1	2	1.86479	48.432	1.16538
2	0	1	1.84542	49.281	0.38481	2	0	1	1.82612	49.535	1.19526
0	0	3	1.67457	54.712	0.4245	0	0	3	1.68095	54.184	1.32427
2	1	1	1.67333	54.756	0.42484	2	1	1	1.65518	55.105	1.35048
2	0	2	1.55699	59.242	0.45937	2	0	2	1.54701	59.361	1.47446
1	0	3	1.54283	59.842	0.46412	1	0	3	1.54479	59.455	1.47728
2	1	2	1.44942	64.145	0.49915	2	1	2	1.43891	64.367	1.62732
1	1	3	1.43797	64.718	0.50396	1	1	3	1.43713	64.458	1.63015
2	2	0	1.403	66.539	0.51944	2	2	0	1.38528	67.201	1.71761
2	2	1	1.35129	69.444	0.5449	2	2	1	1.33579	70.065	1.81193
2	0	3	1.27972	73.953	0.5864	2	0	3	1.27571	73.921	1.9443
3	0	1	1.27916	73.99	0.58676	3	0	1	1.26434	74.704	1.97199
0	0	4	1.25593	75.597	0.6022	0	0	4	1.26071	74.957	1.98101
3	1	0	1.25488	75.672	0.60292	3	1	0	1.23903	76.513	2.03711
2	2	2	1.22488	77.87	0.62466	2	2	2	1.21411	78.392	2.1065
2	1	3	1.21795	78.399	0.63	2	1	3	1.21304	78.475	2.10962
3	1	1	1.21747	78.435	0.63037	3	1	1	1.20324	79.244	2.13857

Table A21: lattice constants $a = b$, and c of pristine and different metal doped α-PbO obtained from Rietveld refinement by using GSAS-II software.

Materials	Lattice constants (Å)		
	a	*c*	Cell volume $(Å)^3$
Pristine α-PbO	3.97729(19)	5.02313(29)	79.460(7)
Sn:α-PbO	3.9716(4)	5.0154(4)	79.109(18)
Co:α-PbO	3.9182(29)	5.0429(30)	77.42(14)
Cu:α-PbO	3.9689(7)	5.0202(8)	79.08(4)
Ni:α-PbO	3.9683(12)	5.0237(17)	79.11(7)
Li: α-PbO	3.9726(5)	5.0177(4)	79.188(21)

Table A22: hkl plane, d-space, 2-theta position, and FWHM of pristine and different metal doped β-PbO obtained from Rietveld refinement by using GSAS-II software.

β-PbO						Li:β-PbO					
h	**k**	**l**	**d-space**	**2-theta**	**FWHM**	**h**	**k**	**l**	**d-space**	**2-theta**	**FWHM**
0	1	0	5.88674	15.016	0.10613	0	1	0	5.89127	15.073	0.1115
1	1	0	4.01341	22.108	0.10767	1	1	0	4.01759	22.154	0.11368
1	1	1	3.06552	29.083	0.10955	1	1	1	3.06856	29.123	0.11625
0	2	0	2.94337	30.319	0.10993	0	2	0	2.94563	30.365	0.11676
2	0	0	2.74303	32.595	0.11065	2	0	0	2.74654	32.621	0.11771
2	1	0	2.59366	34.531	0.1113	2	1	0	2.59594	34.568	0.11858
1	2	0	2.48636	36.072	0.11184	1	2	0	2.4893	36.097	0.11929
0	2	1	2.37535	37.821	0.11248	0	2	1	2.37817	37.844	0.12013
2	0	1	2.37478	37.831	0.11248	2	0	1	2.37697	37.863	0.12014
2	1	1	2.27636	39.534	0.11314	2	1	1	2.27839	39.566	0.12099
1	2	1	2.20278	40.913	0.11368	1	2	1	2.20527	40.934	0.1217
1	0	2	2.20233	40.922	0.11369	1	0	2	2.20431	40.953	0.12171
1	1	2	2.04379	44.259	0.1151	1	1	2	2.04574	44.284	0.12353
2	2	0	2.00671	45.122	0.11548	2	2	0	2.00879	45.142	0.12402
3	0	0	1.96225	46.203	0.11597	3	0	0	1.96376	46.235	0.12466
2	2	1	1.84849	49.231	0.11742	2	2	1	1.85038	49.246	0.1265
2	0	2	1.84822	49.238	0.11742	2	0	2	1.84982	49.262	0.12651
0	2	2	1.84762	49.255	0.11743	0	2	2	1.84914	49.281	0.12652
3	1	0	1.79541	50.788	0.1182	3	1	0	1.79734	50.799	0.1275
2	1	2	1.7515	52.157	0.11892	2	1	2	1.75308	52.175	0.12841
1	3	0	1.74637	52.322	0.11901	1	3	0	1.74852	52.321	0.12851
1	2	2	1.72192	53.123	0.11944	1	2	2	1.72336	53.144	0.12907
1	3	1	1.71731	53.276	0.11952	1	3	1	1.71911	53.285	0.12917
3	1	1	1.63908	56.038	0.12108	3	1	1	1.64104	56.034	0.13112
3	2	0	1.59594	57.694	0.12206	3	2	0	1.59744	57.703	0.13236
2	3	0	1.55331	59.434	0.12314	2	3	0	1.55507	59.429	0.1337
2	2	2	1.53276	60.313	0.1237	2	2	2	1.53428	60.316	0.1344

3	2	1	1.51282	61.193	0.12427	3	2	1	1.51424	61.199	0.13512
3	0	2	1.51267	61.2	0.12427	3	0	2	1.51393	61.212	0.13513
2	3	1	1.47636	62.874	0.1254	2	3	1	1.47801	62.865	0.13651
1	1	3	1.47274	63.047	0.12552	1	1	3	1.47413	63.05	0.13666
0	4	0	1.47169	63.097	0.12555	0	4	0	1.47282	63.112	0.13672
3	1	2	1.45825	63.747	0.126	3	1	2	1.45951	63.754	0.13727
4	1	0	1.42143	65.603	0.12733	4	1	0	1.42257	65.613	0.13891
1	3	2	1.4069	66.367	0.12789	1	3	2	1.40849	66.352	0.13959
4	4	0	1.37152	68.312	0.12937	4	4	0	1.37327	68.282	0.14139
0	2	3	1.37119	68.331	0.12939	0	2	3	1.37258	68.321	0.14143
4	1	1	1.36175	68.871	0.12981	4	1	1	1.36286	68.876	0.14197
2	1	3	1.35133	69.479	0.13029	2	1	3	1.35256	69.475	0.14255
3	3	0	1.3378	70.284	0.13094	3	3	0	1.3392	70.269	0.14334
1	4	0	1.33574	70.409	0.13105	1	4	0	1.33741	70.377	0.14345
1	2	3	1.33544	70.427	0.13106	1	2	3	1.33677	70.415	0.14348
3	2	2	1.32461	71.09	0.13161	3	2	2	1.32585	71.082	0.14416
0	4	1	1.31768	71.521	0.13197	0	4	1	1.31932	71.487	0.14457
2	3	2	1.29993	72.653	0.13293	2	3	2	1.30132	72.631	0.14577
4	2	0	1.29683	72.854	0.13311	4	2	0	1.29797	72.849	0.146
3	3	1	1.2877	73.455	0.13364	3	3	1	1.28903	73.436	0.14662
1	4	1	1.28586	73.578	0.13374	1	4	1	1.28744	73.542	0.14674
4	2	1	1.25103	75.983	0.13593	4	2	1	1.25214	75.973	0.14943
4	0	2	1.25095	75.989	0.13594	4	0	2	1.25196	75.986	0.14944
2	4	0	1.24318	76.55	0.13647	2	4	0	1.24465	76.512	0.15005
2	2	3	1.24293	76.568	0.13649	2	2	3	1.24414	76.549	0.15009
4	1	2	1.21964	78.306	0.13818	4	1	2	1.22066	78.297	0.15215
2	4	1	1.20266	79.63	0.13951	2	4	1	1.20407	79.588	0.15372
3	1	3	1.2022	79.667	0.13955	3	1	3	1.20326	79.652	0.1538
Sn:β-PbO						**Cu:β-PbO**					
h	**k**	**l**	**d-space**	**2-theta**	**FWHM**	**h**	**k**	**l**	**d-space**	**2-theta**	**FWHM**
0	1	0	5.88651	15.009	0.12185	0	1	0	5.88733	15.038	0.13097
1	1	0	4.01263	22.106	0.12492	1	1	0	4.01363	22.131	0.13326
1	1	1	3.06539	29.078	0.12858	1	1	1	3.06599	29.102	0.13604
0	2	0	2.94326	30.314	0.1293	0	2	0	2.94366	30.34	0.13659
2	0	0	2.74213	32.599	0.13068	2	0	0	2.74307	32.618	0.13766
2	1	0	2.59339	34.528	0.13191	2	1	0	2.59386	34.552	0.13861
1	2	0	2.48567	36.076	0.13294	1	2	0	2.48643	36.095	0.1394
0	2	1	2.37518	37.817	0.13415	0	2	1	2.37555	37.842	0.14034
2	0	1	2.37486	37.822	0.13415	2	0	1	2.37547	37.843	0.14034
2	1	1	2.27626	39.529	0.13537	2	1	1	2.27665	39.552	0.14129
1	2	1	2.20264	40.909	0.1364	1	2	1	2.20297	40.933	0.14209

1	0	2	2.20238	40.914	0.1364	1	0	2	2.20291	40.934	0.14209
1	1	2	2.04395	44.249	0.13902	1	1	2	2.04426	44.272	0.14414
2	2	0	2.00632	45.124	0.13973	2	2	0	2.00682	45.143	0.1447
3	0	0	1.96217	46.198	0.14063	3	0	0	1.96244	46.222	0.14541
2	2	1	1.84839	49.227	0.14328	2	2	1	1.84866	49.249	0.1475
2	0	2	1.84823	49.231	0.14329	2	0	2	1.84862	49.25	0.1475
0	2	2	1.84748	49.252	0.14331	0	2	2	1.84778	49.274	0.14752
3	1	0	1.79533	50.784	0.14471	3	1	0	1.79572	50.803	0.14863
2	1	2	1.75158	52.147	0.14601	2	1	2	1.75184	52.169	0.14966
1	3	0	1.74584	52.332	0.14618	1	3	0	1.74641	52.344	0.14979
1	2	2	1.72185	53.118	0.14695	1	2	2	1.72212	53.14	0.1504
1	3	1	1.71724	53.272	0.1471	1	3	1	1.7176	53.29	0.15052
3	1	1	1.63867	56.046	0.14991	3	1	1	1.63917	56.058	0.15276
3	2	0	1.59572	57.695	0.15166	3	2	0	1.59605	57.713	0.15416
2	3	0	1.55292	59.443	0.15359	2	3	0	1.55337	59.455	0.1557
2	2	2	1.53269	60.309	0.15457	2	2	2	1.53299	60.327	0.15649
3	2	1	1.51274	61.19	0.15558	3	2	1	1.51296	61.211	0.15731
3	0	2	1.51266	61.194	0.15559	3	0	2	1.51294	61.211	0.15731
2	3	1	1.47605	62.882	0.15758	2	3	1	1.47645	62.894	0.15892
1	1	3	1.47292	63.031	0.15776	1	1	3	1.47312	63.052	0.15907
0	4	0	1.47163	63.093	0.15784	0	4	0	1.47183	63.114	0.15913
3	1	2	1.45828	63.738	0.15863	3	1	2	1.45849	63.759	0.15977
4	1	0	1.42135	65.6	0.16095	4	1	0	1.42156	65.62	0.16165
1	3	2	1.40671	66.371	0.16194	1	3	2	1.40707	66.382	0.16245
4	4	0	1.37125	68.321	0.16453	4	4	0	1.37154	68.335	0.16455
0	2	3	1.37106	68.331	0.16454	0	2	3	1.37149	68.337	0.16455
4	1	1	1.3617	68.867	0.16527	4	1	1	1.3619	68.886	0.16516
2	1	3	1.35146	69.464	0.16609	2	1	3	1.35164	69.484	0.16583
3	3	0	1.33754	70.293	0.16725	3	3	0	1.33788	70.303	0.16676
1	4	0	1.33549	70.417	0.16742	1	4	0	1.33577	70.431	0.16691
1	2	3	1.33532	70.427	0.16744	1	2	3	1.33573	70.433	0.16691
3	2	2	1.32455	71.087	0.16837	3	2	2	1.32479	71.102	0.16769
0	4	1	1.31729	71.538	0.16902	0	4	1	1.31773	71.542	0.16821
2	3	2	1.29977	72.656	0.17066	2	3	2	1.30008	72.667	0.16956
4	2	0	1.29669	72.856	0.17096	4	2	0	1.29693	72.871	0.1698
3	3	1	1.28748	73.463	0.17187	3	3	1	1.28779	73.473	0.17054
1	4	1	1.2855	73.595	0.17207	1	4	1	1.28591	73.598	0.1707
4	2	1	1.25097	75.981	0.17577	4	2	1	1.25115	75.998	0.17376
4	0	2	1.25093	75.984	0.17577	4	0	2	1.25114	75.999	0.17376
2	4	0	1.24297	76.558	0.17669	2	4	0	1.24322	76.571	0.17452
2	2	3	1.24283	76.568	0.17671	2	2	3	1.24318	76.573	0.17452

4	1	2	1.21965	78.299	0.17956	4	1	2	1.21982	78.316	0.17688
2	4	1	1.20236	79.647	0.18185	2	4	1	1.20272	79.649	0.17876
3	1	3	1.20228	79.654	0.18186	3	1	3	1.20245	79.671	0.17879
Co:β-PbO						**Ni:β-PbO**					
h	**k**	**l**	**d-space**	**2-theta**	**FWHM**	**h**	**k**	**l**	**d-space**	**2-theta**	**FWHM**
0	1	0	5.88845	15.086	0.1024	0	1	0	5.88873	15.119	0.08235
1	1	0	4.01415	22.179	0.10615	1	1	0	4.01411	22.213	0.09153
1	1	1	3.06643	29.149	0.11161	1	1	1	3.06643	29.183	0.10143
0	2	0	2.94423	30.385	0.11275	0	2	0	2.94436	30.417	0.10327
2	0	0	2.74327	32.667	0.11498	2	0	0	2.74311	32.702	0.10677
2	1	0	2.59429	34.597	0.117	2	1	0	2.59435	34.63	0.1098
1	2	0	2.48666	36.142	0.1187	1	2	0	2.48657	36.177	0.11229
0	2	1	2.37588	37.887	0.1207	0	2	1	2.37589	37.921	0.11515
2	0	1	2.37578	37.889	0.1207	2	0	1	2.37568	37.924	0.11516
2	1	1	2.27703	39.596	0.12275	2	1	1	2.27707	39.629	0.11802
1	2	1	2.20329	40.978	0.12447	1	2	1	2.20332	41.011	0.12039
1	0	2	2.20321	40.979	0.12447	1	0	2	2.20315	41.015	0.12039
1	1	2	2.04459	44.315	0.12886	1	1	2	2.0446	44.349	0.12629
2	2	0	2.00707	45.188	0.13006	2	2	0	2.00705	45.222	0.12787
3	0	0	1.96282	46.264	0.13157	3	0	0	1.96291	46.295	0.12985
2	2	1	1.84895	49.292	0.136	2	2	1	1.849	49.325	0.13557
2	0	2	1.84891	49.293	0.13601	2	0	2	1.84889	49.328	0.13558
0	2	2	1.84811	49.316	0.13604	0	2	2	1.84818	49.348	0.13562
3	1	0	1.79595	50.847	0.13839	3	1	0	1.79591	50.882	0.13861
2	1	2	1.75214	52.211	0.14053	2	1	2	1.75216	52.244	0.14132
1	3	0	1.74655	52.39	0.14082	1	3	0	1.74647	52.427	0.14169
1	2	2	1.72242	53.18	0.1421	1	2	2	1.72248	53.213	0.14328
1	3	1	1.71783	53.334	0.14235	1	3	1	1.7178	53.368	0.14359
3	1	1	1.63932	56.104	0.14698	3	1	1	1.63925	56.14	0.14935
3	2	0	1.59629	57.754	0.14985	3	2	0	1.59631	57.787	0.15288
2	3	0	1.55353	59.499	0.15298	2	3	0	1.55349	59.535	0.15671
2	2	2	1.53322	60.368	0.15457	2	2	2	1.53321	60.402	0.15865
3	2	1	1.51322	61.25	0.15622	3	2	1	1.51326	61.282	0.16064
3	0	2	1.51319	61.251	0.15622	3	0	2	1.51321	61.284	0.16065
2	3	1	1.47662	62.937	0.15944	2	3	1	1.47658	62.972	0.16454
1	1	3	1.47337	63.092	0.15974	1	1	3	1.47337	63.125	0.1649
0	4	0	1.47211	63.151	0.15985	0	4	0	1.47218	63.182	0.16503
3	1	2	1.45875	63.797	0.16111	3	1	2	1.45879	63.829	0.16655
4	1	0	1.42182	65.657	0.16483	4	1	0	1.42188	65.688	0.171
1	3	2	1.40723	66.425	0.1664	1	3	2	1.40719	66.461	0.17289
4	4	0	1.3717	68.377	0.17049	4	4	0	1.37168	68.412	0.17776

0	2	3	1.37164	68.38	0.1705	0	2	3	1.37156	68.419	0.17778
4	1	1	1.36215	68.923	0.17166	4	1	1	1.3622	68.954	0.17914
2	1	3	1.35187	69.521	0.17295	2	1	3	1.35189	69.554	0.18068
3	3	0	1.33805	70.344	0.17475	3	3	0	1.33804	70.379	0.18282
1	4	0	1.33593	70.472	0.17504	1	4	0	1.33592	70.506	0.18315
1	2	3	1.33587	70.475	0.17504	1	2	3	1.3358	70.513	0.18317
3	2	2	1.325	71.14	0.17652	3	2	2	1.32501	71.173	0.1849
0	4	1	1.31783	71.586	0.17752	0	4	1	1.31776	71.625	0.1861
2	3	2	1.30024	72.707	0.18008	2	3	2	1.30022	72.742	0.1891
4	2	0	1.29715	72.908	0.18054	4	2	0	1.29718	72.94	0.18964
3	3	1	1.28796	73.513	0.18194	3	3	1	1.28795	73.547	0.1913
1	4	1	1.28602	73.642	0.18225	1	4	1	1.28596	73.68	0.19166
4	2	1	1.25137	76.033	0.18797	4	2	1	1.25142	76.064	0.19835
4	0	2	1.25136	76.034	0.18797	4	0	2	1.25139	76.066	0.19836
2	4	0	1.24338	76.61	0.18938	2	4	0	1.24338	76.644	0.20002
2	2	3	1.24333	76.613	0.18939	2	2	3	1.24328	76.651	0.20004
4	1	2	1.22004	78.35	0.19375	4	1	2	1.22008	78.381	0.20511
2	4	1	1.20284	79.691	0.19721	2	4	1	1.20279	79.728	0.20916
3	1	3	1.20266	79.705	0.19725	3	1	3	1.20268	79.737	0.20919

Table A23: lattice constants *a*, *b*, and *c* of pristine and different metal doped β-PbO obtained from Rietveld refinement by using GSAS-II software.

Materials	**Lattice constants (Å)**			
	a	*b*	*c*	Cell volume $(Å)^3$
Pristine β-PbO	5.88674(26)	5.4861(4)	4.7496(3)	153.387(21)
Sn:β-PbO	5.8865(3)	5.4843(3)	4.7504(3)	153.357(22)
Co:β-PbO	5.88845(20)	5.48655(22)	4.75176(20)	153.517(13)
Cu:β-PbO	5.88733(19)	5.48615(21)	4.75094(20)	153.450(13)
Ni:β-PbO	5.88873(21)	5.48623(20)	4.75179(18)	153.516(13)
Li: β-PbO	5.89127(11)	5.4931(4)	4.7539(3)	153.843(11)